

Scatterometer Contamination Mitigation

Michael Paul Owen

A dissertation submitted to the faculty of  
Brigham Young University  
in partial fulfillment of the requirements for the degree of

Doctor of Philosophy

David G. Long, Chair  
Richard W. Christiansen  
Brian D. Jeffs  
Michael A. Jensen  
Wynn C. Stirling

Department of Electrical and Computer Engineering

Brigham Young University

December 2010

Copyright © 2010 Michael Paul Owen

All Rights Reserved



# ABSTRACT

## Scatterometer Contamination Mitigation

Michael Paul Owen

Department of Electrical and Computer Engineering

Doctor of Philosophy

Microwave scatterometers, which use radar backscatter measurements to infer the near-surface wind vector, are unique in their ability to monitor global wind vectors at high resolutions. However, scatterometer observations which are contaminated by land proximity or rain events produce wind estimates which have increased bias and variability, making them unreliable for many applications. Fortunately, the effects of these sources of contamination can be mitigated. Land contamination of backscatter measurements occurs when land partially fills the antenna illumination area. This reduces and masks the wind-induced backscatter signal. Land contamination is mitigated by quantifying the amount of contamination in a single observation using a metric referred to as the land contribution ratio (LCR). LCR levels which give rise to inadmissible levels of error in the wind estimates are determined and used to discard land-contaminated observations. Using this method results in contamination-free wind estimates which can be made as close to the coast as 5 km, an improvement of 25 km compared to previous methods.

Rain contamination of scatterometer observations results from rain-induced scattering effects which modify the wind-induced backscatter. Rain backscatter effects are modeled phenomenologically to assess the impact of rain on the observed backscatter. Given the backscatter effects of wind and rain, there are three estimators: wind-only (WO), simultaneous wind and rain (SWR) and rain-only (RO), which have optimal performance in different wind and rain conditions. Rain contamination of wind estimates is mitigated using a new Bayes estimator selection (BES) technique which optimally selects WO, SWR, or RO estimates as they are most appropriate. BES is a novel adaptation of Bayes decision theory to operate on parameter estimates which may have different dimensions. The BES concept is extended to include prior selection and noise reduction techniques which generalizes BES to a wider variety of wind fields and further increase wind estimate accuracy. Overall, BES has wind estimation performance which surpasses that of either the WO or SWR wind estimates individually, and also provides a viable rain-impact flag.

Keywords: scatterometry, scattering, wind, rain, land, contamination mitigation



## ACKNOWLEDGMENTS

Thank you Dr. Long for years of excellent advice, counsel and mentoring. Your comments and instruction have been invaluable to me and have made this dissertation possible.

To my wife Claire: Thank you for your support, patience, encouragement and help. Thank you for putting up with late nights and early mornings during the final stretch to finish this.

To my daughters Abby and Eliza: This is for you. Thank you for making it worth the effort.



# Table of Contents

<b>List of Tables</b>	<b>xiii</b>
<b>List of Figures</b>	<b>xviii</b>
<b>1 Introduction</b>	<b>1</b>
1.1 Overview . . . . .	1
1.2 Approach . . . . .	2
1.3 Summary of Contributions . . . . .	4
1.4 Outline . . . . .	5
<b>2 Background</b>	<b>7</b>
2.1 Introduction to Scatterometry . . . . .	7
2.2 The QuikSCAT Scatterometer . . . . .	8
2.3 Wind Retrieval . . . . .	10
2.4 Accuracy . . . . .	13
2.5 Resolution . . . . .	14
2.6 Measurement Contamination . . . . .	17
2.6.1 Land Contamination . . . . .	18
2.6.2 Rain Contamination . . . . .	18
2.7 Summary . . . . .	19
<b>3 Ultra-high Resolution Rain Backscatter Modeling</b>	<b>21</b>

3.1	QuikSCAT and TRMM Background . . . . .	21
3.2	UHR Rain Model . . . . .	22
3.2.1	Spatial Resolution . . . . .	24
3.2.2	Temporal Resolution . . . . .	26
3.2.3	Attenuation Model . . . . .	27
3.2.4	Effective Rain Model . . . . .	28
3.2.5	Phenomenological Model . . . . .	30
3.2.6	Model Comparisons . . . . .	35
3.3	Conclusions . . . . .	37
<b>4</b>	<b>ASCAT Rain Model</b>	<b>39</b>
4.1	Backscatter Model . . . . .	39
4.1.1	Atmospheric and Surface Scattering . . . . .	40
4.1.2	Combined Scattering Effects . . . . .	43
4.2	Model Comparisons . . . . .	44
4.3	Case Study . . . . .	45
4.4	Conclusions . . . . .	45
<b>5</b>	<b>Ultra-high Resolution Simultaneous Wind and Rain Retrieval</b>	<b>49</b>
5.1	QuikSCAT and TRMM Background . . . . .	50
5.2	Simultaneous Wind and Rain Retrieval . . . . .	51
5.2.1	Estimating $K_{pe}$ for Retrieval . . . . .	52
5.3	SWR Accuracy . . . . .	54
5.3.1	Cramer-Rao Bound . . . . .	54
5.3.2	Wind and Rain Backscatter Simulation . . . . .	55
5.3.3	Theoretic Performance Limits . . . . .	56

5.3.4	SWR Performance . . . . .	59
5.4	Conclusions . . . . .	64
<b>6</b>	<b>M-ary Bayes Estimator Selection for QuikSCAT Simultaneous Wind and Rain Retrieval</b>	<b>65</b>
6.1	Problem Formulation . . . . .	66
6.2	Background . . . . .	67
6.2.1	Estimator Bounds . . . . .	70
6.3	M-ary Bayes Estimator Selection . . . . .	73
6.3.1	Cost Function . . . . .	76
6.3.2	Optimality . . . . .	77
6.3.3	Limitations and Advantages . . . . .	78
6.3.4	Terminology . . . . .	79
6.4	Application to QuikSCAT . . . . .	80
6.4.1	Normalization . . . . .	80
6.4.2	Wind-Rain Prior . . . . .	81
6.4.3	Estimator Likelihood Function . . . . .	83
6.4.4	Optimality . . . . .	84
6.5	Results . . . . .	87
6.5.1	Case Study . . . . .	87
6.5.2	Monte-Carlo Performance . . . . .	90
6.5.3	Overall Decision Performance . . . . .	92
6.6	Conclusion . . . . .	98
<b>7</b>	<b>Prior Selection and UHR BES</b>	<b>99</b>
7.1	Bayes Estimator Selection . . . . .	100

7.2	Prior Selection . . . . .	102
7.2.1	Prior Selection Loss Function . . . . .	104
7.3	Bayes Estimator Selection with Prior Selection . . . . .	105
7.3.1	Estimator Likelihood Function . . . . .	105
7.3.2	Candidate Priors . . . . .	106
7.3.3	Prior Selection Weighting Function . . . . .	108
7.3.4	Optimal BES for Candidate Priors . . . . .	109
7.3.5	Distribution of Priors . . . . .	110
7.4	Noise Reduction for Estimator Selections . . . . .	111
7.4.1	Estimator Selection Noise Reduction . . . . .	111
7.4.2	Consistency Check . . . . .	114
7.5	Results . . . . .	115
7.5.1	Case Study . . . . .	115
7.5.2	Overall Performance . . . . .	119
7.6	Summary . . . . .	123
<b>8</b>	<b>Land-Contamination Mitigation</b>	<b>125</b>
8.1	QuikSCAT Overview . . . . .	126
8.2	Contamination Detection Metrics . . . . .	129
8.2.1	Minimum Distance to Land . . . . .	130
8.2.2	Land Contribution Ratio . . . . .	130
8.2.3	Metric Comparisons . . . . .	131
8.2.4	Threshold Detection . . . . .	133
8.2.5	Metric Choice . . . . .	134
8.3	LCR Threshold Determination . . . . .	136

8.3.1	Compass Simulation . . . . .	137
8.3.2	Land Contamination Simulation . . . . .	137
8.3.3	Simulation Results . . . . .	138
8.3.4	CRB Based LCR Thresholds . . . . .	143
8.3.5	LCR Threshold Comparisons . . . . .	145
8.4	Wind Retrieval . . . . .	146
8.4.1	Wind Retrieval Using the Land Contribution Ratio . . . . .	148
8.5	Conclusion . . . . .	154
<b>9</b>	<b>Conclusion</b>	<b>155</b>
9.1	Areas for Further Research . . . . .	157
9.2	Summary . . . . .	158
	<b>Bibliography</b>	<b>159</b>
	<b>A List of Acronyms</b>	<b>167</b>
	<b>B The Cramer-Rao Bound for Estimates from Contaminated Observations</b>	<b>169</b>
B.1	Statistical Models . . . . .	169
B.1.1	Fisher Information Matrix . . . . .	170
B.1.2	Cramer-Rao Lower Bound . . . . .	172
B.2	Contaminated Observations - Known Contamination . . . . .	172
B.3	Contaminated Observations - Random Contamination . . . . .	173
B.4	Application of the Fisher Information for Contaminated Observations . . . . .	174
B.4.1	Application to Land Contaminated Wind Retrieval . . . . .	174
B.4.2	Application to Rain-Contaminated Wind Retrieval . . . . .	175
B.4.3	Application to Wind-Contaminated Rain Retrieval . . . . .	175

B.4.4	Fisher Information for Simultaneous Wind and Rain Retrieval . . . . .	175
B.5	Summary . . . . .	176
<b>C</b>	<b>The Rain Likelihood Flag: An Ultra-High Resolution Rain Flag</b>	<b>177</b>
<b>D</b>	<b>Rain Fraction-Based Estimator Performance Prior</b>	<b>181</b>
D.1	Rain Fraction . . . . .	182
D.2	Regime Boundaries . . . . .	184
<b>E</b>	<b>Interference Information</b>	<b>189</b>
E.1	Motivation . . . . .	189
E.2	Problem Formulation . . . . .	189
E.3	Interference Information . . . . .	190
E.3.1	Estimator Regimes . . . . .	191
E.4	Application . . . . .	192
E.5	Summary . . . . .	193

## List of Tables

2.1	QuikSCAT 25 km accuracy requirements . . . . .	14
3.1	Rain model parameters . . . . .	37
6.1	Wind and rain estimator summary . . . . .	69
6.2	Normalization matrix values . . . . .	81
6.3	Probability of wind and rain vector given the estimator selection performance	94
6.4	Number of missed SWR selections as a function of rain rate . . . . .	94
7.1	Candidate prior mean wind speeds and standard deviations . . . . .	108
7.2	Probability of wind and rain vectors occurring which have estimator selection performance in the indicated ranges . . . . .	119
7.3	Overall probability of optimal estimator selection for 1 year of co-located data	121
7.4	Wind speed RMS error for one year dataset . . . . .	124
7.5	Wind speed bias for one year dataset . . . . .	124
D.1	Rain fraction regime boundaries . . . . .	186



## List of Figures

2.1	The QMOD4 GMF . . . . .	12
2.2	Possible wind speeds and directions corresponding to each observation flavor of a vector of noise-free QuikSCAT observations . . . . .	13
2.3	Wind retrieval: 25 km and 2.5 km winds . . . . .	16
2.4	Wind and rain interaction . . . . .	19
3.1	QuikSCAT rain attenuation model . . . . .	29
3.2	QuikSCAT effective rain backscatter model . . . . .	31
3.3	QuikSCAT atmospheric backscatter model . . . . .	33
3.4	QuikSCAT surface rain backscatter model . . . . .	35
3.5	QuikSCAT rain model comparison . . . . .	36
4.1	C-band rain backscatter . . . . .	41
4.2	C-band rain model comparisons as a function of incidence angle . . . . .	42
4.3	Simulated ASCAT wind and rain backscatter example . . . . .	46
5.1	Average SWR squared error as a function of $K_{pe}$ . . . . .	53
5.2	Histograms of the rain estimates produced using both the effective and phenomenological rain models for fixed speed and rain rate . . . . .	56
5.3	Cramer-Rao bound for QuikSCAT SWR . . . . .	58
5.4	Wind speed geophysical model function . . . . .	59
5.5	Scatter density of QuikSCAT ‘true’ observed rains and TRMM PR-measured rains . . . . .	60

5.6	Scatter density plots of QuikSCAT ‘true’ rain rates and QuikSCAT retrieved rain rates . . . . .	62
5.7	TRMM PR-measured rain rate and QuikSCAT-estimated rain rate for one overlapping region . . . . .	63
6.1	Cramer-Rao Bounds on wind speed and rain rate for the WO, SWR and RO estimators . . . . .	71
6.2	Estimator regimes determined by the overall CRB . . . . .	72
6.3	Wind-rain prior for a single wind direction . . . . .	82
6.4	Estimator likelihood functions . . . . .	84
6.5	Probability of correct estimator selection as a function of cross-track index . . . . .	85
6.6	25 km resolution Bayes estimator selection case study . . . . .	88
6.7	25 km resolution Bayes selected rain estimates as a function of TRMM PR measured rain rates . . . . .	90
6.8	Monte-Carlo performance for wind and rain estimation . . . . .	91
6.9	Probability of correct estimator selection as a function of NCEP wind speed and TRMM PR rain rate . . . . .	93
6.10	Scatter densities for NCEP and QuikSCAT wind estimates for conditions with and without rain-impact . . . . .	95
6.11	Normalized scatter density in dB of BES rain estimates and TRMM PR rain measurements. . . . .	96
6.12	Comparison of IMUDH rain flag to WO, SWR and Bayes selected wind accuracy . . . . .	97
7.1	Spatial autocorrelation functions for rain rate and wind speed . . . . .	107
7.2	Optimal values of $\kappa$ for BES-PS at UHR . . . . .	110
7.3	Minimum acceptable rain rate as a function of the candidate prior mean wind speed . . . . .	110
7.4	Case study showing WO, SWR, RO estimates with BES, and BES-PS selections at UHR . . . . .	116

7.5	Probability of optimal estimator selection for UHR wind estimates for BES and BES-PS . . . . .	120
7.6	Scatter densities for NCEP and QuikSCAT wind estimates for conditions with and without rain-impact . . . . .	123
8.1	The QuikSCAT slice spatial response function . . . . .	127
8.2	Vertically polarized backscatter fields for Cape Cod, Massachusetts . . . . .	128
8.3	The LCR in dB as a function of the distance from the center of the slice to the coastline . . . . .	132
8.4	LCR and MDL comparisons . . . . .	135
8.5	RMS error for simulated wind retrieval with land contamination . . . . .	139
8.6	RMS error contours for land-contaminated simulated wind retrieval . . . . .	140
8.7	RMS speed error as a function of wind speed and direction . . . . .	141
8.8	LCR thresholds as a function of wind speed . . . . .	142
8.9	LCR thresholds as a function of speed for multiple land backscatter levels . .	143
8.10	Biased CRB levels for land-contaminated wind retrieval . . . . .	144
8.11	LCR thresholds as a function of speed for multiple land backscatter levels calculated using the CRB . . . . .	145
8.12	L2B wind speeds for the Aegean Sea . . . . .	147
8.13	UHR wind speeds for the Aegean Sea without removing land contamination	148
8.14	UHR wind speeds for the Aegean Sea with 30 km land mask . . . . .	149
8.15	25 km wind speeds for the Aegean Sea after removing land contamination . .	150
8.16	UHR wind speeds for the Aegean Sea after removing land contamination . .	151
8.17	Wind speed distributions for the Cape Cod Region during the year 2006 . .	153
C.1	TRMM rain rate, QuikSCAT rain rate and the RLF for one overlapping region	178
C.2	Probability of false and alarm and probability of missed detection for rain using the RLF . . . . .	178

D.1	Conditional densities of $C(\vartheta)$ for each regime for each look geometry . . . . .	185
D.2	Estimator performance prior defined using the rain fraction . . . . .	187
E.1	Estimator regimes as defined using the interference information . . . . .	192

# Chapter 1

## Introduction

### 1.1 Overview

Our ability to understand the global climate is highly dependent on frequent global observations of wind, rain, humidity, atmospheric pressure, and many other factors. Such observations are key inputs for climate models and weather forecasting. Microwave remote sensing instruments are ideal tools for climate monitoring as they operate independently of solar illumination, regardless of cloud cover, and are capable of global coverage at high spatial resolution on orbiting platforms. To measure the various climatological parameters, microwave sensors have been designed to measure atmospheric moisture, ocean winds, rain, soil moisture, ice, land cover, sea-surface temperature, sea level, ocean salinity and a variety of other indicators. This dissertation focuses on microwave sensors known as scatterometers. Scatterometers are typically designed to indirectly measure ocean-surface winds, though their measurements have many other applications.

Scatterometers directly measure the normalized radar cross-section of the surface of the earth. Over the ocean, the surface backscatter is a function of near-surface winds due to Bragg-scattering effects induced by wind-generated small-scale waves. Since the wind-induced surface roughness is a function of the near-surface wind vector, the backscatter measured by a scatterometer can be used to infer the near-surface wind vector over the ocean, given a sufficient number of observations with appropriate geometry.

Scatterometer-inferred wind estimates can be degraded by any phenomena capable of modifying the wind-induced backscatter. Such phenomena include rain events, land, ice and to a lesser degree smaller-scale phenomena such as sea-spray, sea-surface swell and occasional oil slicks. Contamination of the wind-induced backscatter due to ice sheets is limited to near-polar regions. Measurement contamination due to land proximity and rain, however, has

substantial effects on the observed backscatter and occurs frequently on significant spatial scales. Thus, ignoring the effects of land and rain contamination can have a detrimental impact on the overall wind estimates. To reduce the effects of contamination, these degraded observations have typically been discarded, resulting in reduced sensor coverage of coastal and rainy areas.

This dissertation addresses the two most significant sources of scatterometer measurement contamination: rain and land, using the approaches introduced in Section 1.2. The effects of contamination-degraded wind estimates are mitigated by optimally discarding and where possible, optimally correcting scatterometer observations. The techniques presented in the following chapters increase usable sensor coverage while maintaining the accuracy levels attained in contamination-free regions. The mitigation techniques presented in this dissertation are both novel and highly effective. Application of these techniques is focused here on the QuikSCAT scatterometer, though the techniques can be applied to other scatterometers as well.

## 1.2 Approach

Land and rain contamination have distinctly different consequences for successful contamination mitigation. The resulting mitigation techniques are related, but they are approached separately here.

Land contamination of backscatter measurements occurs when land partially fills the antenna illumination area on the surface. This reduces and masks the desired wind-induced backscatter signal, which causes increased variability and bias in the wind estimates. Land contamination is quantified by identifying the amount of contamination in a single observation using a metric referred to as the land contribution ratio (LCR). Two approaches are used to determine intolerable levels of land contamination: Monte-Carlo simulations and the wind estimate Cramer-Rao lower bound. Measurements which have intolerable levels of land contamination are discarded prior to performing wind estimation. This enables contamination-free wind estimation as close to the coast as 5 km, an improvement of 25 km compared to previous methods.

Rain contamination can be utilized to permit estimation of both rain and wind, rather than discarding observations as in land contamination mitigation. Rain contamination of scatterometer observations results from rain-induced scattering effects which modify the wind-induced backscatter. To assess the impact of rain on wind-induced backscatter, the effects of rain are modeled using a phenomenological approach. Parametric models for the rain-induced scattering effects enable simultaneous wind and rain (SWR) estimation using the scatterometer observations.

In addition to SWR estimation, scatterometer data can be used to perform wind-only (WO) and rain-only (RO) estimation using special cases of the wind and rain backscatter model. The differences in the model functions cause the WO, SWR and RO estimators to have varied performance characteristics. The SWR estimator particularly has greater estimate uncertainty than the WO estimator in non-raining conditions due to the additional degree of freedom. Similarly, the SWR estimator has higher estimate uncertainty than the RO estimator during rain-dominated conditions. Thus each type of estimator, SWR, WO and RO, has optimal performance for different wind and rain conditions. The WO estimate is ideal when rain effects are small, the SWR estimate is appropriate when wind and rain effects are similar, and the RO estimate is used when rain effects dominate the observations.

With three types of estimators, rain contamination of wind estimates is mitigated for 25 km resolution products using a new Bayes estimator selection (BES) technique which optimally selects the WO, SWR, or RO estimate that is most appropriate. BES is a novel extension of Bayes decision theory to operate on parameter estimates which may have different dimensions. The BES concept is extended to include a prior selection technique which generalizes BES to a wider variety of wind fields with higher noise levels and further increases wind estimate accuracy. BES with prior selection is used with an additional noise reduction technique to mitigate rain contamination for 2.5 km resolution wind products which have greater variability and noise than 25 km wind products. The BES estimator selections can be treated as a rain-impact flag which identifies wind estimates that are significantly affected by rain. Overall, BES for 25 km products and BES with prior selection for 2.5 km products have wind estimation performance which surpasses that of either the WO or SWR wind estimates individually.

### 1.3 Summary of Contributions

Major contributions to scatterometer contamination mitigation are summarized in this section.

The contributions to scatterometer land contamination mitigation introduced in this dissertation include: the derivation of a metric to both identify and quantify land contamination of wind-induced backscatter; the quantification of land contamination effects on wind estimation through Monte-Carlo simulation and a Cramer-Rao lower bound for wind estimation from land-contaminated observations; creation of a look-up-table to remove land-contaminated backscatter measurements and enable land contamination mitigation in near-real-time processing [1, 2]. Together each of these contributions allow for the accurate estimation of near-coastal winds under many conditions. Previously, wind estimates within 30 km of the coastline were discarded to prevent land contamination of wind estimates. This work enables accurate wind retrieval up to 2.5 km from the coast in many conditions without significantly degrading the accuracy of the wind estimates. A complete validation of the near-coastal winds is being conducted by other investigators [3, 4].

Contributions in this dissertation to scatterometer rain contamination mitigation include: a description of temporal and spatial sampling issues related to 2.5 km resolution wind and rain estimation; the quantitative description and modeling of rain-induced backscatter effects for Ku-band observations; calculation of the Cramer-Rao lower bound for simultaneous wind and rain estimation at 2.5 km; implementation and validation of simultaneous wind and rain estimation for 2.5 km resolution products [5]. The quantitative analysis and modeling of rain-induced backscatter effects for the C-band ASCAT scatterometer is also included in this dissertation in Chapter 4 and was published as a conference paper [6].

In addition to the backscatter modeling and simultaneous wind and rain estimation techniques, this dissertation extends previous work on simultaneous wind and rain estimation using QuikSCAT to optimally use multiple estimator types [7]. The contributions to scatterometer rain contamination mitigation include: a derivation of the Cramer-Rao lower bound for rain-contaminated wind-only estimation and wind-contaminated rain-only estimation; the derivation of a generally applicable Bayes estimator selection technique to

optimally select a single estimate produced by one of several estimators; and the adaptation and validation of Bayes estimator selection to QuikSCAT 25 km wind and rain estimation.

The remaining contributions in this dissertation adapt the concept of Bayes estimator selection to QuikSCAT 2.5 km wind and rain estimation and further extends the concept to include a prior selection technique in addition to noise reduction. Major contributions to scatterometer rain contamination mitigation include: adaptation of Bayes estimator selection to QuikSCAT 2.5 km wind and rain products; derivation of a novel prior selection technique used to improve and extend Bayes estimator selection to a wide variety of wind and rain conditions; introduction of a noise reduction technique to guarantee spatially consistent wind and rain fields with lower noise levels; and validation of Bayes estimator selection, prior selection and noise reduction techniques for QuikSCAT 2.5 km wind and rain estimation.

#### **1.4 Outline**

This dissertation is structured as follows. Chapter 2 provides background on scatterometers generally, and the QuikSCAT scatterometer specifically, in addition to briefly discussing and motivating the contamination mitigation problem. Additional background detail is contained in each chapter. Chapters 3 and 4 evaluate and model the effects of rain-induced backscatter for Ku- and C-band observations, respectively. Chapters 5, 6 and 7 are focused on rain contamination mitigation at increasing levels of complexity. Specifically, Chapter 5 discusses the concept of simultaneous wind and rain estimation and Chapter 6 introduce the concept of Bayes estimator selection and adapts the concept to 25 km wind and rain estimation. Chapter 7 extends Bayes estimator selection to include prior selection and noise reduction and applies the improved technique to 2.5 km wind and rain estimation for QuikSCAT. Chapter 8 addresses the identification and mitigation of land contamination after which Chapter 9 summarizes the most important results and discusses areas for future research and application to future scatterometers.



## Chapter 2

### Background

#### 2.1 Introduction to Scatterometry

After radar became widespread during World War II, succeeding decades have been marked by continued research and development of radar platforms and applications. In the 1960's and 1970's it was demonstrated that the radar scattering coefficient was related to wind speed over the ocean. This led to the first radar scatterometer specifically designed to measure wind speeds and directions over the ocean, the Seasat-A satellite scatterometer [8]. The Seasat scatterometer demonstrated the viability of space-based ocean wind measurement.

Scatterometers are active radars designed to measure the normalized radar cross section, also known as the backscatter or  $\sigma^o$ , of a target. To do so they send a radar pulse to the target and measure the power of the pulse echo. Scatterometers are used to measure target characteristics on a large scale, typically many kilometers. The backscattered return power from the target is a function of the target orientation, size, roughness, and geometry as well as the orientation, frequency and polarization of the incident power. The measured  $\sigma^o$  of an object can be used to infer characteristics about the target such as size, orientation and range.

For distributed targets like the ocean surface, where the target is much larger than the antenna spatial response, the backscatter return is a function of characteristics of the target surface such as orientation and roughness. Multiple observations of a single target with different observation geometries give additional information about the target, so scatterometers typically observe targets with multiple azimuth and incidence angles, in addition to possibly using multiple frequencies and polarizations.

Ocean wind measurement by scatterometers is possible due to the interaction of the wind and the ocean surface. Wind blowing over the water generates gravity-capillary waves, small scale waves with a wavelength in the cm range [9]. Early scatterometers demonstrated that the amplitude and wavelength of the wind-induced waves is a function of the wind speed. Scatterometer frequencies are selected so that the transmit wavelength is similar to that of the wind-induced gravity-capillary waves [9]. With similar wavelengths the backscattered power is produced by Bragg-scattering from the periodic nature of the wind-induced backscatter [9, 10]. As the troughs of the wind-induced waves lie roughly perpendicular to the wind direction there is a strong directional dependence of the backscatter, since Bragg-scattering has a reduced effect when the scatterers are not oriented in the antenna look direction.

Although significant work has been performed at analytically developing the relationship between the wind and the backscattered power [11], typically the backscattered power is modeled by an empirically-based tabular model function [12, 13]. This model function is referred to as the geophysical model function (GMF).

To improve measurement resolution, range and Doppler processing are typically used to subdivide the antenna beam into smaller independent observations. The resulting ‘slices’ of the antenna beam have a smaller antenna spatial footprint at the target so they can be used to infer target characteristics at a finer resolution [14].

Accurate backscatter measurements produced by scatterometers are valuable aids in many fields. In addition to ocean surface wind estimation, scatterometer data products have a variety of demonstrated applications. Additional applications include: sea ice detection [15, 16, 17], iceberg detection and tracking [18], glacial ice sheet monitoring [19, 20, 21], vegetation classification [22, 23], soil moisture measurement [24] and sand dune observation [25, 26].

## **2.2 The QuikSCAT Scatterometer**

The SeaWinds instrument is a third generation scatterometer which was designed to measure near-surface ocean wind vectors, building on the success of the earlier Seasat-A and NSCAT scatterometers also launched by NASA [27, 28, 29]. SeaWinds operates at Ku-band at 13.4 GHz. It uses a scanning dual-polarization rotating pencil-beam antenna resulting in

a measurement swath 1800 km wide. With orbits selected to maximize global coverage, the SeaWinds instruments cover 90% of the ocean daily and every point on the globe at least once every 4 days. This regular and nearly complete global coverage is key to the value of the SeaWinds instrument.

The SeaWinds instrument design is advantageous for a variety of reasons. A rotating pencil beam results in a wide swath without a gap along the nadir track. SeaWinds makes dual-polarization measurements using offset antenna feeds for H and V polarizations resulting in fixed incidence angles for H-pol observations at  $46^\circ$  and V-pol observations at  $54^\circ$ . The resulting observation geometry makes backscatter measurements at each location with a variety of azimuth angles. The observations at a single location can be classified into four ‘flavors’ or ‘looks’: forward looking H-pol, aft looking H-pol, forward looking V-pol and aft looking V-pol. This observation geometry was selected to maximize swath coverage while maintaining the measurement azimuthal diversity which is fundamental to wind retrieval.

SeaWinds is most favorable for wind retrieval when there are both V and H-pol observations with wide azimuthal diversity. The region of the swath where observation geometry is ideal is termed the ‘sweet-spot’. Although the SeaWinds geometry is favorable for wind studies for most swath locations, there are two regions for which the geometry is not ideal. At the swath edge there are no H-pol observations since the H-pol incidence angle limits the H-pol swath width. Also, near the satellite track there is little azimuthal diversity in the observations since all observations are looking nearly parallel to the satellite track. Because the observation geometry is non-ideal in these two regions wind estimates in these regions have higher noise levels and are more susceptible to directional errors.

SeaWinds was flown twice, first on the QuikSCAT mission and later on the ADEOS-II mission. Following an established convention, the SeaWinds instrument on QuikSCAT satellite is hereafter referred to simply as QuikSCAT, while SeaWinds on ADEOS-II is referred to as SeaWinds.

QuikSCAT was launched in July of 1999 and operated continuously until November of 2009, far surpassing its design lifetime of 3 years. The resulting 10 year data set has proved to be a powerful tool in understanding many aspects of the environment on a global scale. QuikSCAT wind products have enabled a vast number of wind-related studies which

include tropical storms [30, 31, 32], coastal studies [33], rain-interaction [34], wind spectrum [35], El Nino [36], marine weather [37], global climatology [38], and ocean circulation [39, 40].

The work in this dissertation refers to QuikSCAT but is equally applicable to SeaWinds as well. Further, although the techniques introduced in the following chapters are directly applied to QuikSCAT, they are valid for other scatterometer platforms as well. The application of the contamination mitigation techniques discussed in this dissertation to other scatterometer platforms is not addressed here. The following sections give an introduction to wind retrieval using the QuikSCAT scatterometer. More detailed background information is also included as needed in Chapters 3 to 8.

### 2.3 Wind Retrieval

QuikSCAT uses simultaneous measurements of the signal echo power and noise power to make accurate measurements of  $\sigma^o$ . In addition to accurately estimating the signal return power, this method has the additional advantage that it allows the  $\sigma^o$  estimates to be well approximated with a normal distribution [41]. The probability of the observed backscatter  $\sigma^o$  given the true backscatter of the surface  $\sigma_t^o$  can be written

$$p(\sigma^o|\sigma_t^o) = \frac{1}{\sqrt{2\pi\zeta^2}} \exp\left(-\frac{(\sigma^o - \sigma_t^o)^2}{2\zeta^2}\right), \quad (2.1)$$

where  $\zeta^2$  is the variance of the backscatter measurements.

The noise realizations for backscatter measurements made at different times are independent since the observation noise is dominated by amplifier noise which is uncorrelated. Thus since different observation flavors have separated observation times the observations made of a given location can be treated as independent random variable realizations.

For conventional wind retrieval, the true backscatter is given as a function of the true wind vector by the geophysical model function (GMF). The GMF is a set of tabulated observations which returns the mean backscatter as a function of the wind vector and the observation geometry [12]. Several GMFs have been developed and utilized for Ku-band backscatter. The most recent GMF, QMOD4, has been tuned to more accurately depict low and extreme wind conditions. The GMF is shown in Fig. 2.1 for a fixed incidence angle.

The backscatter generally increases with wind speed but is also strongly dependent on the angle between the antenna azimuth and the wind vector, the relative azimuth angle  $\chi$ .

Figure 2.1 also demonstrates the need for observations from multiple azimuth angles. Because a single backscatter observation may have come from any wind direction, uniquely determining the wind direction requires multiple observations. Despite making observations from multiple azimuth angles, the observation geometry is still not favorable for all wind directions. Wind estimates are obtained using maximum likelihood estimation by finding the wind vector,  $\mathbf{w}$ , which maximizes the likelihood function

$$l(\sigma^o|\mathbf{w}) = - \sum_k \log(\varsigma_k) + \frac{1}{2} \frac{(\sigma_k^o - \mathcal{M}(\mathbf{w}))^2}{\varsigma_k^2} \quad (2.2)$$

given the vector of backscatter observations,  $\sigma^o$ , where  $\mathcal{M}(\mathbf{w})$  is the GMF. For every retrieved wind vector there are typically several maxima of the likelihood function. These other maxima are also valid wind vector estimates and are thus referred to as ‘ambiguities’. Figure 2.2 shows the possible wind vectors corresponding to the modeled backscatter for noiseless observations. The intersection of all four curves marks the true wind and rain vector. The near intersections of the four curves indicate the ambiguities. Although the intersection of the curves is clear for noiseless observations, noise often makes the correct solution indistinguishable from the other ambiguities.

To form a field of wind estimates requires that one of the ambiguities be selected as the best estimate for each WVC. This process is referred to as ambiguity selection. Ambiguity selection is often an ad-hoc step which is performed independently from wind retrieval often using median filters and information from outside sources [42, 43].

The variability of the  $\sigma^o$  observations can be attributed to two main sources. The first is uncertainty of the GMF. Because the GMF is empirically derived, it is inherently subject to uncertainty. Further, the GMF does not attempt to model all sources of backscatter variability. In addition to the wind vector and observation geometry, the surface backscatter is dependent to a small degree on the ocean salinity, sea-surface temperature, and contaminants present in the water. The effects of these other parameters are small and are lumped into a modeling uncertainty term with normalized standard deviation  $K_{pm}$ .

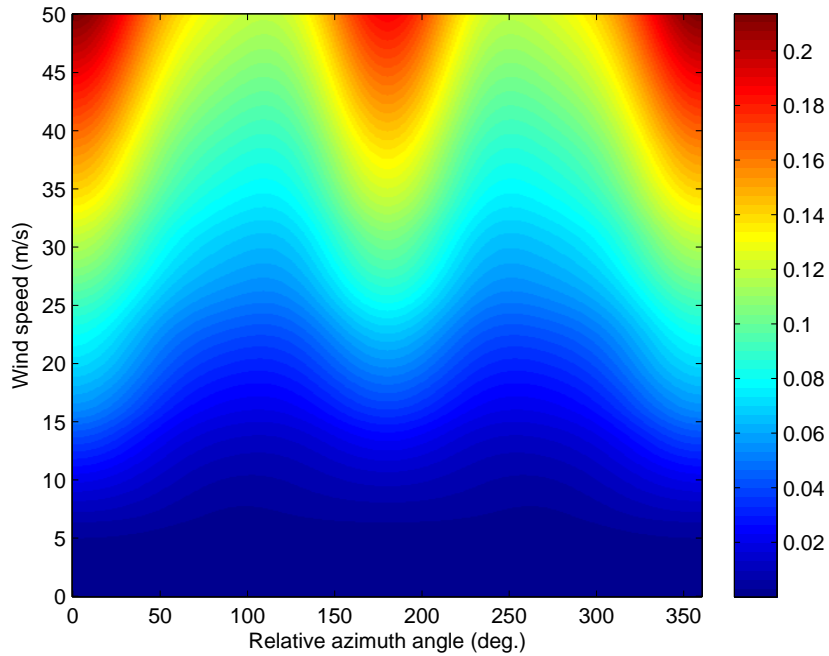


**Figure 2.1:** The QMOD4 GMF for a fixed incidence angle. The backscatter increases with wind speed and has a strong directional dependence.

The major cause of measurement variability is referred to as communication noise. The communication noise is the combination of physical noise sources which include Raleigh fading of the signal, atmospheric noise, and the noise characteristics of the receiver. To complicate matters, the communication noise is dependent on the mean of the backscatter, which indicates that the QuikSCAT noise is multiplicative. Scatterometer measurement accuracy is determined by the uncertainty due to communications noise. The QuikSCAT system parameters are selected such that the communications noise is comparable to the modeling uncertainty [14, 44], thereby minimizing the backscatter measurement uncertainty.

The variance of the backscatter observations accounts for both modeling uncertainty and variability due to communications noise using the normalized standard deviation,  $K_p$  [44]. The normalized standard deviation can be written

$$K_p^2 = K_{pm}^2 + K_{pc}^2 + K_{pm}^2 K_{pc}^2, \quad (2.3)$$

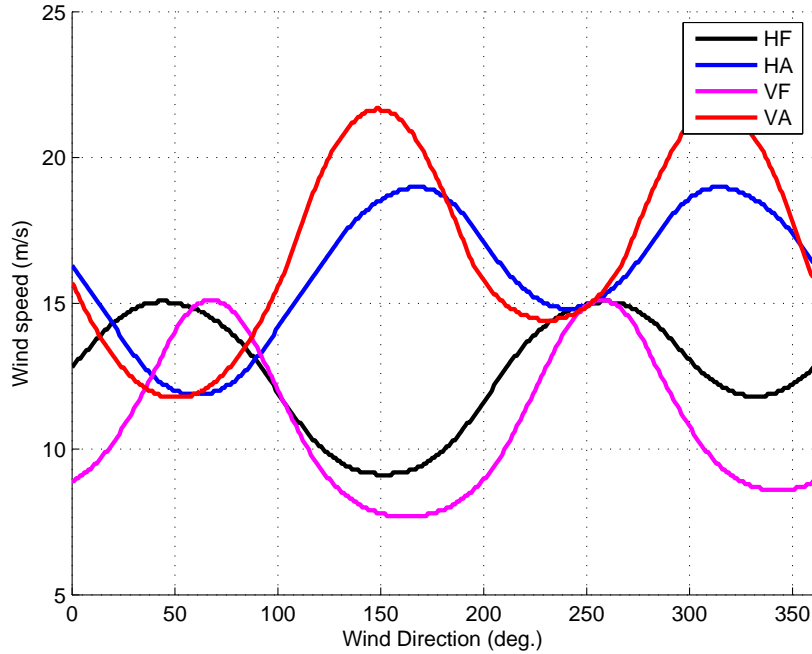


**Figure 2.2:** Possible wind speeds and directions corresponding to each observation flavor of a vector of noise-free QuikSCAT observations for a true wind speed of 15 m/s and direction of 250°. The intersection of the curves marks the true wind vector while other near intersections indicate the ambiguities.

where  $K_{pc}$  is the normalized standard deviation of the communication noise, and  $K_{pm}$  is the normalized standard deviation representing the GMF uncertainty.

Wind estimation for the SeaWinds instruments is typically performed using a maximum likelihood (MLE) method: given the probability model for the backscatter, the wind estimates are the wind vectors which maximize the likelihood function. Maximum likelihood estimation for wind and rain retrieval is discussed in greater detail in the following chapters.

## 2.4 Accuracy

As a part of the mission objectives, QuikSCAT has stringent accuracy requirements for its 25 km wind products [45]. A summary of these requirements is shown in Table 2.1.

Demonstrating that QuikSCAT meets the design requirements is a difficult task since there are no alternative validation datasets with identical temporal and spatial resolution.

**Table 2.1:** QuikSCAT 25 km accuracy requirements

Quantity	Requirement	Applicable Range
Wind Speed	2 m/s (rms)	3-20 m/s
	10%	20-30 m/s
Wind Direction	20°	3-30 m/s
Spatial Resolution	25 km	
Location Accuracy	25 km	
Coverage	90% of ice-free ocean daily	

To overcome this limitation, numerical weather products such as those available from the National Center for Environmental Prediction (NCEP) and the European Center for Medium-range Weather Forecasting (ECMWF) are often used as comparison datasets. While numerical weather products do not measure winds and therefore may not accurately reflect local wind conditions, on a large scale they provide useful estimates of QuikSCAT estimation accuracy.

Numerical weather products are often subject to systematic bias [46] which must be accounted for to accurately compare against scatterometer derived wind products. Despite this limitation, numerical weather products have been key in a number of studies using QuikSCAT data on both regional and global scales [38, 47].

As an alternative to numerical weather products, QuikSCAT wind estimates can be compared to in situ wind measurements from ships and off-shore wind buoys. Several studies have used this method and demonstrated that QuikSCAT winds are reliable and useful as long as they are free from rain and land contamination [4, 48, 49].

## 2.5 Resolution

The SeaWinds instrument makes two types of  $\sigma^o$  measurements. The first, referred to as eggs, represents the backscattered power received without any range or Doppler processing. Thus the egg measurements are produced using the full spatial response function of the antenna. The second measurement type, referred to as slices, represents the backscattered power after range and Doppler processing [50]. There are 10 slices for every egg, but the

outermost slices are typically discarded since they have prohibitively high noise levels. The remaining 8 slice measurements represent the  $\sigma^o$  value for subregions of the full antenna spatial response. Egg measurements have lower noise levels than slices since they represent a larger spatial area, however, they also cannot convey as much spatial information.

The SeaWinds instrument was designed to produce wind vector estimates at a 25 km resolution. The 25 km wind products are produced using  $\sigma^o$  images produced using ‘drop-in-the-bucket’ imaging [51]. For ‘drop-in-the-bucket’ imaging, the egg measurements with centers that fall in a given wind vector cell (WVC) are used together to produce a wind estimate. This method results in multiple measurements in each WVC of each observation flavor. However, the QuikSCAT antenna spatial response is larger than a resolution cell, so there is some spatial averaging inherent in the 25 km products. Despite the spatial averaging, since egg measurements have relatively low noise levels and there are multiple observations for each flavor in each WVC, the 25 km wind products have low noise levels.

The slice measurements are used to produce a 12.5 km resolution product using the same ‘drop-in-the-bucket’ imaging method as the 25 km wind products. Since slice measurements have higher noise levels than eggs, the 12.5 km products are noisier than the 25 km product; however, the finer spatial resolution yields more information about the wind field.

Although slice measurements are intended to produce 12.5 km wind products, they can also be used to produce higher resolution wind products. This is possible because the slice measurements form a dense but irregularly sampled version of the surface wind field. The density of the slice measurements allows for resolution enhancement of the observations enabling ultra-high resolution UHR wind retrieval at 2.5 km [51, 52, 53, 54]. UHR wind products have higher noise levels than other wind products, but they can give much greater information about wind phenomena with small-scale structure such as hurricanes, coastal jets and lees, and rain.

Figure 2.3 highlights the differences between 25 km wind products and UHR products. The 25 km wind estimates have low noise levels. Despite having higher noise levels, the UHR wind estimates show small-scale wind structure not discernible in the 25 km winds.

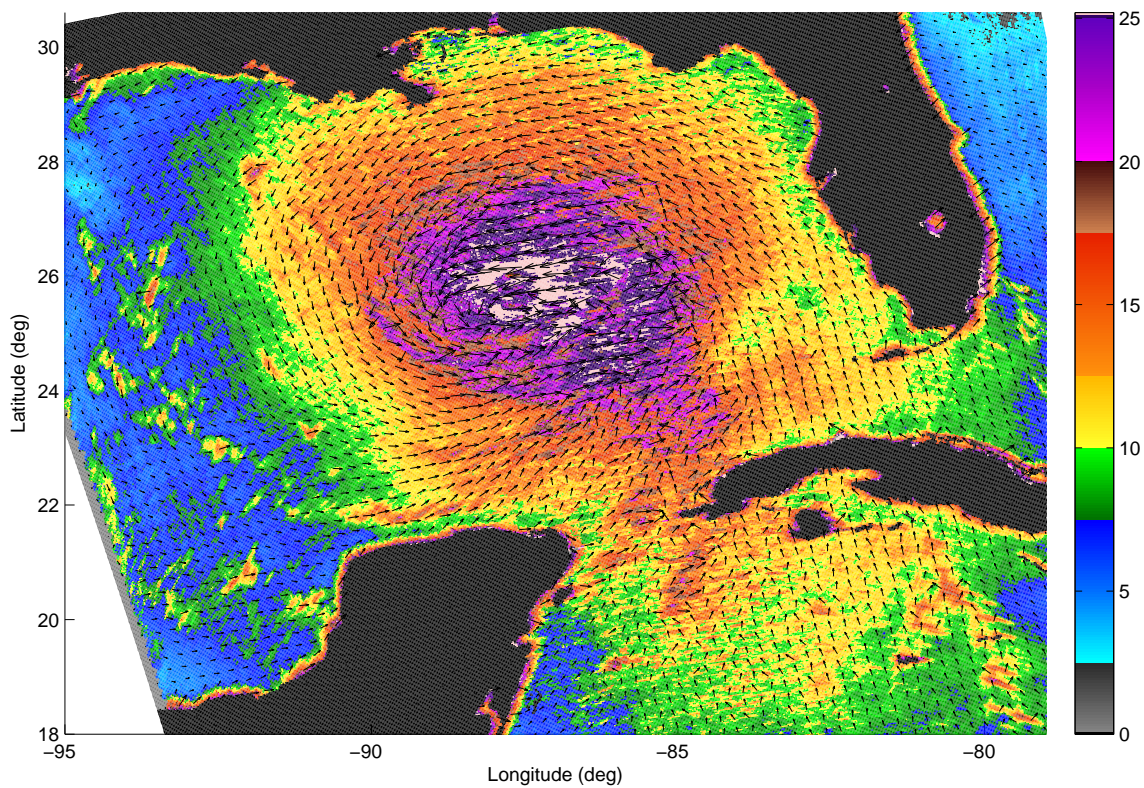
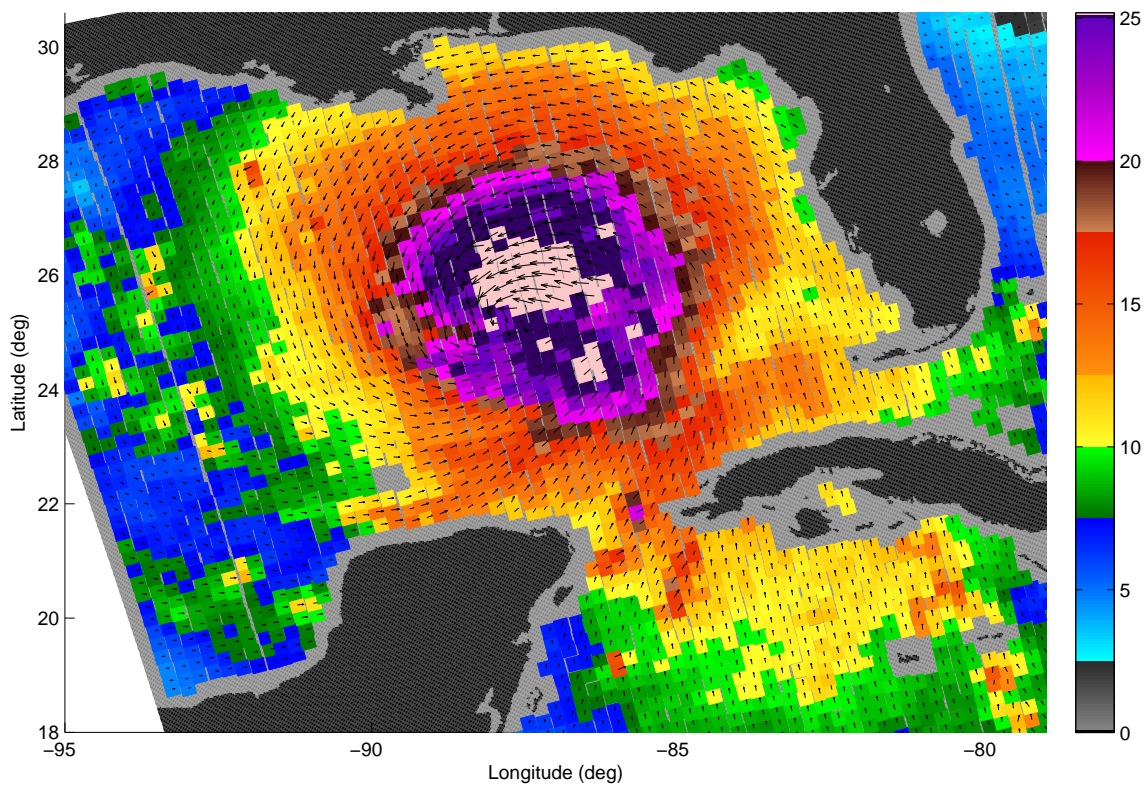


**Figure 2.3:** Wind estimates in m/s for hurricane Katrina from August 28, 2005. Top: L2B 25 km wind estimates. Bottom: UHR 2.5 km wind estimates. The UHR wind estimates have a higher noise level but also show wind structures not apparent in the 25 km winds such as the hurricane eye.

Although UHR products contain greater information about small-scale events, there are some limitations. Because the UHR WVCs are smaller than the slice spatial response function, each slice measurement influences the backscatter estimate in multiple WVCs. This can lead to increases in the variability of the backscatter estimates. A further limitation is that, although UHR wind products are reported at a resolution of 2.5 km, their effective resolution varies. For sections of the swath where the slice sampling is less dense, such as the swath center near the nadir track, the resolution of the UHR product may be lower than 2.5 km although wind estimates are still reported for every 2.5 km WVC.

A variable resolution wind estimation technique has recently been introduced which accounts for the slice sampling and observation geometry to reflect the actual resolution of the data [51]. Although this variable resolution product is not used in this dissertation, the application of the contamination mitigation techniques discussed here to this variable resolution product is an interesting avenue for further research.

## **2.6 Measurement Contamination**

Although it has been demonstrated that QuikSCAT meets the design requirements under the majority of conditions, the estimation accuracy is limited when observations are contaminated. Contamination of QuikSCAT measurements occurs when the backscatter observations include radar observable signals other than that of the wind-induced surface roughness. If wind retrieval is performed using contaminated observations, the retrieval process is biased and can have increased variability. When the contamination is strong the bias can be severe. When the contamination is small, the bias may be negligible. In order to determine what levels of contamination are tolerable there must be a way to quantify both the contamination and the effects of the contamination on the wind estimates.

There are a variety of contaminants which result in degraded wind estimation performance. These include ice, oil spills, land, rain, and anything else which modifies the wind-induced backscatter signal. Ice contamination occurs in the near polar regions when sea ice covers the ocean surface and obscures the wind-induced backscatter signal. Oil spills and other chemical spills cause contamination by modifying the relationship between wind and the ocean surface roughness. Land and rain contamination are the most pervasive types

of contamination and so are briefly introduced in the following subsections and discussed in detail in Chapters 3 to 8.

### **2.6.1 Land Contamination**

Land contamination occurs when the antenna spatial response function is partially over land. Because the land backscatter is typically much brighter than the backscatter over ocean, land-contaminated backscatter measurements typically result in positively biased wind estimates. Land-contaminated wind estimates are apparent in the UHR wind estimates of Fig. 2.3 as high wind speeds surrounding the coastlines. The 25 km L2B wind estimates are free of land contamination, but do not have near-coastal winds estimates. As near-coastal wind are often of particular interest, the wind estimate uncertainty and bias caused by land contamination are extremely undesirable. The effects of land contamination on wind retrieval and mitigation of land contamination are evaluated in depth in Chapter 8.

### **2.6.2 Rain Contamination**

Rain contamination is similar to land contamination in that it modifies the wind-induced backscatter in undesirable ways. Unlike land contamination however, the location of the rain events which cause the contamination is not known before hand, so the contamination must be treated quite differently.

Rain contamination occurs as a consequence of several rain effects. Rain drops striking the ocean surface modify the wind-induced wave field and thereby modify the ocean surface backscatter. Additionally, atmospheric rain drops attenuate the surface backscatter signal in addition to contributing additional backscatter. Further, rain events are often associated with down drafts which modify the wind field surrounding the rain cell. Figure 2.4 illustrates some interactions between wind and rain which can affect the measured backscatter.

Because rain modifies the wind-induced backscatter in many ways, its effect on the wind estimates can be varied as well. Rain contamination of the UHR wind estimates in Fig. 2.3 is visible as small concentrated areas with high wind speeds in the left portion of the image and as bands of high wind speeds following the hurricane circulation pattern corresponding to the hurricane rain bands. For some cases, rain increases the backscatter,

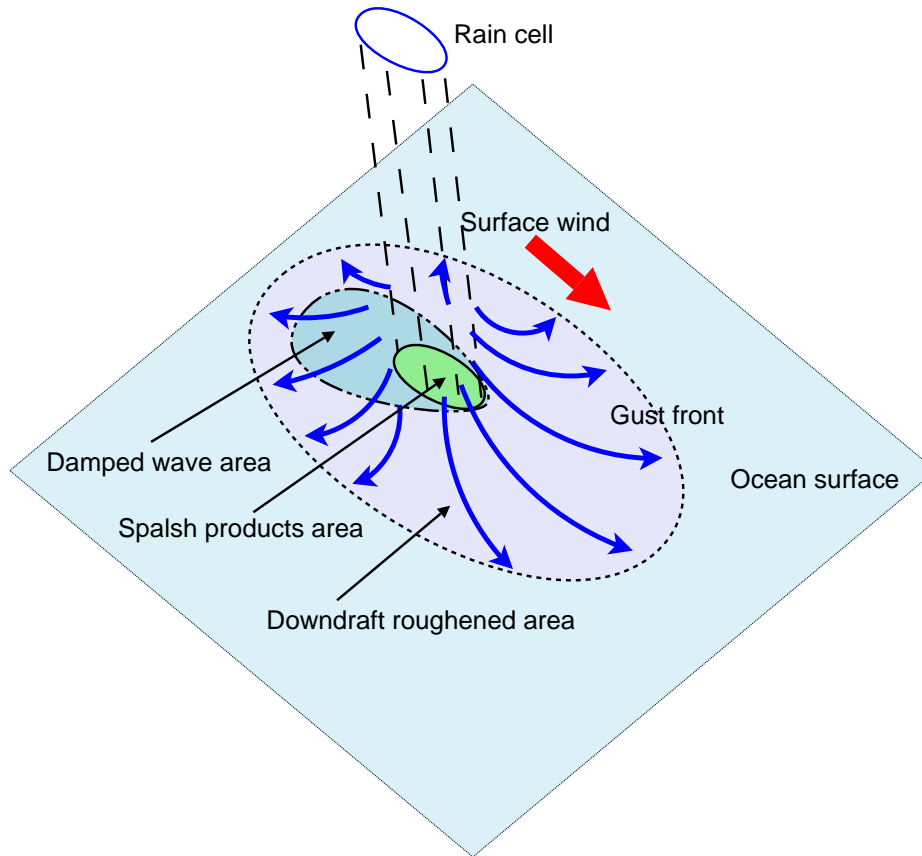


**Figure 2.4:** Wind and rain interaction over the ocean. Intense rain columns are associated with strong downdrafts which modify the surrounding surface wind field. Falling rain drops create radar observable splash products beneath the rain column and which can also dampen the wind-induced surface waves in the surrounding area. Figure taken from [55].

causing a positive bias in the wind speed, while for others the rain can attenuate the wind signal, making wind retrieval impossible with any degree of accuracy. A more complete discussion of rain contamination and its effects on wind retrieval is found in Chapters 3 through 7.

## 2.7 Summary

Scatterometers have demonstrated a unique ability to remotely measure and detect a variety of targets. The 10 year QuikSCAT global wind dataset can be a valuable tool in evaluating the global environment as long as measurement contamination can be ap-

appropriately accounted for. The remainder of this dissertation introduces and demonstrates several techniques for contamination mitigation thereby improving and extending the utility of the QuikSCAT dataset in particular in addition to introducing contamination mitigation techniques which can be applied to other scatterometers.

## Chapter 3

### Ultra-high Resolution Rain Backscatter Modeling

Rain is a significant problem for QuikSCAT measurements if unaccounted for, thus a variety of efforts have been made to identify and flag rain contamination of wind estimates [56, 57, 58, 59, 60]. Typically, rain contamination results in overestimated wind speeds, strong directional bias, and increased wind estimate variability during wind retrieval. To understand the effects of rain contamination on wind estimation, the effects of rain on the observed backscatter must first be characterized. This chapter provides a phenomenologically motivated investigation of the effects of rain on Ku-band wind-induced backscatter. Rain effects on Ku-band backscatter are quantified by forming models for the rain-induced backscatter which are specific to QuikSCAT UHR wind estimates.

Section 3.1 reviews relevant QuikSCAT and TRMM PR background. Section 3.2 considers the issues of temporal and spatial resolution, then develops models for the backscatter effects of rain on QuikSCAT observations after which Section 3.3 concludes.

#### 3.1 QuikSCAT and TRMM Background

The QuikSCAT scatterometer measures the normalized radar cross section or backscatter from the earth's surface using a 13.4 GHz dual-polarization rotating pencil-beam antenna. For wind retrieval, QuikSCAT observations can be categorized into four 'flavors': vertically polarized (V-pol) forward-looking, V-pol aft-looking, horizontally polarized (H-pol) forward-looking and H-pol aft-looking. The nominal incidence angle is  $46^\circ$  for H-pol and  $54^\circ$  for V-pol. Consequently, there is an outer swath region where there are no H-pol backscatter measurements. The region where there are both V-pol and H-pol measurements is termed the inner swath and is the part of the swath where rain retrieval is possible. The development of the rain model uses measured rain data provided by the Tropical Rain Measuring Mission

Precipitation Radar (TRMM PR) as the comparison rain dataset and model winds from the National Centers for Environmental Prediction (NCEP) as the comparison wind dataset.

Operating at 13.8 GHz, TRMM PR provides an ideal comparison dataset for rain. TRMM PR provides rain data at a 4.3 to 5 km resolution with a swath width of 247 km, but is limited to tropical latitudes. The validation data set used here is composed of two years' worth of QuikSCAT and TRMM PR measurements co-located to within 10 minutes. QuikSCAT 2.5 km resolution rain data is compared to co-located and spatially interpolated TRMM PR dataset. To obtain co-located wind data, NCEP winds are interpolated spatially and temporally to match QuikSCAT resolution and measurement times. Although the NCEP wind product is inherently lower resolution than the QuikSCAT UHR product, we assume that any bias can be compensated.

The effects of rain on Ku-band backscatter have been studied and validated at conventional (25 km) resolution [61, 62, 63]. At UHR, however, several additional complications arise in modeling the rain-induced backscatter. Due to the signal processing implementation, QuikSCAT has essentially no range resolution. Because rain occurs up to an altitude of 6 km, the incidence angles used by QuikSCAT can cause up to 6 km of apparent horizontal spreading of the rain signal, which for UHR estimates is significantly larger than a resolution cell. The antenna spatial response and the resolution enhancement algorithm together result in additional horizontal spreading of the rain signal, causing rain contamination of measurements in WVCs near rain events. Further, at high resolution intense rain cells have a stronger effect on the observed backscatter since there is less averaging into the resolution cells than for the 25km product. Consequently, the conventional resolution rain model and associated assumptions may be inappropriate for the UHR case.

### **3.2 UHR Rain Model**

Falling hydrometeors introduce several changes in the observed radar backscatter which must be accounted for in the model. Rain striking the ocean surface increases the surface roughness and observed backscatter [64]. Atmospheric hydrometeors also cause attenuation of the surface backscatter signal in addition to volume scattering from the raindrops themselves. This attenuation can occur in two forms: atmospheric attenuation of the surface

backscatter and attenuation of the wind-induced surface waves by intense rain [65]. Since the wave attenuation only occurs during the most intense rain events, we do not include a separate term in the rain models for this effect. To account for these effects, we adopt a simple model for each of these effects,

$$\sigma_o = (\sigma_w + \sigma_{sr})\alpha_r + \sigma_r, \quad (3.1)$$

where  $\sigma_o$  is observed backscatter,  $\sigma_w$  is the wind-only backscatter,  $\sigma_{sr}$  is the surface backscatter due to rain,  $\alpha_r$  is the attenuation caused by rain, and  $\sigma_r$  is the backscatter from falling rain drops. This model is referred to in the following as the phenomenological rain model.

A modification of the above phenomenological model was adopted in [61] and [63] to reduce the number of model parameters. This modified rain model assumes that the additive backscatter terms due to rain can be combined to form an effective rain backscatter model

$$\sigma_o = \sigma_w\alpha_r + \sigma_e, \quad (3.2)$$

where  $\sigma_e$  is the effective rain backscatter which approximates  $(\sigma_{sr}\alpha_r + \sigma_r)$  from the phenomenological model.

At UHR the effects of localized intense rain cells are magnified when compared to the effects at 25 km resolution. Thus, the rain model must accurately portray the backscatter effects of intense rain events. Here we evaluate both the phenomenological and effective rain models as applied to UHR wind and rain retrieval. There are differences in wind and rain retrieval due to rain model choice which may be attributed to the combined effects of the surface backscatter and atmospheric attenuation. If, for instance, the atmospheric attenuation dominates the surface backscatter, then the effective rain model may be a sufficient characterization of the rain effects. However, the effects of atmospheric attenuation and backscatter vary widely as a function of rain rate; thus the phenomenological model may be more appropriate for UHR.

The rain model parameters are estimated for QuikSCAT using the two independent datasets discussed previously: NCEP winds and TRMM PR rain rates. There are several effects due to both the spatial and temporal differences of the QuikSCAT and TRMM PR

observations which are detrimental to the rain model if not considered. We discuss these effects in the following two subsections before discussing the rain models themselves.

### 3.2.1 Spatial Resolution

Although QuikSCAT UHR estimates are reported at 2.5 km, the effective resolution is somewhat lower due to the limitations of the  $\sigma^o$  resolution enhancement process [66]. When using TRMM PR rain rates to estimate the effective rain backscatter, the resolution enhancement can have significant consequences. The resolution enhanced backscatter used to produce UHR estimates is reconstructed from irregular spatial samples [54]. The reconstruction process creates a backscatter field by averaging the observations that overlap a single resolution cell. The antenna spatial response function is larger than a resolution cell so the backscatter in a single resolution cell is an irregular contribution of the backscatter from the surrounding area. Such averaging is often appropriate for wind events, which have smoother spatial scales. For rain events, which can have rapid spatial variation, it is important to account for the effects of the reconstruction process.

To ensure compatible rain observations for TRMM PR and QuikSCAT, we interpolate the measured TRMM PR rain field to the resolution of QuikSCAT UHR estimates. The interpolated rain field is then ‘sampled’ with a simplified antenna pattern in two steps using the QuikSCAT measurement geometry and spatial response function [50] for each observation flavor. First an estimate of the rain rate observed by each QuikSCAT slice measurement is obtained for each of the  $G_i$  slice measurements using

$$R(G_i) = \frac{\sum_{(a,c) \in G_i} R_{TRMM}(a,c)}{\sum_{(a,c) \in G_i}}, \quad (3.3)$$

where  $R(G_i)$  is the average TRMM-observed rain rate,  $R_{TRMM}(a,c)$ , in the along-track and cross-track cells  $(a,c)$  that contribute to the slice measurement  $G_i$ . After estimating the rain rate observed by each QuikSCAT measurement, the measurements that overlap each along-track and cross-track cell  $(a,c)$  are averaged to mimic the resolution enhancement process using

$$R_{PL}(a,c) = \frac{\sum_{G_i \in H_{PL}(a,c)} R(G_i)}{\sum_{G_i \in H_{PL}(a,c)}}, \quad (3.4)$$

where  $H_{PL}(a, c)$  is the set of measurements  $G_i$  of a given polarization  $P$  and look direction  $L$  which overlap the along-track and cross-track location  $(a, c)$ .  $R_{TRMM}(a, c)$  is the TRMM PR-measured rain rate after spatial interpolation to the QuikSCAT resolution.  $R_{PL}(a, c)$  is the TRMM PR rain rate after QuikSCAT resolution enhancement corresponding respectively to each polarization and look direction. There are four rain fields:  $R_{VA}$ ,  $R_{VF}$ ,  $R_{HA}$  and  $R_{HF}$ , corresponding to the V-pol aft look, V-pol forward look, H-pol aft look and H-pol forward look.

The four resulting rain fields are directly comparable to the resolution enhanced backscatter fields used to produce UHR wind estimates. This process is essentially identical to the resolution enhancement algorithm used to produce UHR estimates [54]. These ‘resolution enhanced’ TRMM PR rain fields thus represent the rain rate observed by QuikSCAT at UHR. The major difference between the TRMM PR-observed rain field and the rain rates observed by QuikSCAT is that due to the large sampling aperture and the resolution enhancement process of QuikSCAT, the QuikSCAT-observed rain fields are a low-pass filtered version of the TRMM PR observations.

When rain events do not uniformly fill the antenna beam, the rain rate corresponding to the measured backscatter may be misrepresented. This effect is commonly referred to as irregular beam-filling. The interpolation and resampling of rain rates described above simplifies the beam-filling problem since the rain rate in each WVC after the above sampling process is the QuikSCAT observed rain rate. Using the QuikSCAT-observed rain in each cell accounts for the effects of irregular beam-filling, thereby reducing variability in the rain backscatter models.

One additional source of variability between the TRMM PR and QuikSCAT observations is the very different incidence angles. TRMM PR is designed to observe nearly vertical rain columns, whereas QuikSCAT operates at an incidence angle of  $46^\circ$  or  $54^\circ$ . Since rain frequently occurs above 5 km and QuikSCAT has limited range resolution, the rain signal may appear in multiple resolution cells. This effect is relatively small compared to the resolution enhancement process and thus we do not explicitly compensate for it in the remainder of this paper.

### 3.2.2 Temporal Resolution

Temporal effects are particularly important for QuikSCAT UHR rain estimates due to the rapid temporal variations involved in rain dynamics. There are two general classes of rain events, stratiform and convective, each of which has a different character. Most stratiform rain events have large spatial scales and low to moderate rain rates throughout. These large rain events are typically associated with slow-moving storm systems. Convective rain events such as microbursts and macrobursts however, typically have small spatial scales and short durations, on the order of 10 minutes [67], and are typically associated with intense fast-moving storms [68]. Additionally, the highest observed rain rates are associated with these types of storms.

Because of the dynamic nature of rain events, there are two fundamental temporal effects which must be addressed to meaningfully compare QuikSCAT and TRMM PR observations at UHR. First, the reported observation times of QuikSCAT and TRMM PR are not identical due to very different orbit geometries. For stratiform rain events, a small difference in observation time has a relatively low impact on the rain backscatter estimates since the events are large and move slowly. However, convective rain events can have such rapid dynamics that the rain event can significantly change and move multiple resolution cells between the TRMM PR and QuikSCAT observation times. Since convective rain events are typically associated with high rains, if the observation time differences due to orbit geometry are unaccounted for, the effects of high rain on QuikSCAT observations may be misrepresented.

In addition to observation time differences due to different orbit geometries, there are observation time differences that can be uniquely attributed to the QuikSCAT sampling geometry. Although a single observation time is reported with the conventional resolution wind estimates for each QuikSCAT location, these times are in reality averages. Due to the helical sampling pattern and different incidence angles, QuikSCAT has observation times for a fixed location which range over a window as large as 4.5 minutes. For example, near the nadir track the V-pol forward- and aft-looking measurements of the same location are made 4.5 minutes apart. Thus, in many cases, intense rain events can move through several 2.5 km resolution cells within the QuikSCAT observation window. This means, in essence, that

each observation type (forward V and H, aft V and H) views a slightly different rain field. Typically, the differences in the rain fields are small and consist of a spatial shift due to the motion of the rain event. This effect is small for low to moderate rain events which typically have large spatial scales and smaller variability, but for high to intense rain events it can cause discrepancies in the rain backscatter estimates.

Here we use a simple approximation to reduce the effects of temporal differences between the QuikSCAT and TRMM PR observations. Because scatterometer  $\sigma^o$  observations of a given flavor have similar measurement times which differ from other flavors, we assume that there is constant spatial shift in the TRMM PR observed rain events for each QuikSCAT observation flavor. This constant shift can be interpreted as the entire rain field moving a fixed amount between the TRMM PR observation time and the observation time for the QuikSCAT flavor of interest. Although this does not fully account for realistic rain dynamics it is a first-order correction.

A simple way to estimate the fixed shift for each QuikSCAT measurement flavor is to use the 2D cross correlation between the array  $R_{PL}$  from Eq. 3.4 and the rain backscatter estimates as calculated in the following sections. The location of the maximum value of the cross correlation gives the shift required to maximally correlate the TRMM PR rain fields to the rain backscatter estimates. Typically, the required data shift is between 2.5 and 7.5 km, or one to three resolution cells. As might be expected, the shifts for the forward-looking observations are similar for both polarizations, as the observation time difference is small for identical look directions. Although the shifts are just a few pixels, correcting for the shift in the data substantially reduces the variability of the rain backscatter estimates as a function of the observed rain rate, particularly for high rain rates.

### 3.2.3 Attenuation Model

The atmospheric attenuation factor  $\alpha_r$  model can be estimated directly using TRMM PR measurements of path integrated attenuation. Note that the path-integrated attenuation,  $pia$ , measured by TRMM PR reflects the path specified by the TRMM PR geometry and must be adjusted for QuikSCAT geometry which has a longer path due to the change in incidence angle. The QuikSCAT  $pia$  estimates are modeled as a function of the rain rate

$R_{dB}$  and polarization  $p$  using

$$pia(R_{dB}, p) = 10^{\sum_{k=0}^2 R_{PL_{dB}}^k p_k / 10}, \quad (3.5)$$

where  $R_{PL_{dB}}$  is the resolution enhanced TRMM PR rain rate in dB, and  $a_k$  are the model coefficients. Path integrated attenuation is related to  $\alpha_r$  according to

$$\alpha_r(R_{dB}, p) = 10^{-pia(R_{dB}, p) / 10}. \quad (3.6)$$

Figure 3.1 shows the attenuation factor  $\alpha_r$ , rain rate from TRMM PR, and the resulting quadratic attenuation model for each polarization. In reality, the atmospheric attenuation may be polarization dependent; however, since TRMM PR reports only a single polarization, we assume, for lack of a better model, that the path integrated attenuation is identical for each polarization and only varies due to the difference in path lengths for each polarization.

The model coefficients  $p_k$  of the atmospheric attenuation factor are estimated by first performing a kernel-smoothing operation on the data. The resulting non-parametric fit is shown with the data in Fig. 3.1. The model coefficients are estimated using a linear least-squares approach of the non-parametric fit in log space. The values of  $a_k$  estimated in this manner are listed in Table 3.1. This approach avoids the limitations of a direct non-linear least-squares approach. Due to the relative simplicity and robustness of this method, this fitting technique is used throughout the remainder of this chapter to determine each set of model coefficients.

The atmospheric rain attenuation is identical in both the effective and phenomenological rain models. The other model terms and parameters are different and are derived and estimated below. The following subsections discuss the estimation of the parameters for each model and then discuss the differences between the models.

### 3.2.4 Effective Rain Model

To estimate the effective backscatter model, Eq. 3.2 is used to solve for  $\sigma_e$ . Thus

$$\sigma_e(R_{dB}, p) = \sigma_o - \sigma_w \alpha_r, \quad (3.7)$$

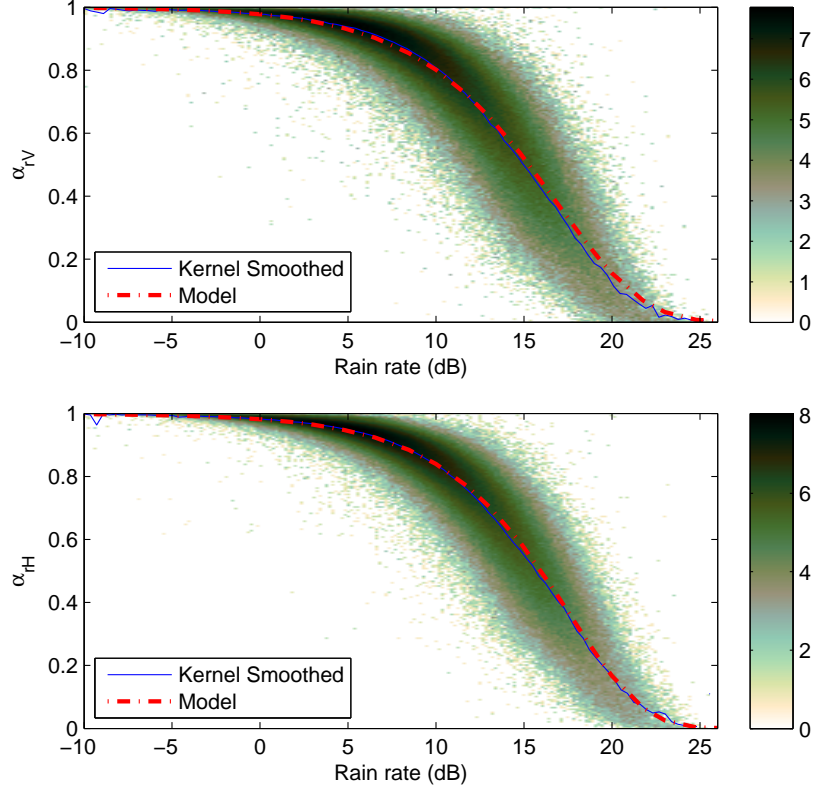


**Figure 3.1:** Rain attenuation models for V and H polarizations. The background color is the path attenuation data measured by TRMM PR adjusted for the QuikSCAT propagation geometry which is used to derive the models. Note that the background color is the log of the scatter density which is shown in the plot to accentuate less common rain rates. This, however, increases the apparent variance.

where  $\alpha_r$  is the TRMM PR-measured atmospheric attenuation,  $\sigma_w = \mathcal{M}(\mathbf{w}_{NCEP})$  is the estimated backscatter induced by the NCEP wind vector  $\mathbf{w}_{NCEP}$ , and  $\sigma_o$  is the QuikSCAT measured backscatter value for the corresponding observation flavor. Due to noise inherent in each of the datasets, some  $\sigma_e$  estimates are negative. This is particularly true for low rain rates where the rain backscatter may be small. Although these negative values are not realistic, if they are discarded they can cause severe bias in the rain model.

The scatter densities of the effective rain backscatter estimates are shown for both H and V polarizations in Fig. 3.2 as a function of the TRMM PR-measured rain rates. Note that the H-pol measurements are more sensitive to rain than V-pol for moderate to high rain rates.

To model the effective backscatter we use a quadratic model of the form [61]

$$\sigma_e(R_{dB}, p) = 10^{\sum_{k=0}^2 R_{dB}^k e_k / 10}, \quad (3.8)$$

where  $e_k$  are the model parameters. The model coefficients  $e_k$  are determined using the kernel-smoothing and linear least-squares technique outlined previously. The non-parametric kernel-smoothed fit is shown with the resulting quadratic model for each polarization in Fig. 3.2. The resulting model parameters are found in Table 3.1.

It is important to note that there is an apparent noise floor in the effective rain backscatter estimates. For low rain rates (below 5 dB km-mm/hr), the variability between the NCEP model winds and QuikSCAT observations entirely dominates the rain signal, creating an apparent noise floor at about 0.001 in the  $\sigma_e$  estimates. This noise floor is not a physical effect, as the rain backscatter decreases as the rain decreases. Thus, to estimate the effective rain model parameters, we ignore effective rain backscatter estimates for rain rates below 5 dB km-mm/hr.

### 3.2.5 Phenomenological Model

This section estimates the backscatter models for  $\sigma_{sr}$  and  $\sigma_r$  which require additional information from TRMM PR. TRMM PR-measured reflectivity is available in TRMM 1C21 files. The TRMM PR total atmospheric backscatter  $\sigma_{r(PR)}$  can be calculated from the measured reflectivity  $Z_m$  using

$$\sigma_{r(PR)} = \int_0^{r_{nc}} 10^{-10} \frac{\pi^5}{\lambda_0^4} |K_w|^2 Z_m(r) dr, \quad (3.9)$$

where  $r_{nc}$  is the no clutter range,  $\lambda_0$  is the wavelength in cm,  $|K_w|^2$  is a coefficient relating the absorption properties of water (assumed to be 0.9), and  $Z_m(r)$  is the TRMM PR-measured reflectivity for the range  $r$  [69].

The TRMM PR atmospheric backscatter  $\sigma_{r(PR)}$  is adjusted for the QuikSCAT resolution and sampling by spatially interpolating to the QuikSCAT resolution followed by spatial averaging using Eqs. 3.3 and 3.4. The TRMM PR observations are adjusted for the

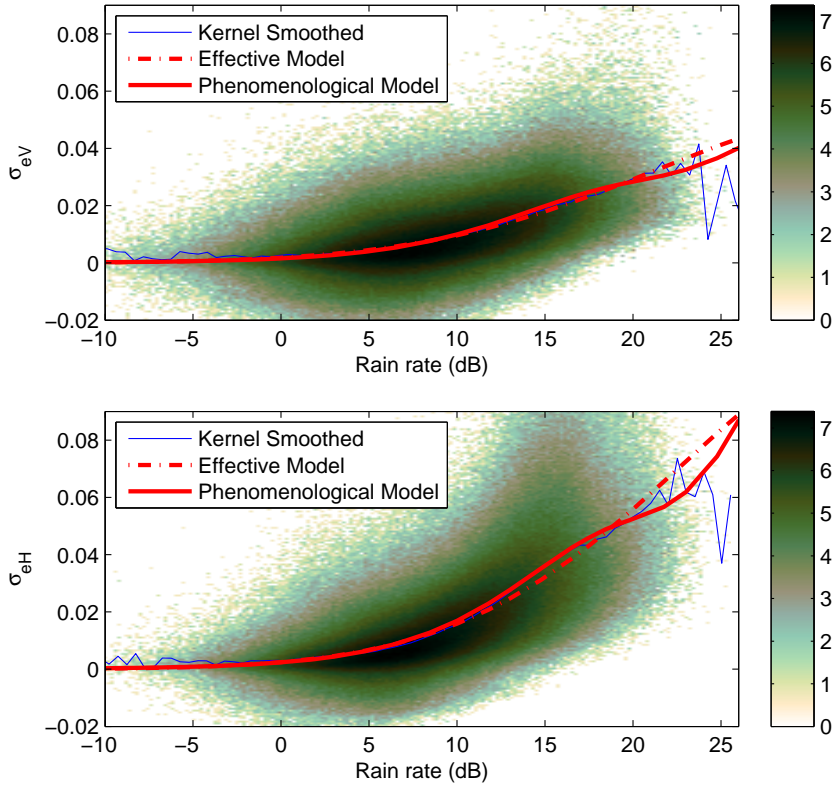


**Figure 3.2:** Effective rain backscatter,  $\sigma_e$ , models for V and H polarizations. The background color is the log of the scatter density of estimated  $\sigma_e$  used to derive the model for both polarizations. Note that there is significant variance in the data used to derive the model.

QuikSCAT geometry by compensating for the change in path lengths due to the change in incidence angle from TRMM PR to QuikSCAT.

Although TRMM PR makes H polarized atmospheric backscatter measurements, they are not directly comparable to QuikSCAT H- or V-polarized atmospheric backscatter estimates. This is primarily due to the large difference in incidence angle which significantly affects the backscatter. This is a serious limitation to creating an appropriate model since there can be a significant difference in the backscatter response as a function of incidence angle and polarization. This change can be largely attributed due to the non-spherical nature of falling rain drops.

This polarization and incidence angle sensitivity can be compensated for using a simple correction factor  $\gamma_p$  for each polarization  $p$ . The polarization-corrected QuikSCAT

observed atmospheric backscatter  $\sigma_{rp}$ , where  $p$  indicates polarization, can be modeled as

$$\sigma_{rp} = \gamma_p \sigma_{r(PR)}, \quad (3.10)$$

where  $\gamma_p$  is the polarization and incidence angle correction factor and  $\sigma_{r(PR)}$  is the TRMM PR-observed atmospheric backscatter after adjusting for QuikSCAT sampling and path length changes. Utilizing this simple correction factor assumes that the difference between H and V polarization atmospheric scatter is not dependent on rain rate. In reality, the correction factor  $\gamma_p$  may be dependent on rain rate. However, since information to create a more informed model is unavailable, this chapter uses the correction factor assumption despite its limitations. Estimation of the correction factor is discussed later in this chapter.

After polarization correction, the QuikSCAT-observed  $\sigma_r$  can be modeled for each polarization using

$$\sigma_r(R_{dB}, p) = 10^{\sum_{k=0}^2 R_{PLdB} a_k / 10}, \quad (3.11)$$

where  $a_k$  are the model coefficients. The model coefficients are determined by fitting the model to the kernel-smoothed data. The resulting model as a function of integrated rain rate in dB is plotted together with the data used to derive the model in Fig. 3.3 and model parameters are indicated in Table 3.1.

Using the QuikSCAT-sampled atmospheric backscatter we can form estimates of the rain-induced surface backscatter by solving Eq. 3.1 for  $\sigma_{sr}$  using

$$\hat{\sigma}_{sr} = (\sigma_m - \sigma_{rp}) \alpha_r^{-1} - \hat{\sigma}_w, \quad (3.12)$$

where  $\sigma_m$  is the QuikSCAT-measured backscatter,  $\sigma_{rp}$  is the measured atmospheric rain backscatter after polarization correction,  $\alpha_r$  is the measured rain attenuation and  $\hat{\sigma}_w$  is the estimated wind backscatter corresponding to the NCEP wind vector. Here we have assumed that the surface backscatter due to rain is not dependent on the wind speed as demonstrated in [64].

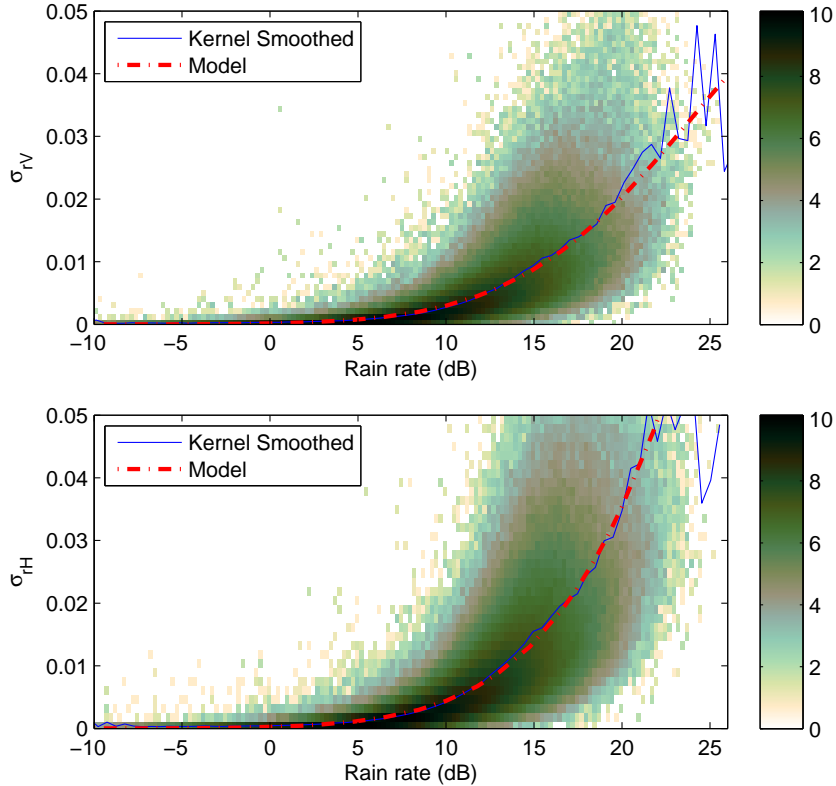


**Figure 3.3:** Atmospheric backscatter,  $\sigma_r$ , with polarization correction as a function of measured rain rate. Note that although there is insufficient data to determine the rain model for the highest rain rates it is anticipated that the atmospheric backscatter continues to increase with rain rate. The background color shows the log of the scatter density of the estimates.

The rain-induced surface backscatter model is written

$$\sigma_{sr}(R_{dB}, p) = 10^{\sum_{k=0}^1 R_{PL_{dB}} s_k / 10}, \quad (3.13)$$

where  $s_k$  are the model coefficients given in Table 3.1 which best fit the kernel-smoothed data. Figure 3.4 shows the estimated  $\sigma_{sr}$  data in addition to the kernel-smoothed fit and the resulting model. Unlike the other parts of the rain model, only two parameters are used in the surface backscatter model. The two parameter model is more appropriate since the surface backscatter is prone to noise for both low rains, due to the noise floor, and high rains, due to atmospheric attenuation. Thus it is not clear that a quadratic model is justified so we adopt a simpler linear model instead.

Note that the rain-induced surface backscatter can be negative. This is largely due to the fact that the rain drops striking the ocean surface can cause destructive interference with the wind-induced wave field thereby reducing the overall backscatter. As indicated by the models, the rain-induced surface backscatter generally increases as a function of the rain rate. However, for moderate to high rain rates the variability in the data suggests that the uncertainty is high. This is consistent with the increase in atmospheric attenuation. As attenuation increases, the ability to observe and estimate the surface backscatter decreases as the overall rain backscatter becomes dominated by atmospheric scattering.

The noise level in the estimates of the rain-induced surface backscatter is readily apparent for high rain rates where attenuation is dominant. While not apparent in Fig. 3.4, there is a similar effect for low rain rates. As with the effective rain backscatter estimates for low rain rates, the NCEP wind variability dominates the rain signal causing an effective noise floor in the estimates of the rain-induced surface backscatter. Such a noise floor is not a physical phenomenon as the rain-induced surface backscatter should decrease to zero as rain rate decreases. To appropriately reflect this low rain effect in the surface backscatter model,  $\sigma_r$  estimates below 5 db km-mm/hr are ignored just as was done for the effective backscatter model. Thus the surface backscatter models decrease indefinitely as rain rate decreases.

Up to this point, estimation of the polarization correction coefficient,  $\gamma_p$ , has not been discussed. Without additional information, one simple way to estimate the correction factor is to perform a non-linear least-squares optimization for  $\gamma_p$  to minimize the error between the combined phenomenological model,  $\alpha_r \sigma_{sr} + \sigma_r$ , and the kernel-smoothed  $\sigma_e$  data. Such an approach is appropriate since the phenomenological model should have similar features to the  $\sigma_e$ . Estimating  $\gamma_h$  and  $\gamma_v$  in this manner leads to estimates of 0.92 and 0.49, respectively. These values indicate that the QuikSCAT-observed atmospheric backscatter is slightly smaller than that observed by TRMM PR for H-pol and almost half that observed by TRMM PR for V-pol. The corrected rain model is shown for each polarization together with the  $\sigma_e$  data in Fig. 3.2.

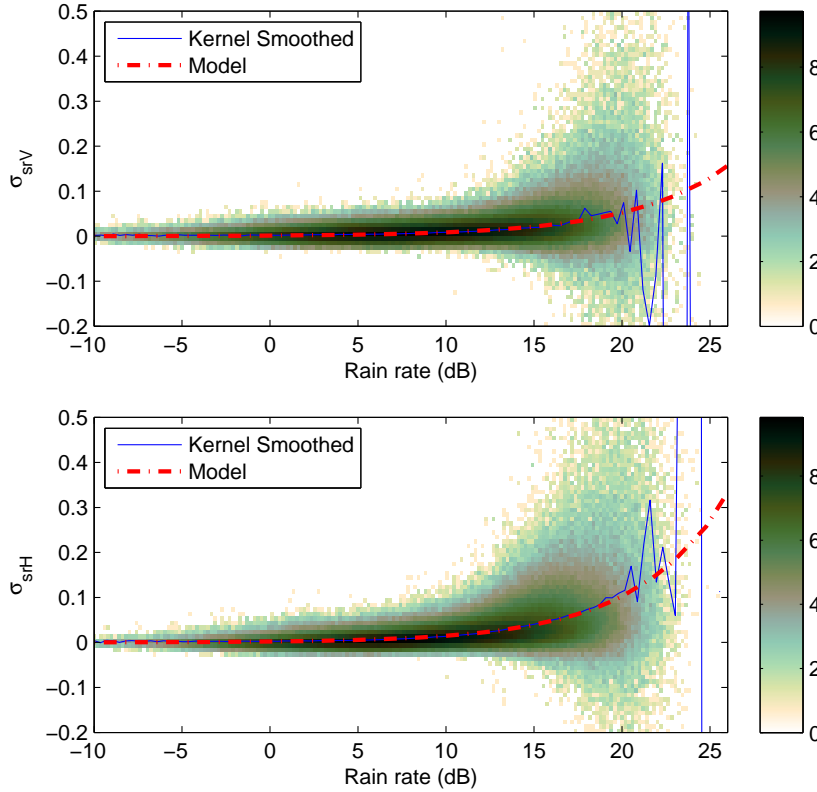


**Figure 3.4:**  $\sigma_{sr}$  as a function of rain rate in dB. Top: v-pol, bottom: h-pol. Note that H-pol is more sensitive to the surface backscatter due to rain. The background color is the log of the scatter density of the data.

### 3.2.6 Model Comparisons

This section considers the differences between the effective and phenomenological rain models. QuikSCAT is not capable of directly discerning between the surface and atmospheric effects of rain thus the lumped effects of rain backscatter are most important. To understand the combined effects of both surface and atmospheric rain backscatter on the QuikSCAT-observed rain backscatter the rain models with the kernel-smoothed fit of the effective backscatter estimates can be directly compared. Such a comparison is made in Fig. 3.5, which shows the backscatter for the kernel-smoothed fit of the effective backscatter data, the effective rain model and the phenomenological rain model.

As indicated in Fig. 3.5, both the effective and phenomenological rain models match the kernel-smoothed data for low to moderate rain rates. For high to extreme rain rates

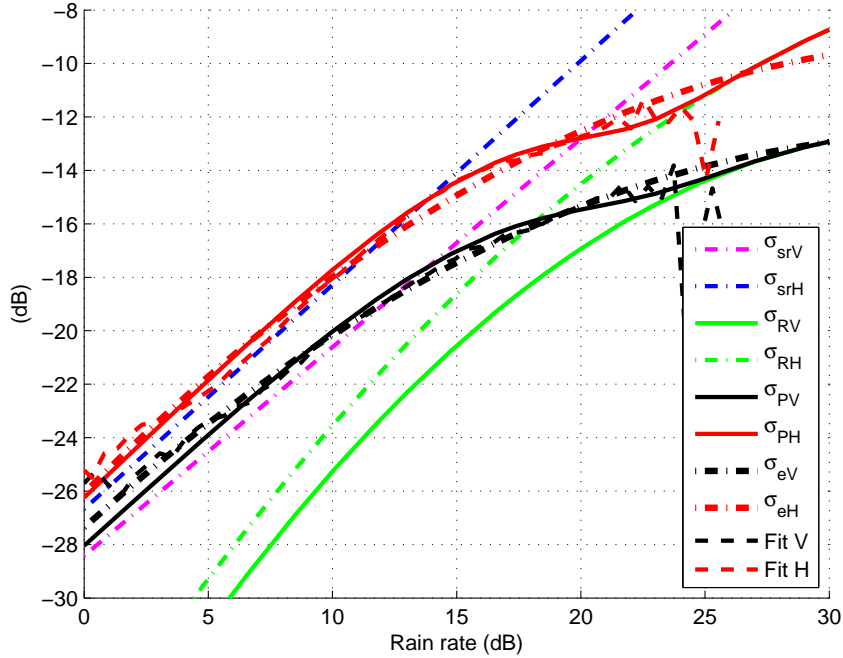


**Figure 3.5:** Effective and phenomenological rain models for both H and V polarizations. Also included is the kernel smoothed fit of the effective rain model data. Note that the plots include intense rain rates above 20 dB km-mm/hr where there are few observations in the data. This can give some insight about whether the model approach is reasonable.

(above 20 dB km-mm/hr) the effective rain model slightly overestimates the kernel-smoothed data, although the phenomenological rain model still fits well. This is a consequence of several factors but can largely be attributed to the effects of rain attenuation.

To further illustrate the effects of rain attenuation, Fig. 3.5 also shows the surface and atmospheric scattering components of the phenomenological rain model. For low to moderate rain rates the surface scattering terms match the kernel-smoothed data well, indicating that the rain backscatter is dominated by surface scattering. For these rain rates the atmospheric backscatter has a negligible effect since it is 10dB lower. While the surface backscatter continues to increase with rain rate, the effective backscatter does not since the atmospheric attenuation begins to dominate the surface scatter as the rain rate exceeds 15 dB km-mm/hr. As the transition occurs from surface dominance to atmospheric dominance the effective rain backscatter model no longer matches the effective backscatter data. For this

**Table 3.1:** Rain model parameters

Polarization	Parameter	k=0	k=1	k=2
H	$p_k$	-10.92	0.95	0.001824
V	$p_k$	-10.02	1.01	-0.0030
H	$e_k$	-26.08	0.94	-0.013
V	$e_k$	-27.36	0.84	-0.012
H	$a_k$	-35.83	1.39	-0.016
V	$a_k$	-37.9	1.48	-0.022
H	$s_k$	-26.67	0.84	
V	$s_k$	-28.42	0.78	

region the effective rain backscatter model overestimates the rain backscatter, since it does not properly describe the increased effects of rain attenuation.

Despite the fact that the rain attenuation is not explicitly accounted for in the effective rain model, the effective rain backscatter models the effects of rain on the backscatter quite well for low to moderate rain rates. Unfortunately for moderate to high rain rates, the model misrepresents the backscatter effects. Thus, from a modeling perspective, if moderate to high rain rates are of interest, then the phenomenological rain model is a more appropriate choice, despite some additional model complexity.

### 3.3 Conclusions

This chapter has shown that the effective and phenomenological rain models are both reasonable approaches to modeling the effects of rain on QuikSCAT UHR observations. As neither model is manifestly superior based on the available data sets, the phenomenological rain model may be a better choice for rain estimation as it more realistically models extreme rain events where atmospheric backscatter is dominant. However, while this conclusion is indicated by the model construction, it is not obvious from the data alone since high rain events are relatively infrequent.

Regardless of the rain model choice however, several observations about Ku-band rain-induced backscatter can be made. For most rain rates, the rain-induced backscatter is dominated by the additional surface scattering due to rain. For moderate to extreme rain

rates, the atmospheric backscatter becomes influential and dominant as the atmospheric rain attenuation increases. Since the wind-induced backscatter is similarly attenuated, the wind backscatter signal can be insignificant during extreme rains.

## Chapter 4

### ASCAT Rain Model

To reduce the influence of rain-induced backscatter, scatterometers such as ASCAT, which was designed by the European Space Agency, operate at C-band. At C-band, the atmospheric attenuation and scattering effects are reduced compared to Ku-band by operating at a lower frequency. However, despite having reduced atmospheric effects, C-band scatterometers are still subject to the effects of rain-induced surface scattering.

This chapter evaluates the overall effects of rain-induced scattering on the C-band scatterometer ASCAT. Section 4.1 reviews background information and develops the rain backscatter models. Section 4.2 discusses features of the backscatter models, Section 4.3 demonstrates the backscattering effects of rain through a case study after which Section 4.4 concludes.

#### 4.1 Backscatter Model

The ASCAT observed backscatter over the ocean surface is a function of the wind vector, which makes wind estimation possible [28]. However, the backscatter signal is sensitive to rain. In raining conditions, the wind backscatter is modified in several ways. Rain drops striking the surface of the ocean cause increased surface roughness due to additional waves in the form of stalks, rings and crowns [64]. Falling hydrometeors cause two effects on the observed backscatter. First, the backscatter from the surface of the ocean is attenuated due to the atmospheric rain, and second, the atmospheric rain causes additional scattering of the radar signal. Although there are other factors which effect the backscatter these terms dominate the overall backscatter. Thus, the backscatter model only accounts for the phenomenological terms.

The observed backscatter  $\sigma^o$  is modeled using the same phenomenological rain model used in Chapter 3 for QuikSCAT, namely

$$\sigma^o = (\sigma_w + \sigma_{sr})\alpha_r + \sigma_r, \quad (4.1)$$

where  $\sigma_w$  is the wind induced surface backscatter,  $\sigma_{sr}$  is the rain induced surface backscatter,  $\alpha_r$  is the attenuation factor of the surface backscatter due to atmospheric rain and  $\sigma_r$  is the additional volume scattering due to atmospheric rain. To model the atmospheric effects of rain requires measurements of the atmospheric parameters. As ASCAT is not capable of resolving the atmospheric effects of rain since it lacks appropriate range resolution, we turn to another instrument.

The Tropical Rain Measuring Mission Precipitation Radar (TRMM PR) uses a 13.8 GHz radar to make atmospheric rain observations. It measures the both columnar rain profile and atmospheric attenuation. Here we use TRMM PR data from observations that are spatially and temporally co-located with ASCAT. The co-located data sets consist of ASCAT backscatter observations together with TRMM PR rain profile data co-located spatially and within 10 minutes temporally. TRMM PR data for each co-location is spatially averaged to have the same resolution as ASCAT. In this paper we utilize data from 180000 such co-located measurements from February of 2007 to June of 2009.

#### 4.1.1 Atmospheric and Surface Scattering

The total atmospheric rain backscatter term  $\sigma_r$  can be estimated from TRMM PR observations of atmospheric reflectivity  $Z_m$  as

$$\sigma_r = \int_0^{r_{nc}} 10^{-10} \frac{\pi^5}{\lambda_0^4} |K_w|^2 Z_m(r) dr, \quad (4.2)$$

where  $r_{nc}$  is the lowest no clutter range,  $|K_w|^2$  is a coefficient related to the absorption properties of water,  $\lambda_0$  is the ASCAT wavelength, and  $Z_m(r)$  is the TRMM PR observed reflectivity at the range  $r$  [70]. Although TRMM PR has a significantly different observation geometry from ASCAT, the rain profiles can be related to C-band observations by adjusting

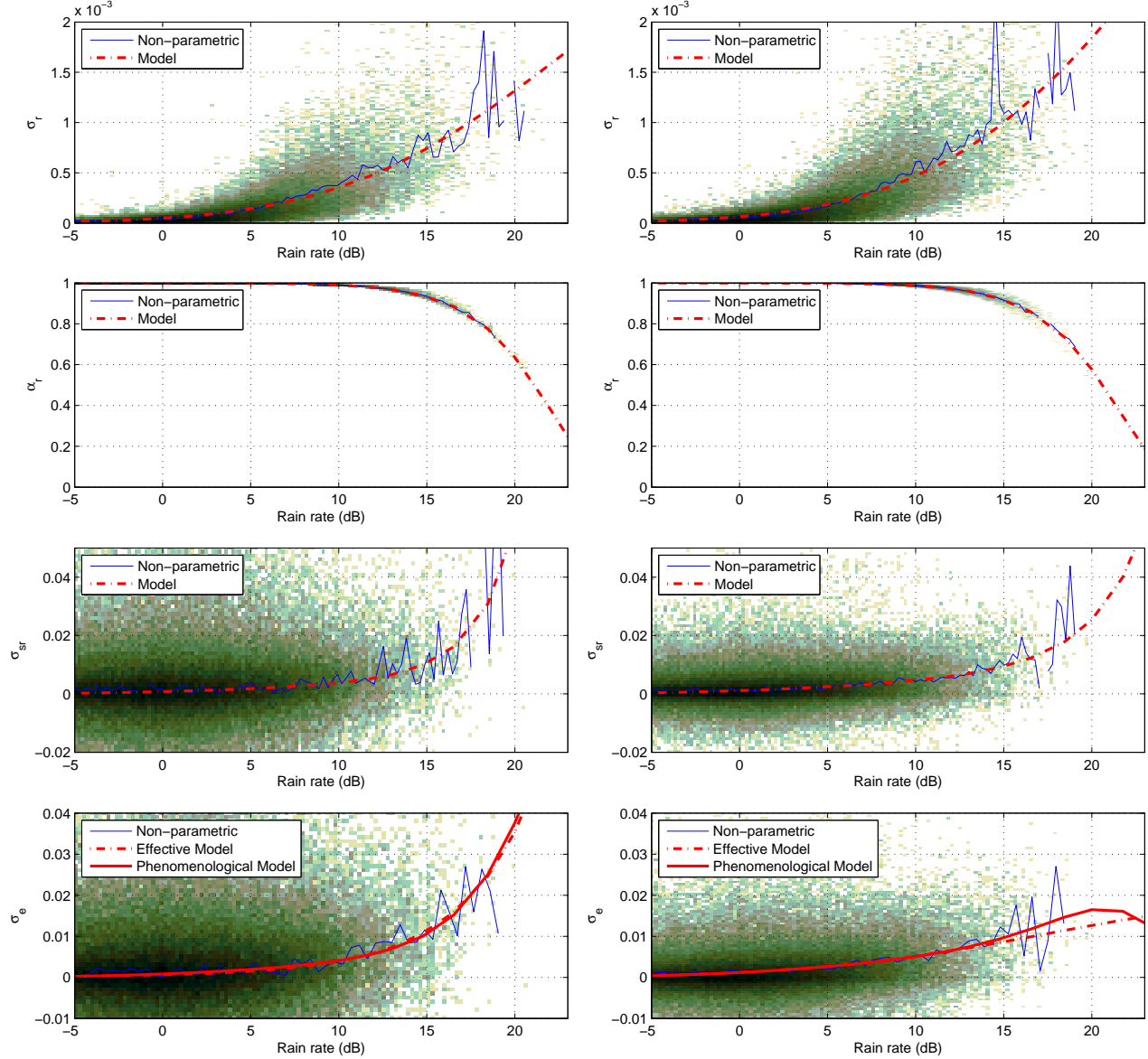


**Figure 4.1:** Top images:  $\sigma_r$  as a function of integrated rain rate in dB (km-mm/hr). Upper-middle images: Two-way atmospheric attenuation  $\alpha_r$  as a function of rain rate. Lower-middle images: Rain induced surface backscatter  $\sigma_{sr}$  estimates as a function of rain rate in dB. Bottom images:  $\sigma_e$  estimates,  $\sigma_e$  model and  $\sigma_{sr}\alpha_r + \sigma_r$  model. The left figures correspond to incidence angles  $> 45^\circ$  and the right to incidence angles  $< 45^\circ$ . Much of the variability in each image is due to the wide range of incidence angles represented.

each of the TRMM PR observed terms for the changes in incident angle from TRMM PR to ASCAT.

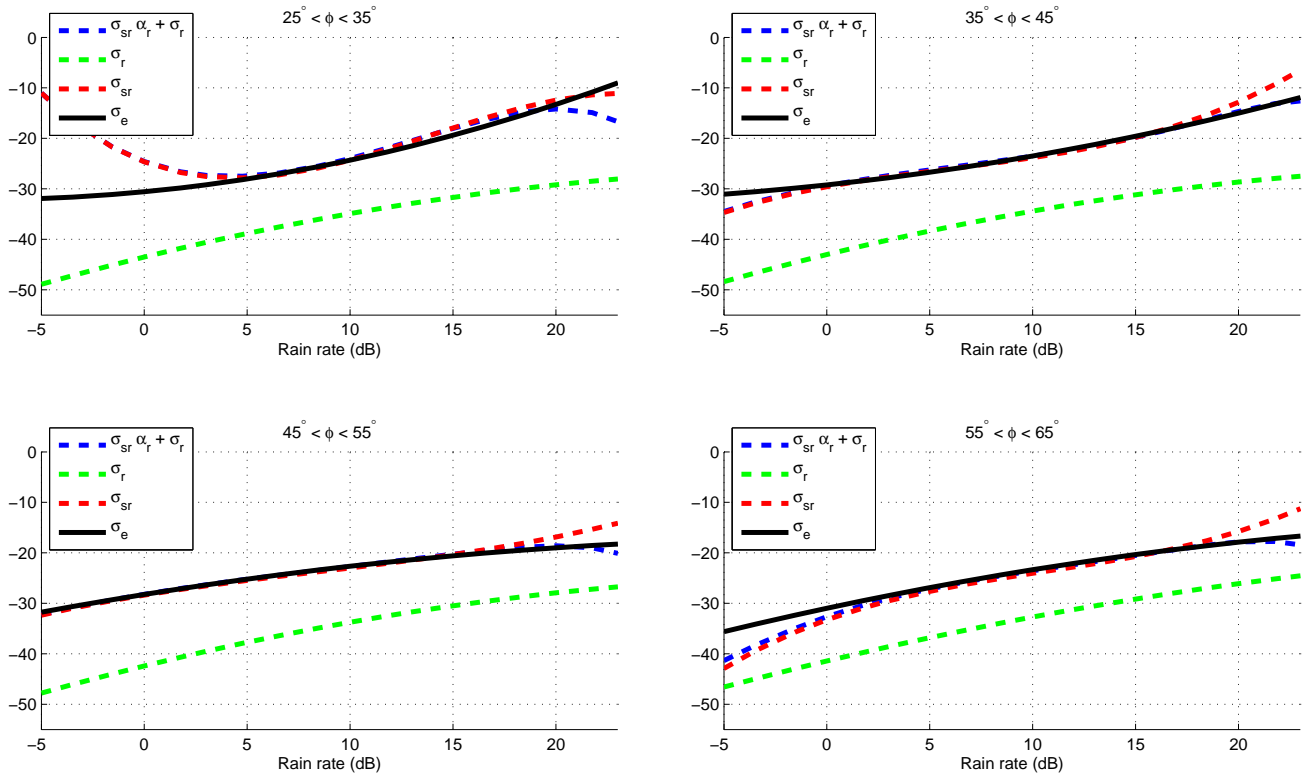


**Figure 4.2:** Model comparisons as a function of incidence angle. Below rain rates of 5 dB and above 25 dB the data to determine each of the models is too noisy to be accurate. However the increase in attenuation as a function of rain rate appears to be a natural consequence. Above a rain rate of 25dB the  $\sigma_e$  model appears to increase, this is not a realistic effect and is instead an artifact of the model choice.

Since the characteristics of rain attenuation are very different at Ku-band (TRMM) and C-band (ASCAT), the TRMM measurements of the path-integrated attenuation are not applicable to ASCAT. The rain attenuation can instead be approximated using the International Telecommunications Union (ITU) rain attenuation model [71], using the integrated rain rates measured by TRMM PR. Figure 4.1 shows the atmospheric backscatter and attenuation models, in addition to the data used to derive the models.

Evaluating the effects of rain on the surface backscatter requires an estimate of the wind backscatter  $\sigma_w$  in addition to the backscatter parameters measured by TRMM PR. Estimates of the wind backscatter can be formed using predictive wind models and the geophysical model function. The European Center for Medium-Range Weather Forecasting

(ECMWF) produces model wind estimates with a 6 hour availability and global coverage. These ECMWF wind fields can be used in conjunction with the geophysical model function, CMOD5 [72], to compute the expected wind backscatter  $\sigma_w$ . The geophysical model function is empirically derived to return the expected value of the backscatter given the wind vector and measurement geometry.

Combining the estimated  $\sigma_w$ , the TRMM PR measurements of  $\alpha_r$  and  $\sigma_r$ , together with the ASCAT observed backscatter  $\sigma_m$ , enables the estimation of the surface backscatter due to rain. The estimates of the surface backscatter  $\sigma_{sr}$  are shown in Fig. 4.1 for both high and low incidence angles.

Rain drops striking the ocean surface can have several effects, not all of which are modeled here. Rain striking the ocean causes additional surface roughness in the form of ring, stalk and crown waves. These waves can increase the surface backscatter causing roughness in addition to that caused by the wind. For intense rain rates, this effect is particularly dependent upon wind speed [65]. However, above a certain rain rate this relationship breaks down as the rain-induced surface-turbulence begins to attenuate all surface waves.

#### 4.1.2 Combined Scattering Effects

Instead of adopting the phenomenological model discussed in the previous section, past efforts at rain modeling for scatterometers have used an effective rain backscatter model, e.g. [73]. The effective rain model assumes that the overall contribution from the surface backscatter and atmospheric backscatter are similar. Based on this assumption, the combined wind and rain backscatter model can be written  $\sigma^o = \sigma_w \alpha_r + \sigma_e$  where  $\sigma_e = \sigma_{sr} \alpha_r + \sigma_r$ . The effective rain model has some advantages. Because there are fewer rain dependent terms the model has fewer parameters to estimate. The effective rain model fits the data quite well for low to moderate rain rates. However for intense rain rates, the scattering effects due to rain may not be modeled well.

The effective rain model is shown together with the estimates of  $\sigma_e$  in Fig. 4.1. The data readily indicates that  $\sigma_e$  increases with rain rate for low to moderate rain rates. Above about 25 dB there is insufficient data to substantiate the model accuracy and below 5 dB the backscatter noise is too high to discern the rain signal. For comparison the phenomenological

model is also shown in Fig. 4.1. Note that, although the phenomenological model is derived using estimates of  $\sigma_r$  and  $\sigma_{sr}$ , it has generally the same fit to the  $\sigma_e$  data as does the effective rain model below 20dB. Above this value the models diverge.

## 4.2 Model Comparisons

Both the effective and phenomenological rain models have advantages and limitations. To compare the two models, the most important issue is to determine which model more accurately portrays the effects of rain on the observed backscatter. To illustrate this comparison, each of the models is shown in Fig. 4.2 on a logarithmic scale as a function of rain rate in dB. Note that the models are shown as a function of incidence angle.

In each case, the model for  $\sigma_{sr}$  is 5 to 20dB higher than the model for  $\sigma_r$ . This implies that the phenomenological model is at first dominated by the surface scatter  $\sigma_{sr}$ , but as the rain rate increases past 20 dB, the phenomenological model transitions slowly to the model for  $\sigma_r$ . Although not shown in the figure, this transition is due to the atmospheric attenuation of the surface scatter for moderate to high rain rates. Thus, for low to moderate rain rates, the rain backscatter is dominated by the surface scatter, but for high rain rates, the atmospheric scattering dominates. This is true for all incidence angles although the point at which the transition from  $\sigma_{sr}$  to  $\sigma_r$  dominance occurs is dependent on incidence angle.

This difference between the two model types is fundamental. The effective rain model parametrization essentially assumes that rain backscatter always increases with increasing rain rate. As there are relatively few of the highest rain rate cases in the co-located dataset, it is easy to adopt this assumption. However, since the surface backscatter dominates the backscatter for low to moderate rain rates, this assumption can be problematic. Although there are few high rain data points to indicate how the surface backscatter behaves for high rain rates, the effects of atmospheric attenuation are well understood even for the highest rain rates. Since the attenuation is dominant for moderate to extreme rain rates, it is less important how the surface backscatter behaves, since it is extremely attenuated. This effect, which is not accounted for in the effective rain model, is the fundamental difference between the two rain models and accounts for the inaccuracy of the effective rain model for high rain rates. Thus, while the effective rain model is a reasonable approximation to the backscatter

due to rain for moderate rain rates, it does not accurately portray the effects of rain on the backscatter for moderate to high rain rates. To accurately portray moderate to high rain rates the phenomenological rain model should be used.

### 4.3 Case Study

To demonstrate the cumulative effects of the rain-induced backscatter, this section presents a simulated case study. Figure 4.3 shows simulated wind and rain fields together with the resulting backscatter observations. The simulated wind speeds are shown as well as the corresponding noise-free backscatter observations given by the CMOD5 GMF. The wind and rain backscatter is also shown where the surface rains are those shown in the image and the rain backscatter is generated from the effective rain backscatter model.

The wind and rain interactions, as indicated by the wind and rain backscatter in Fig. 4.3, are complicated but do indicate several key observations. For the lowest incidence angle range, low cross-track indices, the wind backscatter is high enough to mask the rain backscatter for all but high rain events. On the other hand, for moderate to high incidence angles, high cross-track indices, the effects of rain on the overall backscatter can be observed even for low rain rates.

### 4.4 Conclusions

Although this chapter neglects some important aspects of the rain backscatter model such as irregular beam-filling and wind speed dependence, the model discussed herein reflects the general characteristics of rain induced backscatter at C-band. While the numeric values for the models may change slightly as these aspects are accounted for, it is anticipated that the general trends discussed here will remain the same. The general characteristics of rain backscatter can be summarized for C-band as: for low to moderate rain rates the surface backscatter is dominant, for moderate to high rain rates the atmospheric attenuation begins to affect the surface scattering and for intense and extreme rain rates the attenuation is strong enough that the atmospheric scattering is dominant. Since the effective rain model does not account for the changes in high to intense rain rates, it is not a good modeling choice

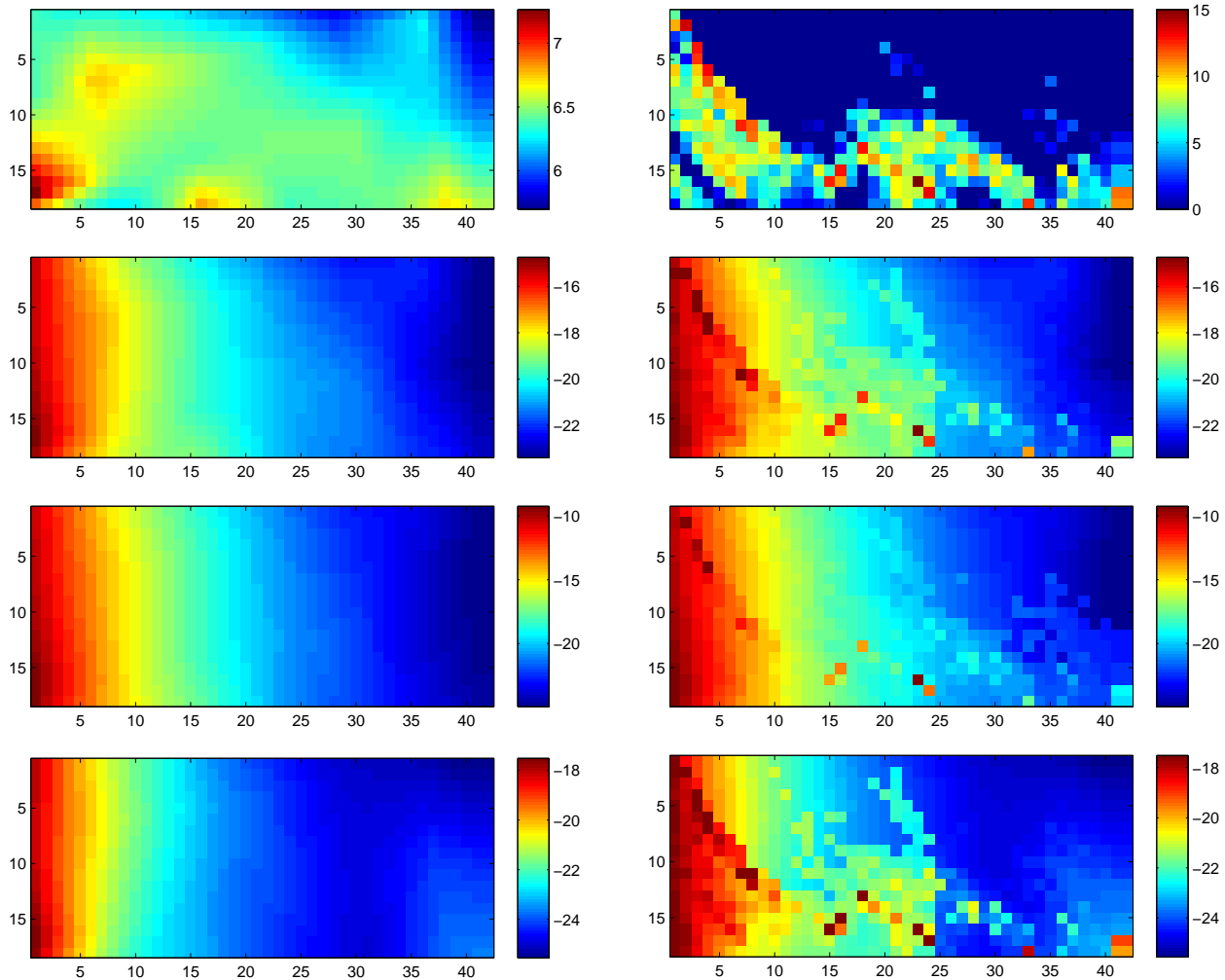


**Figure 4.3:** Simulated wind and rain backscatter for ASCAT. Top-left: Simulated wind speeds (m/s). Top-right: TRMM PR observed surface rain rates (dB mm/hr). Left column bottom three images: Wind backscatter given by CMOD5 in dB for fore, mid, and aft beams (top to bottom). Right column bottom three images: Wind and rain simulated backscatter given by CMOD5 and the effective rain model in dB for, mid and aft beams (top to bottom). In each image the near-swath (low incidence angles) are on the left and the far swath (high incidence angles) are on the right. In each image the x-axis represents cross-track range and the y-axis the along-track range.

for high rain rates. Finally, these results also show that rain contamination is important to consider at C-band.

The differences in the rain-induced backscatter effects at C- and Ku-band can be quite significant. At C-band the rain-induced backscatter is almost exclusively dominated by the surface scattering. At Ku-band, the rain-induced backscatter is dominated by the surface scatter for low to moderate rains and the atmospheric scattering for moderate to extreme rain rates. Although the atmospheric effects of rain are reduced by using a C-band observation frequency, rain can still have a substantial influence on the overall backscatter, particularly for low wind speed conditions.



## Chapter 5

### Ultra-high Resolution Simultaneous Wind and Rain Retrieval

Chapters 3 and 4 are limited to the evaluation and modeling of the backscatter effects of rain and made no steps to mitigate the rain contamination. This chapter takes a first step towards rain contamination mitigation by utilizing the rain backscatter models from Chapter 3 to perform simultaneous wind and rain (SWR) retrieval. This chapter introduces QuikSCAT SWR retrieval at UHR and evaluates the capability of the QuikSCAT scatterometer to improve wind estimation by simultaneously estimating the wind and the rain for UHR wind products. While this chapter and Chapters 6 and 7 are specifically applied to QuikSCAT wind products, the techniques introduced in these chapters can also be applied to ASCAT and other scatterometers subject to rain contamination.

While SWR retrieval has been studied at conventional resolution previously in [61, 63] this chapter discusses the application of the SWR estimation technique proposed in [61] to QuikSCAT 2.5 km UHR estimates. UHR wind and rain estimates have a singular advantage over conventional resolution products in that they can resolve small-scale convective rain events. Convective rain events have relatively small spatial scales and are often associated with extremely high rain rates. Conventional 25 km resolution products cannot resolve such small events and are further limited by the effects of irregular beam-filling [61]. At UHR, the increased resolution allows the rain estimates to resolve rain events on a much finer scale, greatly increasing information about wind and rain dynamics. This chapter adapts the SWR technique to QuikSCAT UHR by addressing temporal and spatial resolution, rain backscatter modeling, and estimation performance limits.

Section 5.1 reviews wind estimation using the QuikSCAT scatterometer and Section 5.2 introduces the concept of SWR estimation and adapts it for UHR wind products. Section

5.3 evaluates simulated and theoretical performance limits for SWR estimation, after which Section 5.4 concludes.

## 5.1 QuikSCAT and TRMM Background

Radar backscatter measurements, termed  $\sigma^o$ , are used to estimate wind vectors via a maximum likelihood estimation technique whereby backscatter measurements are mapped to wind vectors through a geophysical model function (GMF) [12]. When  $\sigma^o$  is viewed as a random variable, the GMF gives an estimate of the backscatter,  $\hat{\sigma}^o$ , which is the expected value of  $\sigma^o$  given a wind speed  $S$  and relative wind direction  $\chi$ , i.e.,

$$\hat{\sigma}^o = E[\sigma^o|S, \chi] = \mathcal{M}(S, \chi), \quad (5.1)$$

where  $E$  denotes the expectation operator,  $p(\sigma^o|S, \chi)$  is the conditional probability of  $\sigma^o$ , and  $\mathcal{M}(S, \chi)$  is the GMF.

The model for the probability of a vector of  $\sigma^o$  measurements,  $\mathbf{z}$ , given a wind speed and direction, is given by

$$p(\mathbf{z}|S, \chi) = \prod_k \frac{1}{\sqrt{2\pi\varsigma_k}} \exp \left\{ -\frac{1}{2} \frac{(z_k - \hat{\sigma}^o)^2}{\varsigma_k^2} \right\}, \quad (5.2)$$

where the variance  $\varsigma_k$  is a function of the wind speed and direction. Note that this model assumes that each measurement is independent. This assumption is not strictly true [66], but is a useful approximation maintained here to reduce complexity. The variance term is calculated to be

$$\varsigma^2(S, \chi) = (K_{pc}^2 + K_{pm}^2 + K_{pc}^2 K_{pm}^2) \mathcal{M}(S, \chi)^2, \quad (5.3)$$

where  $K_{pm}$  is the normalized standard deviation of the geophysical model function representing the uncertainty in the model function, and  $K_{pc}$  represents communication noise and can be written

$$K_{pc} = \sqrt{\alpha + \frac{\beta}{\hat{\sigma}^o} + \frac{\gamma}{\hat{\sigma}^{o2}}}. \quad (5.4)$$

The coefficients  $\alpha$ ,  $\beta$ , and  $\gamma$  are scatterometer specific [44].

Dropping constant terms, the likelihood function of a wind vector given the measurements becomes

$$l(\mathbf{z}|S, \chi) = - \sum_k \log(\varsigma_k) + \frac{1}{2} \frac{(z_k - \hat{\sigma}^o)^2}{\varsigma_k^2}. \quad (5.5)$$

Due to the structure of the GMF the likelihood function typically has several local maxima each of which is a possible wind vector solution. Typically up to four of these maxima, termed ambiguities, are retained after processing [28]. Wind retrieval is the process of calculating the likelihood function and finding the local maxima. The process by which one ambiguity is selected for each wind vector cell (WVC) is termed ambiguity selection.

Simultaneous wind and rain retrieval is possible for the inner swath using QuikSCAT [61] but it requires independent datasets to properly calibrate the QuikSCAT rain model.

Simultaneous wind and rain retrieval for QuikSCAT was first studied and validated at conventional (25 km) resolution [61, 62]. However at UHR, several additional issues arise in SWR retrieval. Due to the signal processing implementation, QuikSCAT has essentially no range resolution. Because rain occurs up to an altitude of 6 km, the incidence angles used by QuikSCAT can cause up to 6 km of apparent horizontal spreading of the rain signal, which for UHR products is significantly larger than a resolution cell. The antenna spatial response and the resolution enhancement algorithm together result in additional horizontal spreading of the rain signal, causing rain contamination of measurements in WVCs near rain events. Further, at high resolution, intense rain cells have a stronger effect on the observed backscatter, since there is less averaging into the resolution cells than for the 25km product. Consequently, the conventional resolution rain model and associated assumptions may be inappropriate for the UHR case.

## 5.2 Simultaneous Wind and Rain Retrieval

Simultaneous wind and rain retrieval is accomplished using maximum likelihood estimation to estimate the wind vector and rain rate that produced the observed backscatter. SWR retrieval differs from the wind-only retrieval method in that the combined rain effect model is used instead of the wind-only model. The combined rain effect model is obtained by substituting the wind GMF,  $\mathcal{M}(S, \chi)$ , for  $\sigma_w$  in Eq. 3.2, where  $S$  is the wind speed and

$\chi$  is the relative wind direction. The combined wind and rain model can then be written

$$\mathcal{M}_R(S, \chi, R) = \mathcal{M}(S, \chi)\alpha_r(R) + \sigma_e(R), \quad (5.6)$$

where  $\alpha_r(R)$  and  $\sigma_e(R)$  are the quadratic rain model terms and  $R$  is the rain rate in dB km-mm/hr. Note that  $\sigma_e(R)$  can be the effective rain model or the lumped term phenomenological rain model. The log-likelihood equation can be written as

$$l(\mathbf{z}|S, \chi, R) = - \sum_k \ln(\varsigma_k) + \frac{1}{2} \frac{(z_k - \mathcal{M}_r(S, \chi, R))^2}{\varsigma_k^2}, \quad (5.7)$$

where  $\mathbf{z}$  is the vector of measured  $\sigma_o$  values,  $k$  is the measurement index, and  $\varsigma_k$  is the model variance. The conventional wind-only variance model can be modified to account for the additional variability due to rain by using the approximation from [61]

$$\varsigma_k^2 \approx (\mathcal{M}_k \alpha_{rk} K_{pm} + \sigma_{ek} K_{pe})^2 (1 + \alpha) + \alpha \mathcal{M}_{rk}^2 + \beta \mathcal{M}_{rk} + \gamma, \quad (5.8)$$

where  $K_{pe}$  is the normalized standard deviation of the rain model. This approximation to the variance is independent of the rain model choice as  $K_{pe}$  can be estimated for both the effective rain model and the phenomenological rain model. For the phenomenological rain model, the effective  $K_{pe}$  is estimated by lumping the effective variance of the  $\sigma_{sp}\alpha_r + \sigma_{rp}$  into the  $K_{pe}$  term.

### 5.2.1 Estimating $K_{pe}$ for Retrieval

Due to variability in the NCEP wind data and temporal variability between QuikSCAT and TRMM PR observations, estimating  $K_{pe}$  from the rain backscatter is problematic and tends to overestimate the true value of  $K_{pe}$  for both rain models. As an example, consider the lowest rain rates. For these rain rates, the rain signal is quite small and the NCEP variability masks any variability due to rain. Similarly, for low to moderate rain rates this additional noise dominates the rain model uncertainty. As the rain signal increases in strength, the variability from the NCEP winds becomes less pronounced and the apparent rain backscatter variability drops.

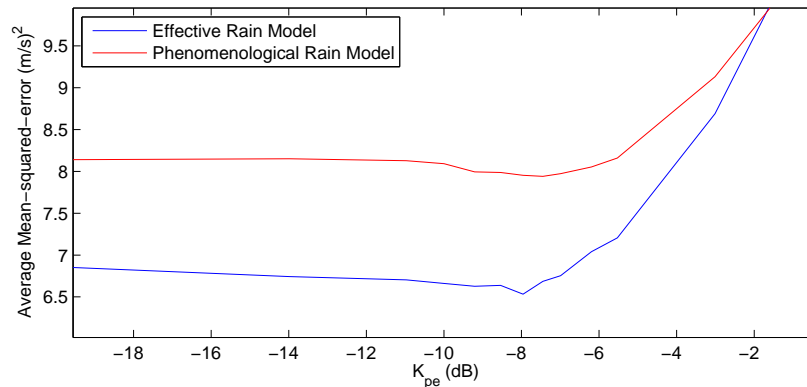


**Figure 5.1:** Average squared-error between SWR wind estimates and NCEP model winds as a function of the retrieval  $K_{pe}$  value. Note that the best value for  $K_{pe}$  is different for the effective and phenomenological rain models.

Attributing all of the additional variability to the rain model is particularly problematic when attempting to perform SWR retrieval. In many cases, the variability attributed to the rain effects is so large that it is not possible to reasonably estimate rain rate. This consequently increases the variability of the rain-contaminated wind estimates. One way to overcome this limitation is to use a fixed value for the rain model  $K_{pe}$  as in [61].

A simple way to estimate  $K_{pe}$  is to perform SWR retrieval on simulated backscatter data using candidate values for  $K_{pe}$ . The ideal  $K_{pe}$  value is that which minimizes the squared-error between the wind estimates and the NCEP model winds. Unfortunately, the effects of the NCEP model wind variability are unavoidable when calculating the squared-error of the wind estimates. To reduce the effects of NCEP variability we evaluate the candidate  $K_{pe}$  values on 75 different QuikSCAT and TRMM co-located observation sets. The average squared error between NCEP and SWR wind estimates is calculated for all observations where TRMM PR observed a non-zero rain rate. The average for all of the collocations is shown as a function of  $K_{pe}$  in Fig. 5.1.

As indicated in Fig. 5.1 the values of  $K_{pe}$  minimize the wind squared error are 0.16 and 0.18 for the effective and phenomenological rain models respectively. While the minimum in Fig. 5.1 is more pronounced for the effective rain model, the wind variability using the phenomenological rain model is not particularly sensitive to the value of  $K_{pe}$ . Thus it is

reasonable to let  $K_{pe}$  be 0.16 for both the effective and phenomenological rain models. It is interesting to note that this is the  $K_{pe}$  value used for conventional resolution wind and rain retrieval in [61]. Thus the rain model variability is not highly dependent on the retrieval resolution.

### 5.3 SWR Accuracy

This section evaluates the accuracy of SWR estimation using both rain models first using a theoretical bound and then evaluates the performance on real data.

#### 5.3.1 Cramer-Rao Bound

The Cramer-Rao lower bound (CRB) provides a lower bound on the variance of an unbiased estimator. Wind and rain estimates are slightly biased due to non-linearities in the model function as well as the noise level of the observations. A detailed discussion of the CRB for SWR estimation is found in Appendix B which is summarized here. The CRB for biased wind and rain estimates can be written

$$E[(\hat{\mathbf{w}} - \mathbf{w})(\hat{\mathbf{w}} - \mathbf{w})^T] \geq \frac{\partial E[\hat{\mathbf{w}}]}{\partial \mathbf{w}} J^{-1}(\mathbf{w}) \left[ \frac{\partial E[\hat{\mathbf{w}}]}{\partial \mathbf{w}} \right]^T, \quad (5.9)$$

where  $\hat{\mathbf{w}}$  is the wind and rain estimate and  $\mathbf{w}$  is the true wind and rain vector.  $J(\mathbf{w})$  is the Fisher Information matrix with components  $J_{ij}$  which can be expressed as

$$J_{ij} = \sum_{k=1}^4 \frac{\partial \mathcal{M}_{rk}}{\partial w_i} \frac{1}{\zeta_k^2} \frac{\partial \mathcal{M}_{rk}}{\partial w_j} + \frac{\partial \zeta_k^2}{\partial w_i} \frac{1}{2\zeta_k^4} \frac{\partial \zeta_k^2}{\partial w_j}, \quad (5.10)$$

where  $k$  indexes each observation,  $\mathcal{M}_{rk}$  is the wind and rain model for the wind and rain vector  $\mathbf{w}$ , and  $\zeta_k^2$  is the observation variance [74].

It is relatively straightforward to calculate the Fisher Information matrix for a given wind and rain vector. However, since there is no analytical form for the wind and rain estimate  $\hat{\mathbf{w}}$ , there is no analytical form for the partial derivatives used to calculate the CRB for a biased estimator. One method to approximate the partial derivative  $\partial E[\hat{\mathbf{w}}]/\partial \mathbf{w}$  was proposed in [74]; however, the noise level in high-resolution data makes it numerically

unstable for some wind vectors. Instead, we adopt an alternative approach by computing  $E[\hat{\mathbf{w}}]$  directly using Monte-Carlo simulations. This approach is a more reliable alternative, provided the simulations are representative of the true wind and rain estimation performance.

### 5.3.2 Wind and Rain Backscatter Simulation

Backscatter due to wind can be simulated using the scatterometer noise model and the geophysical model function. Rain backscatter is slightly more complicated since both candidate rain models are approximations to the observed rain backscatter. There are two methods which could be adopted to simulated rain backscatter. First, we could simply use the rain backscatter model as both the forward and backward rain model. For example, the simulated backscatter values could be given directly by the effective rain model, then after noisy simulation the effective backscatter model could be used in the wind and rain retrieval process.

The second method to simulate rain backscatter, which we adopt here, is to generate the rain backscatter directly from the non-parametric kernel-smoothed fit of the rain backscatter observations (see Fig. 3.5). Wind and rain retrieval is then performed on the simulated backscatter data using either the effective or phenomenological rain models. An advantage of this approach is that it allows the simulated backscatter to closely resemble observed backscatter data. Since both rain models are an approximation to the observed backscatter performance, modeling the rain backscatter from the observed performance allows the retrieval results to realistically account for deviations between the observed rain backscatter and the model. Thus the retrieval performance using each model can closely mimic the estimation performance when used on observed backscatter data.

Before discussing the simulation results it is important to understand the direction squared error. Because wind direction is a circular variable the mean squared error between the true wind direction and the estimated wind direction is calculated as

$$MSE = n^{-1} \sum_{i=1}^n (\Delta_i)^2, \quad (5.11)$$

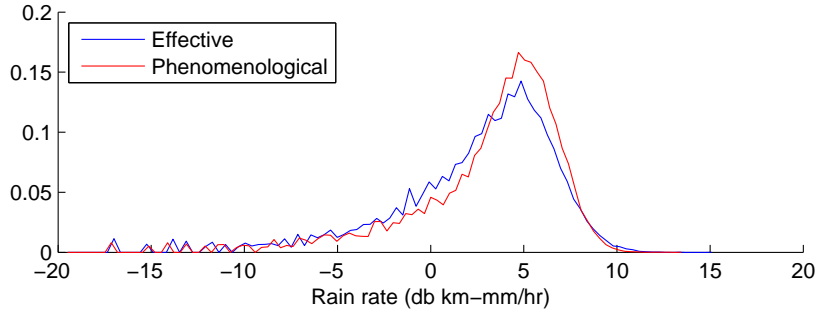


**Figure 5.2:** Histograms of the rain estimates produced using both the effective and phenomenological rain models for a fixed speed of 10 m/s and rain rate of 3 km-mm/hr.

where  $i$  indexes the estimates and  $\Delta_i$  is defined such that  $|\Delta_i|$  is the lesser of  $|\hat{d}_i - d_t|$  and  $360^\circ - |\hat{d}_i - d_t|$ .  $\hat{d}_i$  is the estimated wind direction and  $d_t$  is the true wind direction. Note that the maximum value of  $\Delta d_i$  is  $180^\circ$  and the minimum is  $-180^\circ$ .

Generally the root-mean-squared error for the wind vector estimates is very similar for either rain model. The largest differences between the two rain models are best seen in the distributions of estimated rain rates. Figure 5.2 shows the distribution of estimated rain rates for a true wind speed of 10 m/s and a rain rate of 4.7 dB km-mm/hr. Interestingly, the phenomenological rain model has fewer low ( $< 3$ dB km-mm/hr) rain estimates and few higher ( $> 7$  dB km-mm/hr) which indicates a greater concentration of rain estimates; however, the bias in the phenomenological rain estimates is slightly larger. Before comparing real data we apply the Monte Carlo results for the estimator bias to form the biased CRB.

### 5.3.3 Theoretic Performance Limits

Figure 5.3 shows the CRB for a fixed wind speed and several rain rates as a function of true wind direction. It is immediately apparent that there are several wind directions which are problematic. For these wind directions the standard deviation of the direction estimates are unrealistically high. This is one limitation of the QuikSCAT observation geometry. Winds that are parallel to the antenna azimuth angle are particularly noisy, regardless of the swath location. Near these problematic wind directions the error can be substantial enough to effectively mask all information about wind direction. This causes the Fisher Information

for wind direction to approach zero, thus causing the Fisher Information matrix to approach singularity. For these wind directions, the near-singularity of the Fisher Information matrix causes the bounds for wind speed and rain rate to be greatly overestimated.

Interestingly, although the CRB does not give a physically meaningful result for these directions, in reality there is a more realistic upper bound on the direction variance. Because wind direction is only valid from 0 to  $360^\circ$ , there is a wrapping effect. This implies that a worst case direction estimate distribution is a uniform distribution from 0 to  $360^\circ$ . This effectively upper bounds the wind direction standard deviation at  $103.9^\circ$ , the standard deviation of a uniform distribution from 0 to 360. It may be possible to further reduce this upper bound by evaluating the effects of multiple ambiguities, but we do not pursue this concept here.

In terms of the Fisher Information, a standard deviation that exceeds  $103.9^\circ$  indicates that there is little direction information. When this is so, the Fisher Information is nearly singular, making the speed and rain bounds inaccurate as well. We can obtain an alternative bound on wind speed and rain rate by formulating a separate wind speed and rain rate estimator. The wind speed and rain rate estimator (SRE) is particularly useful for cases where the QuikSCAT observation geometry is poorly suited to wind direction retrieval. In these cases azimuthal dependence of the backscatter is ignored and wind speed and rain estimates can be made from the backscatter magnitude alone.

Because the SRE does not estimate wind direction it remains valid as a lower bound, even when there is little or no direction information. Essentially, the CRB for SRE can be used whenever the direction variability passes realistic limits ( $103.9^\circ$ ). Although in reality the retrieval process always includes a direction estimate, the retrieval process can be approximated by the SRE because the wind direction can be treated as if it is randomly chosen by the retrieval algorithm when there is no direction information.

The CRB for the SRE is calculated in the same way as the SWR estimator. The principle difference is the model function. To approximate a wind speed and rain rate geophysical model we can average the conventional wind vector GMF over wind direction. This gives a model for the wind speed which can be combined with the rain model using

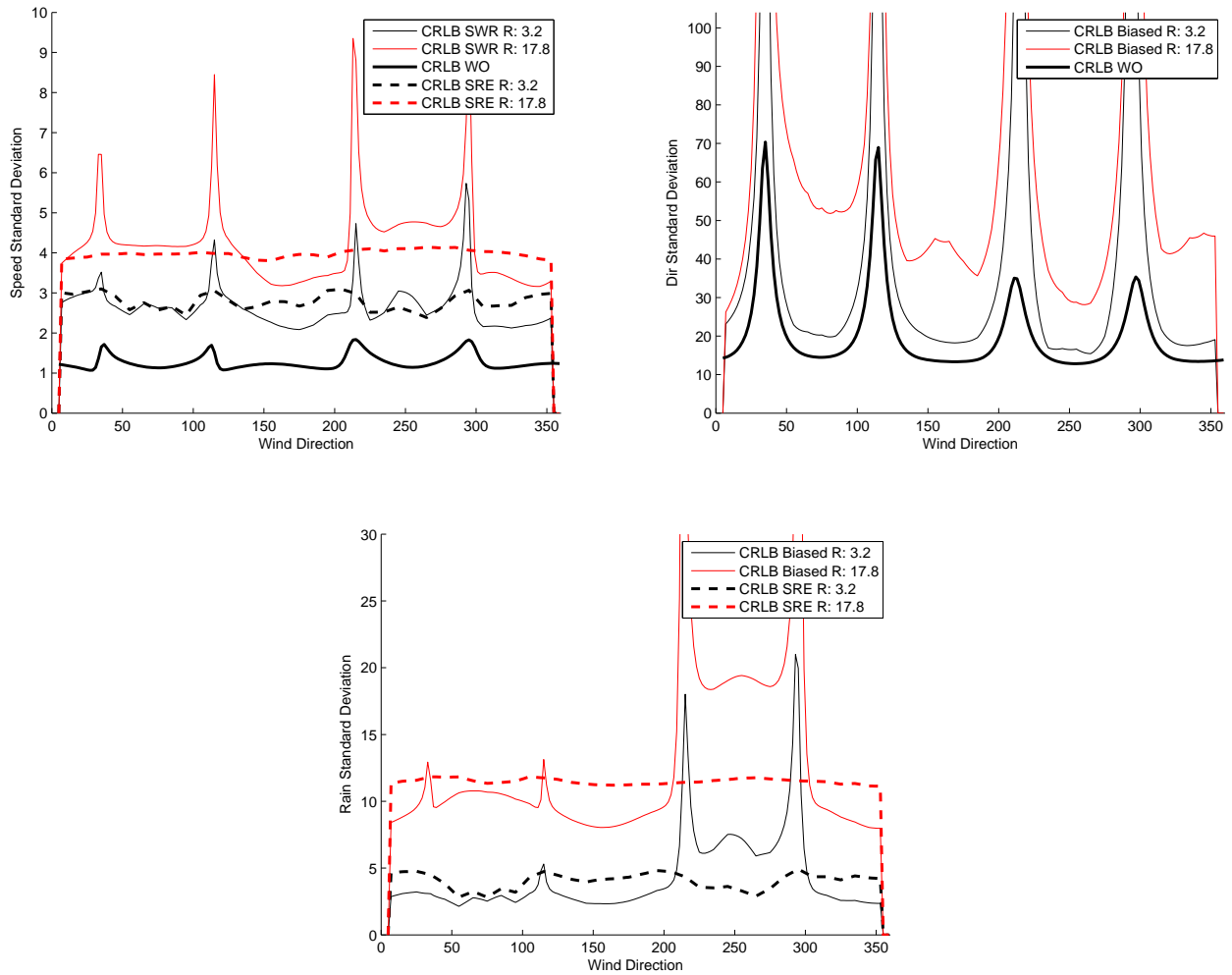


**Figure 5.3:** Solid lines: SWR CRB. Dashed lines: SRE CRB. A reasonable way to interpret the difference between the SWR CRB and the SRE CRB is to assume the overall CRB is the smaller of the two bounds. In each case these bounds correspond to a fixed wind speed of 10 m/s.

Eq. 5.6 as before. The wind speed geophysical model function is shown in Fig. 5.4 for both H and V polarizations.

Although the CRB indicates that it is not possible to reliably estimate the wind direction at ultra-high resolution for some particular true wind directions, all is not lost. Rather, for many of the most common wind and rain vectors, SWR estimation has similar performance to conventional UHR wind estimation. Further, accurate wind direction estimates can still be formed at the conventional QuikSCAT resolution [61, 74]. Additionally, it may

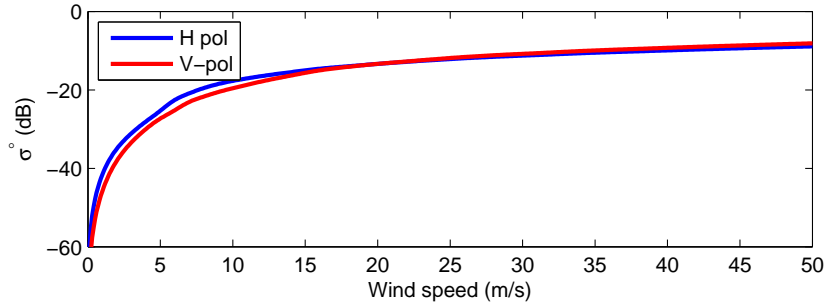


**Figure 5.4:** Wind speed geophysical model function for H and V polarizations.

still be possible to improve the direction estimates using a modified version of the directional interval retrieval algorithm proposed in [75], although this is not investigated here.

### 5.3.4 SWR Performance

It has been demonstrated that SWR retrieval at conventional (25 km) resolution can produce unbiased estimates of the measured rain rate, although there is significant variance in the estimates [61, 62]. SWR estimation using UHR data has several issues that require us to make some additional considerations. First is the issue of noise. At UHR, the noise level of the QuikSCAT observations is substantially greater than the conventional resolution observations. The second issue is resolution. Although QuikSCAT UHR estimates are reported at 2.5 km, their effective resolution is lower.

To make the dependence on temporal resolution and the QuikSCAT sampling pattern clear, we attempt to separate the effects of each as we compare the estimation results. To isolate the effects of observation noise we can define a ‘true’ rain field which accounts for the resolution of the QuikSCAT UHR observations. This ‘true’ rain field is the rain field that QuikSCAT would observe if it used identical sampling geometry but made noiseless measurements. Thus the comparison of the ‘true’ rain field and the QuikSCAT rain estimates gives an indication of the ability of QuikSCAT to detect and estimate the rain from high-noise observations.

Just as in the backscatter modeling, there are two types of resolution in wind and rain estimation, temporal and spatial, the effects of which we must include in defining the

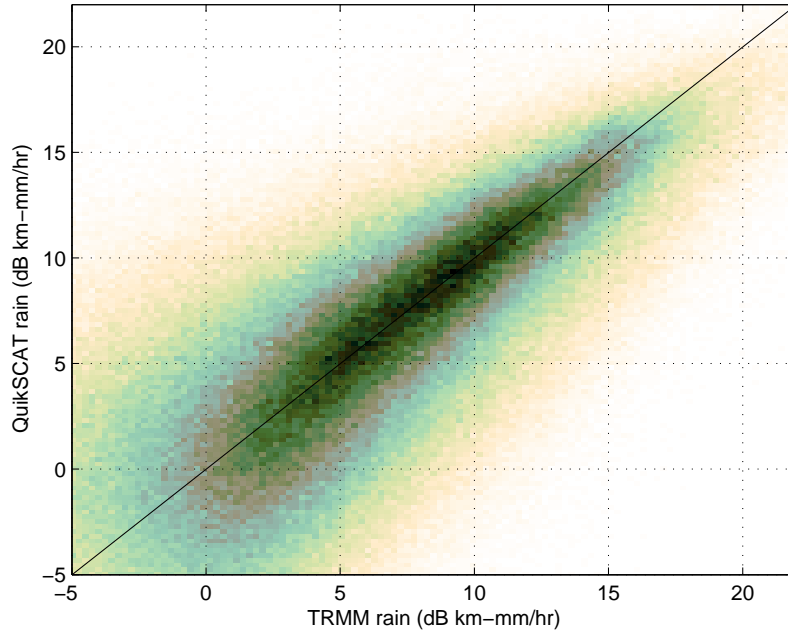


**Figure 5.5:** Scatter density of QuikSCAT ‘true’ observed rains and TRMM PR-measured rains. The QuikSCAT sampling pattern causes some variability about the TRMM PR measurements but does not cause an overall bias of the rain measurements.

‘true’ rain field. To account for spatial resolution and sampling we use the rain field defined by Eq. 3.4 for each observation flavor. To account for QuikSCAT temporal sampling effects we use the constant shift approximation introduced in Section 3.2.2 calculated using the cross-correlation. The shifts are then applied to the rain field for each flavor. There are thus four separate rain fields which are sampled and shifted copies of the TRMM PR observed rain field. These four rain fields thus represent the rain field observed by each QuikSCAT observation flavor.

To assimilate these four different rain fields into a single ‘true’ rain field requires one final assumption. If we assume that each QuikSCAT flavor contributes equally to the overall rain estimate, then a simple way to form an overall ‘true’ rain field is to average the four separate rain fields. While there may be an optimal weighting of the four rain fields that could reflect the sensitivity of a particular polarization to rain, this approximation is simple and yields a good reference rain field without additional complications. We define this ‘true’

rain field to be

$$R_{QSCAT} = (R_{VF} + R_{HF} + R_{HA} + R_{VA})/4, \quad (5.12)$$

where  $R_{VF}$ ,  $R_{HF}$ ,  $R_{HA}$ , and  $R_{VA}$  are time-shifted versions of the rain fields calculated using Eq. 3.4, and  $R_{QSCAT}$  is the ‘true’ rain field for QuikSCAT that accounts for both temporal and spatial sampling effects. Figure 5.5 shows the scatter density plot of QuikSCAT ‘true’ winds and TRMM PR-measured winds. As might be hoped for, the QuikSCAT sampling process does not cause any overall bias for most rain measurements.

With the combined effects of spatial and temporal sampling accounted for, the remainder of the variability in the rain estimates can be attributed primarily to observation noise. Figure 5.6 shows the scatter density plots for QuikSCAT rain estimates and TRMM PR rain rates at UHR for both rain models. The rain estimates are biased slightly low for all rain rates using both models, but this bias can be minimized by bias-correcting the rain estimates. The most prominent feature of Fig. 5.6, unfortunately, is the variance of the QuikSCAT rain estimates, which can exceed 5 dB km-mm/hr. Such a high variance level may be intolerable in many applications; however, although we do not consider it here, resolution reduction can decrease estimate variability by reducing observation noise [76].

Some effects that are not apparent in the scatter density are noise effects such as spurious rain estimates and missing wind estimates. Both of these effects are an inherent part of SWR estimation and occur as a consequence of the smoothness of the likelihood function. At times the maximum of the likelihood function is so flat that the maximum is overlooked by the search algorithm. Similarly there are times when there is no local maximum in the wind and rain space, consequently no SWR estimates can be made. Typically, this occurs when the wind or the rain signal is dominated and obscured by the other.

Although the estimate variability is high, one important observation about QuikSCAT rain estimates that is not apparent in Fig. 5.6 is the ability of QuikSCAT to identify the general structure of rain events. To demonstrate this ability, Fig. 5.7 shows the TRMM PR-measured rain rates and QuikSCAT SWR rain estimates for a case study. Figure 5.7 indicates that although there are spurious rain estimates that are missing, the QuikSCAT rain estimates correctly identify the rain bands observed by TRMM PR. This ability is

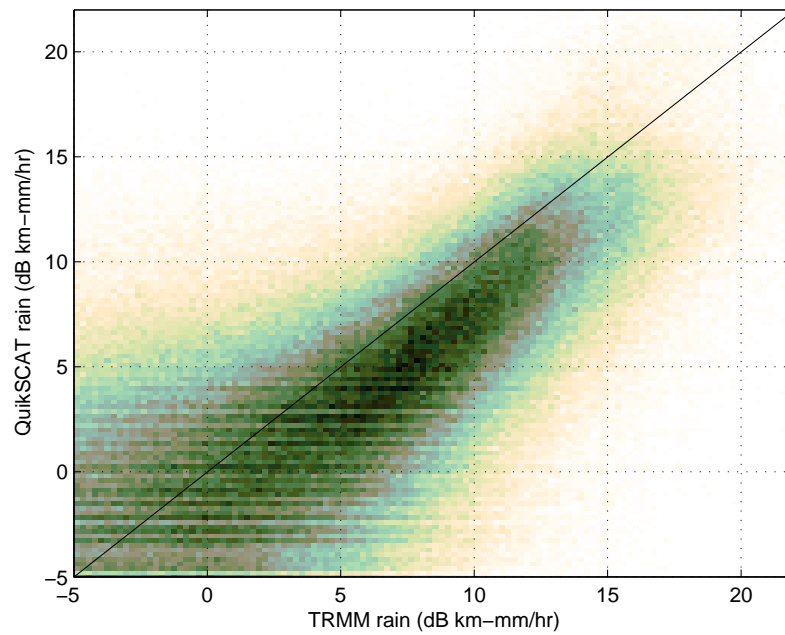
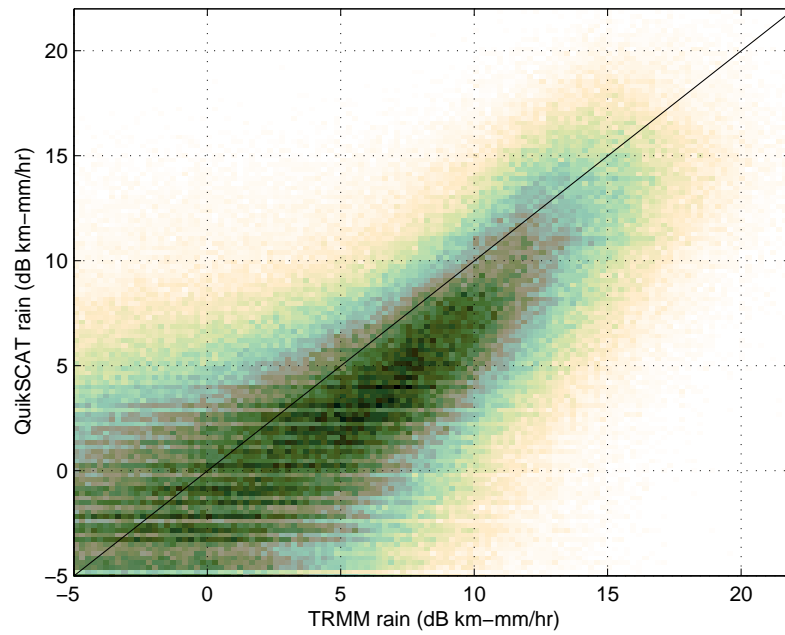


**Figure 5.6:** Scatter density plots of QuikSCAT ‘true’ rain rates and QuikSCAT retrieved rain rates. Top: effective rain model. Bottom: phenomenological rain model. The equality line is shown for comparison. The rain estimates are biased low for all rain rates using both models. Overall the rain estimation performance using either model is very similar and does not give strong evidence that either model is superior.

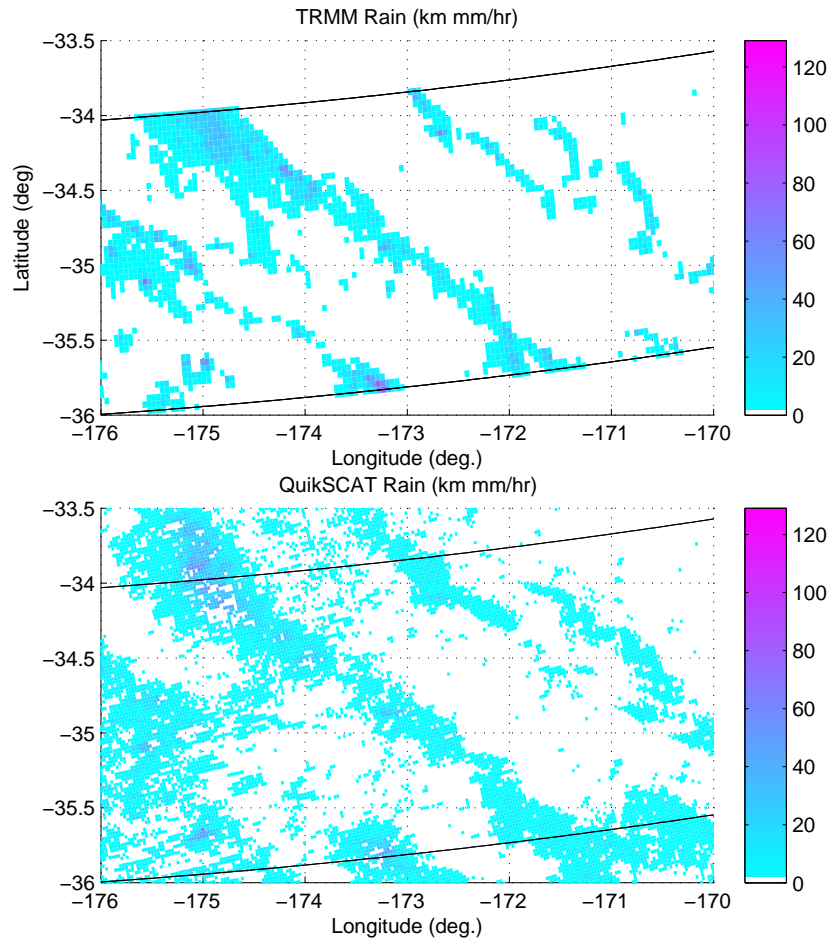


**Figure 5.7:** TRMM PR-measured rain rate (left) and QuikSCAT-estimated rain rate (right) for one overlapping region. TRMM swath edges are indicated by the black lines. Although QuikSCAT fails to detect the lowest rain rates and is noisy, the spatial correlation of the two datasets is quite apparent. The rain rate color scale for this image ranges from 0 to 132 km-mm/hr.

useful as a type of rain flag, but can be of greater utility as an indicator of areas where a rain-only estimator may be of interest to further extract rain information thus overcoming the spurious characteristics of the SWR estimates. A related UHR rain-flagging technique which is phenomenologically based but has reduced computation requirements is introduced in Appendix C.

## 5.4 Conclusions

This chapter has demonstrated that QuikSCAT is capable of measuring the wind and rain simultaneously at UHR. UHR wind and rain estimates offer insights into wind and rain events that are not achievable using any other single sensor. These insights aid understanding of important phenomena such as hurricanes and other large-scale convective storms. This ability is particularly useful in regions outside the tropics which are not observed by TRMM PR or similar instruments. Despite high noise levels, the QuikSCAT UHR wind and rain estimates are valuable tools in understanding large-scale phenomena which have small-scale wind and rain features.

## Chapter 6

### M-ary Bayes Estimator Selection for QuikSCAT Simultaneous Wind and Rain Retrieval

Chapter 5 demonstrated that wind and rain estimation over the ocean is possible at UHR using data provided by the QuikSCAT scatterometer. Similarly, wind and rain retrieval from QuikSCAT measurements has been demonstrated for conventional resolution products [5, 61, 77]. Simultaneous wind and rain (SWR) estimation is not a complete solution to the rain contamination problem as it has limited performance under certain rain conditions, for which a wind-only (WO) or rain-only (RO) estimate may be superior. There are thus three estimators SWR, WO, and RO, none of which have optimal wind and rain estimation performance for all conditions.

This chapter takes an additional step towards rain contamination mitigation by introducing the concept of Bayes estimator selection which can be used for QuikSCAT wind and rain estimation to select a single optimal estimate from the SWR, WO, and RO estimates. To avoid the additional complications associated with UHR products, Bayes estimator selection is applied only to conventional resolution products in this chapter. The Bayes estimator selection concept is adapted and extended to UHR wind products in Chapter 7. Bayes estimator selection is used to choose between the three different estimation techniques which may be employed: wind-only, simultaneous-wind-rain, and rain-only estimation. The performance of each estimator is dependent on the underlying wind-rain conditions. As such, each estimation technique is best under certain backscatter conditions but no single technique is suitable for all conditions. Using the wrong estimator can degrade the estimate accuracy. By adaptively selecting the estimates most appropriate to the true conditions, overall performance can surpass that of any individual estimator.

In this chapter we first introduce Bayes estimator selection, a technique whereby a single ‘best’ estimator can be selected for each wind-rain condition. The technique is then applied to QuikSCAT wind and rain estimation. Section 6.1 discusses and motivates the multiple estimator problem, Section 6.2 gives relevant background information about the QuikSCAT scatterometer, Section 6.3 introduces Bayes estimator selection in a general sense, Section 6.4 discusses the application of Bayes estimator selection to QuikSCAT wind and rain estimation, Section 6.5 gives an overview of Bayes estimator selection results, and Section 6.6 concludes.

## 6.1 Problem Formulation

The QuikSCAT scatterometer was designed for the express purpose of wind estimation over the ocean. The traditional wind estimation process which retrieves only the near-surface wind is what we term WO estimation in the following discussion [78].

SWR estimation has been proposed as an alternative solution to rain-flagging of rain-contaminated winds [61]. SWR estimation improves WO estimation by adjusting the wind-only model to account for both wind and rain effects on the radar backscatter [63, 69]. Replacing the wind model with the joint wind-rain model and estimating both the wind and the rain is what we term SWR estimation [61, 63]. However, for non-raining cases SWR estimation can degrade performance compared to WO estimation. This is due in large part to the fact that noise in the backscatter measurements can sometimes cause non-raining observations to resemble a raining case, resulting in cases where SWR estimation has a non-zero rain estimate yet no rain is occurring. To minimize noise sensitivity, SWR estimation in this chapter is constrained to ignore solutions with zero rain rates and zero wind-speeds. This makes SWR estimation distinct from WO estimation and RO estimation since they cannot retrieve the same wind and rain estimates.

For rain events with high rain rates and rain-dominated backscatter [59] the wind and rain estimates for SWR estimation may be degraded. Essentially, for certain wind speed and rain rate combinations the wind-rain model breaks down due to high rain-induced attenuation and the consequent loss of wind signal, causing the SWR estimates to be inaccurate.

For these rare high rain cases, wind cannot be estimated, though RO estimation can still provide accurate results [77].

In RO estimation [77], the wind model is discarded entirely and only the rain model is used; hence only a rain estimate is produced. RO estimation makes the assumption that wind has essentially no effect on the radar backscatter, which can occur under high rain conditions. For these cases, the rain accuracy is much improved by this assumption versus using SWR estimation.

In summary, there are three different estimation techniques or models which are appropriate under different conditions. Each performs well under appropriate conditions; however, if the estimator is used outside of the intended conditions the estimator performance is degraded. There is therefore no single estimator which is suitable for all conditions. Instead of choosing one estimator and using it under all conditions we propose a Bayesian estimator selection method whereby the three estimators are compared and a single estimate is chosen from the various estimates from the set of estimators.

## 6.2 Background

For a wind vector  $\mathbf{w} = [s, d]$  with wind speed  $s$  and direction  $d$ , rain rate  $r$  and a wind-rain vector  $\vartheta = [\mathbf{w}, r]$  the backscatter  $\sigma^o$  can be modeled phenomenologically as [61, 69, 79]

$$\sigma^o = \alpha_r \sigma_w + \sigma_e, \tag{6.1}$$

where  $\sigma_w$  is the backscatter from the ocean surface due to wind,  $\alpha_r(r)$  is the attenuation factor of the ocean wind backscatter due to atmospheric rain, and  $\sigma_e(r)$  is the effective rain backscatter from both the rain volume scattering and attenuated surface scattering due to additional splashes and waves. For wind and rain retrieval the phenomenological model is calculated for each measurement using

$$\mathcal{M}_r(\vartheta, \chi, \psi, p) = \mathcal{M}(\mathbf{w}, \chi, \psi, p) \alpha_r(r, p) + \sigma_e(r, p), \tag{6.2}$$

where  $\mathcal{M}_r(\vartheta, \chi, \psi, p)$  is the combined wind and rain model. Here  $\mathcal{M}(\mathbf{w}, \chi, p)$  is the wind geophysical model function (GMF) which gives the expected wind backscatter for a wind

vector  $\mathbf{w}$  given the antenna azimuth angle  $\chi$ , incidence angle  $\psi$  and polarization  $p$ . The rain model terms  $\alpha_r(r, p)$  and  $\sigma_e(r, p)$  correspond to the phenomenological model of Eq. 6.1 with subscripts to indicate they are functions of rain rate  $r$  and polarization  $p$ . The rain attenuation and backscatter model parameters are specified in [61] and are assumed to be independent of wind velocity and observation angle. Because the terms  $\chi$ ,  $\psi$ , and  $p$  are determined by the measurement geometry, we simplify notation in the following by dropping them and leaving only the wind and rain dependence.

Wind and rain estimation is performed using the backscatter model and the QuikSCAT backscatter measurement noise model. The scatterometer measurement model assumes a Gaussian noise distribution with mean  $\mathcal{M}_r(\vartheta)$  and can be written

$$f(\sigma_i^o | \vartheta) = \frac{1}{\sqrt{2\pi\zeta}} \exp\left(-\frac{1}{2\zeta^2}(\sigma_i^o - \mathcal{M}_r(\vartheta))^2\right), \quad (6.3)$$

where  $\sigma_i^o$  is the backscatter observation for the  $i$ th measurement,  $\vartheta$  is the true wind-rain vector,  $\mathcal{M}_r(\vartheta)$  is the model backscatter as a function of the true wind-rain vector and  $\zeta^2$  is the measurement variance. The measurement variance can be written [61]

$$\zeta^2 = (1 + K_{pc}^2) [\alpha_r(r)^2 \mathcal{M}(\mathbf{w})^2 K_{pm}^2 + \sigma_e(r)^2 K_{pe}^2] + \mathcal{M}_r(\vartheta)^2 K_{pc}^2, \quad (6.4)$$

where  $K_{pc}$  is the normalized standard deviation of the communication noise,  $K_{pm}$  is the normalized standard deviation of the wind backscatter model and  $K_{pe}$  is the normalized standard deviation of the effective rain backscatter model. The communications noise term for QuikSCAT is modeled as

$$K_{pc} = \sqrt{\alpha + \frac{\beta}{\mathcal{M}_r(\vartheta)} + \frac{\gamma}{\mathcal{M}_r(\vartheta)^2}}, \quad (6.5)$$

where the parameters  $\alpha$ ,  $\beta$  and  $\gamma$  are geometry and resolution dependent [44].

Maximum likelihood estimates for wind and rain can be formed using the log-likelihood function of the measurement model [78]. The maximum likelihood estimate is the wind-rain

**Table 6.1:** Wind and rain estimator summary

Estimator	$\mathcal{M}_r(\vartheta)$	$\zeta^2$	$\hat{\vartheta}$
WO	$\mathcal{M}(\mathbf{w})$	$(1 + K_{pc}^2) [\mathcal{M}(\mathbf{w})^2 K_{pm}^2] + \mathcal{M}(\mathbf{w})^2 K_{pc}^2$	$\hat{\mathbf{w}}$
SWR	$\mathcal{M}(\mathbf{w})\alpha_r(r, p) + \sigma_e(r, p)$	$(1 + K_{pc}^2) [\alpha_r(r)^2 \mathcal{M}(\mathbf{w})^2 K_{pm}^2 + \sigma_e(r)^2 K_{pe}^2] + \mathcal{M}_r(\vartheta)^2 K_{pc}^2$	$\hat{\mathbf{w}}, \hat{r}$
RO	$\sigma_e(r)$	$(1 + K_{pc}^2) [\sigma_e(r)^2 K_{pe}^2] + \sigma_e(r, p)^2 K_{pc}^2$	$\hat{r}$

vector which maximizes the likelihood function and can be written

$$\hat{\vartheta} = \arg \max_{\vartheta} \sum_i \left( -\log(\sqrt{2\pi\zeta}) - \frac{1}{2\zeta^2} (\sigma_i^o - \mathcal{M}_r(\vartheta))^2 \right), \quad (6.6)$$

where the summation is over the vector of backscatter observations. The WO, RO and SWR estimators are each calculated similarly and differ only by the models used for the mean and variance in Eq. 6.3, which are specified for each estimator in Table 6.1. For WO estimation  $\mathcal{M}_r(\vartheta) = \mathcal{M}(\mathbf{w})$ , for RO  $\mathcal{M}_r(\vartheta) = \sigma_e(r)$  and for SWR  $\mathcal{M}_r(\vartheta)$  is used as defined in Eq. 6.2. The variance model for each estimator also changes accordingly.

The simple phenomenological model in Eq. 6.1 can be used to motivate each estimation technique. When rain is not present, i.e.  $\alpha_r = 1$  and  $\sigma_e = 0$ ,  $\sigma^o$  is only a function of  $\sigma_w$  and wind-only estimation produces the best estimate. Similarly, when  $\sigma_w$  is dominated by  $\sigma_e$  and  $\alpha_r$ , i.e.  $\alpha_r \ll 1$ , rain-only estimation is appropriate. When the wind and rain signals are of similar magnitude, estimating them jointly using SWR estimation produces the best performance. In essence, depending on the true conditions, one of the estimators produces a better estimate of wind, wind and rain, or rain.

A subtle difference in the several estimator models is that WO estimation assumes that backscatter is unaffected by rain. This is a stronger statement than assuming simply that the rain is zero. Rather, it is the assumption that the backscatter is not affected by rain. Similarly, RO estimation operates on the assumption that wind does not affect the backscatter. The WO and RO estimation models are approximations to the true wind and rain model and are only appropriate under certain conditions.

### 6.2.1 Estimator Bounds

Before discussing estimator selection it is important to quantify the limitations of each of the estimators. One method to quantify estimator performance is to evaluate the theoretic limitations of each estimator using the Cramer-Rao Bound (CRB). As discussed previously, the introduction of contamination to the signal causes a bias in the estimates. Thus we must adopt the biased form for the CRB. A detailed discussion of the CRB for each type of estimator is found in Appendix B. The CRB for WO, SWR and RO retrieval [5, 74] can be written as

$$E[(\hat{\vartheta} - \vartheta)(\hat{\vartheta} - \vartheta)^T] \geq \frac{\partial E[\hat{\vartheta}]}{\partial \vartheta} J^{-1}(\vartheta) \left[ \frac{\partial E[\hat{\vartheta}]}{\partial \vartheta} \right]^T, \quad (6.7)$$

where the elements  $J_{ij}$  of the Fisher information matrix  $J$  are

$$J_{ij}(\vartheta) = \sum_{k=1}^N \frac{\partial \mathcal{M}_{rk}}{\partial w_i} \frac{1}{\varsigma_k^2} \frac{\partial \mathcal{M}_{rk}}{\partial w_j} + \frac{\partial \varsigma_k^2}{\partial w_i} \frac{1}{2\varsigma_k^4} \frac{\partial \varsigma_k^2}{\partial w_j}. \quad (6.8)$$

Here, the Fisher-Information is represented for wind and rain estimation. The Fisher-Information for WO estimation is a special case of the wind and rain information where the rain rate is 0. Note that for wind-only retrieval  $J$  is a 2x2 matrix since  $\hat{\vartheta} = \hat{\mathbf{w}}$ , whereas for simultaneous wind and rain retrieval  $J$  is a 3x3 matrix since  $\hat{\vartheta} = (\hat{\mathbf{w}}, \hat{r})$ .

The biased CRB can be calculated similarly for rain-contaminated wind-only retrieval by adjusting the Fisher-Information matrix for the rain contamination

$$J_{ij}(\vartheta) = \sum_{k=1}^N \frac{\partial \mathcal{M}_k}{\partial w_i} \frac{\alpha_r^2}{\varsigma_k^2} \frac{\partial \mathcal{M}_k}{\partial w_j} + \frac{\partial \varsigma_k^2}{\partial w_i} \frac{1}{2\varsigma_k^4} \frac{\partial \varsigma_k^2}{\partial w_j}. \quad (6.9)$$

Like the wind-only Fisher-Information, the rain-contaminated Fisher-Information is a 2x2 matrix since  $\hat{\vartheta} = \hat{\mathbf{w}}$ . However, for rain contamination, the Fisher-Information is also dependent on  $r$  so we can write  $J_{ij}(\mathbf{w}, r)$ .

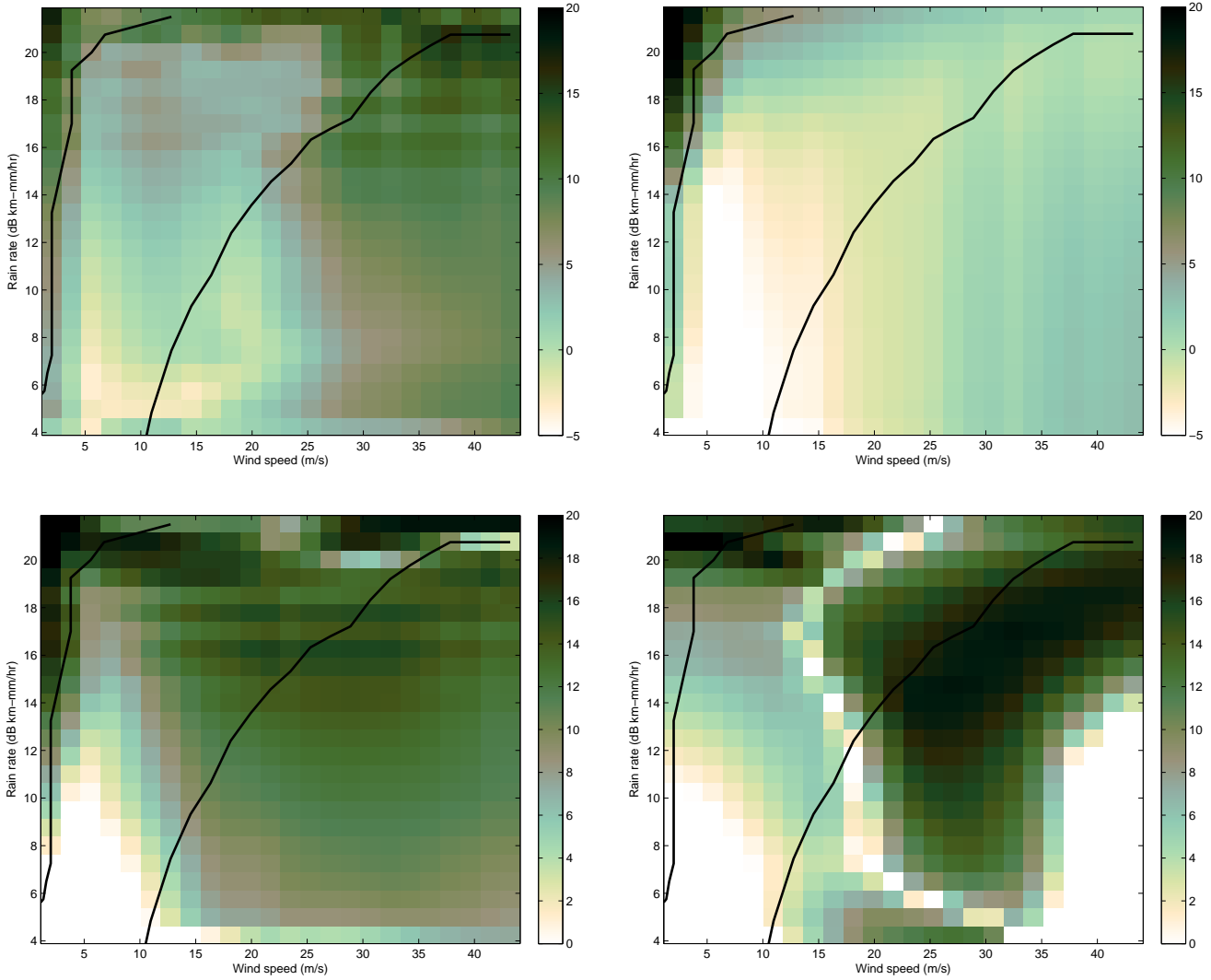


**Figure 6.1:** Cramer-Rao bounds in dB on wind speed and rain rate for the various estimators. Upper-left: CRB for SWR wind speed. Upper-right: CRB for WO wind speed. Lower-left: CRB for SWR rain rate. Lower-right: CRB for RO rain rate. Note that each estimator has a region in wind speed and rain rate where the CRB is lower than the others. The bounds shown are for a single wind direction ( $53^\circ$ ) and cross-track location (cell 13) which have performance which is representative of all other wind directions. Estimator characteristics have some slight changes as a function of cross-track location due to the changing observation geometry but are generally similar. For reference the smoothed boundaries from Fig. 6.2 are included in each image.

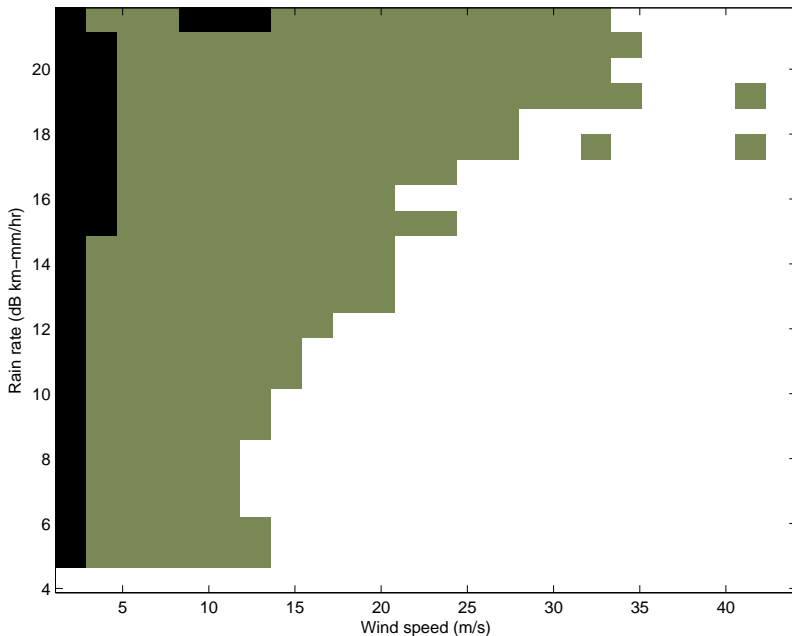


**Figure 6.2:** Estimators with total minimum normalized CRB as a function of wind speed and rain rate: WO (white), SWR (gray), RO (black). As expected the WO estimator is best for low rain rates and substantial wind speed, the SWR estimator is best for comparable wind speed and rain rate and the RO estimator is best when the wind is low and rain is substantial.

Similarly the biased CRB can be calculated for wind-contaminated RO retrieval using

$$J(\mathbf{w}, r) = \sum_{k=1}^N \left( \mathcal{M}_k \frac{\partial \alpha_r}{\partial r} + \frac{\partial \sigma_e}{\partial r} \right)^2 \frac{1}{\zeta_k^2} + \frac{\partial \zeta_k^2}{\partial r} \frac{1}{2\zeta_k^4} \frac{\partial \zeta_k^2}{\partial r}. \quad (6.10)$$

Here we have explicitly separated the wind vector  $\mathbf{w}$  and rain rate  $r$  in the notation to make it clear that the derivatives are with respect to the rain rate and that the wind-contamination is a function of the wind vector. Also, note that the RO CRB is a scalar value only valid for the rain rate estimate.

The CRBs for 25km resolution wind speed and rain estimators are shown in Fig. 6.1. To jointly compare the bounds on wind and rain estimation accuracy, we form an *overall* CRB by taking a linear combination of the wind speed and rain rate bounds for each estimator where the weighting coefficients are selected to reflect the relative importance we place on wind or rain accuracy. Comparing the estimation bounds for the several estimators makes

it apparent that there are regions in the wind and rain space where a particular estimator outperforms the others. For example, Fig. 6.1 indicates that ignoring rain under low rain conditions, as the WO estimator does, results in wind estimates with a lower-overall mean-squared error. Similarly, when the wind speed is low and the rain rate is moderate to high, the RO estimator has lower mean-squared-error than the SWR estimator. Figure 6.2 summarizes Fig. 6.1 by indicating the estimator which has the minimum overall CRB for each wind and rain vector. Note that the SWR estimates often have a larger bound than either the WO or the RO estimators. This observation is central to the remainder of the chapter and prompts the question: if one estimator does not always have the lowest overall CRB, how can the estimator with the lowest overall CRB be selected consistently?

This section motivates the need for multiple estimators in terms of an *overall* CRB. An alternative motivation is given in Appendix E using an information theoretic approach.

### 6.3 M-ary Bayes Estimator Selection

M-ary Bayes estimator selection is a modification of Bayes decision theory. It operates on the estimates produced by  $M$  different estimators. In M-ary Bayes estimator selection, we attempt to select one ‘best’ estimate from among  $M$  candidate estimates. To introduce the method, we follow the discussion and notation for Bayes decision theory outlined in [80].

The objective of the Bayes decision technique is to choose a decision rule which minimizes the Bayes risk function given a realization  $\mathbf{x}$  of the observation random variable  $\mathbf{X}$ . For estimator selection, the ‘observations’ are the various estimates and the parameter  $\theta$  corresponds to true conditions. Although in the previous section  $\vartheta$  referred specifically to a wind vector, here we generalize and treat  $\vartheta$  as a realization of the random variable  $\theta$  which represents the true conditions. The observations, or estimates, are realizations  $\mathbf{x}_i$  of the random variable  $\mathbf{X}$ . The decision rule  $\phi_j(\mathbf{x}_i)$  is the rule for choosing estimate  $\mathbf{x}_j$  as best based on the observation of the estimate being tested,  $\mathbf{x}_i$ .

The loss function  $L[\vartheta, \phi_j(\mathbf{x}_i)]$  represents the loss resulting from choosing the estimate  $\mathbf{x}_j$  when  $\vartheta$  is the true condition. For our application, we choose the loss function

$$L[\vartheta, \phi_j(\mathbf{x}_i)] = C(\vartheta, \mathbf{x}_j)(\kappa_j \delta_{ij} + \tau_j(1 - \delta_{ij})), \quad (6.11)$$

where  $C(\vartheta, \mathbf{x}_j)$  is a cost function, i.e. the cost of selecting  $\mathbf{x}_j$  using the decision rule  $\phi_j$  when  $\vartheta$  is the true condition. Because the decision rule  $\phi_j$  selects estimate  $\mathbf{x}_j$  regardless of the estimate being tested, the cost of a decision rule  $\phi_j$  only depends on the estimate  $\mathbf{x}_j$  and the true conditions  $\vartheta$ . The term  $(\kappa_j \delta_{ij} + \tau_j(1 - \delta_{ij}))$ , where  $\kappa_j$  and  $\tau_j$  are scalar weighting factors and  $\delta_{ij}$  is a Kronecker delta function, allows the loss function to vary depending on which estimate is being tested. For example, when  $\kappa_j = 1$  and  $\tau_j = 0$ , the loss function for the decision rule is zero when testing other estimators. When  $\kappa_j = 0$  and  $\tau_j = 1$ , the loss is zero when testing the selected estimator but non-zero when other estimators are tested. The  $\kappa_j$  and  $\tau_j$  terms thus allow for tuning the algorithm to optimize performance. The weighting coefficients  $\kappa_j$  and  $\tau_j$  must be related; however, we postpone the definition of their relationship until later.

Using the established notation, the risk function,  $R(\vartheta, \phi_j)$ , is defined to be the expected loss of using decision rule  $\phi_j$  under the true conditions  $\vartheta$

$$\begin{aligned}
R(\vartheta, \phi_j) &= E_{\mathbf{X}}(L[\vartheta, \phi_j(\mathbf{x}_i)]) \\
&= \sum_{i=0}^M L[\vartheta, \phi_j(\mathbf{x}_i)] f_{\mathbf{X}|\theta}(i|\vartheta) \\
&= \sum_{i=0}^M C(\vartheta, \mathbf{x}_j) (\kappa_j \delta_{ij} + \tau_j(1 - \delta_{ij})) f_{\mathbf{X}|\theta}(i|\vartheta) \\
&= C(\vartheta, \mathbf{x}_j) (\tau_j(1 - f_{\mathbf{X}|\theta}(j|\vartheta)) + \kappa_j f_{\mathbf{X}|\theta}(j|\vartheta)) \\
&= C(\vartheta, \mathbf{x}_j) (\tau_j f_{\mathbf{X}|\theta}(\sim j|\vartheta) + \kappa_j f_{\mathbf{X}|\theta}(j|\vartheta)), \tag{6.12}
\end{aligned}$$

where  $E_{\mathbf{X}}$  denotes the expectation operator over  $\mathbf{X}$  and we define the density  $f_{\mathbf{X}|\theta}(\sim j|\vartheta) = 1 - f_{\mathbf{X}|\theta}(j|\vartheta)$ .

The Bayes risk,  $r(f_\theta, \phi_j)$ , is the posterior expected risk function

$$\begin{aligned}
r(f_\theta, \phi_j) &= E_\theta(R(\vartheta, \phi_j)) \\
&= \int_{\theta} R(\vartheta, \phi_j) f_\theta(\vartheta) d\vartheta \\
&= \int_{\theta} C(\vartheta, \mathbf{x}_j) (\tau_j f_{\mathbf{X}|\theta}(\sim j|\vartheta) + \kappa_j f_{\mathbf{X}|\theta}(j|\vartheta)) f_\theta(\vartheta) d\vartheta. \tag{6.13}
\end{aligned}$$

Using Bayes rule, the Bayes risk can be rewritten in terms of expectations, resulting in

$$r(f_\theta, \phi_j) = \tau_j E_{\theta|\sim \mathbf{x}}[C(\vartheta, \mathbf{x}_j)]f(\sim j) + \kappa_j E_{\theta|\mathbf{x}}[C(\vartheta, \mathbf{x}_j)]f(j), \quad (6.14)$$

where  $E_{\theta|\sim \mathbf{x}}[C(\vartheta, \mathbf{x}_j)]$  represents the expected loss associated with the estimate  $\mathbf{x}_j$  given that it is not best,  $E_{\theta|\mathbf{x}}[C(\vartheta, \mathbf{x}_j)]$  is the expected loss associated with the estimate  $\mathbf{x}_j$  given that it is best,  $f(j) = \int_\theta f(j|\vartheta)f(\vartheta)d\vartheta$ , and  $f(\sim j) = 1 - f(j)$ . This formulation gives insight into the role of  $\tau_j$  and  $\kappa_j$ . We can interpret the Bayes risk for a given estimator rule as a weighted linear combination of the expected loss given the estimator is best and the expected loss given the estimator is not best.

To compare the Bayes risk for the different estimators, it is important that the risks be comparable. A major impediment to this utility are the weighting factors  $f(j)$  and  $f(\sim j)$ . If an estimator is superior more often than the others, then the Bayes risk for that estimator is more strongly weighted. This effect is ameliorated by defining  $\tau_j$  and  $\kappa_j$  such that

$$\tau_j = \frac{\tau}{f(\sim j)}, \quad (6.15)$$

$$\kappa_j = \frac{\kappa}{f(j)}, \quad (6.16)$$

where  $\tau$  and  $\kappa$  are weighting factors that apply to all estimates.

The Bayes risk can then be written

$$r(f_\theta, \phi_j) = \tau E_{\theta|\sim \mathbf{x}}[C(\vartheta, \mathbf{x}_j)] + \kappa E_{\theta|\mathbf{x}}[C(\vartheta, \mathbf{x}_j)]. \quad (6.17)$$

Thus the Bayes risk for a given estimator is a linear combination of the conditional expected costs. Without loss of generality we can add the constraint  $\tau + \kappa = 1$ . This additional constraint defines the Bayes risk for an estimator as a convex combination of the expected costs.

The Bayes decision rule for estimator selection is the rule which minimizes the Bayes risk. Such a rule can be written

$$k = \arg \min_j r(f_\theta, \phi_j) \quad (6.18)$$

$$= \arg \min_j \tau E_{\theta|\sim \mathbf{X}}[C(\vartheta, \mathbf{x}_j)] + \kappa E_{\theta|\mathbf{X}}[C(\vartheta, \mathbf{x}_j)], \quad (6.19)$$

where  $k$  indicates that estimator  $\mathbf{x}_k$  is best.

Although notationally M-ary Bayes estimator selection is similar to traditional Bayes decisions, the M-ary Bayes decision concept is distinct. In Bayes decision theory, decisions are based on realizations of a random variable. Bayes estimator selection makes a distinction from Bayes decisions because the random variable realizations are parameter estimates made from other observations. With this generalized perspective, the estimates can be produced with any estimation method, such as maximum likelihood, maximum a posteriori, or any other function of the measurements. Additionally, Bayes estimator selection places no constraints on the dimensionality of the estimators, which can be different for each. The lack of constraint on the dimensionality makes this technique particularly useful to QuikSCAT wind and rain estimation.

### 6.3.1 Cost Function

With the basic framework of Bayes estimator selection established, the structure can be adapted to meet particular performance criteria for the estimators  $\mathbf{x}_i$ . The desired performance criteria is specified by means of the cost function  $C(\vartheta, \mathbf{x}_i)$  which reflects the goal of choosing the best estimator given the observations.

Although there are many cost functions which could be appropriate for a particular problem, for this case we consider the squared error of the observed estimator  $\mathbf{x}_i$  given  $\vartheta$ , the true conditions. The cost function  $C(\vartheta, \mathbf{x}_i)$  is written

$$C(\vartheta, \mathbf{x}_i) = (\vartheta - \mathbf{x}_i)^2, \quad (6.20)$$

where

$$(\vartheta - \mathbf{x}_i)^2 \triangleq (\vartheta - \mathbf{x}_i)^T N (\vartheta - \mathbf{x}_i) \quad (6.21)$$

is a shorthand notation for the total normalized squared error. In this case the matrix  $N$  is a diagonal matrix with normalization coefficients to ensure that vector components which may have different dimensions are comparable. Inserting this cost function into Eq. 6.17 results in

$$r(f_\theta, \phi_j) = \tau E_{\theta|\sim \mathbf{X}}[(\vartheta - \mathbf{x}_j)^2] + \kappa E_{\theta|\mathbf{X}}[(\vartheta - \mathbf{x}_j)^2]. \quad (6.22)$$

This notation helps clarify the meaning of Bayes risk in estimator selection. The Bayes risk for a decision is a linear combination of the expected squared-error given that the estimator is best and the expected squared-error of the estimator given that it is not best. Thus, while the ideal selection is the estimator with minimum squared-error, the Bayes estimator selection decision can be interpreted as approximating the ideal selection by choosing the estimator with minimum expected squared-error.

To use this mechanism for estimator selection, the conditional mass function  $f_{\mathbf{X}|\theta}(j|\vartheta)$ , referred to as the estimator likelihood function; the prior  $f_\theta(\vartheta)$ ; the normalization matrix  $N$ ; and the weighting factors  $\kappa$  and  $\tau$  must first be determined. Once these have been determined, the selection of a best estimator, in a minimum expected-squared-error sense, is straightforward using Eqs. 6.22 and 6.18.

### 6.3.2 Optimality

The squared-error cost function of Eq. 6.20 specifies that Bayes estimator selection choose the estimator with minimum squared error. The optimal estimator selection is defined to be the selection of the decision rule that corresponds to the estimate which has minimum squared error. It is not possible to choose the optimal selections for all realizations; however, the probability of selecting the optimal decision rule can be maximized, ensuring that the optimal decision is selected as often as possible.

The conditional probability of selecting the optimal decision rule given the true conditions can be expressed as

$$p(\phi_{opt}|\vartheta) = \sum_{j=1}^M p(\phi_j | C(\vartheta, \mathbf{x}_j) < C(\vartheta, \mathbf{x}_i) \forall i \neq j), \quad (6.23)$$

which can be used to calculate the overall probability of selecting the optimal decision  $p(\phi_{opt})$  using Bayes rule

$$p(\phi_{opt}) = \int p(\phi_{opt}|\vartheta) f_{\theta}(\vartheta) d\vartheta. \quad (6.24)$$

For Bayes estimator selection with the specified loss function, the weighting parameters  $\tau$  and  $\kappa$  can be viewed as parameters which allow for tuning to achieve optimal performance. As  $\tau$  and  $\kappa$  are related, the optimal operating point can be determined by solving

$$\frac{\partial p(\phi_{opt})}{\partial \kappa} = 0 \quad (6.25)$$

for  $\kappa$ . Although in general there is no closed form for  $p(\phi_{opt})$ , it can be approximated reliably via Monte-Carlo simulation.

### 6.3.3 Limitations and Advantages

There are several advantages of adopting the Bayes estimator selection technique. For instance, there is no requirement on how the estimators be formed. For example the estimates can be maximum a posteriori estimates, maximum likelihood estimates, or a combination of the two. This advantage allows estimates to be formed with or without priors. Further, the technique can be adapted to include multiple priors based on factors not normally included in the estimation process. For example, in the case of wind and rain estimation, such priors could include regional or topographic features, wind models for hurricanes or other phenomena, latitude-dependent rain models or other models which may be appropriate to a local area. Considering such priors is beyond the scope of this paper.

A principle advantage of the method is that the dimensionality of the estimators need not be identical. Thus an estimator can estimate only a subset of parameters involved. This can reduce variability and sensitivity to particularly noisy or dominant components.

This allows Bayes estimator selection to produce overall performance improvements as some component sensitivities are reduced by selecting estimators which minimize such sensitivities. Finally, in addition to selecting estimates which have lower overall error, the estimator selections can be viewed as a type of contamination or impact flag. Such a flag can indicate where a particular estimate component may be particularly noisy or prone to error.

Despite these advantages there are some limitations. As with any Bayesian technique, the overall performance is strongly dependent on the prior density. If the prior densities needed to compute the posterior expected loss are poorly defined or unknown, there may be little benefit in adopting a Bayes estimator selection structure. However, in many cases an approximate prior is appropriate and can lead to overall performance improvement despite uncertainty in the prior. Another limitation is that the computation of the posterior expected loss can be computationally intense, especially when it must be computed for every estimator. Fortunately, the posterior expected loss can be tabulated for many cases and the real-time computation can be significantly reduced by approximating the Bayes risk calculation with a look up table.

#### **6.3.4 Terminology**

From another perspective, the Bayes estimator selection concept may be classified as a type of model selection technique. For application of Bayes estimator selection for wind and rain estimation that follows, the estimators are realizations of a maximum likelihood estimator using different models, WO, SWR and RO. In this light, what is referred to in this dissertation as estimator selection is perhaps more aptly termed Bayes model selection. However, since the name Bayes model selection has already been used to describe a fundamentally different model selection technique [81], throughout this dissertation the process of choosing the WO, SWR or RO estimates is referred to as Bayes estimator selection. Further, although the wind and rain application of Bayes estimator selection utilizes maximum likelihood estimates with different models, the Bayes estimator selection technique is more general and could as easily be used to compare MLE and MAP estimates in which case the estimator selection terminology is certainly more appropriate than simply model selection.

Although this dissertation uses the terminology Bayes estimator selection throughout, some discussion of the technique in the context of model selection is appropriate. A practical definition of model selection is given in [82] as: “Model selection is the task of choosing a model of optimal complexity for the given (finite) data.” Many model selection techniques attempt to choose the ideal model by balancing model fit and complexity given the data. Bayes estimator selection is an alternative method where the models are given; for wind and rain estimation the models are the WO, SWR and RO models. Rather than selecting a model or estimator based on the fit of the observations to the model, Bayes estimator selection chooses the best model or estimator using the model parameter values. For wind and rain estimation the model parameter values are the wind and rain estimates. To summarize, while conventional model selection techniques choose a model based on the data and some complexity metric, Bayes estimator selection uses a fundamentally different approach and chooses a model based on the model parameters or estimates themselves.

## 6.4 Application to QuikSCAT

### 6.4.1 Normalization

To apply Bayes estimator selection to QuikSCAT wind and rain estimation, a normalization matrix  $N$  is required that defines the relative importance of wind and rain error. It is important that the normalization matrix be selected so that wind and rain error are comparable. A useful normalization matrix has the components shown in Table 6.2. Note that the direction error is neglected. For QuikSCAT wind and rain retrieval there are multiple possible wind and rain vectors, called ‘ambiguities,’ for both WO and SWR estimation. Typically, the wind speed and rain rates of the ambiguities are comparable but the wind direction estimates are separated by 90 or 180 degrees. Choosing a single ambiguity for each estimator is termed ‘ambiguity selection’ and is typically performed independently of wind and rain estimation [42], though in some cases model-based retrieval can minimize the need for ambiguity selection [83]. Because of the ambiguous nature of wind estimation we ignore the ambiguity selection step and choose a normalization of 0 for wind direction.

To account for the different wind speed and rain rate scales, we use the normalized squared error cost function defined in Eq. 6.21. The normalization matrix  $N$  is selected to

**Table 6.2:** Normalization matrix values

Parameter	Maximum Value	Normalization Coefficient
Wind Speed	50 m/s	$1/50^2$
Wind Direction	360 deg	0
Rain Rate	250 km-mm/hr	$1/250^2$

weight the components according to the selection criteria. For wind and rain estimation we select values for the matrix  $N$  to weight each component according to the maximum retrievable value. Thus the normalization factors for wind speed and rain rate in Table 6.2 are ‘the reciprocal of the maximum retrievable value squared.

Additionally, although directional ambiguities exist [43] in both WO and SWR estimates, the estimated wind speeds and rain rates for each estimator are typically quite close in magnitude for all ambiguities. In this paper we simplify the ambiguity selection process by always choosing the ambiguity which is nearest to the National Centers for Environmental Prediction (NCEP) model winds. Although always choosing the ambiguity nearest NCEP winds simplifies the ambiguity selection procedure, the low resolution of NCEP winds can lead to selection errors. NCEP wind estimates are produced at a lower temporal and spatial resolution than QuikSCAT wind products so there can be significant local variations. Additionally, NCEP wind models do not account for rain events or coastal topography which can have small-scale but significant influences on wind directions. However, to simplify the estimator selection problem and minimize directional bias from the estimators or NCEP winds, we choose to ignore the estimated direction in the estimator selection error function. Thus the normalization factor for wind direction in Table 6.2 is set to 0. Similarly, to calculate the squared-error (Eq. 6.21) for estimators which do not estimate all parameters, the parameters which are not estimated are treated as 0.

#### 6.4.2 Wind-Rain Prior

The wind-rain prior  $f_{\theta}(\vartheta)$  used in Eq. 6.21 requires knowledge of the distribution of wind and rain. Since wind and rain interactions are not entirely understood, we choose to

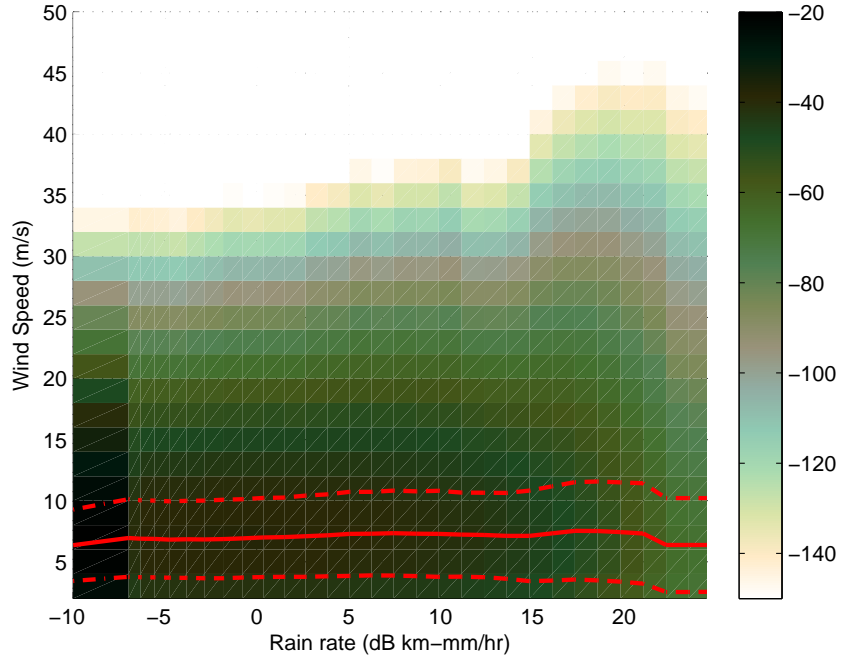


**Figure 6.3:** Wind-rain prior distribution for a single wind direction. The color scale represents the value of  $f_{\theta}(\vartheta)$  in dB for a specific wind speed and rain rate. The solid line corresponds to the mean wind speed of the prior and the dashed lines mark one standard deviation above and below the mean. Note that the standard deviation increases with rain rate. The zero rain rate prior is plotted as well and corresponds to the lowest rain rate in the figure. Note that the wind-only prior is significantly greater than the non-zero rain priors.

approximate the true wind-rain distribution using a combination of NCEP wind estimates and measured rain data from the Tropical Rain Measuring Mission Precipitation Radar (TRMM PR) [84]. Using data from one year of QuikSCAT and TRMM PR co-located measurements, we form an empiric prior by binning numeric wind estimates and measured rain rates. Limitations of this prior are that it is susceptible to the bias of the NCEP predicted wind and the effects of the limited sample size of the data.

To mitigate bias due to the sample size of the data we assume that on a global scale the wind direction distribution is uniform. Although this neglects orographic effects and trade winds, a global prior is appropriate for wind estimation on a global scale.

After smoothing the prior, we adjust it to compensate for bias from NCEP winds in the wind model. Although there are several treatments to adjust and tune the winds, we limit our adjustments to compensating for the fact that NCEP winds poorly represent the highest wind speed cases. Since NCEP winds are predicted at a lower resolution than QuikSCAT UHR products, the highest wind speeds are consistently averaged out of the NCEP product, since they are typically not sustained over large areas. This is in addition to a fixed maximum model wind speed used in NCEP winds. In essence, the wind speed distribution of NCEP winds is truncated above a moderate wind speed.

The distribution of wind speed has Weibull characteristics [85]; therefore, to extend the wind-rain prior to high wind speeds, we perform a non-linear least-squares fit of a Weibull distribution to the empiric speed distribution for each rain rate bin and wind direction. The resulting wind-rain distribution shown in Fig. 6.3 is nearly identical to the empiric distribution and includes a non-zero probability of high wind speeds. The simple distribution fitting technique used here is adequate for our needs, although other fitting techniques exist [85, 86, 87].

### 6.4.3 Estimator Likelihood Function

The estimator likelihood function  $f_{\mathbf{x}|\theta}(j|\vartheta)$  is the probability of an estimator having minimum squared error given the true conditions. As there is no closed form for the probability densities of each estimator, there is no closed form for the estimator likelihood function. This limitation can be overcome in one of several ways. Here we adopt a simple method based on Monte-Carlo simulation. An alternative model-based estimator likelihood function is derived in Appendix D based on a signal to interference ratio (SIR) concept.

For each wind and rain vector we generate multiple simulated backscatter observations. These are inputs to the WO, SWR and RO estimators. The estimator likelihood function is calculated from the estimates as the percentage of the realizations for which a given estimator has lower normalized squared error than the other estimators according to Eq. 6.21.

Figure 6.4 shows the Monte-Carlo simulated estimator likelihood function for a fixed wind direction and cross-track location. The SWR estimator is best for most wind and rain

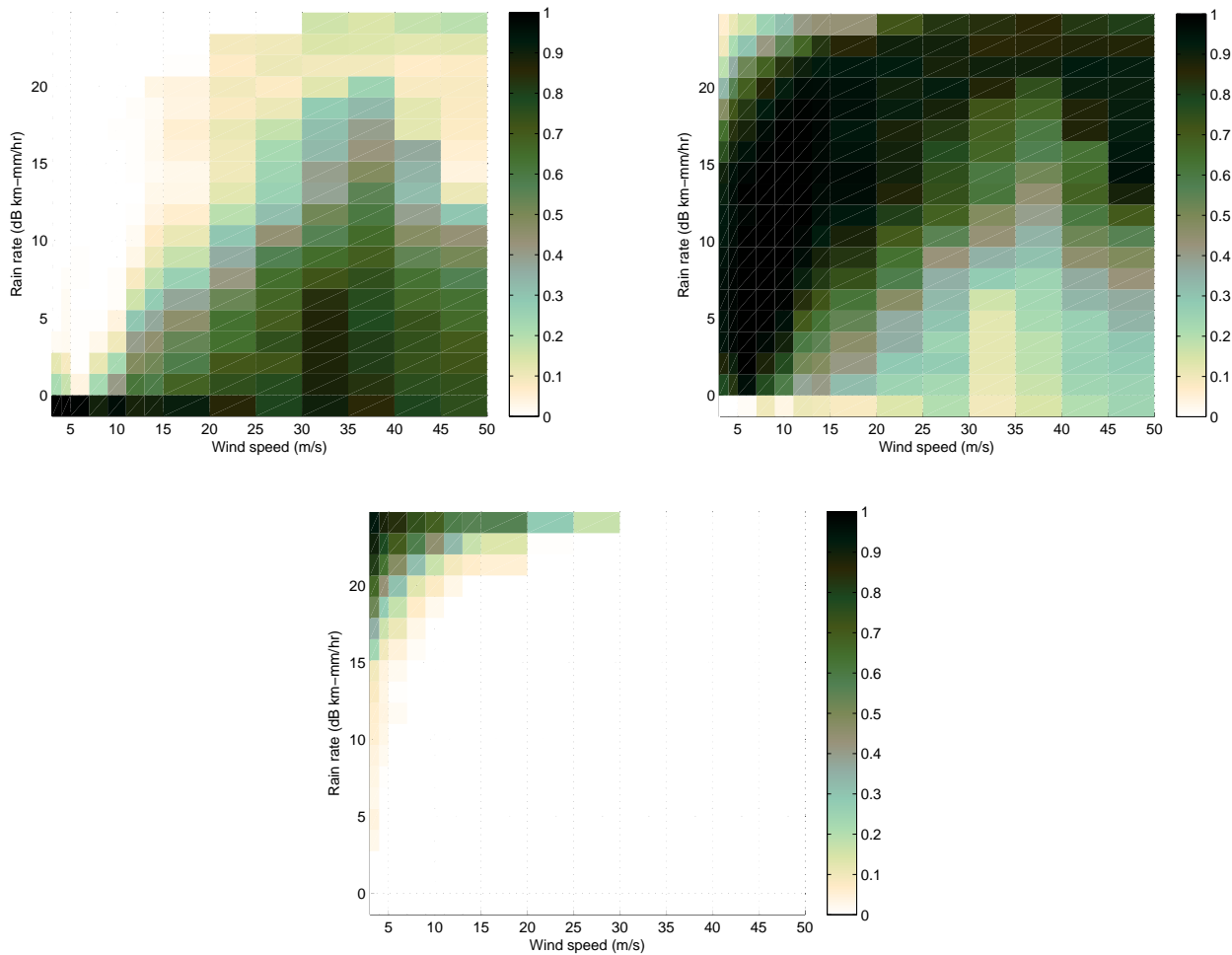


**Figure 6.4:** Monte-Carlo simulated probability of each estimator having minimum squared error. Each image represents the percentage of the time that a given estimator was selected for the underlying simulated wind and rain conditions. Top-left: wind-only. Top-right: simultaneous wind-rain. Bottom: rain-only.

vectors. As expected however, when the wind speed is low and rain is high, the RO estimator is superior. Likewise, when the wind is high and the rain is low, the WO estimator has better performance. As expected, there are relatively few cases where the RO estimator is superior.

#### 6.4.4 Optimality

Finding the optimum operating point consists of finding the value for  $\kappa$  which maximizes the probability of correct estimator selection,  $p(\phi_{opt})$ . Lacking a closed form for the

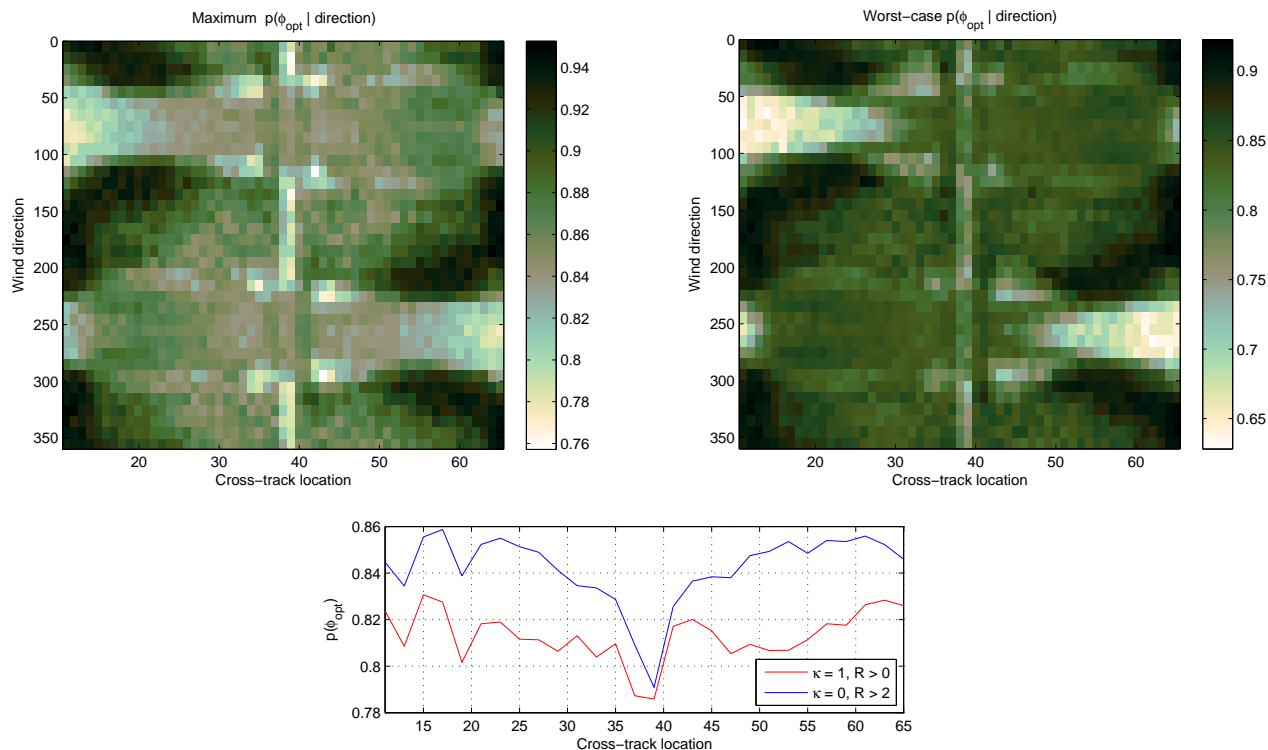


**Figure 6.5:** Probability of correct estimator selection as a function of cross track index. Top-left: Best possible probability of correct selection given the wind direction. Top-right: Worst-case probability of correct selection given the wind direction. Bottom: Overall probability of correct estimator selection, for  $\kappa = 1$  using all SWR rains and  $\kappa = 0$  ignoring rains lower than 2 km-mm/hr. Note that there is a relatively strong directional dependence in the estimator selection performance.

probability densities of the individual estimators, we turn to Monte-Carlo simulation to approximate  $p(\phi_j | C(\vartheta, \mathbf{x}_j) < C(\vartheta, \mathbf{x}_i) \forall i \neq j)$  which can be used to calculate  $p(\phi_{opt})$ .

The Monte-Carlo simulation consists of generating 1000 independent sets of backscatter realizations for each true wind and rain vector. Bayes estimator selection is performed for candidate values of  $\kappa$  on the resulting WO, SWR and RO estimates. The optimal value for  $\kappa$  is that which maximizes  $p(\phi_{opt})$ . The probability of correct estimator selection is shown as a function of  $\kappa$  in Fig. 6.5.

An interesting feature of Fig. 6.5 is that wind direction can influence the probability of correct selection even though the direction error is ignored during estimator selection. Cross-track winds ( $90^\circ$  and  $270^\circ$ ), a known signature of rain contamination, have the lowest probability of correct selections. Near the nadir track (cells 38 and 39), the probability

of correct selection is particularly low for along-track winds. This is not surprising as the observation geometry for along-track winds is particularly poor along the nadir track so wind and rain estimates are noisier than other swath locations. With noisier estimates it is more difficult to choose the estimate with minimum squared error consistently so the probability of correct selection drops.

Also shown in Fig. 6.5 is the probability of correct selection corresponding to the worst-case value of  $\kappa$ . The worst case performance has similar characteristics to the optimal performance but is 16% lower for the worst cases. However, for most cases, the difference between optimal and worst-case performance is 2 to 4%, which indicates that estimator selection is not particularly sensitive to the selected value for  $\kappa$ . The minimum value of the worst-case estimator selection performance is 63%, which is a lower bound on the average estimator selection performance. This is not a very high lower bound, but it is almost twice the probability of correct selection compared to a simple ternary randomized rule, which would choose correctly 33% of the time. The worst-case estimator selection performance occurs for cross-track winds for certain observation geometries. Wind and rain estimation is particularly difficult for these conditions as the wind and rain signals are not orthogonal [61]. The worst-case estimator selection performance for other wind directions and observation geometries is significantly better, thus allowing the average probability of correct estimator selection to be above 80% for most cases.

The optimum value for  $\kappa$  has an interesting interpretation. When  $\kappa = 1$ , the best estimator selection is given by minimizing the error associated with the correct estimator. When  $\kappa = 0$ , the optimum selection can be interpreted as choosing the estimator which minimizes the error associated with using an incorrect estimator. This interpretation leads to a simple explanation for the optimum values of  $\kappa$ . When estimator noise is high it is best to minimize errors associated with incorrect selections by setting  $\kappa$  close to 1. When estimator noise is low, it is best to minimize the error associated with the correct selection, so  $\kappa$  is close to 0.

The optimum value for  $\kappa$  based on Fig. 6.5 is 1 for all cross-track locations which results in the values of  $p(\phi_{opt})$ . Based on the above interpretation, this implies that estimator noise is high. This noise may be largely attributed to the SWR estimator, which has high

noise levels for low rain rates. Much of this noise can be removed by discarding any SWR solution with a rain rate below a threshold. Setting a threshold at 2 km-mm/hr increases  $p(\phi_{opt})$  by up to 4% overall and changes the optimal  $\kappa$  value to 0, implying that estimator noise levels for these cases are lower. Since the impact of such low rains on the WO estimates is quite small and SWR estimates are particularly noisy for low rains, thresholding low rain rates for SWR reduces estimator noise without significantly increasing the overall estimate error.

## 6.5 Results

We evaluate the performance of Bayes estimator selection in several ways. First, we consider an illustrative case study. Then we evaluate the overall estimator selection skill and consider how close Bayes estimator selection approaches the optimal decision rule. Finally, we compare overall wind and rain performance by comparing Bayes estimator selection performance to that of the individual estimators.

### 6.5.1 Case Study

To illustrate the functionality of Bayes estimator selection on real data, we consider a case study from QuikSCAT rev 2882 on January 7, 2000.

The WO estimates are shown in the upper left image of Fig. 6.6. Comparing the WO estimates to the TRMM PR measured rain rates (lower left image in the same figures) illustrates the effects of rain contamination. Rain events cause an increase in the wind speed estimates as large as 10-20 m/s. Note that for this case the true underlying wind field varies between 5 and 10 m/s as indicated by the NCEP winds. In locations where TRMM PR did not measure rain, the WO estimates are between 5 and 10 m/s due to the underlying wind field.

The corresponding RO estimates are shown in the middle left image in Fig. 6.6. Comparing the RO estimates to the TRMM PR measurements shows that the RO estimates are spatially correlated with the TRMM PR measured rain rates. As expected, the RO estimates where TRMM PR measured no rain are biased high.

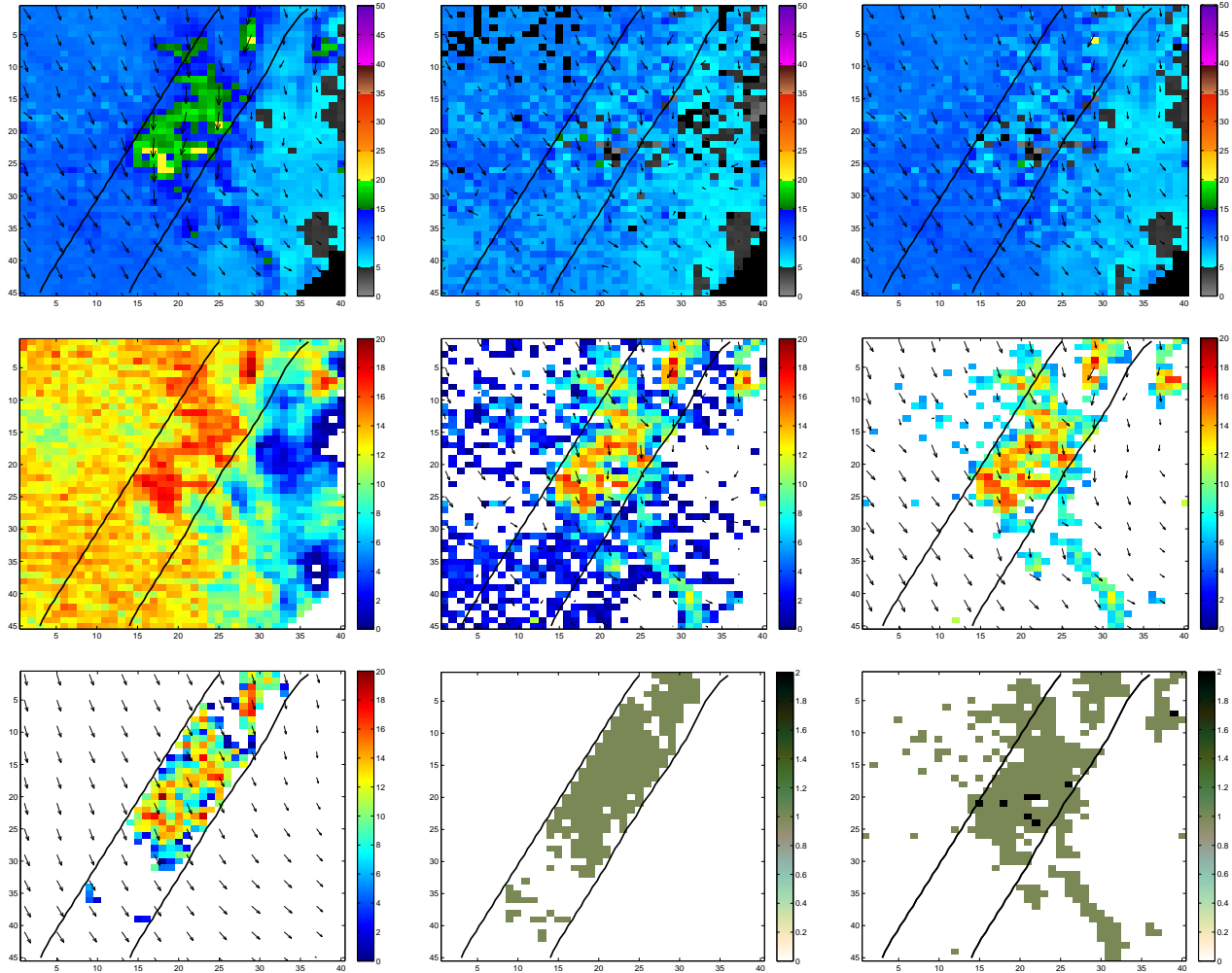


**Figure 6.6:** 25 km resolution estimator results and Bayes estimator selection for a single case (QuikSCAT rev 2882, Jan. 7, 2000). The top row shows wind speed estimates with overlaid direction vectors. From left to right: WO, SWR, Bayes selected wind. The middle row shows rain estimates with relevant direction vectors overlaid. From left to right: RO, SWR, Bayes selected rain. For comparison, the bottom row shows the TRMM PR measured rain with the model wind vector field overlaid (bottom left), the ideal estimator selections (bottom center) and the Bayes estimator selections (bottom right). For estimator selections 0 corresponds to a wind-only selection, 1 to a simultaneous wind-rain, and 2 to a rain-only selection. Note that the Bayes selected estimates have visually less noise than the SWR estimates and have smooth wind fields in non-raining cases.

The SWR estimates overcome many of the problems associated with the WO and RO estimators but also have limitations. The SWR wind estimates are shown in the upper middle image of Fig. 6.6 and the SWR rain estimates are shown in the center image. The SWR wind

estimates are visually noisier than the WO estimates, particularly in areas where there is no rain. The opposite is true of the SWR rain estimates. The SWR rain estimates correspond well with the TRMM PR measured rain estimates for moderate rain rates; however, for the most extreme rain events there is no SWR rain estimate. In essence, this corresponds to the case where the rain backscatter so completely dominates the wind backscatter that a wind estimate is not possible. For rain-free and low-rain cases, the SWR rain estimates are quite noisy, which helps illustrate why it is reasonable to discard the lowest SWR rain estimates as discussed in Section 6.4.4.

The wind-rain estimates produced using the Bayes estimator selection in effect attempt to use the best features of each estimator. The Bayes selected wind estimates are shown in the upper right image in Fig. 6.6, the Bayes selected rain rates are shown in the middle right image, and the Bayes estimator selections are shown in the lower right image. Note the visually improved wind and rain performance. Rain estimates match the TRMM PR measured rain rates quite well. The wind field is visually smoother in non-raining conditions and the high wind speeds due to rain contamination are no longer apparent. For reference, the ideal estimator selections, the selections which minimize the normalized squared-error between the estimate and the true values, are shown in the bottom image. Note that the Bayes estimator selections and the ideal selections are noisy but are often identical.

Although there is significant improvement gained by using the Bayes selected estimates, some drawbacks remain. For the highest rain rates, the RO estimator is selected and consequently there is no wind estimate. Similarly, the wind estimates corresponding to moderately high rain rates where the SWR is selected have wind estimates which underestimate the true wind speed. These wind under-estimates correspond to cases where the rain attenuation of the wind signal is significant enough to lower the wind estimates but not quite large enough to make wind estimation impossible.

The visual correlation between the Bayes selected rain estimates and the TRMM PR measurements is good, but gives no information about the point-wise accuracy of the estimates. To evaluate the point-wise performance of the estimator selection the selected rain estimates and the TRMM measurements are shown in the scatter plots in Fig. 6.7. The

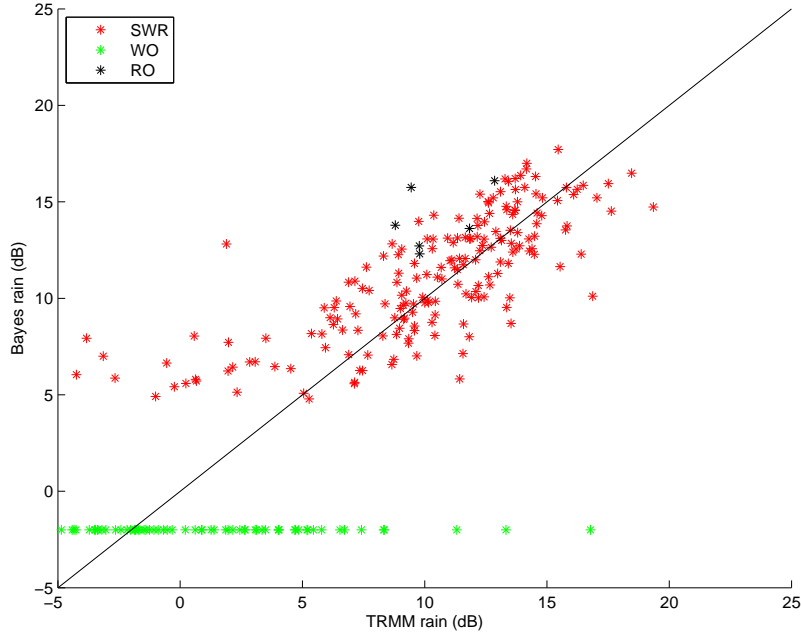


**Figure 6.7:** 25 km resolution Bayes selected rain estimates as a function of TRMM PR measured rain rates. Both axis show rain rate in dB km-mm/hr. The red points correspond to SWR rain estimates, the black to RO estimates and the green show TRMM PR rain rates corresponding to WO selections. The one-to-one line is shown for comparison. Note that above a TRMM rain rate of 5dB the correlation between QuikSCAT estimates and TRMM measurements is clear.

correlation for QuikSCAT rain estimates and TRMM PR rain measurements above 5 dB km-mm/hr is 0.76.

### 6.5.2 Monte-Carlo Performance

The Bayes estimator selection technique may be viewed alternatively as a technique to approach the theoretical wind and rain estimation limits indicated by the CRB. The unbiased CRB gives the estimation bound for an ideal unbiased wind and rain estimator given knowledge of the backscatter observation noise. From this alternative point of view, Bayes estimator selection attempts to approach the wind and rain performance indicated by the unbiased CRB by using the WO, SWR and RO estimators as appropriate.

Since wide-scale truth wind and rain data is unavailable, the Bayes estimator selection wind and rain estimation performance are evaluated using Monte-Carlo simulation as follows.

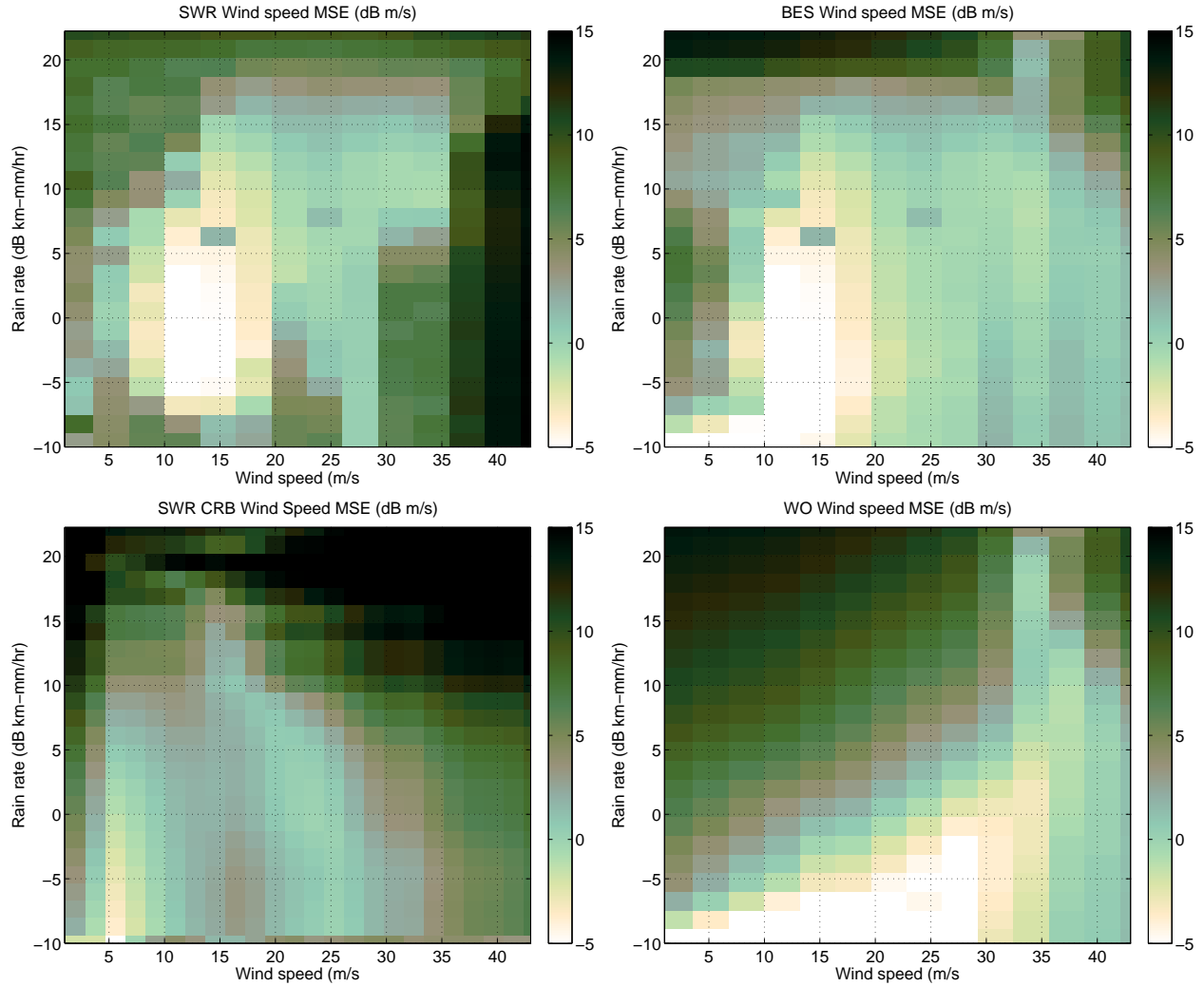


**Figure 6.8:** Monte-Carlo wind estimation MSE in dB m/s for the SWR wind estimates (upper-left), the BES selected wind estimates (upper-right), and the WO wind estimates (lower-right) as well as the CRB for the unbiased SWR estimator (lower-left). As expected the BES MSE is lower than the SWR for some cases and lower than the WO for others. The Bayes selected winds have lower MSE than that indicated by the SWR CRB for most wind speeds and rain rates (see text).

To approximate the estimator performance 1000 realizations are performed for each simulated wind and rain vector and cross-track location. The mean-squared error is calculated from the 1000 realizations and shown in Fig. 6.8 for the WO wind speed, the SWR wind speed, and the Bayes selected wind speeds.

As illustrated by Fig. 6.8, the Bayes selected wind speed MSE has performance which matches that of the SWR and WO wind estimates nearly ideally. For most wind and rain

vectors the Bayes selected MSE is the minimum of the SWR and WO MSE for the corresponding wind and rain vector. While this is not true for the highest rain rates and some of the lowest wind speeds, it indicates that Bayes estimator selection generally improves the wind estimation accuracy, in a MSE sense, for almost all wind and rain vectors.

Interestingly, the Monte-Carlo simulated MSE is often lower than the noise-model derived CRB for the SWR estimates. While this is unexpected, it is not unusual as the SWR and WO estimators are biased, and biased estimators can have lower MSE than the CRB of the unbiased estimator. Despite the difference between the theoretic bounds given the by CRB and the Monte-Carlo MSE, the Monte-Carlo results do clearly indicate how Bayes estimator selection can be effective at improving wind estimation during raining conditions.

### 6.5.3 Overall Decision Performance

The success of the Bayes estimator selection technique can be summarized most succinctly by determining how close to optimal selection the technique performs on real data. As discussed previously, optimal estimator selection consists of selecting the estimate which has minimum squared error. The percentage of time that the minimum squared error estimate is selected gives a measure of the algorithm performance.

To demonstrate actual estimator selection performance, Fig. 6.9 shows the percentage of time that the Bayes estimator selections chose the optimal estimate as a function of NCEP wind speed and TRMM PR rain rate over one year of QuikSCAT and TRMM PR co-located data. Although some wind and rain cases are not found in the data set, the dataset gives a good idea of the general performance. Noticeably, there are some wind and rain combinations, low wind speeds and non-zero rain rates particularly, for which estimator selection does not work well. Fortunately the cases with poor selection accuracy are relatively rare. Further, although the optimal estimator is not always selected for many of these cases, the difference between the WO and SWR estimators are small. For example, during low winds and non-zero rain, the probability of optimal selection is low as the WO estimate is typically selected when the SWR is often best. For low rains the effects of rain are small, so a choice of the WO estimate when the SWR is better only causes a small change in the overall error. This is also true for moderate to high speeds when the rain is low.

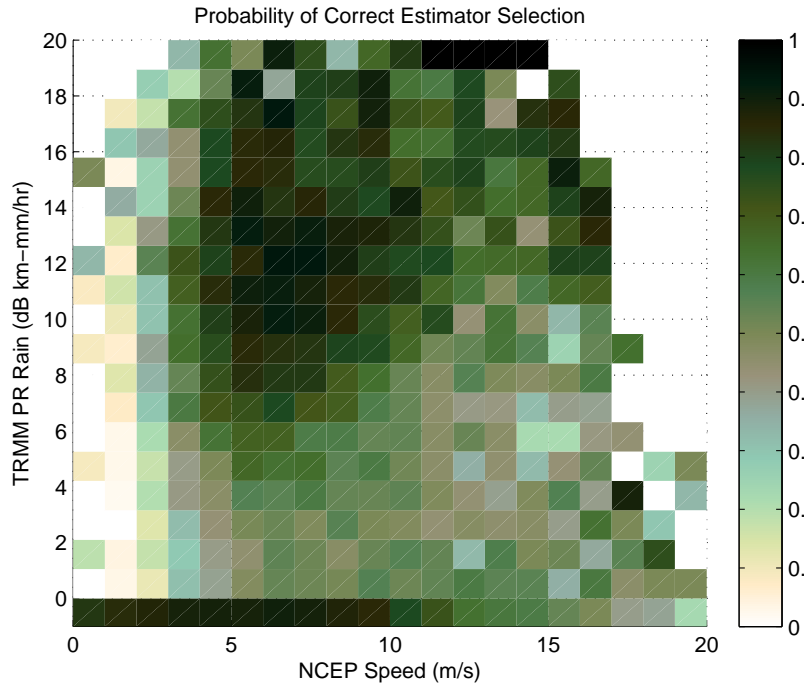


**Figure 6.9:** Probability of correct estimator selection as a function of NCEP wind speed and TRMM PR rain rate. Non-raining performance is shown as rain rates below 0 dB km-mm/hr. Data is missing for some wind and rain vectors which did not occur in the dataset. Note that although there is poor selection performance for some cases (low speed and non-zero rain particularly) the probability of correct selection is high for the most common winds and rains.

The probability of wind and rain conditions occurring, given that the probability of correct estimator selection is in a certain range, is shown in Table 6.3. As shown in the table, wind and rain conditions for which the estimator selection performance is poor are relatively rare.

As expected, the Bayes estimator selections are best for conditions with wind speeds which are close to the mean of the wind and rain prior used to calculate the Bayes risk. This implies that the estimator selection algorithm is sensitive to the wind and rain prior. This sensitivity can be reduced by using a prior selection technique discussed in the following chapter.

An evaluation of the effectiveness of Bayes estimator selection looks at the performance of the Bayes selected estimates compared to the performance of the individual estima-

**Table 6.3:** Probability of wind and rain vector given the estimator selection performance

Probability of correct selection range	Probability of wind and rain vector
0 - 25%	1.0%
25% - 50%	4.8%
50% - 75%	10.0%
75% - 100%	84.2%

**Table 6.4:** Number of missed SWR selections as a function of rain rate

Rain rate range	Number of occurrences	% of Total
0 - 1	13826	59.4%
1 - 2	7246	31.1%
2 - 5	1520	6.5%
5 - 10	213	0.9%
10 - 50	114	0.5%
Total	23266	100%

tors as well as the optimally selected estimates. To make such a comparison, we first define rain-impact. Rain-impact is a condition in which the rain has a large enough impact on the WO estimate that the SWR or RO estimate has minimum squared error. This is equivalent to the optimal estimator selection being SWR or RO. With this definition for rain-impact, the optimal estimator selections are the WO estimator when there is no rain-impact, and the SWR estimator when there is rain-impact. Figure 6.10 compares the wind estimate effects of rain-impact using the WO estimates, the Bayes selected estimates, and the SWR estimates.

Without Bayes estimator selection or something equivalent, only a single estimator is used. There are two choices, use the WO estimator all the time and discard rain-impacted winds, or reduce rain-impact by using the SWR estimator all the time. Choosing the SWR estimator can reduce the impact of rain but suffers degraded performance when there is no rain. Bayes estimator selection balances both the strengths and weaknesses of the individual estimators by making an optimal choice between them. Figure 6.10 shows that choosing the first option has good wind performance in conditions with no rain-impact but there is

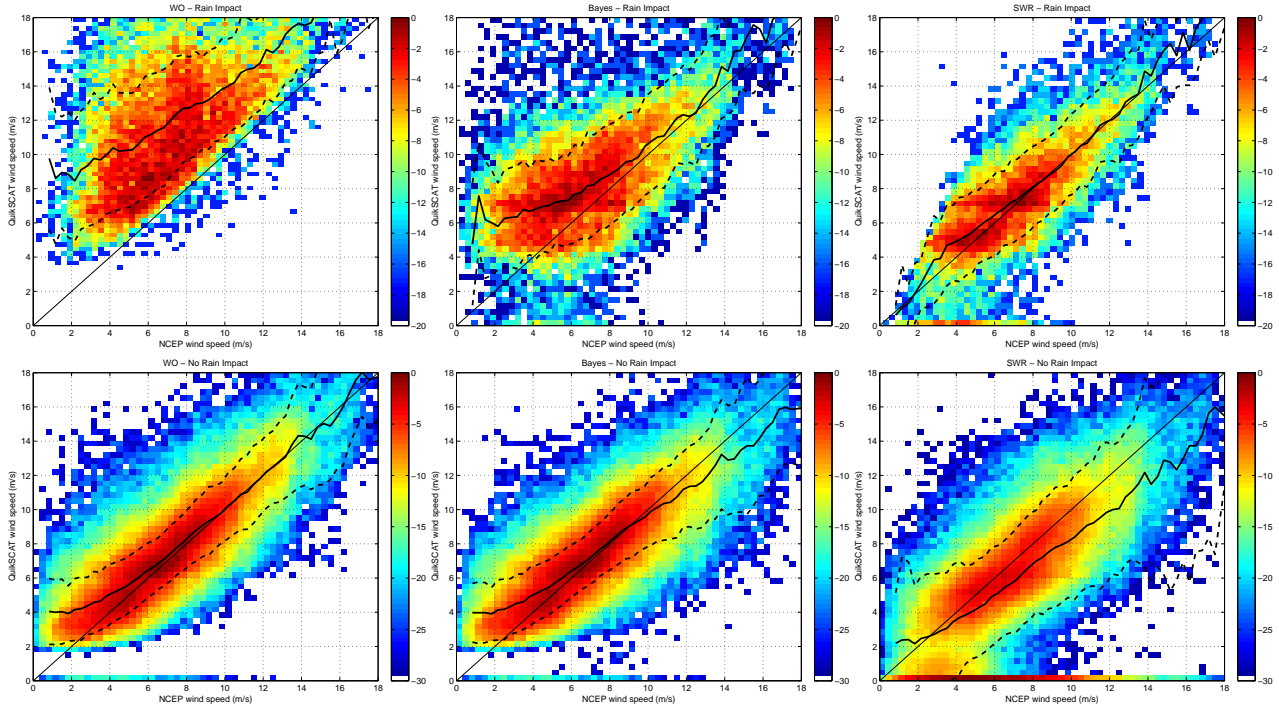


**Figure 6.10:** Scatter densities (in dB) for NCEP and QuikSCAT wind estimates for conditions with a rain impact (top row), i.e. the optimal selection should be the SWR estimator, and without a rain impact (bottom row), for which the optimal selection is the WO estimator. From left to right the columns show the WO estimates, the Bayes selected estimates, and the SWR estimates. Each figure also includes the mean of the QuikSCAT estimates (solid black line) plus and minus one standard deviation (dashed black lines). Note that the Bayes selected estimates have significantly reduced the wind bias in rain impact cases for all but the lowest wind speeds and have no bias in cases with no rain impact cases. Ideally the Bayes estimates have the performance of the WO estimator in conditions with no rain-impact, and the same performance as SWR in conditions with rain-impact. The differences observed are due to non-optimal estimator selection.

strong bias and high variability in rain-impact conditions. On the other hand, Fig. 6.10 shows that using the SWR estimates gives good wind performance in rain-impact conditions but has biased performance in conditions without rain-impact. In fact, there are many times when there are no valid SWR wind estimates. Bayes estimator selection attempts to obtain optimal performance, using the WO estimates when there is no rain-impact and the SWR estimates when there is. Thus, as shown in Fig. 6.10, the Bayes estimator selections have wind performance which is similar to that of the WO estimates when there is no rain-impact and the SWR estimates when there is rain-impact.

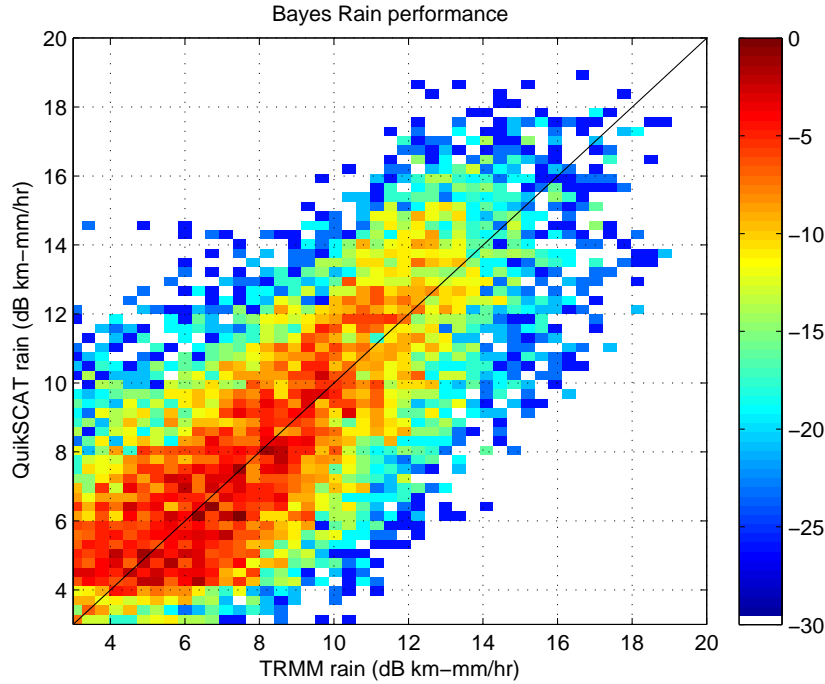


**Figure 6.11:** Normalized scatter density in dB of BES rain estimates and TRMM PR rain measurements.

The IMUDH rain flag is a modified version of the MUDH rain flag [57] that is included with standard QuikSCAT 25 km wind estimates [88]. IMUDH is designed to indicate the likelihood of rain-impact on a given wind estimate. For the IMUDH rain flag, rain-impact is defined as the wind estimate being perturbed by rain from the true wind by more than 2 m/s. Although this definition is different from the definition of rain impact used previously in this paper, the IMUDH rain flag is a useful comparison tool.

An evaluation of the effectiveness of Bayes estimator selection at reducing the effects of rain can be performed using the IMUDH flag. Such a comparison requires knowledge of the true conditions. Since true wind data is unavailable, the estimate error for the WO, SWR and Bayes selected wind estimates is calculated using NCEP model wind speeds which have additional uncertainty. The additional uncertainty in NCEP wind speeds increases the probability that the wind estimates have error greater than 2 m/s, the original threshold for wind perturbation used in the IMUDH rain flag [88].

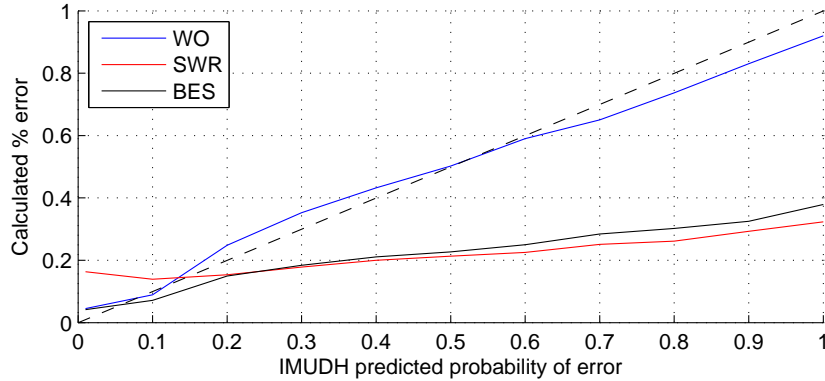


**Figure 6.12:** Probability of the wind estimates having error greater than 3.92 m/s, as a function of the IMUDH rain flag value. The IMUDH flag correctly predicts the number of perturbed WO estimates, whereas the BES and SWR estimates are perturbed by rain far less often than predicted by the IMUDH rain flag. The dashed line in the image is the 1 to 1 line shown for comparison.

An appropriate IMUDH error threshold for use with NCEP model winds can be obtained. The threshold is chosen by minimizing the difference between the probability that the WO estimate error is greater than the threshold and the probability predicted by the IMUDH rain flag. For the comparison data in this paper, the threshold which minimizes the difference between WO estimate error and the IMUDH flag is 3.92 m/s. This value allows us to use the IMUDH rain flag with NCEP winds as validation wind data. Fig. 6.12 shows the probability of the WO, SWR and Bayes selected wind estimates having speed errors greater than 3.92 m/s as a function of the IMUDH rain flag.

By construction, the WO estimates in Fig. 6.12 correspond quite well with the IMUDH rain flag. The SWR wind estimates however, have significantly lower rain perturbation for high IMUDH values. For low IMUDH values the SWR speed estimates have more error than predicted by the IMUDH rain flag. The speed estimates selected using Bayes estimator selection have improved performance over both the WO and SWR estimates. For low IMUDH values the speed estimates selected using Bayes estimator selection are perturbed similarly or less often than the WO estimates, and for high IMUDH values the selected speed estimates are perturbed far less often than the WO estimates and only slightly more than the SWR speed estimates.

Thus the Bayes estimator selection performance as a function of the IMUDH flag agrees with the rain-impact performance shown in Fig. 6.10. In both cases using the Bayes selected estimates results in improved performance over the individual WO or SWR estimates for situations with and without rain-impact. To summarize, Bayes estimator selection, as applied to QuikSCAT wind and rain retrieval, can reduce the effects of rain impact thereby improving wind estimates by reducing rain contamination. It also produces estimates of the rain for rain-impacted situations.

## 6.6 Conclusion

Bayes estimator selection is a unique way of addressing QuikSCAT wind and rain estimation. Rather than rely solely on one type of estimator, Bayes estimator selection can be used to reduce the effects of rain impact without discarding information. This improves the overall quality and reliability of the wind and rain estimates. Further, Bayes estimator selection is a highly flexible and robust technique which can be adapted to a variety of problems regardless of estimator technique or dimension. Although the technique does not always make the optimal selections, it does do so a large majority of the time. This reliability makes Bayes estimator selection a valuable tool to increase the functionality of QuikSCAT data products. Additionally, the Bayes estimator selection technique can be applied to other scatterometers like ASCAT, using the rain models from Chapter 4 to similarly improve the instrument reliability.

## Chapter 7

### Prior Selection and UHR BES

Chapter 6 showed that although each estimation technique WO, SWR and RO, is optimal for some conditions, no single estimator is appropriate for all conditions. Chapter 6 introduced Bayes estimator selection (BES) to optimally choose between the several estimators for conventional resolution wind products.

Although conventional resolution wind and rain products have lower noise levels than UHR products, the conventional 25 km resolution is coarser than many rain cells. UHR wind and rain products can be valuable for rain studies since their 2.5 km resolution approaches that of rain events. At UHR, BES is complicated by significantly higher noise levels in addition to higher variability of the wind and rain fields due to the increased resolution. The increased noise and variability in UHR wind and rain estimates have two main consequences. The additional variability in UHR estimates both increases their sensitivity to the wind and rain prior distribution used in BES, and increases the probability of selecting an estimator which is inappropriate for the true conditions.

The sensitivity to the prior distribution for UHR BES can be reduced by choosing a prior distribution that is appropriate for each wind field. Uncommon wind events such as tropical storms, frontal features and other wind events are particularly sensitive to the prior distribution since each type of event is rare and is thus not well-modeled by a global prior. This Chapter extends the BES concept by introducing a prior selection technique whereby a single prior distribution is selected from among several candidate priors for each wind field.

To further reduce the probability of selecting an inappropriate estimator and to increase wind and rain field spatial consistency, this Chapter also introduces an estimator selection noise reduction step. Estimator selection noise reduction corrects certain types of

estimator selection errors by exploiting known spatial characteristics of wind and rain fields to identify and correct incorrect estimator selections.

This Chapter adapts the concept of Bayes estimator selection from Chapter 6 to the UHR 2.5 km wind product and further extends the technique to include prior selection and noise reduction thereby reducing some limitations of BES which are unique to UHR. Section 7.1 reviews BES and introduces some new notation. Prior selection is introduced in Section 7.2 and is applied to QuikSCAT UHR products in Section 7.3. Section 7.4 describes estimator selection noise reduction and Section 7.5 evaluates estimator selection performance using BES, prior selection, and noise reduction after which Section 7.6 concludes.

## 7.1 Bayes Estimator Selection

As previously noted, for QuikSCAT wind and rain estimation there are three types of estimators, WO, SWR and RO. Each estimator is appropriate under different conditions: WO when rain effects are insignificant, SWR when wind and rain effects are comparable, and RO when rain effects are dominant. If the estimators are used under conditions for which they are not appropriate, the estimates are degraded, sometimes severely. This effect is described in detail in terms of the overall Cramer-Rao lower bound in the previous Chapter where it is demonstrated that the minimum bound can only be achieved using the estimators under conditions for which they are appropriate. For UHR wind products, the observation noise is higher than for 25 km wind products. This increases the estimate variability and generally increases the CRB for the different estimators.

To approach optimal overall wind and rain estimation performance, BES can be used to select the most appropriate wind-rain estimate without additional information. BES for QuikSCAT conventional resolution is introduced and demonstrated in Chapter 6. It is also shown in Chapter 6 that the estimates selected using BES have overall improved performance, lower bias and lower mean squared-error, than the estimates from any single estimator.

In BES the Bayes risk  $r(\phi_j, F_\theta)$  for a decision rule  $\phi_k$  and a prior  $F_\theta$  is the expected value of the risk function  $R(\vartheta, \phi_j)$  and can be written as

$$\begin{aligned} r(\phi_j, F_\theta) &= \int_{\theta} R(\vartheta, \phi_j) F_\theta(\vartheta) d\vartheta \\ &= \tau E_{\theta|X}(C(\vartheta, \hat{\vartheta}_j)) + \kappa E_{\theta|X}(C(\vartheta, \hat{\vartheta}_j)), \end{aligned} \quad (7.1)$$

where  $\vartheta$  is the true wind and rain,  $\tau$  and  $\kappa$  are weighting coefficients,  $C(\vartheta, \hat{\vartheta}_j)$  is the squared error cost function between the estimate  $\hat{\vartheta}_j$  and the true conditions  $\vartheta$ ,  $E_{\theta|X}(C(\vartheta, \hat{\vartheta}_j))$  represents the expected squared error of not selecting  $\hat{\vartheta}_j$  when  $\vartheta$  is true, and  $E_{\theta|X}(C(\vartheta, \hat{\vartheta}_j))$  represents the expected squared error of selecting  $\hat{\vartheta}_j$  when  $\vartheta$  is true. In Bayes estimator selection a decision rule is selected by choosing the rule which minimizes Eq. 7.1. The optimal selection, denoted  $\phi_{opt}$ , for Bayes estimator selection is to choose the estimate which minimizes  $C(\vartheta, \hat{\vartheta}_j)$ . Optimal values for  $\tau$  and  $\kappa$  are selected to maximize the probability of making the optimal selection,  $p(\phi_{opt})$ , using Monte-Carlo simulation.

Despite cases where performance is nearly optimal, there are cases where BES is not as reliable, particularly high wind events which are relatively uncommon. This limited performance is strongly related to the wind and rain prior distribution,  $F_\theta$ , used in BES. When the wind and rain field matches the prior, BES has nearly optimal selection performance, but when the wind and rain field does not match the prior, BES performance is degraded.

As BES is dependent on the wind and rain prior distribution  $F_\theta$ , it is helpful to explicitly include this dependency. The selected decision rule is written with this dependence as  $\hat{\phi}(F_\theta)$  which is a shorthand notation for

$$\hat{\phi}(F_\theta) = \arg \min_j \{r(\phi_j, F_\theta)\}. \quad (7.2)$$

Similarly, the dependence on the prior can be included in the Bayes risk, or error, for the selected decision rule

$$e(\hat{\phi}(F_\theta)) = \min_j \{r(\phi_j, F_\theta)\} \quad (7.3)$$

$$= r(\hat{\phi}(F_\theta), F_\theta). \quad (7.4)$$

where  $e(\hat{\phi}(F_\theta))$  is the Bayes risk associated with the decision rule selected using the prior density  $F_\theta$ .

It is demonstrated in Chapter 6 that BES functions well at conventional resolution, i.e.  $p(\phi_{opt})$  is high, for cases where the observed wind and rain field is well-represented by the wind and rain prior distribution,  $F_\theta$ . For most wind fields (roughly 80% of winds), the global wind and rain prior used in Chapter 6 is appropriate. However, for wind and rain fields which are misrepresented by the prior, BES has diminished performance, i.e.  $p(\phi_{opt})$  is low. This reduced performance is not a breakdown of the BES technique but is instead a consequence of using a prior that is inconsistent with underlying conditions.

At UHR, the sensitivity to the wind and rain prior distribution is greater due to greater spatial variability in the UHR wind and rain fields. Wind events such as hurricanes are particularly sensitive to the wind and rain prior since they are uncommon on a global scale and are thus not well-represented by a global prior. However, since these rare cases are often of particular interest, it is important that BES can address them reliably. To increase the reliability of BES for wind and rain conditions which are not well-represented by a global prior we introduce the concept of prior selection.

## 7.2 Prior Selection

Sensitivity to the prior distribution is common to all Bayes techniques, from Bayes decisions to MAP estimation. When the prior does not reflect the distribution of observations, accuracy and reliability are diminished. One method to ameliorate this limitation is to use a prior which more appropriately fits the observed wind and rain field. In our application we consider multiple priors which can be selected to better model wind and rain interaction such as storm dynamics, as in [83] where a hurricane model-based prior is derived and utilized, or can compensate for regional characteristics such as trade winds or topography.

Attempting to create a single prior distribution to match a potentially infinite variety of wind and rain fields is not feasible. An alternative method pursued here is create a reasonably sized set of candidate prior distributions from which to choose a suitable prior. As a mechanism to select a best prior distribution from among multiple candidate priors, we introduce a prior selection technique based upon a Bayes decision formulation.

Adapting a Bayes decision mechanism for prior selection implies that the true prior distribution is a random variable with some distribution. Treating the true prior distribution as a random variable is a concept that is particularly well-suited for UHR wind and rain fields which can have a variety of distributions over relatively small areas.

Because wind and rain retrieval is not performed for the entire globe simultaneously it makes little sense to blindly use a global wind and rain distribution when small-scale features are of interest. Rather, it is more appropriate to consider a set of candidate wind and rain distributions which represent a variety of wind and rain phenomena on the spatial scales of interest and select from it one that best matches the local conditions, ranging from hurricanes to doldrums. This set of wind and rain distributions has a distribution which can represent the frequency with which each type of phenomena occurs. To decide which of these wind and rain distributions is most appropriate for observed conditions requires a prior selection technique which we now introduce.

Let  $F_{\theta_i}$  denote a candidate prior and let  $F_{\Theta_t}$  denote the true prior. To form the Bayes risk for prior selection requires the definition of a loss function  $L(\Phi_i(\phi), F_{\Theta_t})$  where  $\Phi_i(\phi)$  is the prior selection decision rule based on observing  $\phi$  and  $F_{\Theta_t}$  represents the true prior. The Bayes risk also requires a prior distribution on the candidate priors. We denote the probability of prior  $F_{\Theta_i}$  being best as  $f_{\Theta}(i)$ . The Bayes risk also requires a conditional distribution which represents the probability of prior  $F_{\theta_i}$  being best given that the ‘true’ prior is  $F_{\Theta_j}$ . This probability mass function is written as  $f(i|j)$ . With this notation the risk function can be written

$$\begin{aligned} R(\Phi_i, \Theta_t) &= E_{\theta_j|\Theta_t}[L(\Phi_i(\hat{\phi}(F_{\theta_j})), F_{\Theta_t})] \\ &= \sum_j L(\Phi_i(\hat{\phi}(F_{\theta_j})), F_{\Theta_t})f(i|j). \end{aligned} \quad (7.5)$$

To form the Bayes risk requires one final distribution,  $f_{\Theta}$ , which represents the distribution of prior distributions. The Bayes risk for prior selection is the posterior expected loss and can be written

$$r(\Phi_i, f_{\Theta}) = \sum_t \sum_j L(\Phi_i(\hat{\phi}(F_{\theta_j})), F_{\Theta_t})f(j|t)f_{\Theta}(t). \quad (7.6)$$

A shorthand notation for the rule that selects the prior which minimizes the Bayes risk is

$$\hat{\Phi} = \arg \min_i r(\Phi_i, F_{\Theta}), \quad (7.7)$$

where  $\hat{\Phi}$  represents the selected prior.

### 7.2.1 Prior Selection Loss Function

The definition of the loss function is fundamental to the success of the prior selection technique. The definition of a suitable loss function must account for several unique aspects of the estimator selection problem.

For a single WVC there are at most three different estimates, WO, SWR and RO. With three data points there is often sufficient information to make an informed estimator selection using BES, however, there may be insufficient information to select a prior as well. Prior selection must therefore include information from more than a single WVC. Additional information is available, particularly at UHR, by changing from a point-wise formulation, where each WVC is considered independently, to a field-wise formulation, where each WVC is related to the surrounding WVCs. Field-wise techniques have been previously implemented for wind retrieval [83][89]; however, prior selection is unique in that it makes field-wise decisions about point-wise estimates.

A field-wise formulation for prior selection exploits spatial consistency in wind and rain fields by incorporating information from the surrounding WVCs. This spatial correlation can be utilized in prior selection by defining a loss function for the prior selection decision rules which incorporates the spatial characteristics of the wind field.

Such a loss function can be written

$$L(\Phi_i(\hat{\phi}(F_{\theta_j})), F_{\Theta_i})_{(x,y)} = e(\hat{\phi}(F_{\theta_j}))_{(x,y)} * W(x, y) \delta_{ij}, \quad (7.8)$$

where the subscript  $(x, y)$  indicates location,  $*$  denotes spatial convolution,  $W(x, y)$  is a weighting function, and  $\delta_{ij}$  is a Dirac delta function. This definition for the prior selection loss function ensures that the loss associated with candidate prior  $F_{\theta_j}$  at pixel  $(x, y)$  depends on the BES Bayes risk associated with the estimator selections in the surrounding area. The

Dirac delta function  $\delta_{ij}$  ensures that the loss for candidate prior  $F_{\theta_j}$  is zero when it is not selected using decision rule  $\Phi_i$ .

Note, this definition for the loss function does not depend on the true prior  $F_{\Theta_t}$ . This is by design for several reasons. First, identifying the true prior is not the objective; rather it is to choose the candidate prior which results in the lowest estimation error over a region. Second, there is no way to determine the true distribution of wind and rain vectors in a WVC from a single wind and rain estimate, at least not without additional information.

The loss function accounts for spatial consistency using the weighting function  $W(x, y)$  which must reflect the expected spatial consistency of the wind and rain field.

### 7.3 Bayes Estimator Selection with Prior Selection

This section discusses the application of both BES and prior selection to the QuikSCAT UHR product. Previously in Chapter 6, BES was applied only to 25 km wind products using a single universal wind and rain prior.

#### 7.3.1 Estimator Likelihood Function

The estimator likelihood function  $f(i|\vartheta)$  for UHR BES is independent of the wind and rain prior as it depends only on the performance of the estimators. For performance evaluation we use a Monte-Carlo approach. Although model-based approaches can lend to the simplicity of the prior, the Monte-Carlo approach we pursue here is advantageous in that it is simple to implement and the results can be easily interpreted. This approach is identical to that pursued for the conventional resolution estimator likelihood function except that the Monte-Carlo simulation parameters are those for UHR wind products [90][5]. At UHR, the general structure of the estimator likelihood function reflects estimator performance similar to that of conventional resolution, however the higher noise level in the UHR estimates causes greater variability in the optimal estimator selections for any wind and rain vector. This is because UHR wind and rain retrieval is not as sensitive to low rain events as 25 km wind and rain estimates.

### 7.3.2 Candidate Priors

The choice of candidate priors is critical to overall algorithm performance. One approach to choosing a wind and rain prior is to estimate the parameters of the wind and rain prior distribution from the data. This approach is complicated for wind and rain estimation because it is unclear which estimates, WO, SWR or RO, should be used to estimate the prior parameters. Instead, prior selection is essentially a two step approach where BES is performed with each candidate prior, after which prior selection uses the selected estimates from each candidate prior to select the best prior distribution. For this approach, prior selection requires a number of candidate priors. While there are a potentially infinite number of viable wind and rain distributions, with some additional information about wind and rain fields in general, a set of useful candidate priors may be formed.

Wind fields are relatively smooth on small-spatial scales as wind spectra are dominated by low wavelengths, although storms and weather fronts can cause higher spatial variability. Rain fields, on the other hand, are characterized by high spatial variation, particularly for convective storm systems where rain cells can be as small as 2.5 km [91]. Although rain events modify the wind field, the distribution of wind speeds over the surrounding region remains largely unchanged. Thus for moderate spatial scales, between 25 and 100 km, there is potentially high variability for rain, but low variability for wind, i.e. the wind is dominated by a local mean flow.

The spatial auto-correlation of wind and rain is estimated using NCEP model winds and TRMM PR measured rains and is shown in Fig. 7.1. As expected, the wind auto-correlation is very smooth over large scales whereas the rain auto-correlation falls off very quickly.

Prior selection for BES works to reduce the estimator selection errors associated with BES by choosing the appropriate wind and rain prior distribution. BES has the greatest limitations when the mean wind speed over a region is significantly different from the global wind prior. This, together with rain spatial characteristics, implies that useful candidate priors can have similar rain distributions with different mean wind speeds.

The candidate priors are selected so that each has a different mean wind speed than the global wind-rain prior. To ensure that these prior distributions reasonably match ob-

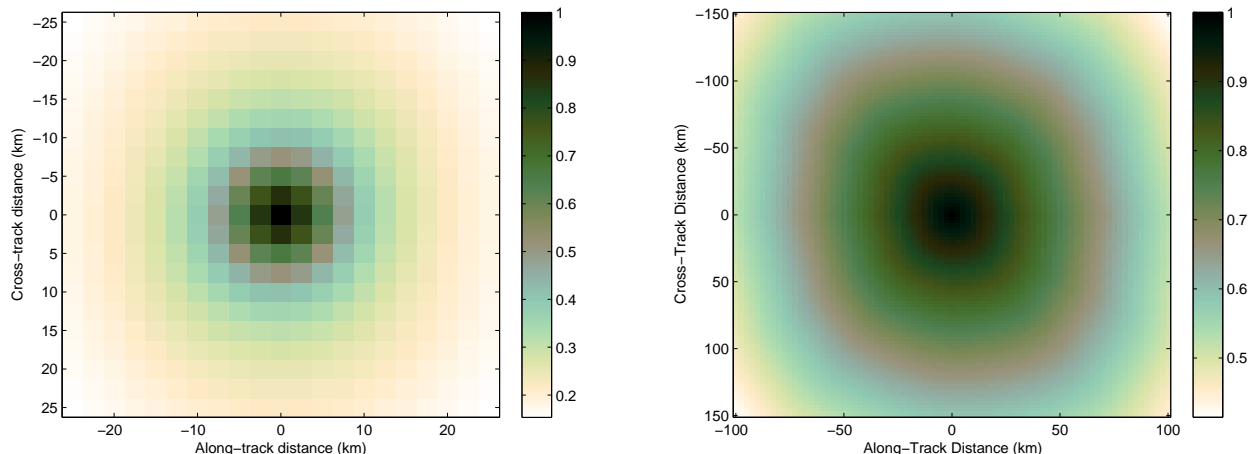


**Figure 7.1:** Empiric rain (left) and wind speed (right) correlation functions relative to the QuikSCAT geometry as calculated from TRMM PR measured rain rates and NCEP interpolated wind fields. Each cell is 2.5km wide corresponding to QuikSCAT UHR. Note that the rain autocorrelation falls off very quickly while the wind autocorrelation is quite smooth over large spatial scales.

served wind and rain conditions they can be formed by shifting the mean of the global wind and rain prior density for UHR which is formed the same way as the conventional resolution wind and rain prior in [92]. Thus each candidate prior has a uniform direction distribution, identical marginal distributions for rain, and Weibull wind speed distributions with different means and similar variances.

Prior selection is not particularly sensitive to the number of candidate priors considered in this Chapter. Fewer priors may leave artifacts in the estimator selection fields as BES characteristics are prior dependent. Using more priors can reduce artifacts but significantly increases the required computation for prior selection. To balance simplicity with effectiveness, in this Chapter we use 12 candidate prior distributions with wind speed means and standard deviations given in Table 7.1. The prior distributions are selected to represent wind conditions from low to high wind speeds. As low wind speeds occur far more frequently the candidate priors have mean wind speeds which are spaced more densely. For high wind speeds the candidate priors have slightly greater spacing to reduce the computation involved in prior selection while maintaining coverage for higher wind speed conditions. As the candidate priors only differ in the distributions of wind speed, each candidate prior can be

**Table 7.1:** Candidate prior mean wind speeds and standard deviations

$\mu$	$\sigma$
5	2.8
7	2.9
9	3.0
11	3.1
13	3.2
15	3.3
17.5	3.3
20	3.4
22.5	3.4
25	3.5
27.5	3.5
30	3.6

uniquely identified by the mean non-raining wind speed (  $\mu$  in Table 7.1 ) as is done in the following sections.

### 7.3.3 Prior Selection Weighting Function

The weighting function  $W(x, y)$  is fundamental to prior selection. The weighting function incorporates spatial characteristics of the wind over a large area enabling prior selection. To utilize known spatial characteristics of the wind fields we choose to use the two-dimensional autocorrelation function of the wind field as the prior selection weighting function. When the spatially weighted BES error is a minimized by a candidate prior, it implies that the surrounding area is well-represented by the candidate prior.

Prior selection is partly motivated by the fact that rain-free high winds can be easily mistaken for lower speed rain-contaminated winds. Since rain events typically have small spatial extent they can be differentiated from high wind events using prior selection. To differentiate such events the size of the weighting function  $W(x, y)$  must be larger than most rain events. For this Chapter the weighting function size is 225 x 225 km. Prior selection is not particularly dependent on the size of the weighting function as long as it is suitably

large. If the weights are too small prior selection has diminished performance since the weight function is not large enough to reliably detect changes in the wind speed distribution.

#### 7.3.4 Optimal BES for Candidate Priors

To realize optimum estimator selection using each candidate prior distribution, the optimum value for  $\kappa$  must be determined for each candidate prior distribution. The optimum values of  $\kappa$  are obtained for each candidate prior density using Monte-Carlo simulation as in [92] for each cross-track location and are shown in Fig. 7.2.

In addition to choosing the optimal value for  $\kappa$ , Bayes estimator selection can be improved by choosing a minimum acceptable value for rain estimates. Based on the estimator likelihood function, there is a rain rate for each wind speed below which the SWR and RO estimators rarely have lower squared-error than the WO estimate, indicating that for lower rain rates the WO estimate should always be selected. By rejecting SWR and RO estimates with rain rates below this threshold the probability of incorrectly selecting the SWR or RO estimator can be reduced dramatically. The minimum rain threshold is determined for each candidate prior using the estimator likelihood function as the rain rate above which the probability of the SWR estimate being correct is greater than 50% for the mean wind speed of the prior. The minimum rain rate for each candidate prior is shown in Fig. 7.3. The minimum acceptable rain rate increases with the mean speed of the wind and rain prior. For low wind speeds, wind is very susceptible to rain contamination so only the lowest rain estimates can be neglected. Similarly for high wind speeds, the wind is relatively unaffected by rain contamination unless the rain is very high, so the low to moderate rain estimates can be discarded.

The optimum values of  $\kappa$  are dependent on both the candidate prior and the observation geometry (cross-track swath location). As the mean wind speed of the prior increases,  $\kappa$  increases sharply. When  $\kappa$  is close to one, Bayes estimator selection attempts to minimize the error associated with the correct estimator selection. This implies that the cost of incorrect selections is similar to that of the correct selection indicating that the estimates have high noise levels. The decreases in  $\kappa$  above a mean speed of 13 m/s can be partly explained by the minimum acceptable rain threshold. By discarding estimates with low rain estimates, the

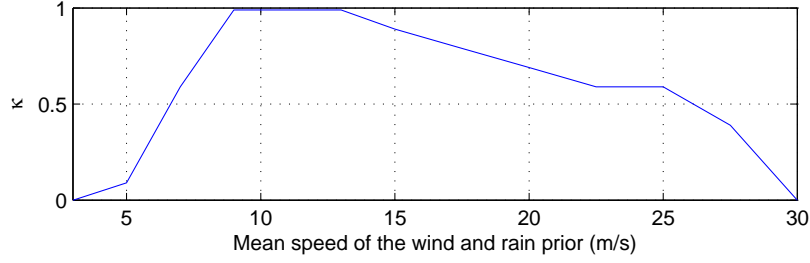


**Figure 7.2:** Optimal values of  $\kappa$  for each of the candidate prior distributions for a single cross-track location.

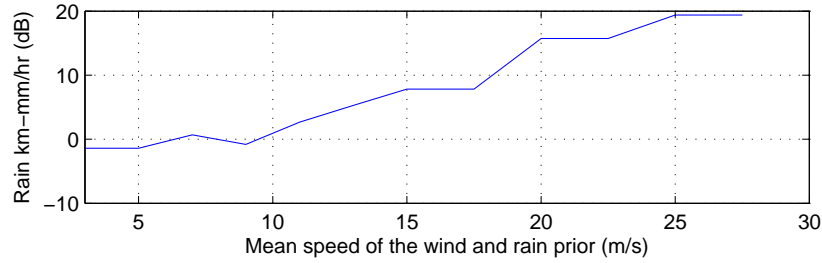


**Figure 7.3:** Minimum acceptable rain rate for the candidate prior distributions for a single cross-track location.

estimator noise is reduced thereby modifying optimal Bayes estimator selection from a minimum cost of correct selection operating principle to a minimum cost of incorrect selection operating principle.

### 7.3.5 Distribution of Priors

Although the distribution of wind vectors can be approximated with a Weibull distribution, it is not as clear how the distribution of priors,  $f_{\Theta}$ , should be represented as there is often no *a priori* information about the realization of the observed wind field. Without definitive *a priori* information, a maximum entropy argument is a logical approach to forming the distribution. Following a maximum entropy argument we adopt a so-called “non-informative” uniform prior for the density of priors, indicating that for a specific spatial area we make no assumptions about the distribution of priors. This choice is particularly useful for wind and rain retrieval on a global scale as the prior selection is thus influenced only by

the estimates and not by an informed prior which may not be appropriate for seasonal or regional variations of the distribution of winds and rain.

## 7.4 Noise Reduction for Estimator Selections

Bayes estimator selection is driven principally by the optimality of the selection parameters and decision rules for point-wise wind and rain estimates. Prior selection is adopted to account for some of the spatial characteristics of wind and rain but it does not ensure spatial consistency of the selected estimates in all cases. Here we diverge from strict point-wise estimator selection optimality and investigate spatial consistency of the estimates as a form of noise reduction. Although the estimator selection uses a statistically optimal criteria, it is a noisy process and some incorrect decisions occur. Incorrect decisions can be apparent due to the structure of the wind and rain fields. By exploiting some general features of wind and rain fields indicated by the wind and rain autocorrelation functions, selection errors can be identified and corrected.

The purpose of noise reduction for wind and rain estimates with prior selection is twofold. First, the Bayes estimator selection is subject to some uncertainty due to noise even when the correct prior is used. Noise reduction aims to reduce selection errors due to high noise levels in the estimates. Second, prior selection can introduce artifacts into selected estimate fields since the characteristics of Bayes estimator selection change depending on the prior used. Noise reduction also aims to reduce these artifacts making the selected wind and rain fields spatially consistent.

To achieve the objectives of noise reduction we exploit the spatial consistency of wind and rain fields to both reduce noise and create spatially consistent fields of selected estimates.

### 7.4.1 Estimator Selection Noise Reduction

Wind estimates are inherently noisy, and with BES and prior selection there are conditions where the noise level can increase due to incorrect estimator selection. Typically estimator selection errors occur for wind and rain events that are difficult to correctly classify. These types of rain events can be generally grouped into several populations: low-rain, high-rain, and high-speed.

Low-rain selection errors typically occur as selection errors between the WO and SWR estimates. Selection errors with low rains typically occur because the WO estimator is selected when the SWR has minimum squared error. High-speed errors occur when the wind speed is quite high and the rain is insignificant. For these cases the WO estimate should be selected but the SWR wind estimate was selected.

High-rain errors occur when the WO estimate is selected because the SWR rain rate is high. To identify areas where these types of estimator selection errors are likely, a filtered field of wind estimates can be formed.

Wiener filtering produces estimates which optimally minimize the mean-square error given a field of noisy estimates and the autocorrelation function of the signal [93]. Wiener-filtered signal estimates can reduce noise and help identify areas where it is likely that the estimator selections are incorrect.

The optimal filter coefficients for noisy observations are given by the Wiener-Hopf equations as

$$[\mathbf{R}_x + \sigma_v^2 \mathbf{I}] \mathbf{w} = \mathbf{r}_x, \quad (7.9)$$

where  $\mathbf{R}_x$  is a Hermitian Toeplitz matrix of autocorrelation values for the desired signal,  $\sigma_v^2$  is the variance of the noise,  $\mathbf{w}$  are the optimal filter weights, and  $\mathbf{r}_x$  is a vector of autocorrelation values [93]. Although Wiener filters are typically defined for vectors, they can be extended to two-dimensional spatial filtering.

Since the autocorrelation is known for both wind and rain, the optimal filter coefficients can be determined using the Wiener-Hopf equations. The noise power,  $\sigma_v^2$ , for wind and rain can be approximated as the mean-squared-error of the wind and rain estimates over a large dataset. For this study, the mean-squared wind and rain error is the error between the ideal estimator selections and the NCEP winds and TRMM PR measured rains. The mean-squared error is calculated from a data set of 17 million co-located TRMM PR and QuikSCAT observations from 1999 and 2000. For this dataset the mean-squared wind error is  $7.83 \text{ (m/s)}^2$  and the mean-squared rain error is  $73.3 \text{ (km-mm/hr)}^2$ , indicating that

the best-case wind estimates have a standard deviation of 2.79 m/s and the best-case rain estimates have a standard deviation of 8.56 km-mm/hr.

Equation 7.9 assumes that the noise is uncorrelated. For UHR QuikSCAT data the observation noise is correlated between WVCs due to the resolution enhancement. Further, the noise is also a function of the QuikSCAT swath location. The spatial correlation of the noise is due to the nature of the overlapping slice measurements used in resolution enhancement. While the resolution enhancement causes correlation of the noise realizations, the extent of the correlation is limited by the spatial extent of the slice spatial response function. The noise is thus only correlated for a maximum extent of 30 km using UHR resolution enhancement. Since the noise level of the estimates is quite high, the spatial correlation of the noise does not have a strong effect on the optimal Wiener filter. We thus treat the noise realizations as uncorrelated.

The Wiener filter coefficients give the minimum-squared-error wind and rain given the observations over a region. The Wiener filtered wind and rain fields form smoothed wind and rain fields with reduced noise. The smoothed estimates of the wind and rain fields are useful in identifying and correcting missed rain selections. Missed rain selections occur as two types of errors, WO selections when the SWR estimate should be selected, and RO selections when the RO estimate should be selected. Each type of error is sufficiently different that they must be treated separately.

For WO selections when the SWR estimate is best, the selection errors are recognizable as holes, or gaps in larger rain events. These errors can be identified by filtering the selected wind and rain fields. If the Wiener-smoothed rain is greater than 1 km-mm/hr and the SWR error is less than the WO error then the WVC is classified as a missed SWR selection. Typically the missed SWR selections occur for low rain rates, where the WO and SWR estimates are similar. For these conditions selecting the SWR estimate instead of the WO estimate has a small impact on the overall estimate error. Although the error may only change a small amount, without correcting for the selection error significant rain events may be classified as non-raining conditions.

WO estimator selections that should be RO selections can be corrected in a second step. RO missed selections often occur for moderate to high rain rates when the SWR

estimator does not produce a wind and rain estimate. For raining conditions, this condition often implies that the RO estimate is likely the better solution than the WO estimate. These errors can be identified as areas where the smoothed rain estimates are high enough to warrant an estimate of the rain despite the smoothed wind speed. Unlike the missed SWR selections, exchanging WO and RO estimates can change the overall estimation error drastically. Thus the RO estimate should only be used when the rain rate is high enough that the wind backscatter signal is entirely lost. WVCs for which the rain rate is sufficient to mask the wind signal can be identified using the Wiener-smoothed wind and rain fields. The rain rates which are high enough to mask the wind signal are those for which the estimator likelihood function for the SWR or RO estimator is greater than 0.5. This indicates that smoothed rain in the WVC is large enough to obscure the wind signal entirely and the RO estimate is likely to be a more appropriate estimator than the WO estimate.

#### **7.4.2 Consistency Check**

The second objective for estimator selection noise reduction is to produce spatially consistent wind and rain fields. This is particularly important for areas with high wind speeds where incorrect selections of SWR or RO estimates are common. For these cases the poor selections can be identified since the rain events do not have a physically consistent structure, as indicated by the known rain spatial correlation. To correct this type of spatial inconsistency, the noise-corrected wind and rain estimates from the previous subsection can be smoothed again using the Wiener filters for wind and rain. Then the estimators which have minimum squared-error with the smoothed wind and rain fields are selected as the correct estimates. This step can change the estimator selections dramatically if the smoothing is performed on too wide a scale. To minimize over-smoothing while maintaining consistency, the smoothing filters are limited to an extent of 25 km for this step.

The estimator selection noise reduction process is not intended to change a lot of the estimator selections made using Bayes estimator selection and prior selection. Rather, the noise reduction steps are designed to reduce small scale selection errors, remove artifacts in the estimator selections due to prior selection, and to increase the spatial consistency of the wind and rain estimate fields. The changes in the selected estimator using noise reduction

after prior selection result in small changes in the overall probability of correct estimator selection, but they can be significant changes in terms of the overall estimation error.

Although the steps taken during noise reduction are somewhat ad-hoc in nature, when used in conjunction with prior selection they improve the overall estimator selection performance and aid interpretation of the estimator selections as a viable rain-impact flag. The improvements in estimator selection and rain-flagging performance are quantified in the following Section.

## **7.5 Results**

To evaluate performance of prior selection and noise reduction on QuikSCAT wind and rain estimates this Section considers a case study and average results over a large dataset. This Chapter uses numerically modeled wind estimates produced by the National Center for Environmental Prediction (NCEP) and rain measurements made by the Tropical Rain Measuring Mission Precipitation Radar (TRMM PR). The NCEP winds used in this study are treated as a truth dataset but are in reality only an approximation to the true wind field. Although the NCEP winds may not model small-scale variations in the wind field, they are accurate on a global scale. TRMM PR rain measurements are very reliable and are an ideal comparison dataset for rain validation. There are some differences in the TRMM PR and QuikSCAT observation geometry and sampling pattern which must be accounted for in order to compare TRMM PR and QuikSCAT rains as in Chapter 3.

### **7.5.1 Case Study**

Bayes estimator selection functions well when the observed wind is well represented by the wind and rain prior employed. If the observed wind changes rapidly over a short region, such as at weather fronts or in severe storms, a single prior cannot be appropriate. Although prior selection performs well under all conditions, the advantages of adopting prior selection are most obvious when the observed wind field consists of multiple wind distributions. To demonstrate the advantages of Bayes estimator selection with prior selection, we consider a case study of QuikSCAT rev 10362 from June 15, 2001.

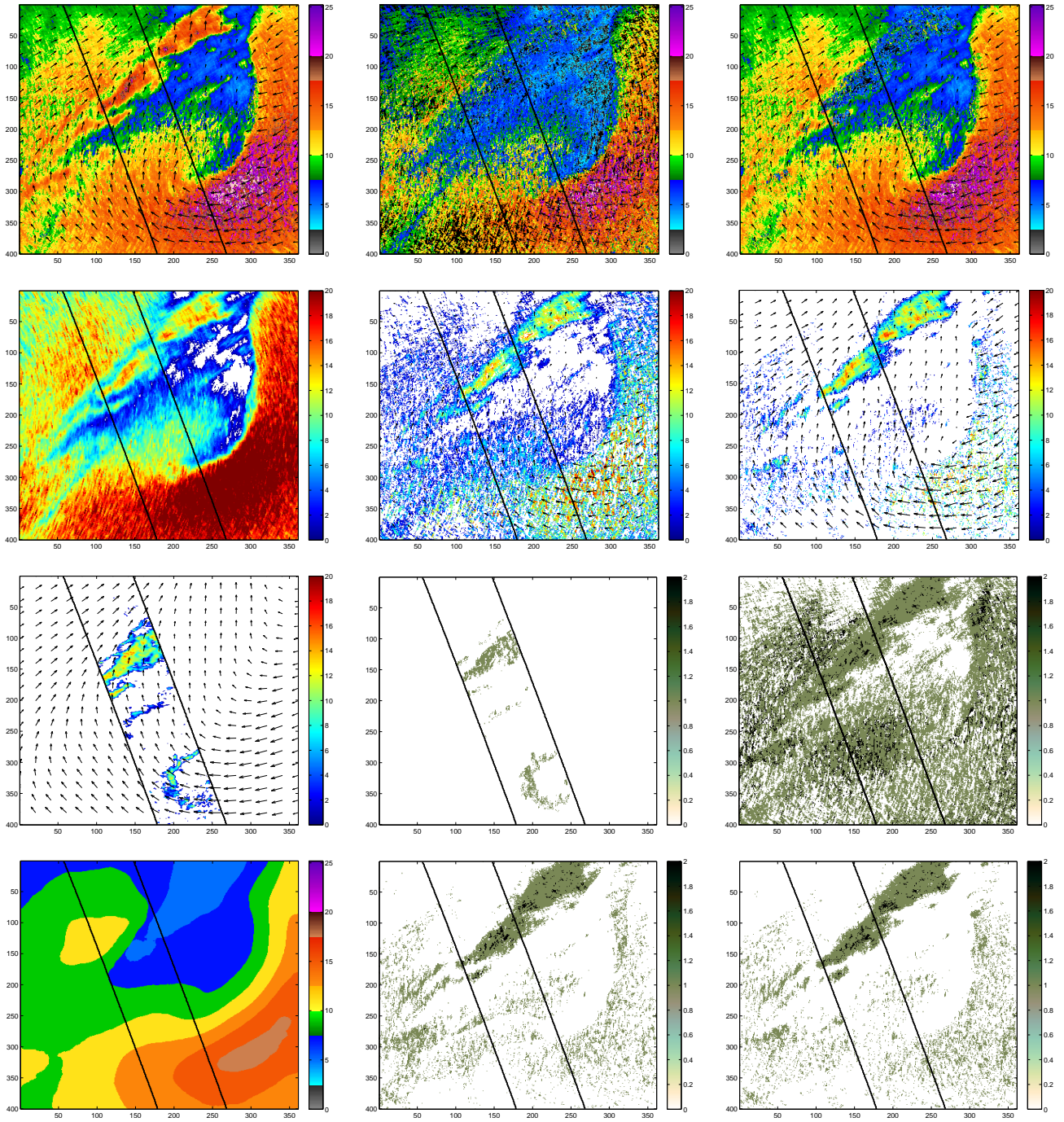


**Figure 7.4:** (Previous page) Estimator results and Bayes estimator selection for QuikSCAT rev 10362, Jun. 15, 2001. Each sub-image corresponds to the same wind and rain field where the x and y axes indicate the QuikSCAT along-track and cross-track dimensions respectively. The top row shows wind speed estimates (m/s) with overlaid direction vectors. From left to right: wind-only, simultaneous wind-rain, Bayes selected wind. The second row shows rain estimates (dB km-mm/hr) with relevant direction vectors overlaid. From left to right: rain-only, simultaneous wind-rain, Bayes selected rain. For comparison, the third row shows the TRMM PR measured rain (dB km-mm/hr) with the model wind vector field overlaid (left), the ideal estimator selections (center) and the Bayes estimator selections without prior selection (right). The bottom row shows the mean wind speed (m/s) for the selected prior (left), the estimator selections made with prior selection (center) and the estimator selections made with prior selection and noise reduction (right). In each image the x-axis shows QuikSCAT along-track range and the y-axis represents cross-track range. For estimator selection fields (lower 2 images in the right two columns), the white WVCs (value of 0) corresponds to a wind-only selection, the gray/green WVCs (value of 1) to a simultaneous wind-rain selection, and the black WVCs (value of 2) to a rain-only selection. Note that the Bayes selected estimates (upper 2 images in the right column) have less noise than the SWR estimates and have smooth wind fields in non-raining cases. Additionally, the Bayes estimator selections after prior selection and noise reduction (lower right image) and the ideal selections (middle of 3rd row) identify similar rain structures, and the selections are identical for 87.1% of the WVCs.

The QuikSCAT wind and rain estimates are shown in Fig. 7.4 in addition to TRMM PR measured rains, estimator selections, and prior selections. The top portion of the wind and rain field has several rain events which cause rain contamination of moderate winds shown as a diagonal band of high wind speeds from the left-center to the top-middle part of the figures. The right and bottom portions of the wind field have high wind speeds which are separated by a front from the rest of the image.

The WO wind estimates (shown in the upper left of Fig. 7.4) near the top of the wind field are contaminated by the rain events causing spurious high wind speed estimates. Near the bottom of the wind field, where there is no rain contamination of the winds, the WO estimates are very accurate.

The SWR wind estimates (upper central image in Fig. 7.4) are generally lower than the corresponding WO estimates. In the raining conditions, SWR wind and rain estimates are quite reasonable. However, in the high wind speed portion, the SWR speeds underestimate the wind and the SWR rain estimates are too high. Selecting the SWR estimate in the high speed region would thus be detrimental to overall performance.

Although the RO rain estimates are reasonable in the raining parts of the rain field, the RO rain estimates should not be used in the rain-free high wind speed area. Despite the fact that there is little or no rain in the high wind speed portion the RO rain estimates are extremely high.

Given the observed performance of the individual estimators for this case study, the ideal estimator selection (shown in Fig. 7.4) is to use the WO estimates for the rain-free cases and the high-speed cases. For the raining areas the SWR or RO estimates should be used.

Bayes estimator selection using the global prior, a mean speed of 7 m/s, for this case correctly identifies the raining areas in the moderate wind speeds. Unfortunately, for the high wind speed region, Bayes estimator selection with the global prior falsely identifies rain events and incorrectly selects the SWR and RO estimators. This is not surprising since the global prior does not model the high speed region well. Using Bayes estimator selection with the global prior the percentage of correct estimator selections for this case is 66.9%.

Prior selection together with Bayes estimator selection reduces the incorrect estimator selections in the high speed region while maintaining correct selection in the rainy portions. Note that the mean wind speed of the selected priors resemble those of the wind estimates, albeit biased slight lower. The corresponding Bayes estimator selections with prior selection identify the raining regions while significantly reducing the incorrect estimator selections associated with the high wind speed area. Although prior selection greatly reduces the number of incorrect selections in the high speed region, it contains some selection artifacts attributable to the number of candidate priors. Prior selection improves the percentage of correct estimator selections to 85.6%.

Noise reduction of the combined Bayes estimator selections and prior selections reduces the noise due to incorrect selections while improving the spatial consistency of the selected wind and rain fields. Although there are still some incorrect estimator selections in the region, noise reduction increases the percentage of correct estimator selections to 87.1%. Noise reduction does not make a large overall improvement in the percentage of correct estimator selections. By design, noise reduction only makes small changes which increase overall

**Table 7.2:** Probability of wind and rain vectors occurring which have estimator selection performance in the indicated ranges

Probability of optimal selection range	without PS	PS	PS and NR
0 - 25%	0.8%	0.2%	0.2%
25% - 50%	10.4%	0.9%	1.0%
50% - 75%	28.2%	8.1%	7.1%
75% - 100%	60.6%	90.7%	91.7%

spatial consistency. These changes are most important and effective in very high speed and rain cases which occur rarely in either a case study or a global dataset.

For this case study we can see that prior selection and noise reduction increase the probability of optimal estimator selection substantially compared to conventional BES. This reduces the frequency of both false and missed rain selections while simultaneously improving the selected wind and rain fields substantially. Although this case study was selected to highlight the improvements which are possible when using prior selection and noise reduction, the performance increase can be also observed over much larger data sets which have a wide variety of wind conditions.

### 7.5.2 Overall Performance

To evaluate the overall performance of the prior selection technique, two separate comparisons are made: 1) How well do prior selection and noise reduction approach optimal estimator selection? and 2) How do the selections affect the accuracy of the selected wind and rain estimates? The first question can be answered by evaluating the estimator selections and the second by evaluating the selected estimates. These evaluations are performed on a dataset of one year of QuikSCAT and TRMM PR co-located observations which contains 11.2 million 2.5 km WVCs.

#### Estimator Selection Accuracy

The performance of estimator selection varies as a function of the true conditions whether prior selection and noise reduction are incorporated or not. Fig. 7.5 shows the

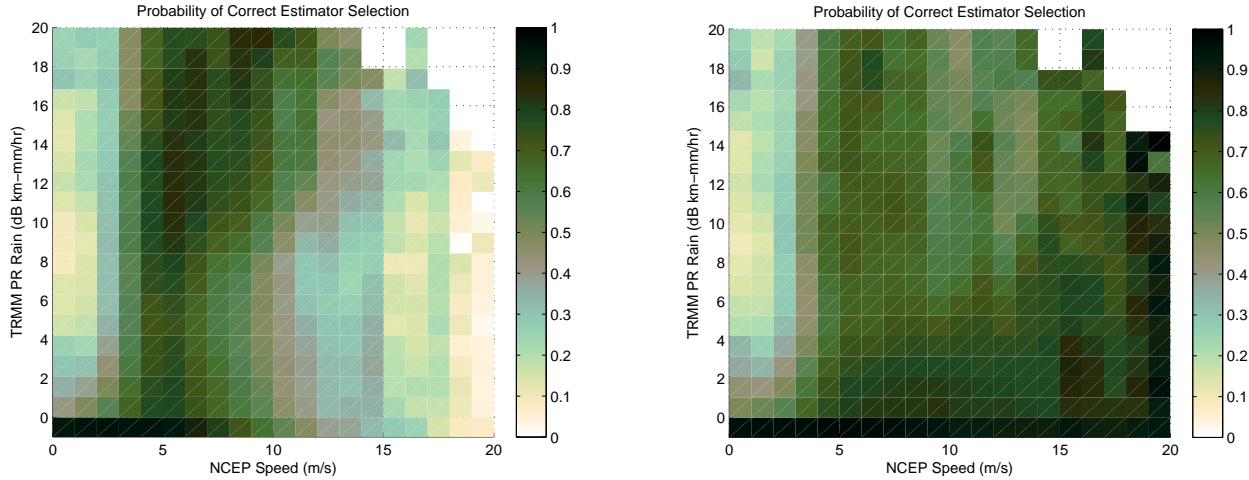


**Figure 7.5:** Probability of optimal estimator selection for UHR wind estimates as a function of NCEP wind speed and TRMM PR measured rain rate. Left: Bayes estimator selection using a single wind-rain prior. Right: Results using prior selection and noise reduction. Although using prior selection slightly reduces the probability of optimal estimator selection for low speeds and moderate to high rain rates, it increases the probability of optimal selection for moderate to high winds for all rain rates.

probability of optimal estimator selection for Bayes estimator selection with and without prior selection and noise reduction as a function of NCEP wind speeds and TRMM PR measured rain rates. Optimal estimator selections are those which have minimum total squared-error where NCEP winds and TRMM PR rains are used as truth data. When prior selection is not used the probability of optimal estimator selection is high for wind speeds close to 5 m/s. For moderate and high wind speeds, however, the estimator selection performance is low if prior selection is not used. Although the addition of prior selection and noise reduction reduces the probability of optimal selection for some low to moderate speed cases, the majority of the time it significantly increases the probability of optimal estimator selection. For moderate and high wind speeds the increase in the probability of optimal estimator selection due to prior selection and noise reduction can be as much as 90%.

The improvements in the probability of optimal estimator selection incurred by adopting prior selection and noise reduction are summarized in Table 7.2 for the one year dataset. Without prior selection, the probability of a wind and rain vector occurring for which the probability of optimal selection is below 75% is 39.4%, with prior selection it is reduced

**Table 7.3:** Overall probability of optimal estimator selection for 1 year of co-located data

Method	Probability of optimal selection
Without PS	77.2%
PS	90.5%
PS and NR	92.5%

to 9.2%, and with noise reduction it is reduced to 8.3%. Additionally, although Table 7.2 indicates that there are wind and rain vectors for which the probability of optimal estimator selection is below 25%, these wind and rain vectors only occur 0.2% of the time when prior selection and noise reduction are used.

The overall improvements in the probability of optimal estimator selection are shown in Table 7.3. Adopting prior selection increase the probability of optimal estimator selection by 13.3% and using noise reduction increases the probability by an additional 2%. Thus while BES alone only made the correct selection 77.2% of the time, BES with prior selection and noise reduction makes the correct estimator selection 92.5% of the time.

### Accuracy of Selected Estimates

To evaluate how estimator selection affects the overall estimation accuracy we first define the concept of rain-impact. For estimator selection we define rain-impact to indicate a rain event which causes sufficient contamination to cause the SWR or RO estimate to have lower squared-error than the WO estimate. Thus for conditions with rain-impact the SWR or RO estimate is the optimal selection; when there is no rain-impact the WO estimate is the optimal selection. Bayes estimator selection with prior selection and noise reduction (BES-PS) is used to evaluate overall results in the following.

Without adopting BES or BES-PS there are essentially two alternatives for wind and rain estimation. Choose to use the WO estimates and discard rain-impacted winds, or reduce the effects of rain-impact by choosing to use the SWR estimates and live with degraded wind performance in non-raining cases. As an improved alternative, BES-PS attempts to make the optimal selections, to choose the SWR estimates when there is rain-impact and to choose the WO estimates for cases without rain-impact.

Although BES-PS is constructed to perform as close to optimally as possible, the method does not always make the optimal estimator selection. The effects of non-optimal estimator selections can be illustrated by analyzing the wind estimates in cases with and without rain-impact. Figure 7.6 shows the scatter density of the wind estimates as a function of the NCEP model wind speed. The mean estimated wind speed and standard deviation is also plotted for reference in each image. For the cases with rain-impact BES-PS works to have the same performance as the SWR estimates, which have optimal performance during rain-impact. For cases without rain-impact BES-PS works to have the same performance as the WO estimates. For the optimal estimates, with and without rain-impact, the bias between the NCEP and QuikSCAT speeds is quite low and the standard deviations are relatively small.

For rain-impact conditions, although the bias and standard deviations are not as low as the optimal SWR estimates, the wind estimates from BES and prior selection have reduced bias and variability when compared with the corresponding WO estimates. Similarly for conditions without rain-impact, the BES-PS wind estimates have nearly identical performance to the WO estimates which is much improved over the corresponding SWR estimates.

The overall wind speed root mean-squared (RMS) error and bias is shown in Tables 7.4 and 7.5 for the WO, SWR and BES-PS, speed estimates for cases with and without rain-impact. For cases free of rain-impact, the BES-PS have lower RMS error than the WO or SWR estimates but the estimates are slightly more biased than the WO speed estimates. For cases with rain-impact the BES-PS RMS error is substantially lower than the WO estimates and somewhat greater than the SWR estimates. The BES-PS wind speed bias for rain-impact cases is again somewhat greater than the SWR estimates but substantially lower than the WO estimates.

An advantage of BES with prior selection and noise reduction is that it does not need a separate rain-impact indicator. In fact the advantages of BES with prior selection are clear without differentiating between cases with and without rain-impact. The overall RMS error and bias for the entire dataset are also shown in Tables 7.4 and 7.5 for the WO, SWR and BES with prior selection wind speed estimates. The overall RMS error and bias for BES-PS

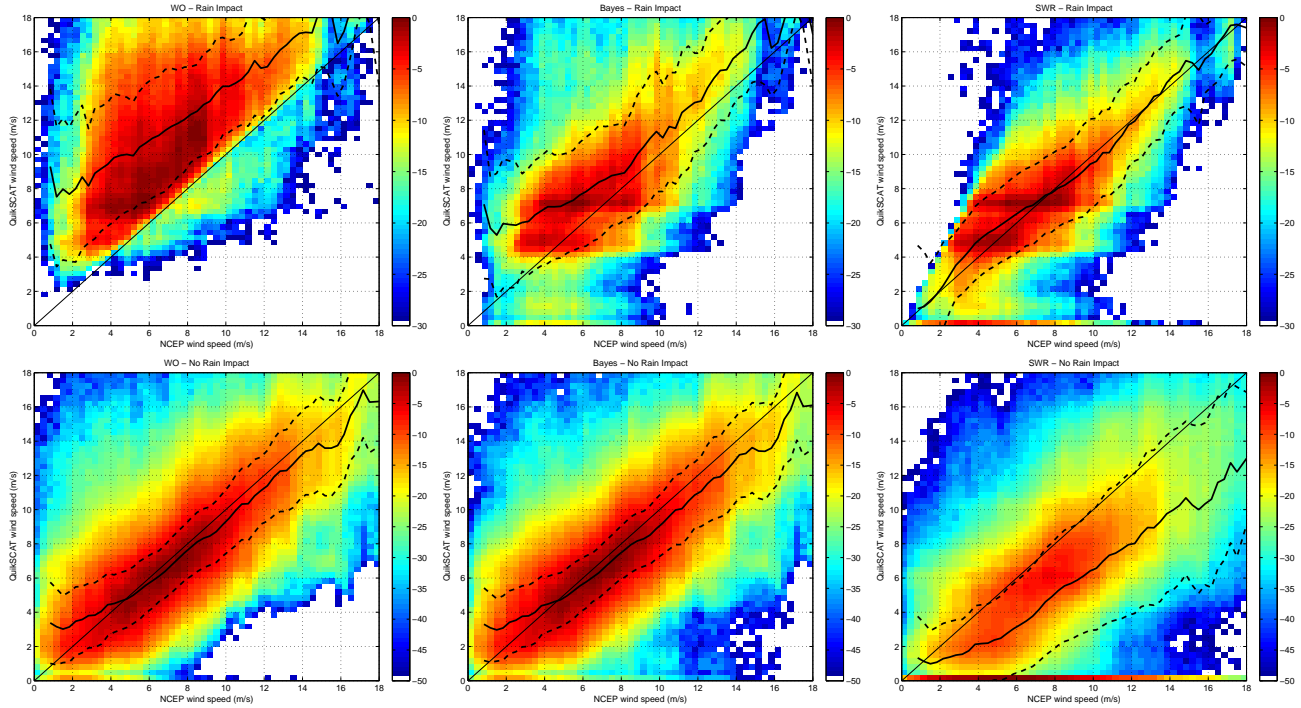


**Figure 7.6:** Scatter densities (in dB) for NCEP and QuikSCAT wind estimates for the one year dataset separated into during rain (top row), and rain-free (bottom row) conditions. From left to right the columns show the WO estimates, the Bayes selected estimates, and the SWR estimates. Each figure also includes the mean of the QuikSCAT estimates (solid black line) plus and minus one standard deviation (dashed black lines). Note that the Bayes selected estimates (middle column) have significantly reduced the wind bias compared to the WO estimates in rain cases for all but the lowest wind speeds and have little bias in cases without rain-impact. Ideally the Bayes estimates (center column) have the same performance as the WO estimator in rain-free conditions (bottom-left), and the same performance as SWR in conditions with rain (top-right). Discrepancies between the Bayes performance and the ideal performance with and without rain are due to non-optimal estimator selection.

are smaller than both the WO and SWR indicating that the BES-PS has performance which surpasses the individual estimators. The fact that the BES-PS RMS error and bias are lower overall than both the WO and SWR estimates indicates that BES-PS yields improved overall wind and rain estimates in both raining and rain-free conditions.

## 7.6 Summary

BES-PS increases the overall accuracy of the wind estimates in addition to providing estimates of the rain during significant rain events. While BES is a useful tool, the addi-

**Table 7.4:** Wind speed RMS error for one year dataset

	WO	BES-PS	SWR
Rain	5.66 m/s	3.71 m/s	2.36 m/s
Rain-free	1.91 m/s	1.88 m/s	4.21 m/s
Overall	2.51 m/s	2.15 m/s	4.14 m/s

**Table 7.5:** Wind speed bias for one year dataset

	WO	BES-PS	SWR
Rain	4.57 m/s	1.67 m/s	0.24 m/s
Rain-free	-0.21 m/s	-0.34 m/s	-2.80 m/s
Overall	0.19 m/s	-0.16 m/s	-2.55 m/s

tion of prior selection generalizes the technique to a much wider variety of wind conditions and substantially improves the estimator selection performance. The improved estimator selection performance indicates that BES-PS approaches optimal estimator selection. This indicates that QuikSCAT is capable of accurately estimating the wind, the wind and rain, or the rain depending on the specific conditions without additional sources of information. The resulting global wind and rain dataset can be used in a wide variety of applications which range from small-scale studies of tropical cyclones and other storms to global climate studies.

## Chapter 8

### Land-Contamination Mitigation

Chapters 3 to 7 have discussed mitigation of rain-contamination effects on scatterometer observations. This Chapter deals with mitigating contamination of backscatter observations which occur due to measurement proximity to land [94]. Unlike rain contamination, which occurs in widely variable locations and intensities, land contamination occurs due to fixed land masses. Additionally, land contamination cannot be modeled phenomenologically the way rain contamination has been. These fundamental differences require that land contamination be treated in a very different way.

Coastal winds are of particular interest due to their large economic and societal impact. Because the radar backscatter from land is much brighter than ocean backscatter for most cases, there is significant contamination of the backscatter measurements, termed  $\sigma^o$ , near the coast due to antenna sidelobes. To facilitate accurate wind retrieval, land-contaminated  $\sigma^o$  measurements must be identified and disregarded during wind retrieval. Previous methods identified all measurements with 3 dB contours within 30 km of the coast and discarded them. This Chapter proposes an improved method to quantify the impact of land contamination and discard only contaminated measurements which degrade wind estimation thereby improving near-coastal wind estimate coverage and accuracy.

In this chapter, after a brief overview of relevant QuikSCAT details, we evaluate two metrics for the detection of land contaminated  $\sigma^o$  measurements: minimum distance to land (MDL) and land contribution ratio (LCR). After comparing each metric, we generate threshold levels for use in wind retrieval using the LCR. Finally, conventional (25 km) and ultra-high-resolution (UHR) (2.5 km)[95] wind retrieval is performed using the LCR as the land contamination metric for an illustrative region. We find that wind retrieval using the

LCR effectively removes land contamination and allows wind retrieval up to 25 km closer to the coast than previously possible.

Section 8.1 gives an overview of relevant information on the Seawinds scatterometer, Section 8.2 introduces and evaluates each land contamination metric, Section 8.3 discusses the creation of the LCR threshold look-up table, and Section 8.4 compares wind retrieval results with and without LCR threshold processing.

## 8.1 QuikSCAT Overview

QuikSCAT uses on-board range and Doppler processors, the backscatter value for each microwave pulse is separated into 12 separate regions. These regions are termed slices [50], each of which has a separate  $\sigma^o$  value. Only 8 to 10 of the slices are used in processing as the others have higher error and noise levels. The spatial response for each slice is known separately and the individual response patterns are typically represented using the 3dB contour for each response during resolution enhancement [96]. The 3dB contours are roughly rectangular or oval with approximate dimensions of 30x7 km where the longer dimension is termed the major axis and the shorter the minor axis [53]. Figure 8.1 shows a contour plot of an example response function for a single slice with color contours spaced every 3dB.

A recently developed resolution enhancement algorithm [54] uses the  $\sigma^o$  value and the 3dB contour for each slice [96]. This resolution enhancement algorithm was originally designed to use multiple passes of data to generate a higher resolution  $\sigma^o$  field for each polarization and look (vertical, horizontal, fore and aft). Multiple passes are inappropriate for wind retrieval due to the change in winds over time so in this study we use the AVE algorithm [52]. The AVE algorithm is a single pass form of the resolution enhancement algorithm which creates high-resolution  $\sigma^o$  fields prior to wind retrieval.

Figure 8.2 shows the high-resolution  $\sigma^o$  fields produced by the AVE algorithm for vertically polarized forward and aft looking measurements and the corresponding 3dB contours. Land contamination of the  $\sigma^o$  values is visually apparent in the way that the higher land  $\sigma^o$  values spread away from the coastline. It is interesting to note that when the major axis is perpendicular to the coastline the land contamination appears to reach further into the ocean than when the major axis is parallel to the coastline.

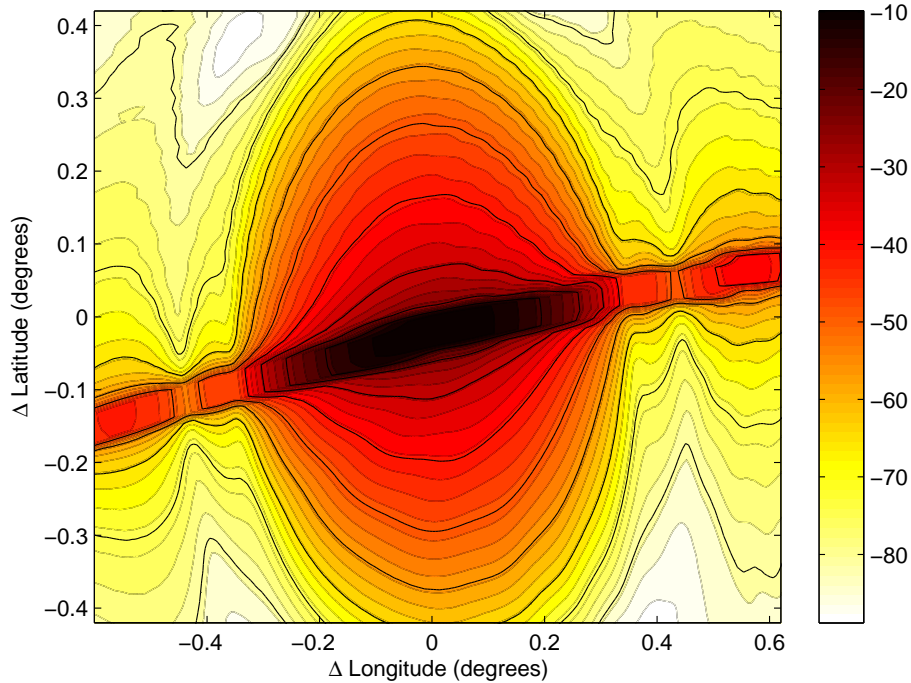


**Figure 8.1:** Contours of the Seawinds response function for a vertically polarized slice spaced every 10dB. For this slice the minor axis direction is approximately up and down and the major axis direction is perpendicular. The background color contours are spaced every 3dB. Note that the spatial response initially falls much faster in the minor-axis direction.

Land contamination of  $\sigma^o$  measurements directly affects wind retrieval, which is the process of inferring the surface wind vector directly from the backscatter fields produced by the AVE algorithm. Wind retrieval is performed using a geophysical model function (GMF) which maps  $\sigma^o$  measurements to wind vectors [12]. The GMF returns multiple possible wind vectors, known as ambiguities [28], for each wind vector cell (WVC). Greater wind speeds are associated through the GMF with higher backscatter values. Land-contaminated  $\sigma^o$  values are typically much higher than ocean  $\sigma^o$  values [97] and so appear as high wind speeds. When land-contaminated  $\sigma^o$  values are used in wind retrieval, the speeds retrieved using the GMF are as much as 20m/s higher than the true wind speed.

Once excessively land contaminated  $\sigma^o$  are identified and discarded, wind retrieval from valid  $\sigma^o$  values can be done at either conventional or high-resolution. This results in

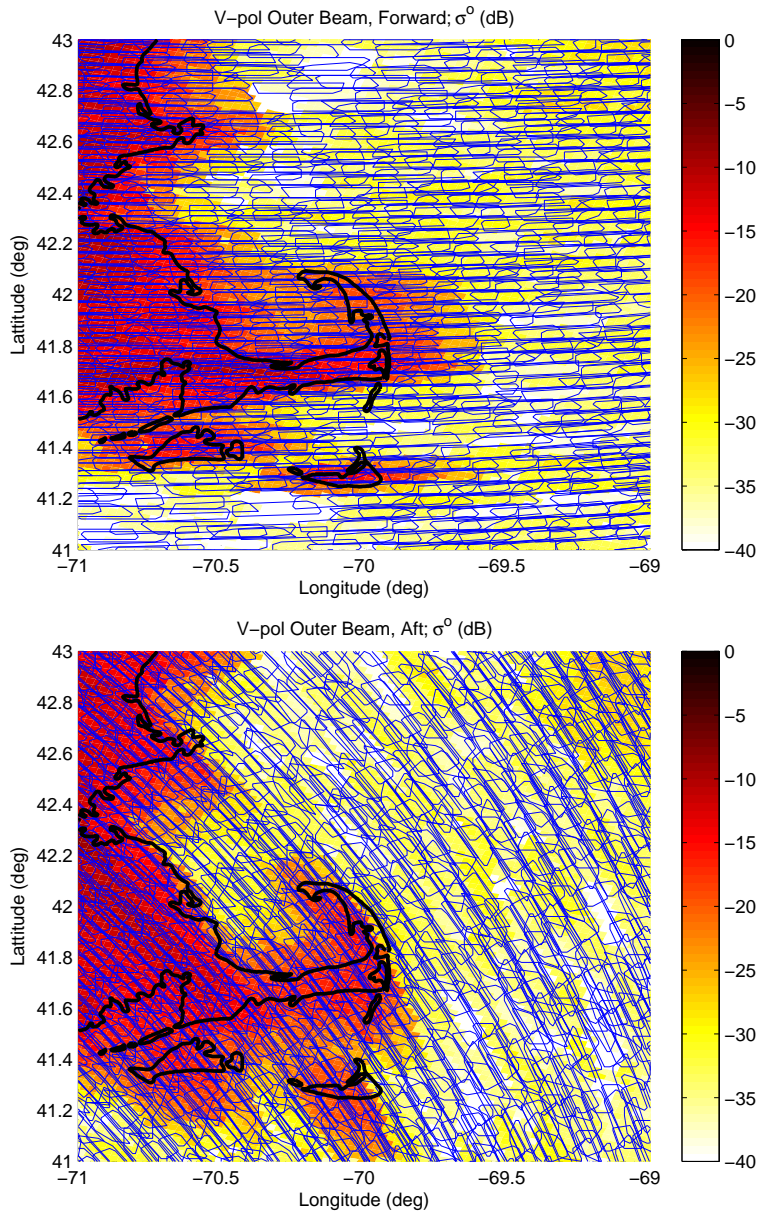


**Figure 8.2:** Cape Cod, Massachusetts coastline region overlaid with forward and aft looking vertically-polarized slices and high-resolution  $\sigma^o$  in dB.  $\sigma^o$  values for land in this region are about  $-10\text{dB} \pm 5\text{dB}$ , and ocean values are between  $-50$  and  $-25$  dB.  $\sigma^o$  values above  $-25\text{dB}$  and below  $-15\text{dB}$  are almost certainly land contaminated. Note particularly that the land contamination spreads away from land most significantly in the same general direction as the major axis of the slices i.e. East-West in the top figure and nearly North-South in the bottom figure.

uncontaminated wind measurements. To determine which measurements are acceptable and which are intolerably contaminated, the level of contamination must first be assessed.

## 8.2 Contamination Detection Metrics

Each observed  $\sigma^o$  value is the sum of the true  $\sigma^o$  over the footprint and a noise term,

$$\sigma_{Obs}^o = \sigma_{True}^o + \eta_o. \quad (8.1)$$

The true backscatter value ( $\sigma_{True}^o$ ) for any measurement is the integral of the surface  $\sigma^o$  over the spatial response of the antenna [98],

$$\sigma_{True}^o = \frac{\iint_{A_{slice}} \sigma_{x,y}^o R_{x,y} dx dy}{\iint_{A_{slice}} R_{x,y} dx dy}, \quad (8.2)$$

where  $R_{x,y}$  is the spatial response function of the particular slice of interest,  $\sigma^o$  is the surface backscatter value and the bounds of integration are the bounds of the spatial response function.

$\sigma_{True}^o$  can also be written as the sum of the land and ocean backscatter values separately as,

$$\sigma_{True}^o = \sigma_{Land\ Contribution}^o + \sigma_{Ocean\ Contribution}^o \quad (8.3)$$

and in integral form,

$$\sigma_{True}^o = \frac{\iint_{A_{Land}} \sigma_{x,y}^o R_{x,y} dx dy}{\iint_{A_{Slice}} R_{x,y} dx dy} + \frac{\iint_{A_{Ocean}} \sigma_{x,y}^o R_{x,y} dx dy}{\iint_{A_{Slice}} R_{x,y} dx dy}, \quad (8.4)$$

where  $A_{land}$  and  $A_{ocean}$  are the regions of the footprint consisting of land and ocean.

Land contaminated  $\sigma^o$  values are those where  $\sigma_{Land\ Contribution}^o$  adversely affects  $\sigma_{Obs}^o$ , resulting in a large bias in the wind estimate. The level of contamination can be determined using a number of metrics but in this paper we evaluate only two: minimum distance to land and land contribution ratio.

### 8.2.1 Minimum Distance to Land

Outside of the 3 dB contour for any slice, the response pattern drops sharply [50]. When the location of the 3dB contour is greater than a certain distance (typically 30 km) from land, the observed  $\sigma^o$  value is not land contaminated. This relationship between land contamination and the 3dB contour is the basis for the minimum distance to land (MDL) metric. The MDL for each slice is the smallest distance to land from any corner of the 3dB contour.

Variations of the MDL metric include using the distance to land along the major and minor axis of the slice or in any direction from the slice. A variant of the MDL is used in the conventional Jet Propulsion Laboratory (JPL) processing of QuikSCAT data[45].

### 8.2.2 Land Contribution Ratio

A second metric for detecting land contamination is the land contribution ratio (LCR). Rather than using distance to the spatial response 3dB contour like the MDL, the LCR uses the full spatial response for each slice. The spatial response is used to weight the calculation of how much land contributes to a measurement. The LCR for a measurement is the normalized and weighted integral of the land contributing to the backscatter. To calculate the LCR, we assume that  $\sigma^o$  for land is constant. The LCR is then the ratio of  $\sigma_{Land\ Contribution}^o$  normalized by the  $\sigma^o$  of a land-only measurement ( $\sigma_{Land}^o$ ) which can be written as

$$LCR = \frac{\sigma_{Land\ Contribution}^o}{\sigma_{Land}^o} = \frac{\int \int_{A_{land}} R_{x,y} dx dy}{\int \int_{A_{slice}} R_{x,y} dx dy}. \quad (8.5)$$

Rather than using the full continuous response function, in practice we simplify computation by using a close approximation sampled at a 1 km resolution. This simplified computation is performed using

$$LCR = \frac{\sum_{x,y} L_{x,y} R_{x,y}}{\sum_{x,y} R_{x,y}}, \quad (8.6)$$

where  $x$  and  $y$  are in kilometers away from the slice center,  $L_{x,y}$  is the land indicator function consisting of a 1 for land and a 0 for ocean,  $R_{x,y}$  is the antenna response, and LCR is the land contribution ratio. The bounds of summation over  $x$  and  $y$  from the center of the slice can vary depending on the desired accuracy.

### 8.2.3 Metric Comparisons

To effectively evaluate the MDL and LCR metrics, both direct and indirect comparisons are used. Initially, a direct comparison is made of the MDL and the LCR. Afterwards, the metrics are indirectly compared, first by using the correlation between the metric value and  $\sigma^o$ . A further comparison is made of the number of  $\sigma^o$  measurements that each metric indicates are contamination-free for an identical coastal region. Although the indirect comparison data plotted throughout this chapter are limited to one pass over the Aegean Sea ( $38^\circ\text{N} \pm 4^\circ$   $25^\circ\text{E} \pm 5^\circ$ , QuikSCAT rev. 21417), it is representative of other coastal data sets.

To perform a direct comparison between the MDL and LCR metrics, a variant of the MDL is used where instead of using the shortest distance to the coast from the 3dB contour, the metric uses the shortest distance to land from the center of the slice. In the comparison a straight coastline is simulated and the distance to the coast and the orientation of the slice is then varied. The LCR in dB is plotted as a function of distance to land and the angle between the minor axis direction and the coastline in Fig. 8.3.

Figure 8.3 illustrates the rapid falloff of the spatial response function in the minor axis direction. When the minor axis direction is perpendicular to the coast ( $90^\circ$  and  $270^\circ$ ), the LCR is lower than when the major axis is perpendicular to the coastline ( $0^\circ$  and  $180^\circ$ ). The significant variation of the LCR with orientation suggests that the distance to land from the slice center alone is not an adequate predictor of land contamination in near coastal regions. Although there is significant variance in the LCR as a function of direction, as the distance increases to greater than 30 km in any direction, the LCR falls below a level that affects wind retrieval. This level varies as a function of land brightness and wind speed and will be discussed later. LCR values in Fig. 8.3 indicate approximately how the LCR behaves in the

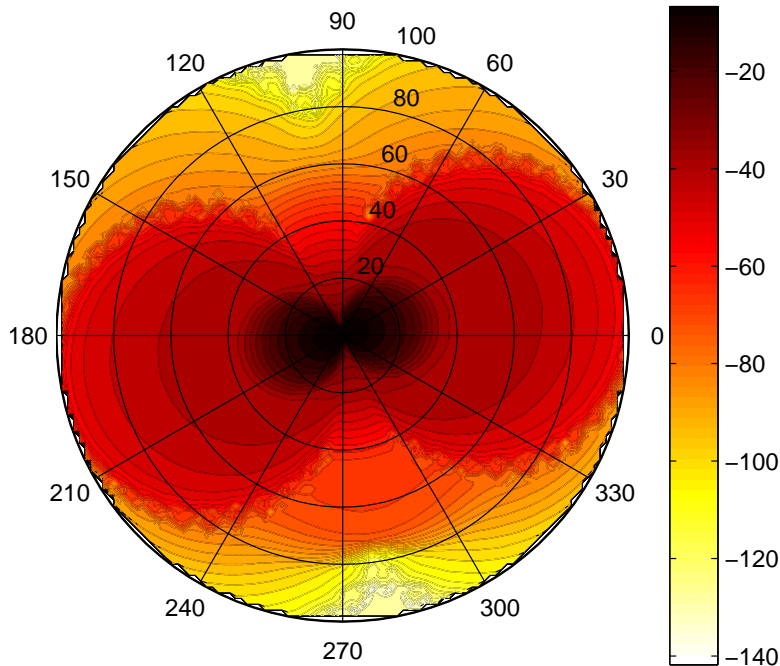


**Figure 8.3:** Contour map of the LCR in dB as a function of the distance in km from the center of the slice to the coastline generated using one slice of the vertical polarization antenna spatial response as plotted in Fig. 8.1. The angles shown refer to the angle between the slice minor axis and the coastline. Note that the LCR has a high directional dependence.

proximity of a straight coastline. We note that in practice coastlines are very rarely straight, so LCR values can be significantly higher or lower for a given distance to the mean coastline.

The results of the direct comparison between the MDL and the LCR shown in Fig. 8.3 provide a general idea of the relation between the two metrics. The direct comparison made between the MDL and LCR metrics is limited, however, because the distance to land from the slice center is used rather than the MDL. To compensate, we compare both metrics to the corresponding  $\sigma^o$  values and then evaluate the results.

A scatter plot of the  $\sigma^o$  value and the MDL for each slice in the test region for the specified orbit is shown in Fig. 8.4(a). One of the principle limitations of the MDL is that slices which overlap or are next to land have low MDL values indicating land contamination, yet some slices are contaminated and some are not. This limitation is particularly apparent in Fig. 8.4(a) where measurement slices with MDL of zero spread from -1dB to -50dB, which includes the range of both land and ocean  $\sigma^o$  rather than just one or the other. In order

for the MDL to be an ideal metric, as the slices approach land there should be a gradual transition from the  $\sigma^o$  of ocean to the  $\sigma^o$  of land. Because there is no such transition in Fig. 8.4(a), it is impossible to quantify the contamination level of slices which lie partially over land.

The corresponding plot of LCR and  $\sigma^o$  is shown in Fig. 8.4(b) for all slices in the region. Note that a smooth rise in backscatter values from the ocean value to the land value is readily apparent. Slices that lie entirely over land have LCR values near 0dB and  $\sigma^o$  values which vary closely around  $\sigma_{Land}^o$  for this region, -10dB. Slices entirely over ocean have LCR values close to -80dB and  $\sigma^o$  values which vary around -30dB, an expected level for ocean with wind speeds below 10m/s. Between insignificant land contribution (LCR values below -30dB) and land (0dB) the backscatter values increase smoothly until they reach  $\sigma_{Land}^o$ .

To quantitatively compare the results shown in Figs. 8.4(a) and 8.4(b), the correlation between the metric and  $\sigma^o$  is used. The correlation of  $\sigma^o$  and the MDL is 44%, while the correlation with  $\sigma^o$  for the LCR is 81% using vertically polarized measurements and 76% using horizontally polarized measurements. The significantly higher correlation between the LCR and  $\sigma^o$  suggests that the LCR offers a more meaningful metric for detecting and removing land contamination. Wind conditions in the study area can have a large effect on the correlation of  $\sigma^o$  with either metric. The data plotted in Figs. 8.4(a) and 8.4(b) are from a calm ocean, which results in a large distinction between land and ocean backscatter.

The indirect comparisons of the MDL and LCR metrics show that the LCR offers better correlation with measured data and a finer transition between land and ocean making the LCR a more suitable metric for land contamination detection. Because the transition between land and ocean using the LCR is less abrupt, it allows for the selection of thresholds for a variety of conditions.

#### 8.2.4 Threshold Detection

An LCR threshold can be used to remove land contamination by discarding any  $\sigma^o$  values with an LCR greater than a given level. Observe that in Fig. 8.4(b) there is a relatively smooth transition of  $\sigma^o$  values as the LCR approaches 0dB. Suppose that an LCR threshold is set at -20dB to remove the section of data where  $\sigma^o$  values start to approach the  $\sigma^o$  of

land. Setting an LCR threshold at -20dB declares all slice measurements below a -20dB LCR to be free of land contamination.

Correspondingly, a threshold using the MDL removes all slices with an MDL below a given level. As an example, an MDL threshold of 20 km indicates that slices in which the MDL is greater than 20 km are not land-contaminated.

We compare the number of slice measurements deemed valid by each method in Fig. 8.4(c) which shows the LCR and MDL for each slice in the region. Setting an LCR threshold at -20dB and discarding all slices with greater contamination levels yields approximately 37036 valid measurements. A conservative comparison of the LCR to the MDL discards all slices that have LCR values above a certain level, and uses the upper MDL value for a given LCR as the smallest MDL allowed. Figure 8.4(c) indicates that the MDL above which all contamination is below a -20dB LCR is around 15 km. A minimum distance threshold of 15 km in this case yields only 31844 valid slice measurements from the same data set. If the MDL is used as a metric to identify and remove land contamination, there will be over 5000 slices discarded in coastal regions that are not significantly contaminated. Using the MDL as the land contamination metric therefore results in larger regions near the coast where no wind can be retrieved.

Figure 8.4(c) indicates that setting a lower MDL threshold allows slices with significant land contamination, as computed by the LCR, to be declared valid. Figure 8.4(c) shows that for the set of slices with a given MDL there is a large range of LCR levels in the set. The worst case land contamination for a fixed MDL is indicated by the largest LCR in the set. For example, a 30 km MDL threshold removes most land contamination but allows up to a -24dB LCR, while a 10 km MDL threshold allows up to a -15dB LCR. A -15dB LCR level indicates relatively high contamination and results in contaminated wind estimates.

### 8.2.5 Metric Choice

We can conclude after comparing both the MDL and LCR land contamination metrics that the LCR is a superior metric for land contamination detection and removal for several reasons. The LCR correlates better with  $\sigma^o$  values as indicated in Fig. 8.4(b). Additionally, the MDL must discard many uncontaminated slice measurements to ensure removal of all

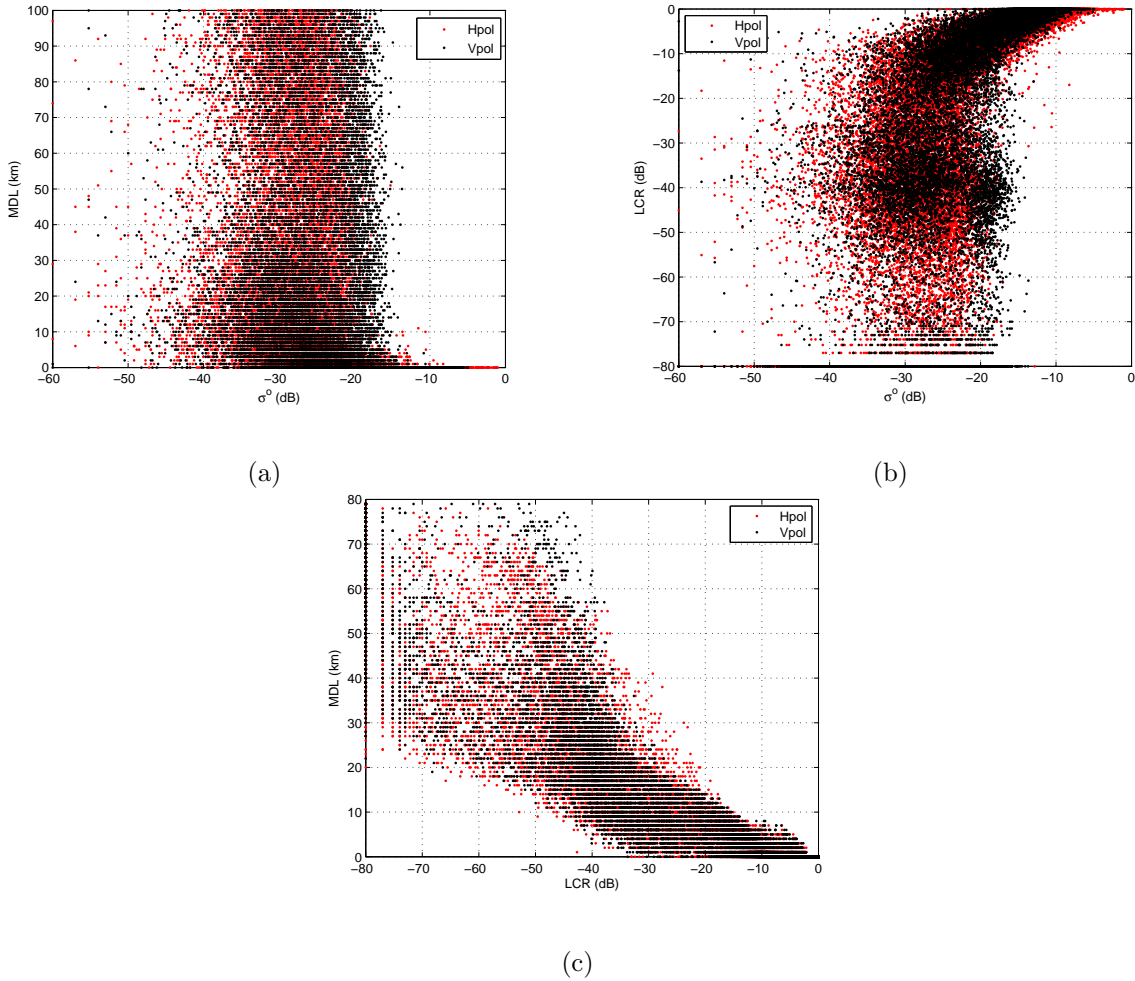


**Figure 8.4:** (a)  $\sigma^o$  versus MDL for V and H polarizations. (Note that since the MDL is in 1 km increments MDL values are quantized to 1 km in the plot.) (b)  $\sigma^o$  versus LCR in dB for vertical and horizontal polarizations. For plotting,  $10^{-8}$  was added to all LCR values so that ocean  $\sigma^o$  values (LCR = 0) can be displayed (c) LCR v. MDL for a calm coastal area.

contamination while the LCR is better able to differentiate between contaminated observations in near coastal regions and thus retains far more slices for wind retrieval as indicated in Fig. 8.4(c). Since the LCR is better correlates with and identifies land contamination it is a more useful metric for land contamination mitigation and is used in the remainder of this chapter.

However, the fixed LCR threshold used in previous examples, is a non-optimal solution to the land contamination problem. To optimally identify land contaminated measurements

in all wind conditions, thresholds must change both temporally and spatially with changes in wind speed and land backscatter levels. As wind speed increases the impact of land contamination is reduced and LCR thresholds increase. Similarly if wind speeds stay the same and land brightness increases then the LCR thresholds decrease as the impact of land on the wind estimates increases.

### 8.3 LCR Threshold Determination

Radar backscatter values over the ocean are a function of antenna azimuth, incidence angle and wind speed. Each factor must be accounted for when setting LCR thresholds. Depending on wind speed, QuikSCAT observed backscatter values over the ocean can be as low as -50dB and as high as -10dB, whereas backscatter values over coastal land regions typically vary between -15dB and -5dB. The large range of ocean backscatter values causes land contamination in near coastal regions to have very different effects depending on the local wind speed. When wind speeds are low, even small levels of land contamination can bias wind retrieval by as much as 20 m/s. When wind speeds are higher, however, a measurement can tolerate much greater land contamination before introducing significant error during wind retrieval. Threshold levels are generated for land contamination detection using the LCR that are based on localized wind speeds, localized land backscatter estimates and the cross-track location of the measurement.

LCR threshold levels can be understood to be the LCR value for a given slice above which land contamination has significant impact on retrieved wind speeds. Below the threshold, any land contamination has negligible impact. Retrieved wind speeds have a non-linear relation to backscatter values and are highly susceptible to error from land contamination. To enable the LCR to be an effective land contamination impact flag, threshold levels are determined via simulation where both non-linear effects and biases are taken into effect.

Ideally, LCR thresholds would be determined by processing the backscatter values from an observed region with a truth wind field. Since appropriate wind data are not readily available, we instead use Monte Carlo simulated backscatter values from simulated wind fields to calculate RMS speed error and choose appropriate LCR thresholds for coastal wind retrieval. As an additional comparison, LCR thresholds are also evaluated in terms of the

Cramer-Rao lower bound (CRB) for land-contaminated wind retrieval. The LCR thresholds from Monte-Carlo simulation are then compared to those generated using the CRB method after which LCR thresholds are applied to a case study.

### 8.3.1 Compass Simulation

Compass simulation is a historically valuable tool in performing Monte Carlo simulations for wind retrieval [78, 74]. To generate accurate and meaningful thresholds for use in wind retrieval, we use compass simulations of land-contaminated winds. Compass simulations use a variety of wind speeds at all compass directions. Compass simulation for land-contaminated winds also varies the land contamination levels. To simplify the simulation problem we use wind fields that are uniform in speed and direction. The QuikSCAT high-resolution wind retrieval algorithm is used in the simulation. To simultaneously gain insights about error levels in land-contaminated regions and to relate land-contaminated wind errors to the average error across the swath, we choose to apply land contamination to the entire simulated wind field.

### 8.3.2 Land Contamination Simulation

Ocean backscatter values,  $\sigma_{Ocean}^o$ , are created for each slice in simulation. We then use Eq. 8.7 to generate simulated land-contaminated backscatter values with multiplicative noise,

$$\sigma_{obs}^o = (\sigma_{Land}^o LCR + \sigma_{Ocean}^o (1 - LCR)) (1 + \eta_0), \quad (8.7)$$

where  $\eta_0$  is zero-mean univariate Gaussian random variable. Both LCR and  $\sigma_{Land}^o$  are constant for each simulation.

Rather than placing land regions in the wind field and calculating the LCR for each slice, the LCR and  $\sigma_{Land}^o$  values are fixed for an entire wind field. Fixed levels are advantageous in that they cause all slice measurements to be uniformly contaminated. Uniform contamination of slice measurements would be otherwise impossible due to the shape of the antenna response pattern and the irregular sampling pattern of the scatterometer. For each

LCR and  $\sigma_{Land}^o$  realization, there are 114,000 total WVCs in each simulated wind field and 1500 WVCs per cross-track index which are used to calculate the land contamination errors.

After generating the land contaminated backscatter measurements from the true wind fields, wind retrieval is performed using the simulated backscatter values and the geophysical model function. To minimize additional errors caused by ambiguity selection, the nearest ambiguity to the simulated wind is chosen in all cases.

### 8.3.3 Simulation Results

After wind retrieval and ambiguity selection, error levels are calculated for each simulated wind field. The RMS wind speed error in m/s is calculated for each cross-track location using the difference between the retrieved and true winds for each wind vector cell in the cross-track direction. RMS wind speed error requirements are defined for 25 km winds in the QuikSCAT mission objectives to be 2 m/s for wind speeds from 2-20 m/s and 10% for wind speeds from 20-30 m/s [45].

The QuikSCAT scatterometer has different instrument skill levels as a function of the cross-track swath location – error levels vary according to the instrument skill. Instrument skill relates mainly to the azimuthal diversity achieved for any cross-track swath location. Cross-track locations near the nadir track and at the far swath have much less azimuthal diversity than do mid-side swath WVCs, so the instrument skill is lower and the cells generally have greater error levels. Figure 8.5 shows the error levels without land contamination for each cross-track bin for each simulated wind speed and illustrates the necessity of different error levels for each cross-track bin due to the instrument skill.

Although excessive levels of land contamination cause errors in the retrieved wind speed, some error is tolerable. Thus for each cross-track index, we choose acceptable RMS error levels that are a percentage of the true wind speed. Choosing acceptable error levels as a function of cross-track index allows any additional error due to land contamination to vary together with instrument skill.

Figure 8.6 is a contour plot of the RMS error in m/s as a function of wind speed and LCR level for one wind direction, one land reflectivity level and one cross-track WVC. The RMS error level contours illustrate how susceptible the wind is to land contamination

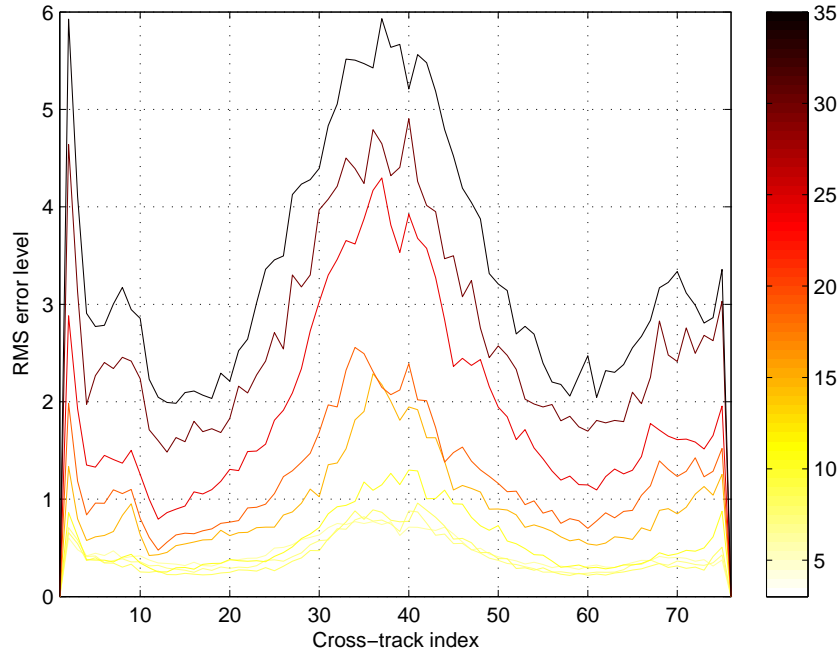


**Figure 8.5:** RMS error levels in m/s as a function of the cross-track WVC for each of the simulated wind speeds in m/s without land contamination. The color scale indicates wind speed. Wind speeds are in ascending order bottom to top. Nadir is at cross-track index 38. The swath edges have non-ideal observation geometry and thus have RMS error similar to the nadir track.

at various wind speeds. For wind speeds above 20m/s, the error levels as a function of land contamination are roughly the same until LCR values reach about -10dB. This effect is due to the fact that for high wind speeds the ocean backscatter can be as high as land, thus the influence of the land backscatter on the measured backscatter is smaller and the wind estimate accuracy is less effected. Lower wind speeds, particularly those below 10m/s, are intolerant of land contamination when LCR values are above -20dB.

Figure 8.7 shows the simulation RMS speed error in m/s as a function of wind speed for each of the simulated directions without land contamination. As expected, error levels for different directions are roughly similar except when winds are near parallel to the along-track direction. Because there is relatively little variation in wind speed error due to wind direction, we choose to eliminate wind direction as a variable in threshold determination.

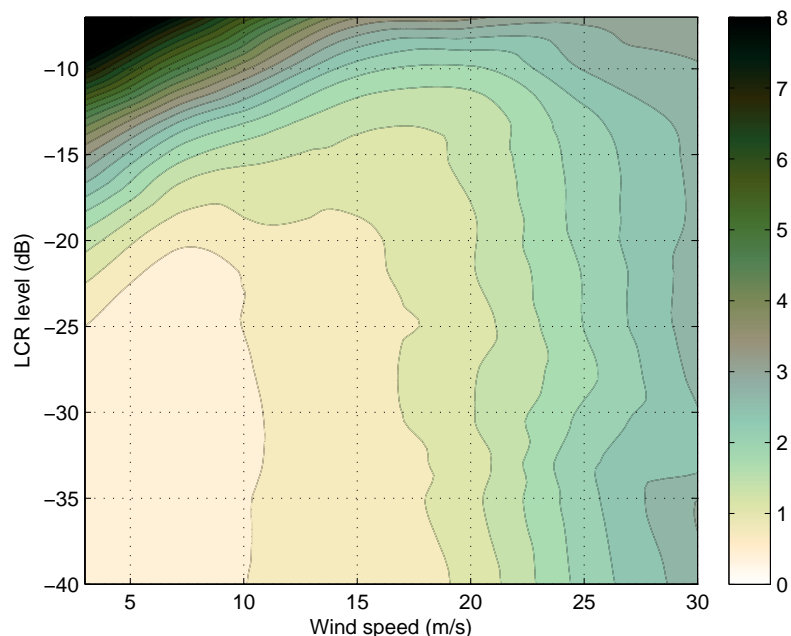


**Figure 8.6:** RMS error contours in m/s from the RMS error surface as a function of the simulated wind speed and the simulated LCR level for a single wind direction and land reflectivity level.

Instead, to determine the LCR thresholds, we choose the worst-case wind direction for each cross-track WVC.

The RMS wind speed error from the simulated wind fields suggest that the dominant variables in determining LCR thresholds are wind speed, cross-track location and land brightness levels. We choose to use these variables simultaneously to choose LCR threshold levels.

Selecting an appropriate LCR threshold for each cross-track location involves several steps. For each cross-track WVC and land reflectivity we first find the wind direction that causes the worst RMS wind speed error without land contamination. Second, using the worst-case wind direction, we determine the RMS wind speed error as a function of wind speed and LCR. Third, we find the maximum LCR value for each wind speed for which the RMS wind speed error is below a percentage of the wind speed. The maximum LCR value becomes the LCR threshold for that wind speed. The percent of the wind speed associated

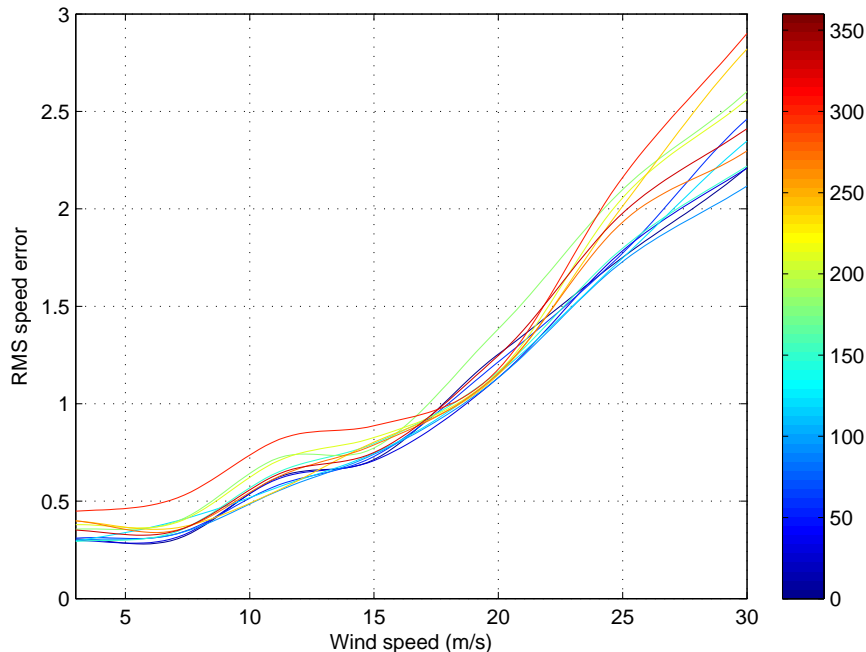


**Figure 8.7:** RMS wind speed error in m/s without land contamination for compass directions spaced every  $30^\circ$  in the central cross-track region (cross-track WVC 27). Error lines with slightly higher error levels correspond to winds in the along track direction. The color scale indicates wind direction.

with the LCR threshold is different for each WVC to reflect the differences in instrument skill across the swath. This percent of the wind speed is the tolerable RMS speed error level for that WVC.

The tolerable RMS speed error level for each cross-track WVC is chosen by finding an error level that is achievable for low wind speeds and sufficiently smooth for high speeds. If the tolerable error level is set too low, the specified error level cannot be met for low wind speeds. For high wind speeds we stipulate that the LCR thresholds resulting from the specified error level must be smooth as wind speed increases.

Figure 8.8 shows the LCR threshold levels resulting from illustrative RMS wind speed errors for 10 to 25% of wind speed for a fixed land reflectivity and cross-track WVC. If error levels are set below 13% of wind speed, it is impossible to meet the criteria for the lowest wind speeds even with relatively little land contamination. Conservative RMS speed error levels can be chosen between 14 and 20% for each WVC. Such conservative RMS speed error

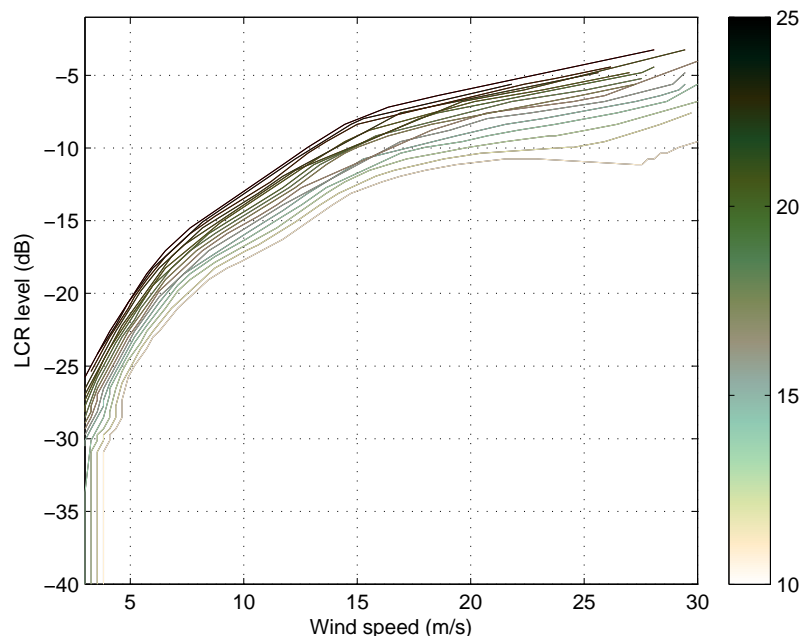


**Figure 8.8:** LCR threshold levels as a function of wind speed for 10% to 25% RMS wind speed error for cross-track WVC 20. Lines are spaced every 1% and the line color indicates the specific RMS speed error level in %. Thresholds for lower error levels are closer to the bottom of the figure.

levels are chosen to effectively maximize the number of retrievable WVCs while maintaining good wind estimation.

After determining the LCR threshold for each cross-track WVC, we observe that the average of the selected error levels for the entire swath is 18%. The average error level of 18% is lower than the QuikSCAT mission specifications for speeds below 10 m/s and slightly higher for wind speeds above 10 m/s.

When the error level from Fig. 8.8 is fixed at 15% of wind speed and land brightness is varied in simulation, Fig. 8.9 shows the necessary LCR thresholds as a function of wind speed for the same cross-track WVC.

As shown in Fig. 8.9, land reflectivity levels effect the LCR threshold levels significantly so it is important to obtain accurate estimates for the land brightness. Practical experience with scatterometer data and land contamination shows that land brightness is quite different for each polarization and look (fore and aft).

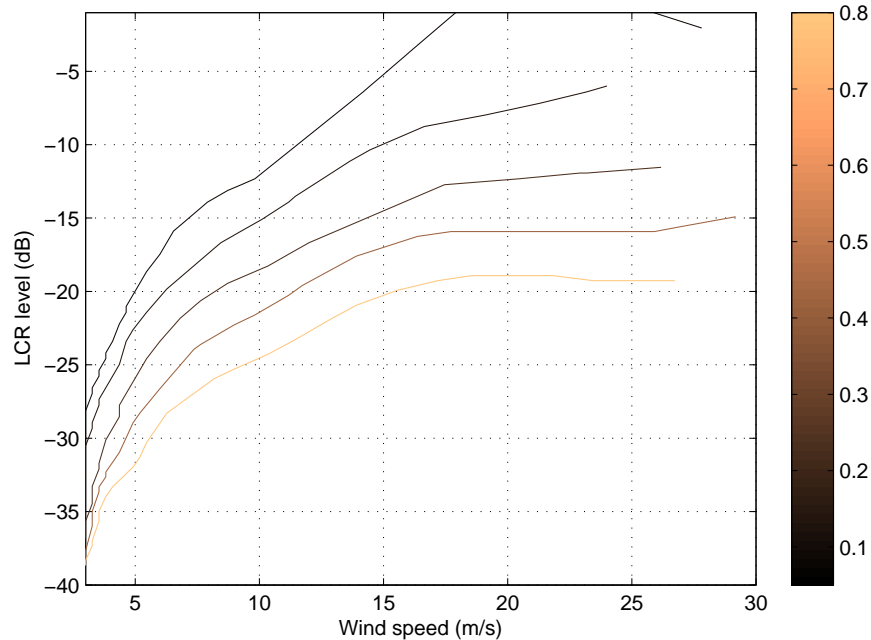


**Figure 8.9:** LCR threshold levels as a function of wind speed for varying land reflectivity levels with 15% RMS wind speed error for cross-track WVC 20. Line color indicates the land reflectivity levels. Thresholds for lower land reflectivity levels are near the top of the figure.

The temporal and spatial variability of land brightness requires land reflectivity estimates that are accurate both temporally and spatially for each polarization and look. The spatial accuracy of the land brightness estimates depends somewhat on the accuracy of the reported slice location and the land map. The QuikSCAT measurement locations have a 2.5 km location accuracy. The land map used to estimate the LCR and land brightness has a 1 km accuracy. The LCR thresholds set in simulation and the mechanisms used to obtain temporal estimates minimize the effects of location errors. The method we use to obtain temporally accurate estimates is explained later.

### 8.3.4 CRB Based LCR Thresholds

An alternative method to generating LCR thresholds is to calculate a bound on the accuracy of land-contaminated wind estimation. Such a bound can be calculated using the

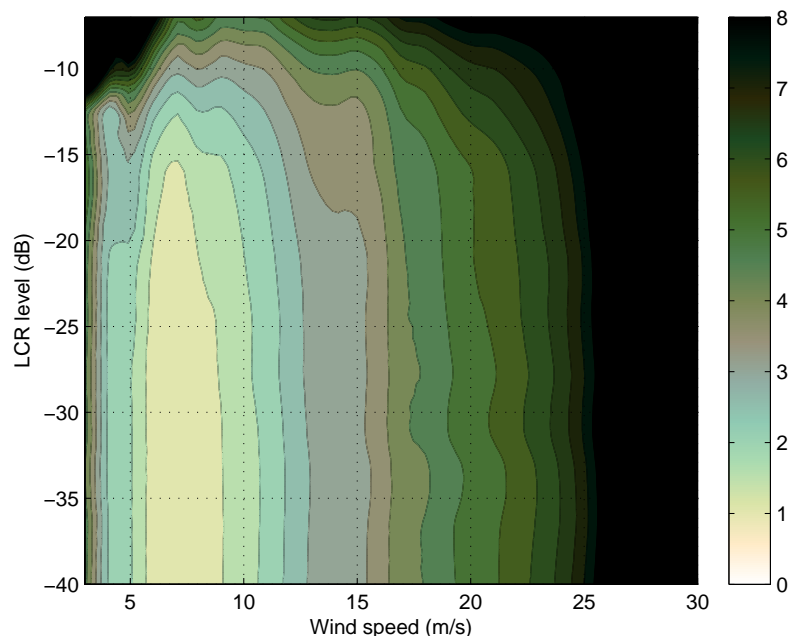


**Figure 8.10:** Biased CRB levels in m/s as a function of the simulated wind speed and the simulated LCR level for a single wind direction and land reflectivity level.

biased Cramer-Rao bound (CRB). A derivation of the biased CRB for scatterometer wind products and land contamination specifically is found in Appendix B.

Land contamination of backscatter observations introduces bias in the wind estimates. The wind estimate bias due to land contamination must be characterized to calculate the biased CRB. Due to the non-linear nature of the QuikSCAT GMF and noise model, there is no closed form for the wind estimates. Further, numeric sensitivities to the observation geometry reduce the effectiveness of techniques which exploit the Hessian matrix to calculate the biased CRB. To avoid these limitations the land contamination-induced wind bias is approximated in this Chapter using 1000 Monte-Carlo simulations for each combination of wind direction, wind speed, LCR level, land brightness level and cross-track location.

The biased CRB levels are shown for a fixed wind direction, land brightness level and cross-track location as a function of the LCR level and wind speed are shown in Fig. 8.10. Note that although the general structure of the CRB derived error bounds is similar to the simulated error levels in Fig. 8.6 the CRB derived error levels are somewhat higher

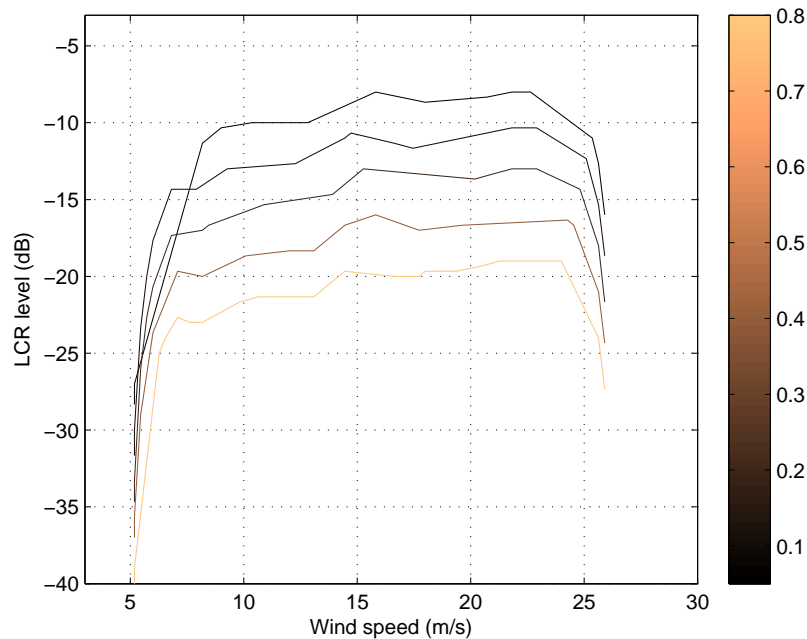


**Figure 8.11:** LCR threshold levels calculated using the CRB as a function of wind speed for varying land reflectivity levels with 30% wind speed error for cross-track WVC 20. Line color indicates the land reflectivity levels. Thresholds for lower land reflectivity levels are near the top of the figure.

generally. These elevated error bounds are not entirely realistic and are largely due to numeric sensitivity to wind direction which occurs in calculating the Fisher-information matrix.

LCR threshold levels can be selected from the CRB-calculated estimator bounds using the steps discussed in Section 8.3.3. For comparison with Fig. 8.9, the LCR thresholds generated using the CRB are shown in Fig. 8.11 but with a error tolerance set at 30%. The CRB-calculated LCR thresholds are less tolerant of land contamination in general and to be useful require that the error tolerance be at a higher level, 30%, than the level used for the Monte-Carlo simulations.

### 8.3.5 LCR Threshold Comparisons

Comparing the LCR thresholds generated using Monte-Carlo compass simulations to those generated using the biased CRB, shows that the CRB-derived thresholds are less

tolerant to land contamination. This is in part due to numerical sensitivities related to wind direction and observation geometry which increases the apparent variability of the wind estimates. In Monte-Carlo simulation the numeric sensitivity is reduced using a large number of simulations. Although the CRB derived LCR thresholds result from a more appealing theoretical perspective, in practice they are too conservative compared to the compass simulation-generated thresholds. Thus in the remainder of this Chapter the compass simulation-generated LCR thresholds are used to identify and remove land-contaminated observations.

To effectively utilize the LCR thresholds determined in simulation, the thresholds are tabulated in a look-up-table. Thresholds are indexed according to the local wind speed, cross-track index and local land reflectivity. Local LCR thresholds are then set during AVE processing so that contaminated measurements are discarded prior to performing wind retrieval. Although LCR processing is performed independently from wind retrieval, to evaluate the success of the LCR algorithm we must evaluate the wind retrieval results.

#### 8.4 Wind Retrieval

The LCR algorithm is implemented as a part of the AVE resolution enhancement algorithm to produce UHR (2.5 km)  $\sigma^o$  fields for use in UHR wind retrieval that are free of land contamination. The LCR algorithm can also be used for conventional (25 km) wind products. This section compares both the conventional and UHR standard wind products to their LCR processed counterparts for a case study of the Aegean Sea ( $38^\circ\text{N}+/-4^\circ$   $25^\circ\text{E}+/-5^\circ$ , QuikSCAT rev. 21417) with results shown in Figs. 8.12 - 8.16.

Previous wind retrieval methods avoid land contamination by using distance thresholds similar to the MDL, resulting in large areas where no wind estimates can be made, rather than determining the impact of land contamination on every measurement as is done with the LCR method. The 25km low-resolution QuikSCAT product produced by JPL, known as L2B, uses a distance threshold of 30 km from the coast within which all measurements are discarded. Figure 8.12 shows the 25 km wind vector cells from the L2B data product file for one pass. Although a 30 km threshold effectively removes all land contamination, the regions without wind estimates are larger than necessary.

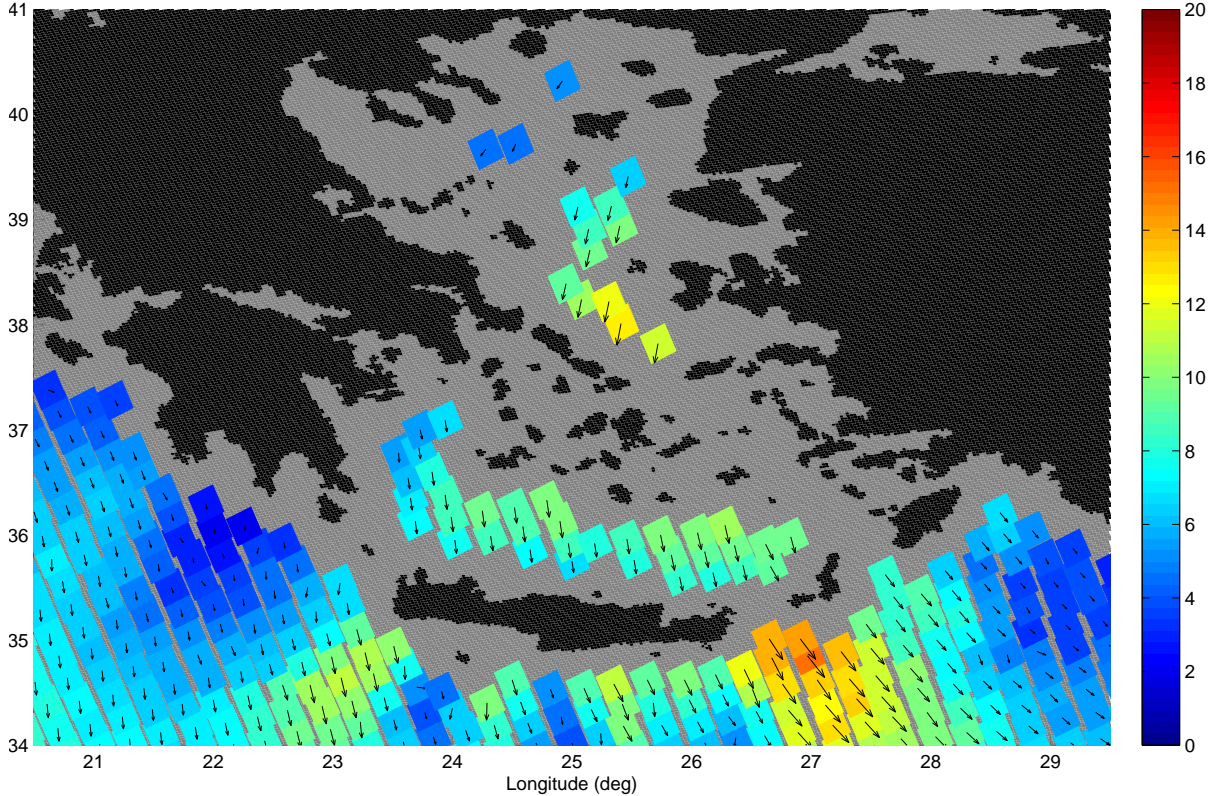


**Figure 8.12:** L2B conventional resolution (25 km) wind speed (m/s) and direction wind product. The conservative distance threshold to remove land contamination causes wind vector cells to be particularly sparse in the region.

UHR wind retrieval is advantageous in that it can be performed on a 2.5 km grid up to the coastline. This method is useful as it often retrieves valid winds closer to the coast than possible with low-resolution wind retrieval; however, due to land contamination, wind speeds next to the coast are often inaccurate, producing wind speed errors of up to 20m/s.

Figure 8.13 shows UHR winds retrieved from  $\sigma^o$  fields created using the AVE algorithm. Land-contaminated winds are readily apparent in Fig. 8.13 as very high wind speeds near the coast. Note that land-contaminated winds do not spread out from land uniformly in all directions due to the varying aspect angles of the antenna response pattern sidelobes over the swath, as illustrated in Fig. 8.2.

To compensate for land contamination in high-resolution wind fields, previous methods have used a 30 km distance threshold as in the low-resolution L2B wind products discussed previously. Figure 8.14 shows that a 30 km distance threshold effectively removes

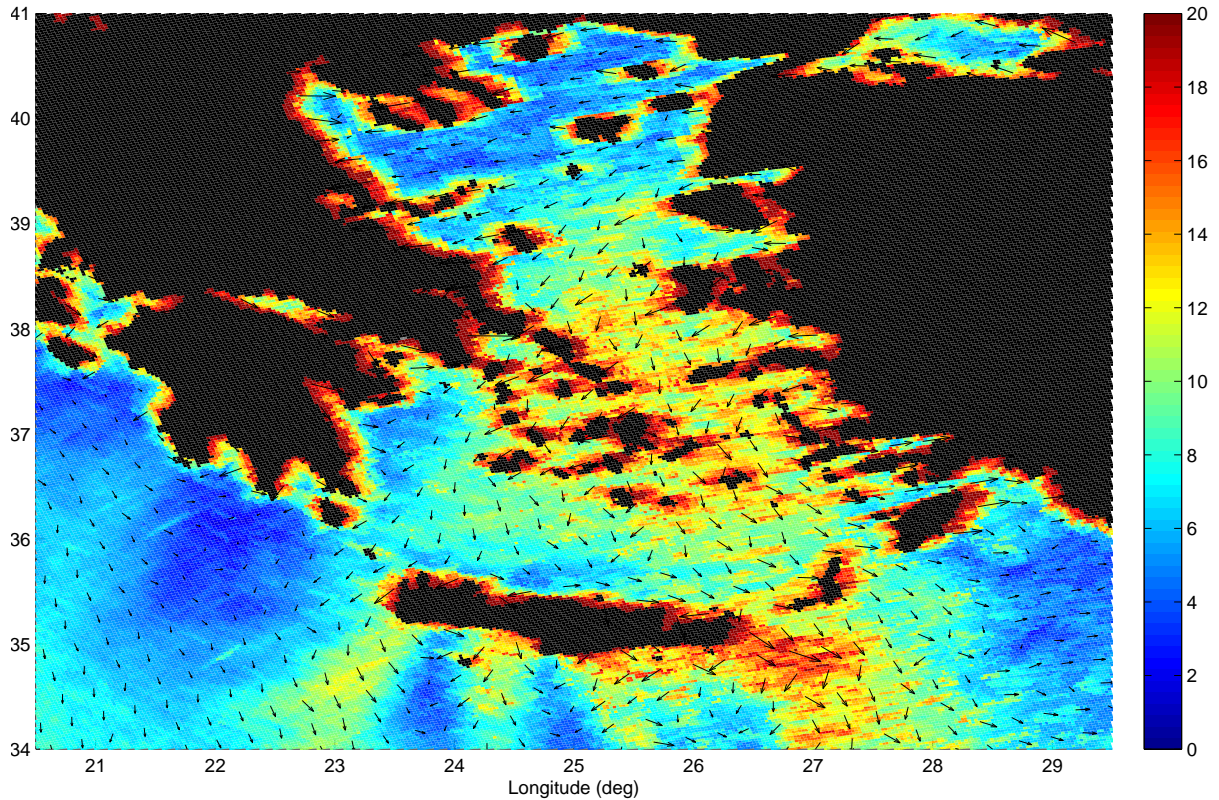


**Figure 8.13:** Wind speed (m/s) with wind direction vectors as retrieved using the UHR wind retrieval algorithm directly for the Aegean Sea. Land contaminated winds are visually apparent as wind speeds near land of roughly 15m/s or more.

land contamination in high-resolution wind fields. Unfortunately, the conservative threshold removes a large number of potentially valid WVCs, resulting in large gaps where wind retrieval could be possible. In this example, there are 53527 fewer WVCs with wind estimates using a 30 km threshold rather than standard UHR wind retrieval. Note that there are several places where apparently reasonable wind estimates in Fig. 8.13 are discarded in Fig. 8.14, such as in the northern region of the Aegean sea.

#### 8.4.1 Wind Retrieval Using the Land Contribution Ratio

The LCR metric is designed to identify significantly contaminated  $\sigma^o$  measurements so that they can be removed before processing and all uncontaminated winds can be retrieved successfully. When contaminated  $\sigma^o$  measurements are removed without discarding usable data, the maximum number of accurate, uncontaminated wind vectors are retrieved.

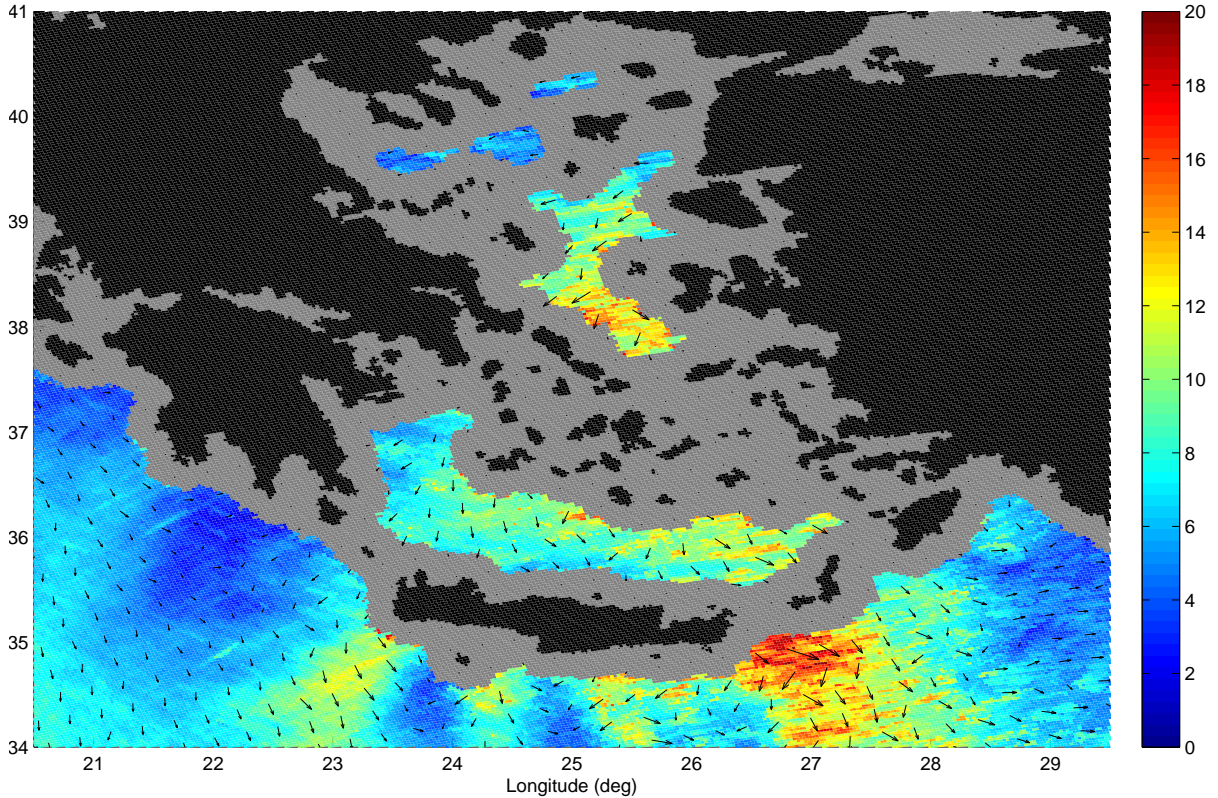


**Figure 8.14:** UHR wind speed (m/s) and direction produced by discarding all slices within 30 km of the coast. Note the large gaps where wind cannot be retrieved.

Estimates of the local wind speeds are obtained during processing from the JPL L2B 25 km resolution product for the corresponding orbit. Because LCR thresholds change significantly as a function of wind speed, conservatively accurate wind estimates are maintained by setting wind speed dependent LCR thresholds using the minimum wind speed in the local area. The local wind speed estimate is the minimum wind speed in a 5x5 along-track by cross-track WVC area according to the L2B file. L2B wind speed estimates are ideal for setting LCR thresholds because L2B wind estimates are generated only for WVCs where there is no significant land contamination. LCR thresholds set according to L2B wind speeds are therefore unbiased by the land contamination. One drawback of using L2B wind speeds is that because they use large distances to avoid land contamination, the L2B wind estimates are sparse and there are areas where there are no L2B estimates in the 5x5 WVC surrounding area. To compensate, if no L2B wind speeds are found within a 5x5 WVC area, a 9x9 WVC

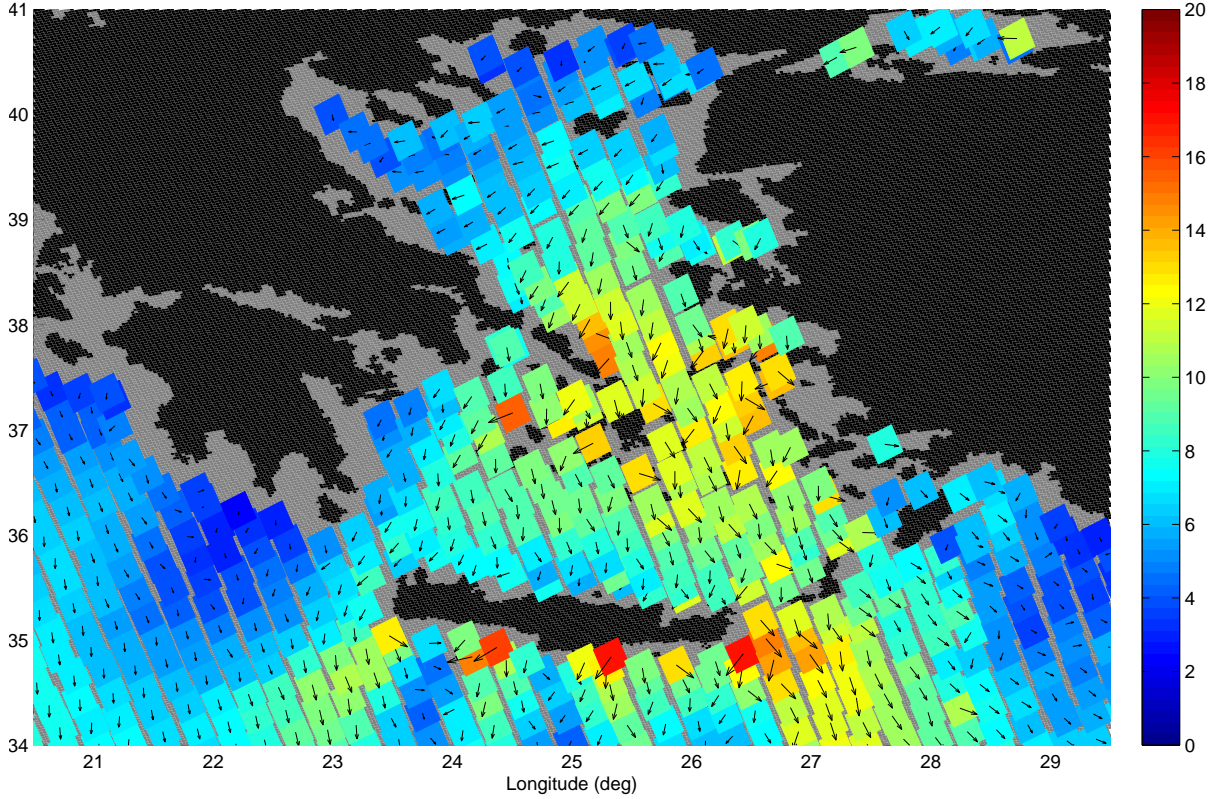


**Figure 8.15:** Conventional resolution wind speed (m/s) and direction produced after land contaminated measurements are discarded. Compare to Fig. 8.12. Note that WVCs are closer to the coast. The irregular spacing of the WVCs is a consequence of averaging the latitude and longitudes of all slices in each cell.

region is searched. If there are no L2B estimates in a 9x9 WVC area, a default threshold is used.

To set LCR thresholds appropriate to the local region, the land backscatter is estimated prior to wind retrieval. Land backscatter is non-isotropic, especially in mountainous regions where the true incidence angle of the antenna beam can vary greatly. To compensate for the directional dependence of backscatter values, the maximum  $\sigma^o$  value for each antenna beam in a local-area region is used to set LCR thresholds. Each look has a separate land reflectivity estimate. To obtain temporal resolution of land reflectivity, an array of maximum backscatter values is created using the current orbit data for each look prior to LCR processing. LCR thresholds are then set according to the maximum backscatter values in a

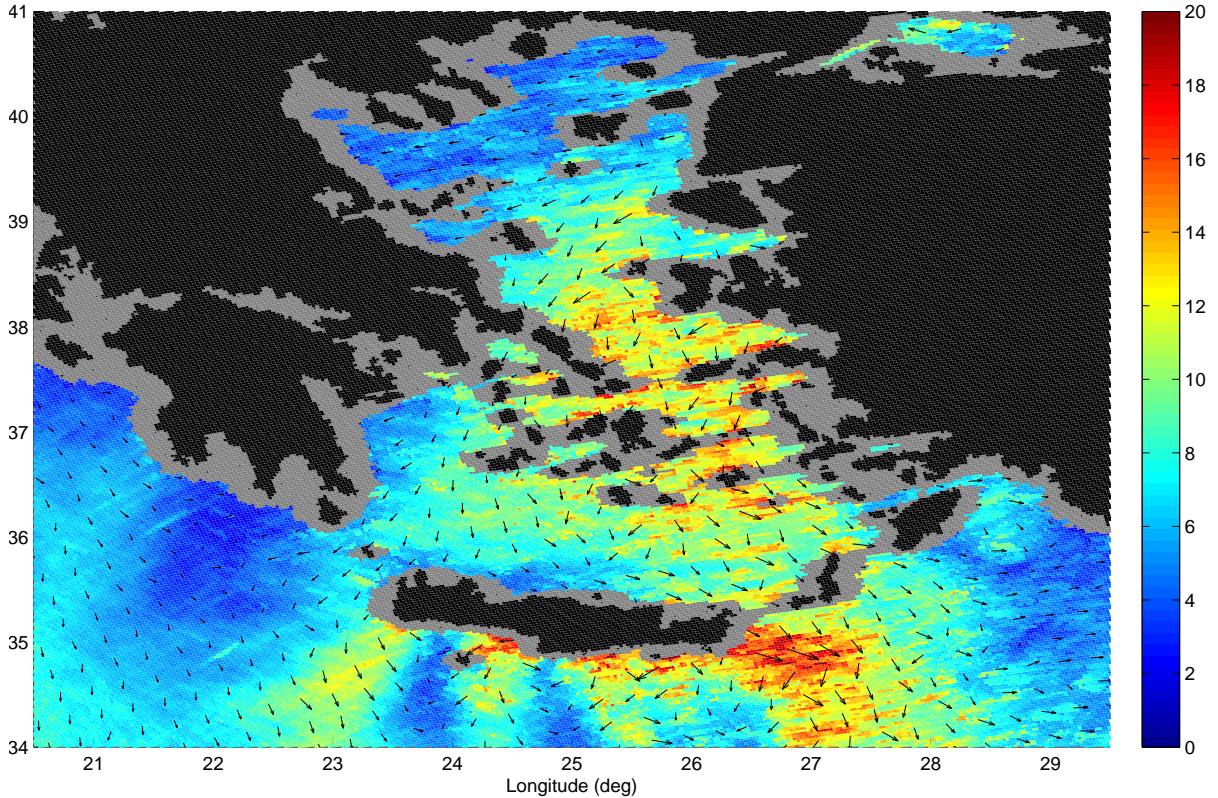


**Figure 8.16:** UHR wind speeds (m/s) and directions retrieved after removing land contaminated slices using the LCR metric.

3x3 along-track by cross-track region according to the worst-case backscatter estimates for each look.

Once LCR thresholds are set, land-contaminated slices are discarded and uncontaminated  $\sigma^o$  fields are created at both conventional and UHR. To create low resolution  $\sigma^o$  measurements, retained slices are averaged by polarization and look direction for each WVC. Wind retrieval is then performed, creating a low-resolution WVC wind product, as shown in Fig. 8.15, that is comparable to the L2B winds.

Several differences are readily apparent between Figs. 8.12 and 8.15. Most notable is the greater number of WVCs with wind estimates in the LCR processed wind fields which are free of the obvious land-contamination artifacts and errors. The greater number of WVCs is a consequence of removing only slices which are land-contaminated instead of those which are within 30 km of land. Not only are there more WVCs in the low-resolution wind field, but

the additional WVCs are typically much closer to the coastline than any WVC from the L2B data. Unfortunately, averaging slices to simulate pulses has two undesirable consequences. First, when land-contaminated measurements are discarded, fewer measurements remain in each WVC and wind estimates in near-coastal WVCs are noisier. This may alter the wind retrieval error distribution. Second, WVCs are no longer as regularly spaced as in L2B winds, as WVC centers are calculated to be the average location of the measurements that they contain. Despite the drawbacks of the pulse approximation, the advantages of LCR processing in low-resolution wind retrieval are still readily apparent.

UHR wind retrieval emphasizes the advantages of land contamination detection and removal using the LCR without the drawback of irregular WVC spacing. Figure 8.16 shows UHR wind speeds retrieved after LCR processing of backscatter values for the same orbit as Fig. 8.13. Comparing Fig. 8.16 with Figs. 8.13 and 8.14, it is apparent that LCR processed winds show the best features of both previous methods. Using LCR processing, it is possible to retrieve wind speeds much closer to the coast than those retrieved using a 30 km threshold. Consequently, wind speeds that appear reasonable in Fig. 8.13 but are not retrieved in Fig. 8.14, such as in the northern Aegean Sea, can be retrieved using the LCR. In addition to the accurate portrayal of mesoscale coastal wind features, in this example the LCR threshold only discards 31053 UHR WVCs, which is a 42% improvement over the number of UHR WVCs discarded using the 30 km threshold.

To validate the performance of the LCR over a much larger data set we compare the distribution of UHR wind speeds for one year of QuikSCAT data. We use wind data from a region on the Atlantic coast of the United States ( $43^{\circ}\text{N} \pm 2.5^{\circ}$   $68^{\circ}\text{W} \pm 2.5^{\circ}$ ) during 2006. Fig. 8.17 shows the wind speed distribution for 4 subsets of the 2006 data set. The four distributions we compare consist of: 1) WVCs greater than 30 km from land; 2) WVCs less than 30 km from land processed using the LCR; 3) WVCs less than 30 km from land processed without the LCR; 4) WVCs processed without the LCR for which LCR processing did not provide a wind estimate.

The distribution of data set 1 consists of uncontaminated winds and thus estimates the true wind distribution. The distribution of near-coastal winds after LCR processing (data set 2) closely resembles the true wind distribution. This indicates that any land contamination is

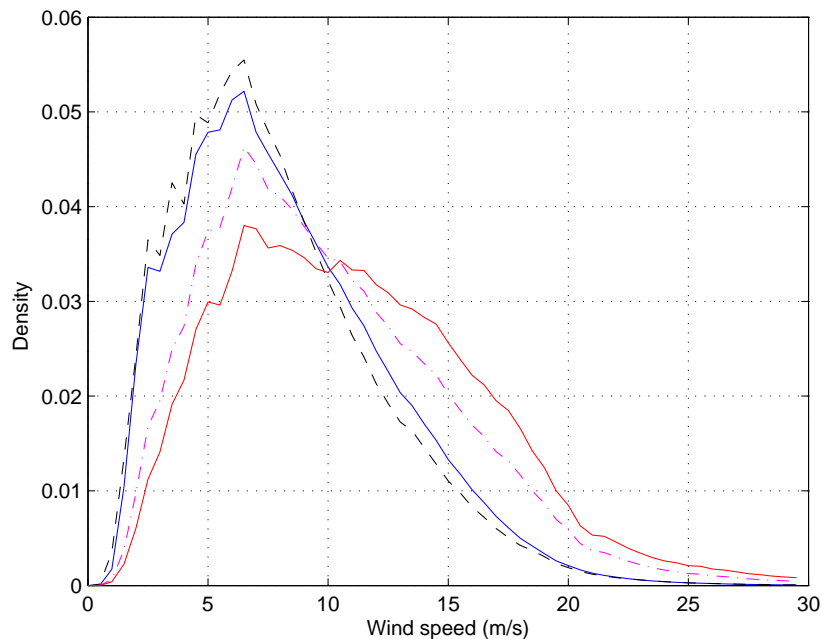


**Figure 8.17:** Wind speed distributions of the Cape Cod region using all QuikSCAT UHR data from 2006. The four different distributions consist of: 1) wind speed > 30 km from the coast; 2) LCR processed wind speed < 30 km from the coast; 3) wind speed < 30 km from the coast; 4) coastal WVCs where LCR reported land contamination. There are over 160 million WVCs in the combined data sets.

successfully mitigated using the LCR. We expect the LCR processed distribution to resemble the ocean wind distribution, however, there may be small differences due to coastal wind features such as coastal jets and lees not in data set 1.

Comparing the near-coastal winds from data sets 2 and 3 it is easy to see the bias towards higher wind speeds that occurs as a result of land contamination. To further illustrate the bias caused by land contamination, data set 4 shows the distribution of speeds of WVCs which the LCR reported as land contaminated. Data set 4 is thus almost purely land-contaminated. The increased bias over the distribution of data set 3 is readily apparent.

Although a thorough validation of near-coastal wind estimation is not included in this Chapter such a study is being conducted by other investigators using buoy data in the Gulf of Maine [3][4]. These validation efforts have shown that the wind products produced using

the LCR have significantly reduced land contamination effects although the wind estimate variability is slightly increased in near-coastal regions.

## 8.5 Conclusion

In summary, this Chapter has shown that although the MDL functions as a land contamination indicator, it is an insufficient metric to be used in land contamination detection and removal. Instead, this Chapter demonstrates that the LCR, when used with thresholds developed using Monte-Carlo simulation, is a more powerful metric for land contamination mitigation. Wind retrieval results using the LCR show that mesoscale coastal wind features such as lees and jets can be accurately portrayed after land contamination mitigation. Additionally, compared to previous methods there is a large increase in the number of valid WVCs at both conventional and UHR in near-coastal regions. Wind fields obtained after LCR processing are more accurate and closer to the coast by as much as 25 km than those retrieved using previous methods as shown in Figs. 8.12 - 8.16. This improved ability to retrieve coastal winds increases the utility of the QuikSCAT scatterometer, enabling large-scale coastal wind studies that were not previously possible.

## Chapter 9

### Conclusion

This Dissertation has developed optimal techniques which mitigate scatterometer contamination due to land proximity and rain. As demonstrated, these contamination mitigation techniques can be used to increase contamination-free sensor coverage while maintaining estimate accuracy. A summary of the major contributions of this Dissertation is found in Chapter 1. A review of principle results follows. Land and rain contamination mitigation result in improved wind estimates, though the optimal contamination mitigation techniques for type of contamination each utilize different approaches.

Improved wind estimates are obtained in the presence of land contamination by identifying and discarding observations which are significantly contaminated. This Dissertation has demonstrated that the LCR metric can be utilized to both identify and discard contaminated observations, thus maximizing the number of valid coastal wind estimates while maintaining wind estimate accuracy. This form of land contamination mitigation is equally effective for both conventional 25 km and UHR 2.5 km resolution products. Wind retrieval results using the LCR show that mesoscale coastal wind features such as lees and jets can be accurately portrayed following land contamination mitigation. Additionally, compared to previous methods there is a large increase in the number of valid WVCs at both 25 and 2.5 km resolutions in near-coastal regions. Wind fields obtained after LCR processing are more accurate and closer to the coast than those retrieved using previous methods by as much as 25 km. This improved ability to retrieve coastal winds increases the utility of the QuikSCAT scatterometer, making feasible large-scale coastal wind studies that were previously impossible due to limited coverage.

Rain contamination mitigation is possible using several techniques which are developed in this Dissertation. Models of the rain-induced effects on the observed backscatter

enable SWR estimation. This Dissertation has demonstrated that QuikSCAT is capable of measuring the wind and rain simultaneously at UHR. UHR SWR estimates offer insights into wind and rain events that are not achievable using any other single sensor.

The application of SWR estimation to QuikSCAT rain contamination mitigation is extended and improved with the introduction of BES. BES is a novel and unique adaptation of conventional Bayes decision theory to address QuikSCAT wind and rain estimation. Rather than rely solely on one type of estimator, BES reduces the effects of rain impact without discarding information available in the scatterometer observations. While rain-flagging methods typically discard rain-contaminated winds, BES optimally selects among the estimators to estimate wind when rain-contamination effects are correctable and rain when wind information is insufficient. This improves the overall quality and reliability of the wind and rain estimates.

While BES successfully reduces the effects of rain contamination for most cases, at UHR, additional noise levels and wind field variability require the extension of BES to include prior selection and noise reduction. BES-PS increases the overall accuracy of the wind estimates by ensuring realistic levels of spatial consistency in the wind and rain fields. The addition of prior selection to BES generalizes the technique to a much wider variety of wind conditions and substantially improves the estimator selection performance. The improved estimator selection performance allows BES-PS to approach optimal estimator selection for UHR wind and rain products.

Further, BES is a highly flexible and robust technique not limited to this application. BES can be adapted to a variety of problems regardless of estimator technique or dimension. Similarly, the addition of prior selection to BES increases the robustness of the technique in the presence of noise for data with greater variability.

The increased reliability of the QuikSCAT scatterometer, due to the rain contamination mitigation techniques introduced here, enables both engineering and scientific studies which were not previously possible. The resulting global wind and rain dataset can be used in a wide variety of applications which range from small-scale studies of tropical cyclones and other storms to global climate studies.

## 9.1 Areas for Further Research

Beyond the techniques developed in this Dissertation for land and rain contamination mitigation, which improve the quality and accuracy of wind estimates, there are many areas of pursuit to extend this work. As QuikSCAT reached end-of-mission in November of 2009, there is a need to extend the contamination mitigation techniques to the currently operating ASCAT. Although the ASCAT observation geometry, operating frequency and antenna pattern are significantly different from QuikSCAT, ASCAT is still subject to land contamination and to rain contamination as demonstrated in Chapter 4.

Another important application of this work is the extension to the planned dual-frequency scatterometer (DFS) which will make dual-frequency observations at Ku- and C-bands. The DFS is still in preliminary design phases [99] so extensions of land contamination mitigation using the LCR, and rain contamination mitigation using SWR estimation, BES and BES-PS may enable design trade-offs which can further increase the planned DFS capabilities. The effects of land contamination specifically have implications about antenna sidelobe levels. As one DFS mission objective is to make near-coastal wind observations, it is important to account for land contamination mitigation which may enable wind estimation closer to the coast than currently possible.

The BES technique is introduced and applied in this Dissertation using MLE estimates of wind and rain. An investigation of BES in conjunction with maximum a posteriori, model-based, and field-wise estimators may yield further improvements in rain contamination mitigation.

Although ice-contamination is limited to polar areas, in these areas it can be a significant limitation for studies involving sea-ice and iceberg monitoring. An extension of the LCR concept to ice-contamination mitigation may enable insights into predictive sea-ice growth and melt as well as iceberg movement and melt events.

Finally, the BES and BES-PS techniques are not limited to scatterometer specific applications. Investigation may reveal that the BES concept is useful in other applications which utilize multiple estimators simultaneously such as image classification, feature recognition, and target detection/identification.

## 9.2 Summary

The contamination mitigation techniques developed in this Dissertation are both generally applicable and effective in the specific application of QuikSCAT land and rain contamination mitigation. Together these land and rain contamination mitigation techniques reduce the effects of the largest sources of scatterometer measurement contamination. The resulting wind and rain fields have greater accuracy and utility, as discussed in Chapters 6, 7 and 8, which can aid understanding of the wind and rain interaction on a global scale for the QuikSCAT mission as well as current and future scatterometers.

## Bibliography

- [1] M. P. Owen and D. G. Long, “Land-contamination compensation for QuikSCAT near-coastal wind retrieval,” *IEEE Trans. Geosci. Remote Sens.*, vol. 47, no. 3, pp. 839–850, March 2009. 4
- [2] M. P. Owen, K. M. Stuart, and D. G. Long, “Ultra-high-resolution near-coastal wind retrieval for QuikSCAT,” R. J. Frouin, Ed., vol. 6680, no. 1. SPIE, 2007. 4
- [3] A. Plagge, D. Vandemark, and D. Long, “Validation and evaluation of quikscat ultra-high resolution wind retrieval in the gulf of maine,” in *Geoscience and Remote Sensing Symposium, 2008. IGARSS 2008. IEEE International*, vol. 4, 7-11 2008, pp. IV– 204–207. 4, 153
- [4] —, “Coastal validation of ultra-high resolution wind vector retrieval from quikscat in the gulf of maine,” *Geoscience and Remote Sensing Letters, IEEE*, vol. 6, no. 3, pp. 413 –417, july 2009. 4, 14, 153
- [5] M. P. Owen and D. G. Long, “Progress toward validation of QuikSCAT ultra-high-resolution rain rates using TRMM PR,” *IGARSS*, vol. 4, pp. 299–302, July 2008. 4, 65, 70, 105
- [6] —, “Towards and improved wind and rain backscatter model for ASCAT,” in *Proc. IGARSS*, July 2010. 4
- [7] —, “Towards bayesian estimator selection for QuikSCAT wind and rain estimation,” in *Proc. IGARSS*, July 2010. 4
- [8] F. T. Ulaby, R. K. Moore, and A. K. Fung, *Microwave Remote Sensing: Active and Passive*. Artech House, 1981, vol. 1: Microwave Remote Sensing Fundamentals and Radiometry. 7
- [9] D. G. Long, R. S. Collyer, R. Reed, and D. V. Arnold, “Dependence of the normalized radar cross section of water waves on Bragg wavelength-wind speed sensitivity,” *IEEE Trans. Geosci. Remote Sens.*, vol. 34, no. 3, May 1996. 8
- [10] M. A. Donelan and W. J. P. Jr., “Radar scattering and equilibrium ranges in wind-generated waves with application to scatterometry,” *Journal of Geophysical Research*, vol. 92, no. 10, pp. 4971–5029, 1987. 8
- [11] Z. S. Wu, J. P. Zhang, L.-X. Guo, and P. Zhou, “An improved two-scale model with volume scattering for the dynamic ocean surface,” *Progress In Electromagnetics Research*, vol. 89, pp. 39–56, 2009. 8

- [12] M. H. Freilich and R. S. Dunbar, "Derivation of satellite wind model functions using operational surface wind analyses: An altimeter example," *J. Geophys. Res.*, vol. 98, no. C8, pp. 14 633–14 649, August 1993. 8, 10, 50, 127
- [13] F. J. Wentz and D. K. Smith, "A model function for the ocean-normalized radar cross section at 14 GHz derived from NSCAT observations," *Journal of Geophysical Research*, vol. 104, pp. 499–514, 1999. 8
- [14] M. W. Spencer, C. Wu, and D. G. Long, "Tradeoffs in the design of a spaceborne scanning pencil beam scatterometer: Application to SeaWinds," *IEEE Trans. Geosci. Remote Sens.*, vol. 35, no. 1, January 1997. 8, 12, 170
- [15] D. Long, M. Drinkwater, B. Holt, S. Saatchi, and C. Bertoia, "Global ice and land climate studies using scatterometer image data," *EOS, Transaction of the American Geophysical Union*, vol. 82, no. 43, p. 503, 2001. 8
- [16] Q. Remund and D. Long, "Large-scale inverse ku-band backscatter modeling of sea ice," *IEEE Transactions on Geoscience and Remote Sensing*, 2003. 8
- [17] J. Haarpainter and G. Spreen, "Use of enhanced-resolution QuikSCAT/SeaWinds data for operational ice services and climate research: Sea ice edge, type, concentration, and drift," *IEEE Transactions on Geoscience and Remote Sensing*, vol. 45, no. 10, pp. 3131–3137, 2007. 8
- [18] J. Smith, Kenneth L., B. H. Robison, J. J. Helly, R. S. Kaufmann, H. A. Ruhl, T. J. Shaw, B. S. Twining, and M. Vernet, "Free-drifting icebergs: Hot spots of chemical and biological enrichment in the Weddell sea," *Science*, vol. 317, no. 5837, pp. 478–482, 2007. 8
- [19] I. Ashcraft and D. Long, "Observation and characterization of radar backscatter over Greenland," *IEEE Transactions on Geoscience and Remote Sensing*, vol. 43, no. 2, pp. 237–246, 2005. 8
- [20] —, "Relating microwave backscatter azimuth modulation to surface properties of the Greenland ice sheet," *Journal of Glaciology*, vol. 52, no. 177, pp. 257–266, 2006. 8
- [21] M. S. L. Wang, B. Rivard, and K. Steffen, "Melt season duration and ice layer formation on the Greenland ice sheet," *Journal of Geophysical Research*, vol. 112, 2007. 8
- [22] D. G. Long and P. J. Hardin, "Vegetation studies of the Amazon basin using enhanced resolution Seasat scatterometer data," *IEEE Transactions on Geoscience and Remote Sensing*, vol. 32, no. 2, pp. 449–460, 1994. 8
- [23] P. J. Hardin and D. G. Long, "Discriminating between tropical vegetation formations using reconstructed high-resolution Seasat-A scatterometer data,," *Photogrammetric Engineering and Remote Sensing*, vol. 60, no. 12, pp. 1453–1462, Dec 1994. 8

- [24] R. D. Magagi and Y. H. Kerr, "Retrieval of soil moisture and vegetation characteristics by use of ERS-1 wind scatterometer over arid and semi-arid areas," *Journal of Hydrology*, vol. 188-189, pp. 361 – 384, 1997. 8
- [25] H. Stephen and D. G. Long, "Spatial and temporal behavior of microwave backscatter directional modulation over the Saharan ergs," *IEEE Transactions on Geoscience and Remote Sensing*, vol. 45, no. 5, pp. 1164–1173, 2007. 8
- [26] —, "Microwave backscatter modeling of erg surfaces in the Sahara desert," *IEEE Transactions on Geoscience and Remote Sensing*, vol. 43, no. 2, pp. 237–246, 2005. 8
- [27] D. G. Long, "Wind field model-based estimation of SEASAT scatterometer winds," *Journal of Geophysical Research*, vol. 98, no. C8, pp. 14,651–14,688, August 1993. 8
- [28] F. M. Naderi, M. H. Freilich, and D. G. Long, "Spaceborne radar measurement of wind velocity over the ocean—an overview of the NSCAT scatterometer system," *Proceedings of the IEEE*, vol. 76, no. 6, pp. 850–866, June 1991. 8, 39, 51, 127
- [29] W. Y. Tsai, M. Spencer, C. Wu, C. Winn, and K. Kellogg, "SeaWinds on QuikSCAT - sensor description and mission overview," in *Proceedings of IEEE 2000 Geoscience and Remote Sensing Symposium*, 2000, pp. 1021–1023. 8
- [30] M. J. Brennan, C. C. Hennon, and R. D. Knabb, "The operational use of QuikSCAT ocean surface vector winds at the National Hurricane Center," *Weather and Forecasting*, vol. 24, no. 3, pp. 621–645, 2009. 10
- [31] R. Halterman and D. Long, "A comparison of hurricane eye determination using standard and ultra-high resolution QuikSCAT winds," in *Geoscience and Remote Sensing Symposium, 2006. IGARSS 2006. IEEE International Conference on*, July 2006, pp. 4134 –4137. 10
- [32] B. Williams and D. Long, "Estimation of hurricane winds from SeaWinds at ultrahigh resolution," *Geoscience and Remote Sensing, IEEE Transactions on*, vol. 46, no. 10, pp. 2924 –2935, Oct. 2008. 10
- [33] N. Perlin, R. M. Samelson, and D. B. Chelton, "Scatterometer and model wind and wind stress in the Oregon-California coastal zone," *Monthly Weather Review*, vol. 132, no. 8, pp. 2110–2129, 2004. 10
- [34] W. T. Lui, X. S. Xie, P. S. Polito, S. P. Xie, and H. Hashizume, "Atmospheric manifestation of tropical instability wave observed by Quikscat and tropical rain measuring mission," in *Geophysical Research Letters*, 2000, vol. 27, no. 16, pp. 2545–2548. 10
- [35] S. Zecchetto and F. De Biasio, "Wavenumber spectra of the Mediterranean Sea winds derived from the NASA QuikSCAT data," in *Geoscience and Remote Sensing Symposium, 2003. IGARSS '03. Proceedings. 2003 IEEE International*, vol. 3, pp. 21-25 2003, pp. 1907 – 1909. 10

- [36] N.-J. Kuo, C.-R. Ho, Y.-T. Lo, S.-J. Huang, and C.-C. Tsao, "Variability of chlorophyll-a concentration and sea surface wind in the south china sea associated with the el nio-southern oscillation," in *OCEANS 2008 - MTS/IEEE Kobe Techno-Ocean*, 8-11 2008, pp. 1–5. 10
- [37] D. B. Chelton, M. H. Freilich, J. M. Sienkiewicz, and J. M. Von Ahn, "On the use of QuikSCAT scatterometer measurements of surface winds for marine weather prediction," *Monthly Weather Review*, vol. 134, no. 8, pp. 2055–2071, 2006. 10
- [38] C. M. Risien and D. B. Chelton, "A global climatology of surface wind and wind stress fields from eight years of QuikSCAT scatterometer data," *Journal of Physical Oceanography*, vol. 38, no. 11, pp. 2379–2413, 2008. 10, 14
- [39] S.-P. Xie, W. T. Liu, Q. Liu, and M. Nonaka, "Far-reaching effects of the Hawaiian islands on the pacific ocean-atmosphere system," *Science*, vol. 292, no. 5524, pp. 2057–2060, 2001. 10
- [40] D. B. Chelton, M. G. Schlax, M. H. Freilich, and R. F. Milliff, "Satellite Measurements Reveal Persistent Small-Scale Features in Ocean Winds," *Science*, vol. 303, no. 5660, pp. 978–983, 2004. 10
- [41] T. E. Oliphant, "New techniques for wind scatterometry," Master's thesis, Brigham Young University, 1996. 10
- [42] S. J. Shaffer, R. S. Dunbar, S. V. Hsiao, and D. G. Long, "A median-filter-based ambiguity removal algorithm for NSCAT," *IEEE Trans. Geosci. Remote Sens.*, vol. 29, no. 1, January 1991. 11, 80
- [43] D. W. Draper and D. G. Long, "An advanced ambiguity selection algorithm for SeaWinds," *IEEE Trans. Geosci. Remote Sens.*, vol. 41, no. 3, March 2003. 11, 81
- [44] D. G. Long and M. W. Spencer, "Radar backscatter measurement accuracy for a spaceborne pencil-beam wind scatterometer with transmit modulation," *IEEE Trans. Geosci. Remote Sens.*, vol. 35, no. 1, pp. 102–114, January 1997. 12, 50, 68
- [45] *SeaWinds on ADEOS-II Level 2B Ocean Wind Vectors in 25km Swath*, D-24902 ed., Physical Oceanography DAAC, Jet Propulsion Laboratory, October 2002. 13, 130, 138
- [46] N. Suzuki, M. A. Donelan, and W. J. Plant, "On the sub-grid-scale variability of oceanic winds and the accuracy of numerical weather prediction models as deduced from QuikSCAT backscatter distributions," *Journal of Geophysical Research*, vol. 112, 2007. 14
- [47] G. V. Mostovoy, P. J. Fitzpatrick, and Y. Li, "Regional accuracy of QuikSCAT gridded winds," *International Journal of Remote Sensing*, vol. 26, no. 18, September 2005. 14

- [48] N. Ebuchi, H. C. Graber, and M. J. Caruso, "Evaluation of wind vectors observed by QuikSCAT/SeaWinds using ocean buoy data," *Journal of Atmospheric and Oceanic Technology*, vol. 19, no. 12, pp. 2049–2062, 2002. 14
- [49] M. H. Pickett, W. Tang, L. K. Rosenfeld, and C. H. Wash, "QuikSCAT satellite comparisons with nearshore buoy wind data off the U.S. west coast," *Journal of Atmospheric and Oceanic Technology*, vol. 20, no. 12, pp. 1869–1879, 2003. 14
- [50] I. Ashcraft and D. Long, "The spatial response function of SeaWinds backscatter measurements," in *Proceedings of SPIE Vol. 5151 Earth Observing Systems VIII*, W. L. Barnes, Ed., 3-6 August 2003, pp. 609–618. 14, 24, 126, 130
- [51] B. A. Williams, "Signal processing methods for ultra high resolution scatterometry," Ph.D. dissertation, Brigham Young University, 2010. 15, 17
- [52] D. G. Long, P. J. Hardin, and P. T. Whiting, "Resolution enhancement of spaceborne scatterometer data," *IEEE Trans. Geosci. Remote Sens.*, vol. 31, no. 3, pp. 700–75, 1993. 15, 126
- [53] M. Spencer, C. Wu, and D. G. Long, "Improved resolution backscatter measurements with the SeaWinds pencil-beam scatterometer," *IEEE Trans. Geosci. Remote Sens.*, vol. 38, pp. 89–104, January 2000. 15, 126
- [54] D. Long, J. Luke, and W. Plant, "Ultra high resolution wind retrieval from SeaWinds," *IGARSS*, pp. 1264–1266, 2003. 15, 24, 25, 126
- [55] C. Nie, "Wind/rain backscatter modeling and wind/rain retrieval for scatterometer and synthetic aperture radar," Ph.D. dissertation, Brigham Young University, 2008. 19
- [56] C. A. Mears, D. K. Smith, and F. J. Wentz, "Detecting rain with QuikSCAT." *IGARSS*, 2000, pp. 1235–1237. 21, 177
- [57] J. N. Huddleston and B. W. Stiles, "A multidimensional histogram rain-flagging technique for SeaWinds on QuikSCAT," in *Proc. IGARSS*, vol. 3, July 2000, pp. 1232–1234. 21, 96, 177
- [58] M. Portabella and A. Stoffelen, "Rain detection and quality control of SeaWinds," *Journal of Atmospheric and Oceanic Technology*, vol. 18, no. 7, pp. 1171–1183, July 2001. 21
- [59] B. W. Stiles and S. H. Yueh, "Impact of rain on spaceborne Ku-band wind scatterometer data," *IEEE Trans. Geosci. Remote Sens.*, vol. 40, no. 9, pp. 1973–1983, September 2002. 21, 66
- [60] D. E. Weissman, M. A. Bourassa, J. J. O'Brien, and J. S. Tongue, "Calibrating the QuikSCAT/SeaWinds radar for measuring rainrate over the oceans," *IEEE Trans. Geosci. Remote Sens.*, vol. 42, no. 7, pp. 2814–2820, July 2004. 21

- [61] D. W. Draper and D. G. Long, "Simultaneous wind and rain retrieval using SeaWinds data," *IEEE Trans. Geosci. Remote Sens.*, vol. 42, no. 7, pp. 1411–1423, 2004. 22, 23, 30, 49, 51, 52, 53, 54, 58, 59, 65, 66, 67, 68, 86, 173, 179, 183
- [62] —, "Assessing the quality of SeaWinds rain measurements," *IEEE Trans. Geosci. Remote Sens.*, vol. 42, no. 7, July 2004. 22, 51, 59
- [63] S. N. Nielsen and D. G. Long, "A wind and rain backscatter model derived from AMSR and SeaWinds data," *IEEE Trans. Geosci. Remote Sens.*, vol. 47, no. 6, pp. 1595–1606, June 2009. 22, 23, 49, 66
- [64] R. F. Contreras, W. J. Pland, W. C. Keller, K. Hayes, and J. Nystuen, "Effects of rain on Ku-band backscatter from the ocean," *J. Geophysical Research*, vol. 108, no. C5, pp. 1–15, 2003. 22, 32, 39
- [65] B. L. Mehaute and T. Khangaonkar, "Dynamic interaction of intense rain with water waves," *J. Physical Oceanography*, vol. 20, pp. 1805–1812, December 1990. 23, 43
- [66] B. A. Williams and D. G. Long, "Scatterometer sampling," *IEEE Trans. Geosci. Remote Sens.*, 2010. 24, 50
- [67] R. K. Crane, *Electromagnetic Wave Propagation Through Rain*. New York, Wiley, 1996. 26
- [68] I. Strangeways, *Precipitation: Theory, Measurement and Distribution*. Cambridge University Press, 2007. 26
- [69] D. W. Draper and D. G. Long, "Evaluating the effect of rain on SeaWinds scatterometer measurements," *J. of Geophys. Res.*, vol. 109, no. C02005, 2004. 30, 66, 67
- [70] F. T. Ulaby, R. K. Moore, and A. K. Fung, *Microwave Remote Sensing*. Artech House, 1981, vol. 1. 40
- [71] L. J. Ippolito, *Satellite communications systems engineering: atmospheric effects, satellite link design, and system performance*. Wiley, 2008. 42
- [72] H. Hersbach, A. Stoffelen, and S. de Haan, "An improved c-band scatterometer ocean geophysical model function," *J. Geophysical Research*, vol. 112, no. C03006, pp. 1–18, 2007. 43
- [73] C. Nie and D. Long, "A C-band wind/rain backscatter model," *IEEE Trans. Geosci. Remote Sens.*, vol. 45, no. 3, pp. 621–631, 2007. 43
- [74] T. E. Oliphant and D. G. Long, "Accuracy of scatterometer-derived winds using the Cramér-Rao bound," *IEEE Trans. Geosci. Remote Sens.*, vol. 37, no. 6, November 1999. 54, 58, 70, 137, 171
- [75] B. W. Stiles, B. D. Pollard, and R. S. Dunbar, "Direction interval retrieval with threshold nudging: A method for improving the accuracy of QuikSCAT winds," *IEEE Trans. Geosci. Remote Sens.*, vol. 40, January 2002. 59

- [76] M. P. Owen and D. G. Long, "Progress toward validation of QuikSCAT ultra-high-resolution rain rates using TRMM PR," vol. 4, July 2008, pp. 299–302. 61
- [77] J. R. Allen and D. G. Long, "An analysis of SeaWinds-based rain retrieval in severe weather events," *IEEE Trans. Geosci. Remote Sens.*, vol. 43, no. 12, pp. 2870–2878, 2005. 65, 67
- [78] C.-Y. Chi and F. K. Li, "A comparative study of several wind estimation algorithms for spaceborne scatterometers," *IEEE Trans. Geosci. Remote Sens.*, vol. 26, no. 2, March 1988. 66, 68, 137
- [79] M. P. Owen and D. G. Long, "Simultaneous wind and rain estimation for QuikSCAT at ultra-high resolution," *IEEE Trans. Geosci. Remote Sens.*, 2010. 67
- [80] T. K. Moon and W. C. Stirling, *Mathematical Methods and Algorithms*. Prentice Hall, 2000. 73
- [81] A. E. Raftery, "Bayesian model selection in social research," *Sociological Methodology*, vol. 25, pp. pp. 111–163, 1995. 79
- [82] V. S. Cherkassky and F. Mulier, *Learning from data: concepts, theory, and methods*. Wiley, 1998. 80
- [83] B. A. Williams and D. G. Long, "Estimation of hurricane winds from SeaWinds at ultrahigh resolution," *IEEE Trans. Geosci. Remote Sens.*, vol. 46, no. 10, pp. 2924–2935, October 2008. 80, 102, 104
- [84] N. Takahashi and T. Iguchi, "Characteristics of TRMM/PR system noise and their application to the rain detection algorithm," *IEEE Trans. Geosci. Remote Sens.*, vol. 46, no. 6, pp. 1697–1704, June 2008. 82
- [85] E. G. Pavia and J. J. O'Brien, "Weibull statistics of wind speed over the ocean," *J. of Climate and Applied Meteorology*, vol. 25, pp. 1324–1332, 1986. 83
- [86] K. Conradsen and L. B. Nielsen, "Weibull statistics for estimation of wind speed distributions," *J. of Climate and Applied Meteorology*, vol. 23, pp. 1178–1183, 1984. 83
- [87] W.-K. Pang, J. J. Forster, and M. D. Troutt, "Estimation of wind speed distribution using markov chain monte carlo techniques," *J. of Climate and Applied Meteorology*, vol. 40, pp. 1476–1484, 2000. 83
- [88] *QuikSCAT science data product user's manual*, D-18053 ed., Physical Oceanography DAAC, Jet Propulsion Laboratory, September 2006. 96
- [89] D. G. Long, "Model-based estimation of wind fields over the oceans from wind scatterometer measurements," Ph.D. dissertation, University of Southern California, January 1989. 104

- [90] B. A. Williams, M. P. Owen, and D. G. Long, "The ultra high resolution QuikSCAT product," in *Proceedings of the 2009 IEEE Radar Conference*. Pasadena, CA: IEEE, May 2009. 105
- [91] R. K. Crane, *Electromagnetic Wave Propagation Through Rain*. Wiley, 1996. 106
- [92] M. P. Owen and D. G. Long, "M-ary Bayes estimator selection for QuikSCAT simultaneous wind and rain retrieval," *IEEE Trans. Geosci. Remote Sens.*, 2010. 107, 109
- [93] M. H. Hayes, *Statistical Digital Signal Processing and Modeling*. Wiley, 1996. 112
- [94] W. Tang, T. Liu, and B. Stiles, "Evaluation of high-resolution ocean surface vector winds measured by QuikSCAT scatterometer in coastal regions," *IEEE Trans. Geosci. Remote Sens.*, vol. 42, no. 8, pp. 1762–1769, August 2004. 125
- [95] D. Long, "High resolution wind retrieval from Seawinds," in *Proceedings of IGARSS*. Toronto, ON, Canada: IEEE, 24-28 June 2002, pp. 751–753. 125
- [96] D. S. Early and D. G. Long, "Image reconstruction and enhanced resolution imaging from irregular samples," *IEEE Trans. Geosci. Remote Sens.*, vol. 39, no. 2, pp. 291–302, 2001. 126
- [97] R. Kennett and F. Li, "Seasat over-land scatterometer data. I. global overview of the Ku-band backscatter coefficients," *IEEE Trans. Geosci. Remote Sens.*, vol. 27, no. 5, pp. 592–605, September 1989. 127
- [98] I. Ashcraft, D. Long, A. Anderson, S. Richards, M. Spencer, and B. Jones, "Sigma-0 retrieval from the SeaWinds on QuikSCAT," in *Proceedings of SPIE Earth Observing Systems IV*, W. L. Barnes, Ed., vol. 3750, Denver, Colorado, 19-20 July 1999, pp. 171–178. 129
- [99] B. W. Stiles, S. M. Hristova-Veleva, R. S. Dunbar, S. Chan, S. L. Durden, D. Esteban-Fernandez, E. Rodriguez, W. L. Poulsen, R. W. Gaston, and P. S. Callahan, "Obtaining accurate ocean surface winds in hurricane conditions: A dual-frequency scatterometry approach," *Geoscience and Remote Sensing, IEEE Transactions on*, vol. 48, no. 8, pp. 3101–3113, aug. 2010. 157
- [100] D. V. Hinkley, "On the ratio of two correlated normal random variables," *Biometrika*, vol. 56, no. 3, p. 635, 1969. 183
- [101] T. M. Cover and J. A. Thomas, *Elements of Information Theory*. Wiley Interscience, 2005. 190

## Appendix A

### List of Acronyms

ASCAT - Advanced Scatterometer  
BES - Bayes Estimator Selection  
BES-PS - Bayes Estimator Selection with Prior Selection and noise reduction  
CRB - Cramer-Rao lower Bound  
ECMWF - European Center for Medium-range Weather Forecasting  
GMF - Geophysical Model Function  
IMUDH - Impact-based MUltri-Dimensional Histogram  
LCR - Land Contribution Ratio  
MAP - Maximum A Posteriori  
MDL - Minimum Distance to Land  
MLE - Maximum Likelihood Estimation  
MSE - Mean-Squared Error  
MUDH - MUltri-Dimensional Histogram  
NCEP - National Center for Environmental Prediction  
RLF - Rain Likelihood Flag  
RMS - Root-Mean-Squared  
RO - Rain-Only  
SIR - Signal to Interference Ratio  
SWR - Simultaneous Wind and Rain  
TRMM PR - Tropical Rain Measuring Mission Precipitation Radar  
UHR - Ultra-High Resolution  
WO - Wind-Only  
WVC - Wind Vector Cell



## Appendix B

### The Cramer-Rao Bound for Estimates from Contaminated Observations

Measurement contamination can cause significant bias on wind estimates. This appendix evaluates the effects of contamination on wind and rain estimation by means of the Cramer-Rao Bound (CRB). Section B.1 reviews the related statistical models for QuikSCAT backscatter observations and derives the Fisher information matrix and CRB for wind-only wind retrieval. Section B.2 derives the Fisher information for known contamination and section B.3 derives the Fisher information for random contamination. Finally, section B.4 applies the results for known and fixed contamination to land-contaminated wind retrieval, rain-contaminated wind retrieval, and wind-contaminated rain-only retrieval in addition to introducing the CRB for simultaneous wind and rain retrieval.

#### B.1 Statistical Models

The Cramer-Rao lower bound is derived directly from the statistical models for the backscatter observations. This section reviews the background information required to derive the Cramer-Rao lower bound.

The vector of backscatter observations  $\mathbf{z}_k$  is modeled for QuikSCAT using a normal distribution where each observation is assumed to be independent. Thus given the wind vector  $\mathbf{w}$  the conditional probability of the observation vector  $\mathbf{z}$  is

$$p(\mathbf{z}|\mathbf{w}) = \prod_{k=1}^4 (2\pi\zeta_k^2)^{-1/2} \exp \left[ -\frac{(z_k - E[z_k])^2}{2\zeta_k^2} \right], \quad (\text{B.1})$$

where  $k$  indexes the individual measurements. The model variance  $\zeta_k^2$  can be written

$$\zeta_k^2 = E[z_k]^2 (K_{pc}^2 + K_{pm}^2 + K_{pc}^2 K_{pm}^2) \quad (\text{B.2})$$

$$= \epsilon_k E[z_k]^2 + (\beta_k E[z_k] + \gamma_k) (1 + K_{pm}^2), \quad (\text{B.3})$$

$$\epsilon_k = \alpha_k (1 + K_{pm}^2) + K_{pm}^2, \quad (\text{B.4})$$

where  $K_{pm}$  represents model uncertainty, and  $K_{pc}$  represents communication noise. The communication noise is modeled as

$$K_{pc} = \sqrt{\alpha_k + \frac{\beta_k}{E[z_k]} + \frac{\gamma_k}{E[z_k]^2}}, \quad (\text{B.5})$$

where  $\alpha_k$ ,  $\beta_k$ , and  $\gamma_k$  are communication noise coefficients which are scatterometer dependent [14].

For wind retrieval the variance is commonly approximated by expanding  $\varsigma_k^2$  and dropping a term as follows

$$\varsigma_k^2 = \alpha_k(1 + K_{pm}^2)E[z_k]^2 + K_{pm}^2E[z_k]^2 + (\beta_k E[z_k] + \gamma_k)(1 + K_{pm}^2) \quad (\text{B.6})$$

$$= K_{pm}^2 \left( (1 + \alpha_k)E[z_k]^2 + \beta_k E[z_k] + \gamma_k \right) + \alpha_k E[z_k]^2 + \beta_k E[z_k] + \gamma_k \quad (\text{B.7})$$

$$\approx K_{pm}^2(1 + \alpha_k)E[z_k]^2 + \alpha_k E[z_k]^2 + \beta_k E[z_k] + \gamma_k. \quad (\text{B.8})$$

The log-likelihood function is

$$L(\mathbf{w}, \mathbf{z}) = \log(p(\mathbf{z}|\mathbf{w})) \quad (\text{B.9})$$

$$= -\frac{1}{2} \sum_{k=1}^4 \log(2\pi\varsigma_k^2) + \frac{(z_k - E[z_k])^2}{\varsigma_k^2}. \quad (\text{B.10})$$

The score function is

$$s(\mathbf{w}, \mathbf{z}) = \frac{\partial}{\partial \mathbf{w}} L(\mathbf{w}, \mathbf{z}) \quad (\text{B.11})$$

$$= -\frac{1}{2} \sum_{k=1}^4 \frac{1}{2\pi\varsigma_k^2} \frac{\partial}{\partial \mathbf{w}} (2\pi\varsigma_k^2) + \frac{-2\varsigma_k^2(z_k - E[z_k]) \frac{\partial E[z_k]}{\partial \mathbf{w}} - (z_k - E[z_k])^2 \frac{\partial \varsigma_k^2}{\partial \mathbf{w}}}{\varsigma_k^4} \quad (\text{B.12})$$

$$= \sum_{k=1}^4 \frac{(z_k - E[z_k])}{\varsigma_k^2} \frac{\partial E[z_k]}{\partial \mathbf{w}} + \left( \frac{(z_k - E[z_k])^2}{2\varsigma_k^4} - \frac{1}{2\varsigma_k^2} \right) \frac{\partial \varsigma_k^2}{\partial \mathbf{w}}, \quad (\text{B.13})$$

where

$$\frac{\partial \varsigma_k^2}{\partial \mathbf{w}} = (2\epsilon_k E[z_k] + \beta_k(1 + K_{pm}^2)) \frac{\partial E[z_k]}{\partial \mathbf{w}}. \quad (\text{B.14})$$

### B.1.1 Fisher Information Matrix

The Fisher information matrix  $J$  is key to determining the CRB and can be calculated using the score function as

$$J = E[s(\mathbf{w}, \mathbf{z})^T s(\mathbf{w}, \mathbf{z})], \quad (\text{B.15})$$

where  $E[\cdot]$  represents expectation. The  $ij$  element of the Fisher information matrix,  $J_{ij}$  can be calculated from the score function as

$$\begin{aligned}
J_{ij} &= E[s(w_i, \mathbf{z})s(w_j, \mathbf{z})] \\
&= E \left[ \sum_{k=1}^4 \sum_{l=1}^4 \left( \frac{(z_k - E[z_k])}{\varsigma_k^2} \frac{\partial E[z_k]}{\partial w_i} + \left( \frac{(z_k - E[z_k])^2}{2\varsigma_k^4} - \frac{1}{2\varsigma_k^2} \right) \frac{\partial \varsigma_k^2}{\partial w_i} \right) \right. \\
&\quad \left. \left( \frac{(z_l - E[z_l])}{\varsigma_l^2} \frac{\partial E[z_l]}{\partial w_j} + \left( \frac{(z_l - E[z_l])^2}{2\varsigma_l^4} - \frac{1}{2\varsigma_l^2} \right) \frac{\partial \varsigma_l^2}{\partial w_j} \right) \right] \\
&= \sum_{k=1}^4 \sum_{l=1}^4 \frac{\partial E[z_k]}{\partial w_i} \frac{E[(z_k - E[z_k])(z_l - E[z_l])]}{\varsigma_k^2 \varsigma_l^2} \frac{\partial E[z_l]}{\partial w_j} \\
&\quad + \frac{\partial E[z_k]}{\partial w_i} \left( \frac{E[(z_k - E[z_k])(z_l - E[z_l])^2]}{2\varsigma_k^2 \varsigma_l^4} - \frac{E[(z_k - E[z_k])]}{2\varsigma_k^2 \varsigma_l^2} \right) \frac{\partial \varsigma_l^2}{\partial w_j} \\
&\quad + \frac{\partial \varsigma_k^2}{\partial w_i} \left( \frac{E[(z_k - E[z_k])^2(z_l - E[z_l])]}{2\varsigma_k^4 \varsigma_l^2} - \frac{E[(z_l - E[z_l])]}{2\varsigma_k^2 \varsigma_l^2} \right) \frac{\partial E[z_l]}{\partial w_j} \\
&\quad + \frac{\partial \varsigma_k^2}{\partial w_i} \left( \frac{E[(z_k - E[z_k])^2(z_l - E[z_l])^2]}{4\varsigma_k^4 \varsigma_l^4} - \frac{E[(z_k - E[z_k])^2]}{4\varsigma_k^4 \varsigma_l^2} \right. \\
&\quad \left. - \frac{E[(z_l - E[z_l])^2]}{4\varsigma_l^4 \varsigma_k^2} + \frac{1}{4\varsigma_k^2 \varsigma_l^2} \right) \frac{\partial \varsigma_l^2}{\partial w_j}. \tag{B.16}
\end{aligned}$$

The expectation terms in Eq. B.16 can be reduced by noting that  $E[(z_k - E[z_k])^2] = \varsigma_k^2$ , thus

$$E[z_k - E[Z_k]] = 0, \tag{B.17}$$

$$E[(z_k - E[Z_k])(z_l - E[z_l])] = \varsigma_k^2 \delta_{kl}, \tag{B.18}$$

$$E[(z_k - E[Z_k])(z_l - E[z_l])^2] = 0, \tag{B.19}$$

$$E[(z_k - E[z_k])^2(z_l - E[z_l])^2] = \varsigma_k^2 \varsigma_l^2 + 2\varsigma_k^4 \delta_{kl}. \tag{B.20}$$

which allows the Fisher information to be conveniently expressed as

$$J_{ij} = \sum_{k=1}^4 \frac{\partial E[z_k]}{\partial w_i} \frac{1}{\varsigma_k^2} \frac{\partial E[z_k]}{\partial w_j} + \frac{\partial \varsigma_k^2}{\partial w_i} \frac{1}{2\varsigma_k^4} \frac{\partial \varsigma_k^2}{\partial w_j}. \tag{B.21}$$

For uncontaminated wind retrieval the mean of the observations is given by the geophysical model function so  $E[z_k] = \mathcal{M}_k(\mathbf{w})$ . To simplify the notation we omit the dependence of  $\mathcal{M}_k$  on the wind vector  $\mathbf{w}$  in the following which allows  $J_{ij}$  to be written as

$$J_{ij} = \sum_{k=1}^4 \frac{\partial \mathcal{M}_k}{\partial w_i} \frac{1}{\varsigma_k^2} \frac{\partial \mathcal{M}_k}{\partial w_j} + \frac{\partial \varsigma_k^2}{\partial w_i} \frac{1}{2\varsigma_k^4} \frac{\partial \varsigma_k^2}{\partial w_j}. \tag{B.22}$$

This form of the Fisher information matrix is first derived for wind-only retrieval in [74].

### B.1.2 Cramer-Rao Lower Bound

Although the conventional wind estimates are asymptotically unbiased, the wind estimates remain biased since there are relatively few observations, particularly for ultra-high resolution. To calculate the Cramer-Rao bound (CRB) for a biased estimator requires the use of the biased form of the CRB which is defined as

$$E[(\hat{\mathbf{w}} - \mathbf{w})(\hat{\mathbf{w}} - \mathbf{w})^T] \geq \frac{\partial E[\hat{\mathbf{w}}]}{\partial \mathbf{w}} J^{-1}(\mathbf{w}) \left[ \frac{\partial E[\hat{\mathbf{w}}]}{\partial \mathbf{w}} \right]^T. \quad (\text{B.23})$$

There is no closed form for  $E[\hat{\mathbf{w}}]$  due to the non-linear nature of the geophysical model function. Calculating the required partial derivatives is therefore non-trivial. Although there are methods to approximate  $\frac{\partial E[\hat{\mathbf{w}}]}{\partial \mathbf{w}}$  these methods depend on the Hessian matrix of the model function. Since the model function is a tabular form, there is no analytic expression for the Hessian, which must be numerically computed. For many wind vectors this is not a problem, but for a significant portion the numeric sensitivity of the Hessian matrix causes inaccurate results. To avoid these numeric sensitivities  $E[\hat{\mathbf{w}}]$  can be estimated using Monte Carlo simulations. The partial derivatives can then be calculated from the Monte-Carlo estimates of  $E[\hat{\mathbf{w}}]$ .

In the following sections the biased Cramer-Rao lower bound is derived for contaminated wind retrieval via the Fisher information matrix. This determines the bounds on the estimator variance under contaminated conditions and is applicable to both land- and rain-contaminated wind retrieval as well as wind-contaminated rain-only retrieval.

## B.2 Contaminated Observations - Known Contamination

Suppose that the backscatter observations  $z_k$  are contaminated by known contaminants such that  $z_k = y_k a_k + c_k$  where  $y_k$  represents the uncontaminated signal due to the wind vector  $\mathbf{w}$ . For this situation the mean value of the observations

$$\begin{aligned} E[z_k] &= a_k E[y_k] + c_k \\ &= a_k \mathcal{M}_k + c_k. \end{aligned} \quad (\text{B.24})$$

The variance of the observations is a function of the mean value so it is

$$\begin{aligned} \varsigma_k^2 &= (a_k \mathcal{M}_k + c_k)^2 (K_{pc}^2 + K_{pm}^2 + K_{pc}^2 K_{pm}^2) \\ &= \epsilon_k (a_k \mathcal{M}_k + c_k)^2 + (\beta_k (a_k \mathcal{M}_k + c_k) + \gamma_k) (1 + K_{pm}^2), \end{aligned} \quad (\text{B.25})$$

$$\epsilon_k = \alpha_k + K_{pm}^2 + \alpha_k K_{pm}^2, \quad (\text{B.26})$$

$$\begin{aligned} \frac{\partial \varsigma_k^2}{\partial \mathbf{w}} &= a_k (2\epsilon_k (a_k^2 \mathcal{M}_k + a_k c_k) + \beta_k (1 + K_{pm}^2)) \frac{\partial \mathcal{M}_k}{\partial \mathbf{w}} \\ &= a_k (2(a_k^2 \mathcal{M}_k + a_k c_k)(\alpha_k + K_{pm}^2 + \alpha_k K_{pm}^2) + \beta_k (1 + K_{pm}^2)) \frac{\partial \mathcal{M}_k}{\partial \mathbf{w}}. \end{aligned} \quad (\text{B.27})$$

Substituting the results in Eq. B.21

$$J_{ij} = \sum_{k=1}^4 \frac{\partial \mathcal{M}_k}{\partial w_i} \frac{a_k^2}{\varsigma_k^2} \frac{\partial \mathcal{M}_k}{\partial w_j} + \frac{\partial \varsigma_k^2}{\partial w_i} \frac{1}{2\varsigma_k^4} \frac{\partial \varsigma_k^2}{\partial w_j}, \quad (\text{B.28})$$

where  $\varsigma_k^2$  is given in Eq. B.25 and  $\frac{\partial \varsigma_k^2}{\partial w_i}$  is defined in Eq. B.27.

As might be expected, for  $a_k > 1$  the SNR increases which reduces the covariance of the estimates since the CRB is dependent on  $J^{-1}$ . More realistically, when  $a_k < 1$  the effect is to decrease the SNR which consequently increases the covariance of the estimates. Also, if  $a_k = 1$  then the result reduces to the uncontaminated Fisher Information matrix of Eq. B.16.

The constant contamination term,  $c_k$ , only effects the variance of the observation. When  $c_k > 0$ , the variance of the observations increases. Together the general effects of  $a_k$  and  $c_k$  can be summarized by stating that  $a_k$  lowers the SNR of the observations while  $c_k$  increases the variance. While these effects are in very similar, summarizing them in this way can provide intuition into the consequences of the contamination.

### B.3 Contaminated Observations - Random Contamination

Suppose now that the additive contamination is a random quantity. In this case  $z_k$  represents the vector of contaminated observations with  $z_k = a_k y_k + C_k$  and  $y_k$  represents the observations due to wind where  $y_k \sim \mathcal{N}(\mathcal{M}_k, \mathcal{M}_k^2 K_{pm}^2)$ .  $C_k$  is a random variable with  $C_k = c_k(1 + K_c \eta_c)$ .  $K_c$  is the normalized standard deviation for  $C_k$  and  $\eta_c$  is zero-mean uni-variate random variable which is independent of other random variables.

With this formulation the mean value of the observations is

$$E[z_k] = E[a_k y_k + C_k] \quad (\text{B.29})$$

$$= a_k \mathcal{M}_k + c_k. \quad (\text{B.30})$$

Based on the scatterometer measurement model the variance for the observations can be approximated by [61]

$$\text{Var}\{z_k\} \approx (\mathcal{M}_k a_k K_{pm} + c_k K_c)^2 (1 + \alpha) + \alpha E[z_k]^2 + \beta E[z_k] + \gamma \quad (\text{B.31})$$

$$= \varsigma_k^2. \quad (\text{B.32})$$

Assuming that the contamination is not a function of the wind, we can approximate the derivative as

$$\begin{aligned}
\frac{\partial \varsigma_k^2}{\partial \mathbf{w}} &= 2(\mathcal{M}_k a_k K_{pm} + c_k K_c) \frac{\partial (\mathcal{M}_k a_k K_{pm} + c_k K_c)}{\partial \mathbf{w}} (1 + \alpha) \\
&\quad + (2\alpha E[z_k] + \beta) \frac{\partial E[z_k]}{\partial \mathbf{w}} \\
&= 2(\mathcal{M}_k a_k K_{pm} + c_k K_c) a_k K_{pm} \frac{\partial \mathcal{M}_k}{\partial \mathbf{w}} (1 + \alpha) \\
&\quad + (2\alpha(a_k \mathcal{M}_k + c_k) + \beta) a_k \frac{\partial \mathcal{M}_k}{\partial \mathbf{w}} \\
&= \frac{\partial \mathcal{M}_k}{\partial \mathbf{w}} a_k (2(\mathcal{M}_k a_k K_{pm} + c_k K_c) K_{pm} (1 + \alpha) + (2\alpha(a_k \mathcal{M}_k + c_k) + \beta)) \\
&= \frac{\partial \mathcal{M}_k}{\partial \mathbf{w}} a_k (2\mathcal{M}_k a_k K_{pm}^2 (1 + \alpha) + 2\alpha a_k \mathcal{M}_k + 2c_k K_c K_{pm} (1 + a_k) + 2\alpha c_k + \beta) \\
&= \frac{\partial \mathcal{M}_k}{\partial \mathbf{w}} a_k (2\mathcal{M}_k a_k (K_{pm}^2 (1 + \alpha) + \alpha) + 2c_k (K_c K_{pm} (1 + \alpha) + \alpha) + \beta). \quad (\text{B.33})
\end{aligned}$$

The Fisher information is identical to that of known contamination; however, the variance is somewhat more complicated as it is modified by the variance of the additive contamination.

## B.4 Application of the Fisher Information for Contaminated Observations

The Fisher information matrix for contaminated observations is used to calculate the Cramer-Rao lower bound. However, since the contamination changes the bias of the estimates, to calculate the biased CRB the bias must be approximated using Monte-Carlo simulation in addition to the contaminated Fisher information. The following subsections discuss how the contaminated Fisher information can be applied to the contamination mitigation problems addressed in this dissertation.

### B.4.1 Application to Land Contaminated Wind Retrieval

Land contamination can be treated as an attenuation of the wind signal with an additive contribution from land. The attenuation is due to the fact that during land contamination the ocean signal does not entirely fill the antenna footprint. Thus the ocean backscatter signal is attenuated. The additive contribution from land is due to the land in the antenna footprint. Assuming that the  $\sigma^o$  value of land is fixed, the overall backscatter can be represented using the LCR as

$$\sigma^o = (1 - LCR)\sigma_{wind} + LCR\sigma_{land}. \quad (\text{B.34})$$

Using this model the Fisher information can be calculated for known land contamination using Eqs. B.25, B.27, and B.21 with  $a_k = 1 - LCR$  and  $c_k = LCR\sigma_{land}$ . The land contaminated form of the Fisher information matrix is used in Chapter 8 to calculate the CRB for land-contaminated wind retrieval.

### B.4.2 Application to Rain-Contaminated Wind Retrieval

Rain contaminated wind retrieval can be treated phenomenologically as an attenuation of the wind-induced backscatter due to atmospheric rain and an additive contribution from the additional backscatter due to increased surface roughness and atmospheric backscatter. This model is discussed in depth in Chapter 5. The overall backscatter can be modeled as

$$\sigma^o = \alpha_r \sigma_w + \sigma_e, \quad (\text{B.35})$$

where  $\alpha_r$  is the rain attenuation,  $\sigma_w$  is the wind-induced backscatter given by  $\mathcal{M}_k$ , and  $\sigma_e$  is the effective backscatter due to rain. The Fisher information for rain-contaminated wind retrieval can be calculated using Eqs. B.31, B.33, and B.21 with  $a_k = \alpha_r$ ,  $c_k = \sigma_e$ , and with  $K_c = K_{pe}$  the rain model uncertainty.

### B.4.3 Application to Wind-Contaminated Rain Retrieval

The backscatter observations for wind-contaminated rain-only retrieval can be modeled using the phenomenological rain model from Chapter 5 as

$$\sigma^o = \sigma_e + \alpha_r \sigma_w, \quad (\text{B.36})$$

where each term is identical to those in rain-contaminated wind retrieval. However, for rain-only retrieval the desired signal is the rain backscatter,  $\sigma_e$ , so the contamination is caused by the rain-attenuated wind backscatter,  $\alpha_r \sigma_w$ . Intuitively, when the rain attenuation is high the contamination due to wind is low, and with the attenuation is low the contamination due to wind can be high if  $\sigma_w$  is much larger than  $\sigma_e$ . The Fisher information for wind-contaminated rain-only retrieval can be calculated using Eqs. B.31, B.33, and B.21 with  $y_k = \sigma_e$ ,  $a_k = 1$ ,  $c_k = \alpha_r \sigma_w$ , with  $K_{pm} = K_{pe}$  and with  $K_c = K_{pm}$ .

### B.4.4 Fisher Information for Simultaneous Wind and Rain Retrieval

Although rain can be a source of contamination in wind-only retrieval, when a model for rain exists the rain can be estimated simultaneously with the wind. The Fisher information for SWR can be calculated using the Fisher information for random contamination. The attenuation term is replaced with the rain attenuation  $a_k = \alpha_r$ , the additive contamination is replaced with the effective rain backscatter  $c_k = \sigma_e$ , and the normalized standard deviation of the contamination with the rain backscatter model uncertainty  $K_c^2 = K_{pe}^2$ .

The principle difference between the SWR Fisher information and that of rain-contaminated wind-only retrieval is that for SWR retrieval the wind vector  $\mathbf{w}$  has three components speed, direction and rain rate. The variance of the observations is thus identical to the random contamination case but the partial derivatives of the variance and the mean are not quite as simple as the contamination is now a function of the wind vector (since the wind vector includes rain). With this in mind the partial derivatives of the variance can be

written as

$$\begin{aligned}
\frac{\partial \varsigma_k^2}{\partial \mathbf{w}} &= 2(\mathcal{M}_k \alpha_{r_k} K_{pm} + \sigma_{e_k} K_{pe}) \frac{\partial (\mathcal{M}_k \alpha_{r_k} K_{pm} + \sigma_{e_k} K_{pe})}{\partial \mathbf{w}} (1 + \alpha) \\
&\quad + (\mathcal{M}_k \alpha_{r_k} K_{pm} + \sigma_{e_k} K_{pe})^2 \frac{\partial \alpha_{r_k}}{\partial \mathbf{w}} + (2\alpha(\alpha_{r_k} \mathcal{M}_k + \sigma_{e_k}) + \beta) \frac{\partial (\alpha_{r_k} \mathcal{M}_k + \sigma_{e_k})}{\partial \mathbf{w}} \\
&= 2(\mathcal{M}_k \alpha_{r_k} K_{pm} + \sigma_{e_k} K_{pe}) (1 + \alpha) \left( K_{pm} \left( \mathcal{M}_k \frac{\partial \alpha_{r_k}}{\partial \mathbf{w}} + \alpha_{r_k} \frac{\partial \mathcal{M}_k}{\partial \mathbf{w}} \right) + K_{pe} \frac{\partial \sigma_{e_k}}{\partial \mathbf{w}} \right) \\
&\quad + (\mathcal{M}_k \alpha_{r_k} K_{pm} + \sigma_{e_k} K_{pe})^2 \frac{\partial \alpha_{r_k}}{\partial \mathbf{w}} \\
&\quad + (2\alpha(\alpha_{r_k} \mathcal{M}_k + \sigma_{e_k}) + \beta) \left( \mathcal{M}_k \frac{\partial \alpha_{r_k}}{\partial \mathbf{w}} + \alpha_{r_k} \frac{\partial \mathcal{M}_k}{\partial \mathbf{w}} + \frac{\partial \sigma_{e_k}}{\partial \mathbf{w}} \right). \tag{B.37}
\end{aligned}$$

The Fisher information matrix  $J$  is

$$\begin{aligned}
J_{ij} &= \sum_{k=1}^4 \left( \mathcal{M}_k \frac{\partial \alpha_{r_k}}{\partial w_i} + \alpha_{r_k} \frac{\partial \mathcal{M}_k}{\partial w_i} + \frac{\partial \sigma_{e_k}}{\partial w_i} \right) \frac{1}{\varsigma_k^2} \left( \mathcal{M}_k \frac{\partial \alpha_{r_k}}{\partial w_j} + \alpha_{r_k} \frac{\partial \mathcal{M}_k}{\partial w_j} + \frac{\partial \sigma_{e_k}}{\partial w_j} \right) \\
&\quad + \frac{\partial \varsigma_k^2}{\partial w_i} \frac{1}{2\varsigma_k^4} \frac{\partial \varsigma_k^2}{\partial w_j}, \tag{B.38}
\end{aligned}$$

which is used in Chapters 5, 6 and 7 to calculate the CRB for SWR retrieval.

## B.5 Summary

The Fisher information matrix for contaminated observations is vital to quantifying the uncertainty in the estimates by way of the CRB. However, the discussion in this appendix only describes the effects of contamination on the Fisher information. As all types of contamination change the bias of the estimates, the effects of contamination on the estimate bias must be evaluated as well. This is performed for each estimator via Monte-Carlo simulation and the results are discussed in more detail in the relevant chapters.

## Appendix C

### The Rain Likelihood Flag: An Ultra-High Resolution Rain Flag

Although, there are several rain flags which are applicable to conventional 25 km QuikSCAT products [56][57], there are no rain flags which function on UHR 2.5 km wind products. This appendix describes the rain likelihood flag (RLF), a proposed rain flag for UHR data which can be used to identify rain-contaminated WVCs. The RLF is an alternative approach to methods in Chapters 6 and 7 but could be used in conjunction with them although such a joint approach is not pursued here.

The RLF is calculated by searching for a maximum of the SWR log-likelihood function, Eq. 5.7, in rain rate while keeping the wind vector fixed at the value given by the wind-only solution. If there is a more likely raining solution, i.e. a maxima exists for a non-zero rain rate, the WVC is flagged as rain-contaminated and SWR retrieval is performed. In addition to identifying rainy WVCs, the RLF is advantageous as it can be used to identify when to perform SWR. This can reduce the required computation for wind and rain estimation as the SWR estimates are only calculated when necessary.

To illustrate the functionality of the RLF, Fig. C.1 shows TRMM rain rates, QuikSCAT rain rates and the RLF for a single co-location. The RLF correctly flags many of the rain events, however some small rain events with low rain rates are not identified. Additionally, note that the RLF flags more WVCs than necessary near large rain events. This can be partially attributed to the spatial smoothing of the backscatter field that is inherent in the resolution enhancement process.

To demonstrate the performance of this simple rain flagging technique, Fig. C.2 shows the probability of missed detection ( $P_{md}$ ) and the probability of false alarm ( $P_{fa}$ ) for the RLF for one year of QuikSCAT and TRMM PR co-located data. The missed detection performance is separated into wind and rain regimes. Regime 0 corresponds to wind-dominated conditions, regime 1 to conditions where wind and rain backscatter is comparable, and regime 2 corresponds to rain-dominated conditions. The indicated rain threshold is the rain rate in km-mm/hr that determines a rain event. When the rain threshold is high, i.e. low rain events are ignored, the probability of missed detection is low as is the probability of false alarm.

The false alarm rate for the RLF is relatively high regardless of the rain threshold. This is acceptable in this application of the RLF since it simply indicates rain is probable so SWR retrieval should be performed. For rain events with high rain rates the probability of missed detection decreases steadily. This indicates that it is rare for the RLF not to flag moderate to high rain rates. The probability of false alarm also increases with the rain threshold, which is not a concern since the RLF is always sensitive to lower rain rates and so false alarms can be triggered by lower, but significant, rain rates. As might be expected,

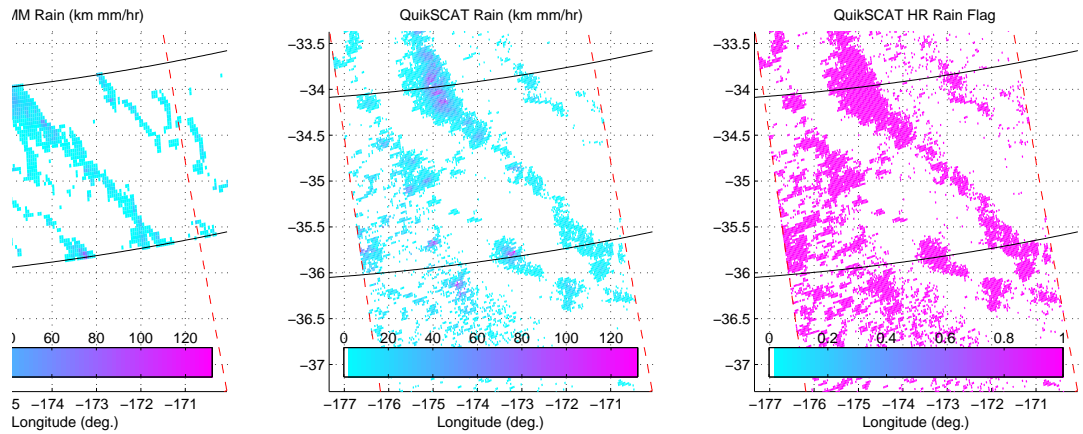


**Figure C.1:** TRMM rain rate (left), QuikSCAT rain rate (middle) and RLF (right) for one overlapping region. TRMM swath edges are indicated by the black lines and the red dashed lines indicate the edges of the processed QuikSCAT data solid black indicates land. Although QuikSCAT fails to detect the lowest rain rates, the spatial correlation of the three data sets is quite apparent. The rain rate color scale for this image ranges from 0 to 132 km-mm/hr.

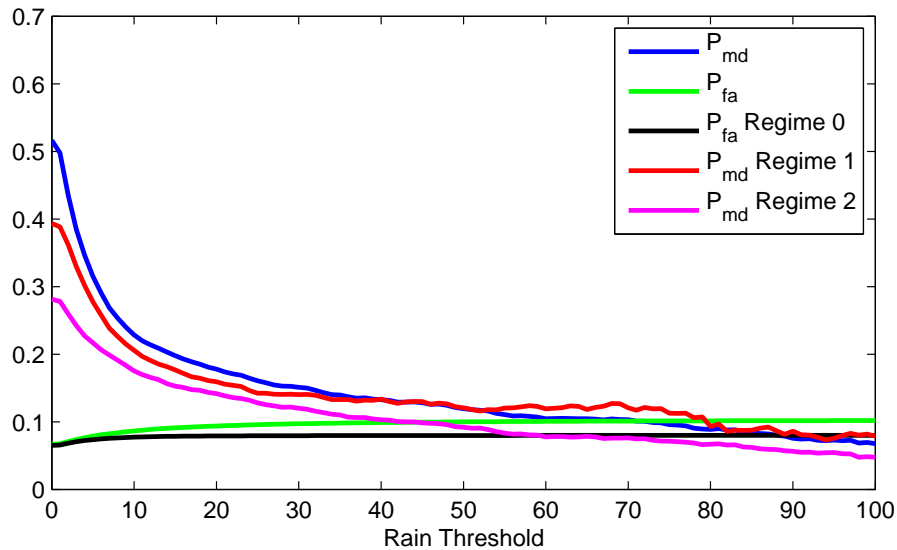


**Figure C.2:** Probability of false and alarm and probability of missed detection for the RLF as a function of rain threshold and regime.  $P_{md}$  is not included for regime 0 since when wind is dominant rain detection is known to be poor.  $P_{fa}$  for regimes 1 and 2 since a dominating rain rates should be flagged regardless of rain rate. The rain threshold is the rain rate which in each comparison indicates a rain event. The decreasing missed detection rate indicates that the RLF correctly identifies high rain rates in most cases.

the false alarm rate is lower for wind dominated conditions and the missed detection rate is lower for rain dominated conditions.

Some performance degradation of the RLF can be attributed to uneven beam-filling. Due in part to the resolution enhancement process, beam-filling can have some misleading effects. The QuikSCAT antenna spatial response is much larger than the pixel size at UHR causing, high rain rates to appear as lower rain rates spread across several WVCs. This can be noted in Fig. C.1 where QuikSCAT appears to widen the north-south rain bands apparent in TRMM PR rain rates. Since the highest rain rates are typically localized to a few WVCs, the RLF missed detection rate can be higher than expected due to beam-filling effects. Draper and Long [61] showed that although beam-filling effects can cause significant variability in the estimates, the bias they introduce is small. It is also possible to adjust the sensitivity of the RLF to further reduce the missed detection rate at the cost of the increasing the number of false alarms.

Although the RLF is not currently included in any publicly available QuikSCAT wind products, it may be implemented readily and at little computational cost. Further, because the concept of the RLF is so simple, it can be easily implemented for any other scatterometer if a rain backscatter model is available.



## Appendix D

### Rain Fraction-Based Estimator Performance Prior

The conditional distribution  $f_{\mathbf{x}|\vartheta}(\mathbf{x}_j|\vartheta)$  in Bayes estimator selection represents the performance of an estimator for a given set of conditions so it is referred to as the estimator performance prior. For the sake of clarity, the estimator performance prior in Chapters 6 and 7 is calculated from Monte-Carlo simulations of wind and rain retrieval. This appendix presents an alternative model-based formulation for the estimator performance prior which lends physical insight into the interaction between wind and rain.

The estimator performance prior can be modeled in several steps. First, define a regime  $S_i$  for each estimator which corresponds to the set of wind and rain vectors where each estimator has minimum squared-error according to the total squared error cost function defined in Chapter 6.

To determine the estimator regimes, instead of attempting to analytically account for the non-linear and empiric natures of wind and rain estimation, empiric estimates of the estimator performance can be formed. For example using NCEP and TRMM PR data as with the wind-rain prior in Chapter 6. Treating NCEP wind and TRMM PR rain data as the true conditions  $\vartheta$ , the squared error for each estimator is  $e_i = (\vartheta - \mathbf{x}_i)^2$  and the best estimator that for which  $e_i$  is a minimum.

This method allows one to empirically determine the regimes  $S_i$  in the wind rain space. Each regime  $S_i$  is the set of vectors  $\vartheta$  for which  $e_i < e_j$  for  $i \neq j$ . The regime  $S_i$  can then be interpreted as the set of wind-rain vectors for which the estimator  $\mathbf{x}_i$  is the best estimator on average (in a squared-error sense) of the true  $\vartheta$ .

Although this definition of the regimes is an appropriate way to characterize the average estimator performance, it has several limitations which impede its utility in estimator selection. Particularly, this definition implies a deterministic estimator selection given the true conditions when in reality the regime boundaries are not sharp. Instead, for a given condition a particular estimator may be best under certain noise realizations while another may be better with a different noise realization. Thus a probabilistic approach to the regime definition is more appropriate. Further the empiric regime definition does not reflect knowledge of the QuikSCAT noise model. Finally, note that QuikSCAT does not directly observe wind and rain, but instead measures the surface radar backscatter  $\sigma^o$  which relates to wind and rain via non-linear model functions. As an alternative to the empiric regime definitions we propose use of the rain fraction as a more physically meaningful regime definition to address the estimator differences at a backscatter level.

## D.1 Rain Fraction

As an initial step in modeling the estimator performance, the various regimes may be defined in terms of the relative signal strengths of the wind and rain backscatter as follows.

First, the rain fraction  $C(\vartheta)$  is defined to be

$$C(\vartheta) = \frac{\sigma_e}{\alpha_r \sigma_w}, \quad (\text{D.1})$$

where  $\sigma_e$  and  $\alpha_r \sigma_w$  are the modeled backscatter quantities. The rain fraction can be intuitively understood to be the signal to interference ratio (SIR) of the effective rain backscatter  $\sigma_e$  and the rain-attenuated wind backscatter  $\alpha_r \sigma_w$ . Because  $\sigma_e$  and  $\alpha_r \sigma_w$  are in reality random variables, the rain fraction is also a random variable with realizations  $c(\vartheta)$  and a distribution controlled by the true wind and rain conditions. Note that the rain fraction is dependent on measurement geometry and polarization although it is not expressly included in the notation. This implies that the rain fraction is different for each antenna look type and polarization due to differing observation geometry; so for any observed wind and rain rate there are 4 different rain fraction values, one for each observation type.

A QuikSCAT backscatter measurement is typically assumed to be a Gaussian random variable with mean determined by the model and variance a function of the model backscatter and communication and receiver noise. For QuikSCAT, the observed effective rain backscatter can be modeled as

$$\sigma_e = \sigma_e(r)(1 + K_{pc}\eta_1)(1 + K_{pe}\eta_2), \quad (\text{D.2})$$

where  $\sigma_e(r)$  is the model backscatter as a function of  $r$  the rain rate,  $K_{pe}$  is the normalized standard deviation of the effective rain backscatter model and  $\eta_1$  and  $\eta_2$  are independent zero-mean unit-variance Gaussian random variables.

$K_{pc}$  is the normalized standard deviation of the communication noise which is defined for QuikSCAT to be

$$K_{pc} = \sqrt{\alpha + \frac{\beta}{\sigma_t} + \frac{\gamma}{\sigma_t^2}}, \quad (\text{D.3})$$

where  $\alpha$ ,  $\beta$  and  $\gamma$  are constants particular to QuikSCAT and  $\sigma_t$  is the total observed backscatter

$$\sigma_t = \alpha_r \sigma_w + \sigma_e. \quad (\text{D.4})$$

The mean of  $\sigma_e$  can be written

$$E(\sigma_e) = \sigma_e(r) \quad (\text{D.5})$$

and the variance is

$$Var(\sigma_e) = \sigma_e(r)^2(1 + K_{pc}^2)(1 + K_{pe}^2) - \sigma_e(r)^2. \quad (\text{D.6})$$

Similarly,  $\alpha_r \sigma_w$  can be modeled as

$$\alpha_r \sigma_w = \mathcal{M}(w)(1 + K_{pc}\eta_1)(1 + K_{pm}\eta_3)10^{-\alpha_{dB}(r)(1+K_{pa}\eta_4)/10} \quad (\text{D.7})$$

$$\cong \mathcal{M}(w)(1 + K_{pc}\eta_1)(1 + K_{pm}\eta_3)\alpha_r(r)(1 + (1 - \alpha_r(r))K_{pa}\eta_4), \quad (\text{D.8})$$

where  $\mathcal{M}(w)$  is the wind-induced model backscatter as a function of the wind vector  $w$ ,  $K_{pm}$  is the normalized standard deviation of the model,  $\alpha_{dB}$  is the path integrated attenuation in dB,  $\alpha_r(r)$  is the attenuation model as a function of the rain rate  $r$ ,  $K_{pa}$  is the normalized standard deviation of the attenuation model and  $\eta_1$ ,  $\eta_3$  and  $\eta_4$  are independent zero-mean unit-variance Gaussian random variables. To simplify the model, the path integrated attenuation term is simplified using a truncated Taylor series expansion of  $10^x$  around  $x = 0$  resulting in Eq. D.8 [61]. Using the approximation in D.8 results in a mean of

$$E(\alpha_r \sigma_w) = \alpha_r(r)\mathcal{M}(w) \quad (\text{D.9})$$

and a variance of

$$Var(\alpha_r \sigma_w) = \alpha_r(r)^2 \mathcal{M}(w)^2 (1 + K_{pm}^2)(1 + (1 - \alpha_r(r))^2 K_{pa}^2)(1 + K_{pc}^2) - \alpha_r(r)^2 \mathcal{M}(w)^2. \quad (\text{D.10})$$

The correlation between  $\sigma_e$  and  $\alpha_r \sigma_w$  can be written

$$\rho = \frac{\sigma_e(r)\alpha_r(r)\mathcal{M}(w)K_{pc}^2}{\sqrt{Var(\sigma_e)Var(\alpha_r \sigma_w)}}. \quad (\text{D.11})$$

Supposing that  $\sigma_e$  and  $\alpha_r \sigma_w$  are approximately Gaussian, the rain fraction distribution is then a ratio distribution of two correlated Gaussian random variables. Such a distribution is studied in [100] where it was shown that the cumulative distribution function of the rain fraction,  $F_C(c)$ , is

$$F_C(c) = L \left\{ \frac{\sigma_e - \alpha_r \sigma_w c}{\varsigma_e \varsigma_w a(c)}, -\frac{\alpha_r \sigma_w}{\varsigma_w}, \frac{\varsigma_w r - \rho \varsigma_e}{\varsigma_e \varsigma_w a(c)} \right\} + L \left\{ \frac{\alpha_r \sigma_w c - \sigma_e}{\varsigma_e \varsigma_w a(c)}, \frac{\alpha_r \sigma_w}{\varsigma_w}, \frac{\varsigma_w c - \rho \varsigma_e}{\varsigma_e \varsigma_w a(c)} \right\}, \quad (\text{D.12})$$

where  $\rho$  is the correlation coefficient between the numerator and denominator,  $\sigma_e$  is the mean of the numerator with standard deviation  $\varsigma_e$ , and  $\alpha_r \sigma_w$  is the mean of the denominator with standard deviation  $\varsigma_w$ . The function  $a(r)$  is defined to be

$$a(c) = \sqrt{\frac{c^2}{\varsigma_e^2} - \frac{2\rho c}{\varsigma_e \varsigma_w} + \frac{1}{\varsigma_w^2}} \quad (\text{D.13})$$

and  $L(\cdot, \cdot, \cdot)$  is bivariate normal integral defined as

$$L(h, k, \gamma) = \frac{1}{2\pi\sqrt{1-\gamma^2}} \int_h^\infty \int_k^\infty \exp\left\{-\frac{x^2 - 2\gamma xy + y^2}{2(1-\gamma^2)}\right\} dx dy. \quad (\text{D.14})$$

## D.2 Regime Boundaries

Since the rain fraction cumulative distribution is known, an indicator function can be defined  $X$  in terms of the rain fraction  $r(\vartheta)$  for each antenna look

$$X = \begin{cases} 0 & \text{for } C(\vartheta) < A \\ 1 & \text{for } A < C(\vartheta) < B \\ 2 & \text{for } C(\vartheta) > B \end{cases}, \quad (\text{D.15})$$

where the values taken by  $X$  are the estimator regimes and  $A$  and  $B$  are constants. When  $X$  equals 0, 1 or 2 then the best squared-error estimate of  $\vartheta$  is produced using the wind-only estimate, the simultaneous-wind-rain estimate or the rain-only estimate respectively. Using the rain fraction distribution the distribution of the indicator variable  $X$  can be written conditioned on  $\vartheta$

$$\begin{aligned} P(X = 0|\vartheta) &= F_C(A), \\ P(X = 1|\vartheta) &= F_C(B) - F_C(A), \\ P(X = 2|\vartheta) &= 1 - F_C(B). \end{aligned} \quad (\text{D.16})$$

This formulation for the distribution of the indicator variable  $X$  is the desired estimator performance model. All that remains is to determine the constants  $A$  and  $B$  for each antenna look which characterize the regime boundaries.

Determining the regime boundaries  $A$  and  $B$  for each look in the rain fraction space requires an evaluation of the actual performance of the estimators. Using the QuikSCAT and TRMM PR co-located measurement sets described in Chapter 6, the average squared error can be computed for each of the estimators as a function of the ‘true’ wind conditions and rain rates as predicted by NCEP and measured by TRMM PR. The best estimator for a wind-rain vector is thus the estimator with the smallest average squared error over the data set. Using this definition of the best estimator each wind-rain vector can be assigned to a regime corresponding to a specific estimator thereby dividing the wind-rain space into 3 disjoint regions or regimes.

Using the models for wind and rain backscatter enables the determination of the density of rain fractions for each regime  $f_{C(\vartheta)|X}(c(\vartheta)|x)$ . The conditional rain fraction densities are shown in Fig. D.1 for each antenna look. Although the empirical regimes are disjoint in the wind-rain space the rain fraction densities are not. As illustrated by Fig. D.1 the rain fraction is a good indicator of the regime. The rain fraction densities are relatively distinct, and although they are not disjoint, the regions where they overlap are understandable. The slight overlap of the rain fraction densities represent the fact that where the rain fraction indicates that simultaneous wind and rain retrieval is best, occasionally wind-only or rain-only retrieval might be better.

It is important to remember that the densities shown in Fig. D.1 are in reality distributions of the nominal rain fraction, the rain fraction given by the wind and rain models. Figure D.1 shows the densities of the modeled or expected rain fraction for the wind-rain vectors in each regime. Although this is only an approximation to the density  $f_{C(\vartheta)|X}$ , it allows reasonable estimates of the thresholds  $A$  and  $B$  to be formed. Additionally, the data used to determine estimator performance lacked high-wind cases and so they are underrepresented in the regime analysis. Despite this limitation, an advantage of the rain fraction

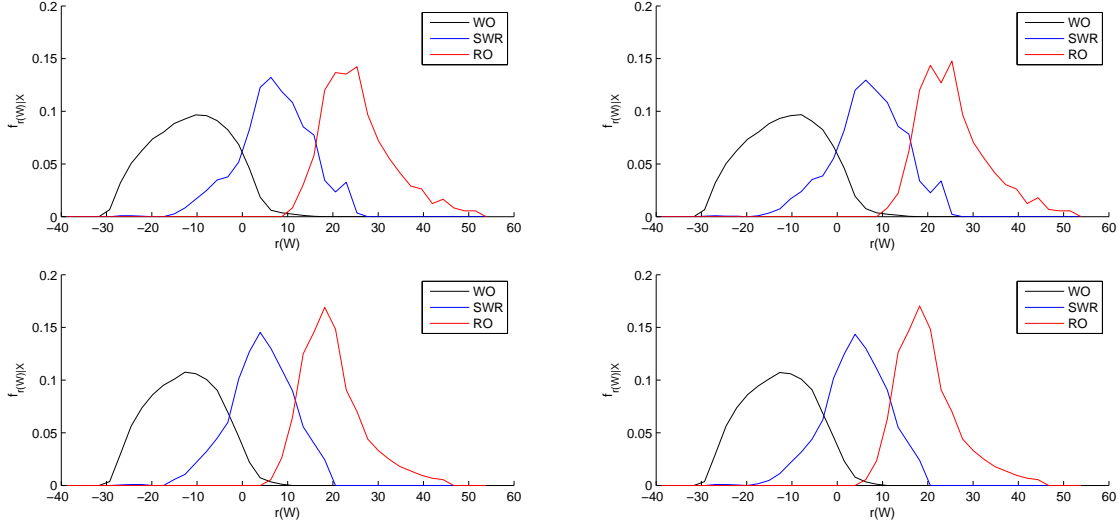


**Figure D.1:** Conditional densities of  $C(\vartheta)$  for each regime for each look geometry. H-pol measurements are on top and V-pol measurements the bottom with foreward looks on the left and aft looks on the right.

definition is that it applies to all wind and rain vectors based on the assumption that the estimators have similar performance for similar rain fractions even if the wind and rain rates are significantly higher.

The regime definition adopted using this approximation is then the interval for which  $f_{C(\vartheta)|X}(c(\vartheta)|x = i) \geq f_{C(\vartheta)|X}(c(\vartheta)|x = j) \forall i \neq j$ . With this definition the thresholds  $A$  and  $B$  for each observation flavor are the intersections of the conditional distributions shown in Fig. D.1 with values shown in Table D.1. Although using the rain fraction with these thresholds does not perfectly characterize the estimator performance, only 18% of wind-rain vectors are inaccurately classified using the specified rain fraction thresholds and of those, the errors are predominately in the rain-only regime which have lower probability of occurrence. Additionally, the misclassification of the rain-only regime typically causes a simultaneous-wind-rain estimate to be used. This degrades the rain estimate but results in an estimate of the wind as well, thereby providing information that rain-only retrieval otherwise would not. Similarly, some misclassification errors occur between the wind-only and simultaneous-wind-rain estimators. As before, this type of error is tolerable because rain rates are typically small in this regime so the additional error in not estimating or falsely estimating the rain is relatively small.

The rain fraction definition of the estimator performance is inherently an approximation to the actual estimator performance. As such there are classification errors which are unavoidable. These classification errors often occur between the WO and SWR, and the SWR and RO estimates. For example, although the overall performance may be degraded slightly when the SWR estimator is selected when the WO estimate has minimum squared error, the additional information provided by the SWR rain estimate makes this type of error more acceptable. In short, although there is some misclassification of the regimes inherent

**Table D.1:** Rain fraction regime boundaries

Polarization	Direction	A	B
V	fore	-2.8	11.7
H	fore	-0.06	16.3
H	aft	-0.24	16.2
V	aft	-2.9	11.7

in the rain fraction definition, the majority of misclassification errors indicate SWR retrieval which is typically a suitable alternative to WO or RO estimation.

A similar misclassification occurs when the SWR estimate is best and the WO or RO estimate is selected. In this case some information is lost as an estimate of wind or rain is not formed but this degradation is balanced somewhat by the fact that the increased accuracy of the wind or rain estimate.

In terms of the signal to interference ratio of the wind and rain signals, the regime thresholds offer interesting insights into the performance of the various estimators. Wind-only retrieval is best when the wind signal magnitude is greater than twice that of the rain signal. As the strength of the rain signal increases simultaneous wind and rain retrieval offers good performance, but after a cutoff point at  $B$  wind information is rarely retrievable or useful.

After determining the coefficients  $A$  and  $B$ , the estimator performance model can now be written in terms of the probability of an estimator being best for a given wind condition,  $f(X|\vartheta)$  for  $X = 0, 1, 2$ . The estimator performance prior of a single direction for each estimator is shown in Fig. D.2. The rain fraction-derived estimator performance priors in Fig. D.2 correspond quite well to the Monte-Carlo derived priors in Chapters 6 and 7 indicating that approximating the estimator performance using the rain fraction may be a useful approximation.

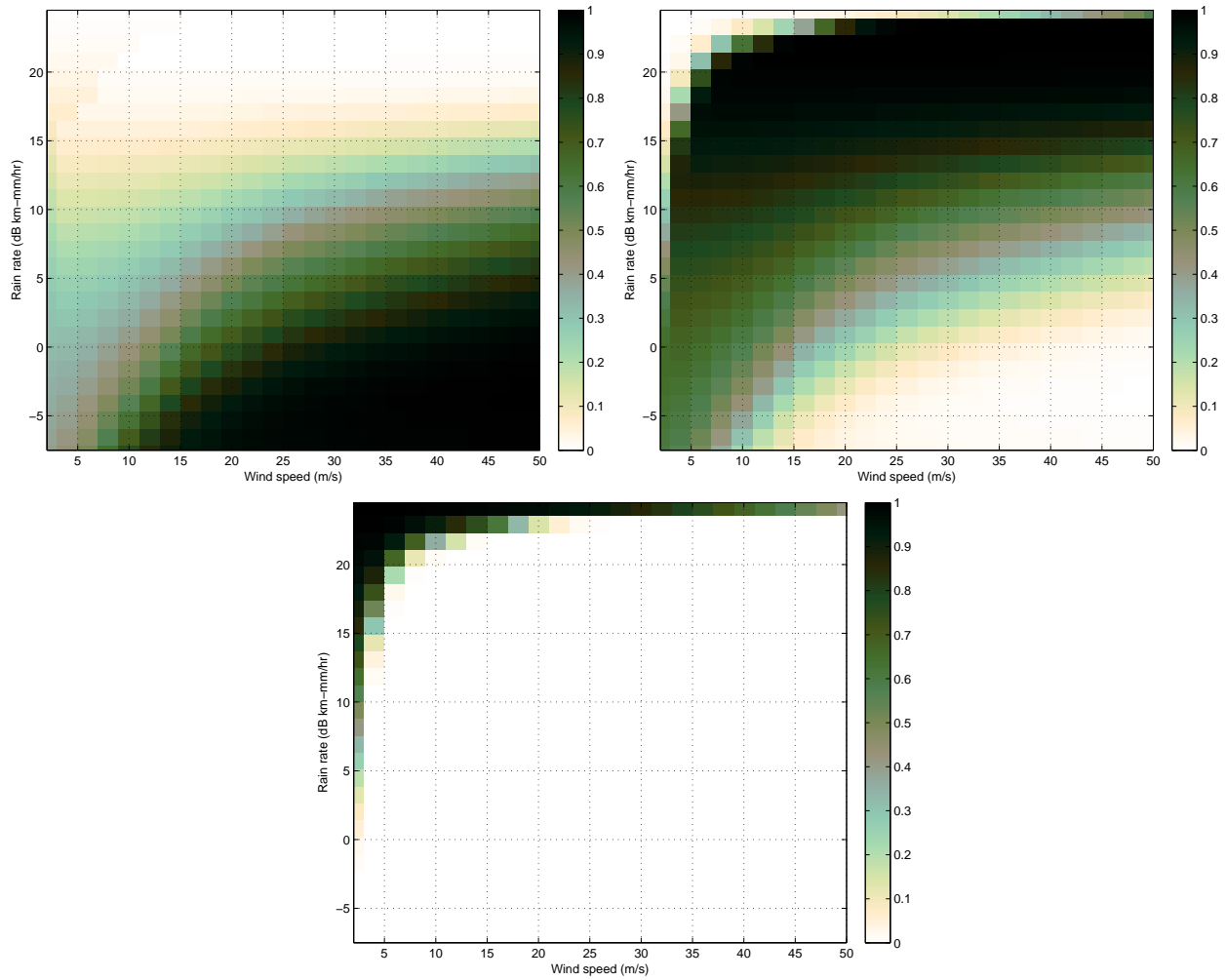


**Figure D.2:** Estimator performance densities  $f_{\mathbf{X}|\theta}(\mathbf{x}_j|\vartheta)$  using the rain fraction formulation plotted for one wind direction. Top-left: wind-only. Top-right: Simultaneous wind-rain. Bottom: rain-only. Darker areas correspond to wind-rain vectors where a particular estimator has better performance.



## Appendix E

### Interference Information

Chapter 6 motivates the need for multiple estimators using the total squared error and the Cramer-Rao lower bound. This appendix introduces an alternative information theoretic motivation for multiple estimators using the concept of interference information based on the Kullback-Leibler divergence. In this appendix, interference information is defined and its significance is discussed. Then interference information is used to define the parameter space for which a given reduced-order model is suitable. Applying the interference information concept to simultaneous wind and rain retrieval for the QuikSCAT scatterometer yields intuitively pleasing results which correspond clearly to the estimator regimes defined in chapter 6 using the CRB and the estimator performance prior.

#### E.1 Motivation

Model-based estimation is a powerful technique for inferring true conditions based on a set of observations. An appropriate model can allow for the estimation of several distinct phenomena at the cost of model complexity and computation time. Under certain conditions however, the model variance together with observation variance can lead to degraded estimator performance with the true model. Under these conditions, usage of a reduced-order approximate model can lead to improved performance by simplifying the estimation problem.

#### E.2 Problem Formulation

An estimate, denoted  $\hat{\underline{\theta}}$ , of a vector valued parameter  $\underline{\theta} = \{\theta_1, \theta_2\}$  is desired where  $\theta_i$  can be individual components or subsets of components of  $\theta$ . The parameter  $\underline{\theta}$  determines the distribution of the observations  $\mathbf{X}$ . The conditional distribution of the observations given the true parameter is  $f_{\mathbf{X}|\underline{\theta}}(\mathbf{x}|\underline{\theta})$ . This distribution is the true model to be used in model-based estimation of  $\underline{\theta}$ .

Estimating a vector quantity is not equivalent to separately estimating the components and recombining, i.e.  $\hat{\underline{\theta}} \neq \{\hat{\theta}_1, \hat{\theta}_2\}$  due to correlation between components of  $\theta$  and observations. The model  $f_{\mathbf{X}|\underline{\theta}}(\mathbf{x}|\underline{\theta})$  accounts for component and observation correlation thus making estimation possible under a variety of conditions. Under some conditions, however, a subset of the components of  $\underline{\theta}$  may dominate the observations.

For example, given a particular parameter value  $\{\theta_1, \theta_2\}$  the observations may be dominated by the parameter components of  $\theta_1$ . In such a case the relatively small contribution to the observations due to  $\theta_2$  may make any estimates of  $\underline{\theta}$  particularly poor for the parameter components in  $\theta_2$  and may further degrade the parameter estimates of  $\theta_1$ . For

such a case the estimate error in  $\hat{\theta}$  can be reduced by estimating only the parameters with significant contribution to the observations thereby forming an estimate of  $\theta_1$  alone. The question that remains to determine is: Under what conditions is it advantageous to simplify the estimation problem by reducing the model order and estimating only certain components of  $\theta$ ?

### E.3 Interference Information

The answer to this question can be approached by dividing  $\theta$  into two possibly disjoint subsets of components,  $\theta_1$  and  $\theta_2$ . After division, approximate models can be formed that neglect any parameters that have insignificant contributions to the observations. When the observations are dominated by the parameter components in  $\theta_1$ , an approximate conditional density  $\hat{f}_{X|\theta_1}(x|\theta_1)$  can be constructed. This conditional density is formed by making the assumption that the observations do not depend on  $\theta_2$ . For the case where observations are dominated by  $\theta_2$  the density  $\hat{f}_{X|\theta_2}(x|\theta_2)$  is formed. By replacing the combined model  $f_{X|\theta}(x|\theta)$  with an approximate model, estimates for  $\theta_1$  or  $\theta_2$ , which are denoted  $\hat{\theta}_1$  and  $\hat{\theta}_2$  respectively, can be formed based on the observations.

Although the partial estimators  $\hat{\theta}_1$  and  $\hat{\theta}_2$  can have improved performance under certain conditions, neither is suited for all possible conditions. Additionally, forming both partial estimators and recombining to form an estimate of  $\theta$  is not equivalent to forming the estimate  $\hat{\theta}$  using the true model outright.

This situation leads naturally to the question of how to determine the conditions for which it is best to use a given estimator. To apply existing mechanisms to answer this question, it can be rephrased. Instead it reads, under what conditions is the approximate model  $\hat{f}_{X|\theta_1}(x|\theta_1)$  close enough to the true density  $f_{X|\theta}(x|\theta)$  that the estimate  $\hat{\theta}_1$  is preferred to the estimate  $\hat{\theta}$ ? Since the answer to this question depends on a difference between probability densities, we turn to the Kullback-Leibler divergence [101].

The Kullback-Leibler divergence, defined as

$$D(f||g) = \int f(x) \log \frac{f(x)}{g(x)} dx \quad (\text{E.1})$$

is a measure of the difference between the probability densities  $f(x)$  and  $g(x)$ . Note that the Kullback-Leibler divergence is related to mutual information  $I(X; Y)$  by

$$D(f_{XY}||f_X f_Y) = I(X; Y) \quad (\text{E.2})$$

indicating that the mutual information is the Kullback-Leibler divergence of the joint density and the product of the marginals.

In a similar way we define the interference information for an estimator to be the Kullback-Leibler divergence of the true conditional density and the approximate. For  $\hat{\theta}_1$  the interference information becomes

$$I_{\hat{\theta}_1}(\theta) = D(f_{\theta}||\hat{f}_{\theta_1}) = \int_X f(x|\theta) \log \frac{f(x|\theta)}{\hat{f}(x|\theta_1)} dx. \quad (\text{E.3})$$

The interference information for  $\hat{\theta}_2$  is defined similarly to be

$$I_{\hat{\theta}_2}(\theta) = D(f_\theta || \hat{f}_{\vartheta_2}) = \int_X f(x|\theta) \log \frac{f(x|\theta)}{\hat{f}(x|\vartheta_2)} dx. \quad (\text{E.4})$$

Interference as used in the interference information given above differs from interference in the usual communications sense. ‘‘Interference information’’ is information not accounted for in the approximate model which interferes with the estimation process resulting in a contaminated estimate. Restated, the interference information for the estimators can be understood to be the amount of information in the true density which ‘‘interferes’’ with an estimate made using an approximate density for the parameter  $\theta$ .

The interference information for the combined estimate  $\hat{\theta}$  is slightly different. We define it to be

$$I_{\hat{\theta}}(\theta) = D(f_\theta || \hat{f}_{\vartheta_1} \hat{f}_{\vartheta_2}) = \int_X f(x|\theta) \log \frac{f(x|\theta)}{\hat{f}(x|\vartheta_1) \hat{f}(x|\vartheta_2)} dx. \quad (\text{E.5})$$

Here the interference information is a measure of the difference between the joint density and the product of the approximate densities. For the joint estimator, the ‘interference’ is the information in the true density which interferes with separate estimation of  $\theta_1$  and  $\theta_2$  using the approximate reduced-order models.

Interestingly, the interference information for each estimator is related by

$$I_{\hat{\theta}}(\theta) = I_{\hat{\theta}_1}(\theta) + I_{\hat{\theta}_2}(\theta) - \int_X f(x|\theta) \log f(x|\theta) dx, \quad (\text{E.6})$$

which can be rewritten in terms of the conditional entropy as

$$I_{\hat{\theta}}(\theta) = I_{\hat{\theta}_1}(\theta) + I_{\hat{\theta}_2}(\theta) + H(X|\theta), \quad (\text{E.7})$$

which indicates that the interference information for the estimators are all related to each other and the entropy of the observations.

### E.3.1 Estimator Regimes

With the interference information defined, the problem of determining what conditions are best for each estimator reduces to finding the estimator with the minimum interference information for each value of  $\theta$ . The best estimator to use in an interference information sense is then the estimator which has the minimum interference information. For the cases of the partial estimators  $\hat{\theta}_1$  and  $\hat{\theta}_2$  this means that there is little difference between the approximate model and the true model indicating that a reduced order estimation problem is superior. For the complete estimator  $\hat{\theta}$  a low interference information indicates that there is correlated information in the joint model not accounted for in the partial approximate models.

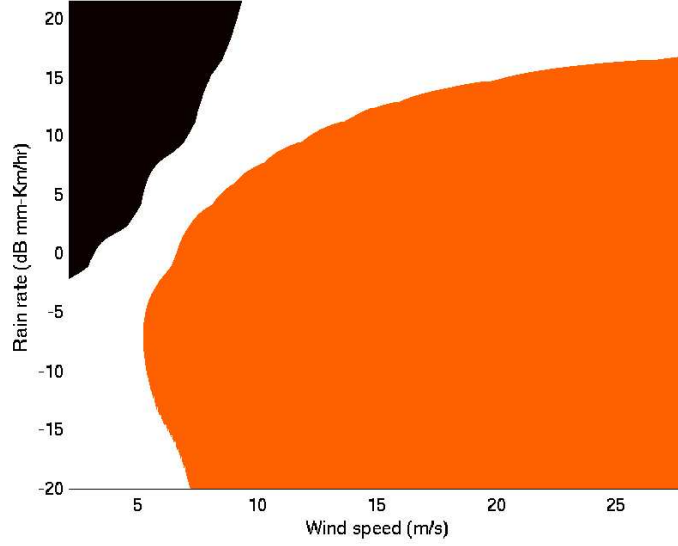


**Figure E.1:** Estimator regions as defined using interference information corresponding to wind-only, rain-only and simultaneous wind and rain estimation. The black region corresponds to  $R_{\hat{R}}$ , the white to  $R_{\hat{S}}$  and the gray to  $R_{\hat{W}}$ . As might be expected, when rain is high and wind is low, the rain-only estimator is best. When wind is high and rain is low the wind-only estimator is best. When both wind and rain are moderate to high the simultaneous wind and rain estimator is preferred.

This interpretation allows for the definition of a regime for each estimator

$$R_{\hat{\theta}} = \{\theta : I_{\hat{\theta}} < I_{\hat{\theta}_i}; \forall i\}, \quad (\text{E.8})$$

$$R_{\hat{\theta}_i} = \{\theta : I_{\hat{\theta}_i} < I_{\hat{\theta}} < I_{\hat{\theta}_j}; \forall i \neq j\}. \quad (\text{E.9})$$

With this definition, the regime for an estimator is the set in the parameter space where the interference information of the estimator is less than all other estimators. The introduction of regimes lends itself to this intuitive interpretation. When an estimator is used outside of its particular estimation regime the estimates are contaminated and degraded by the interference information and another estimator with lower interference information is preferred.

#### E.4 Application

As an application of the interference information concept, this section uses the above method to divide a parameter space into regions suitable for separate estimators. For simultaneous wind and rain retrieval using QuikSCAT data, an estimate can be produced of the wind and rain based on observations of the normalized radar cross section or backscatter,  $\sigma^o$ . Under certain conditions simultaneous estimation of both wind and rain has degraded performance and it is better to estimate the wind or the rain. In terms of the interference

information concept, we define the simultaneous wind and rain estimators to be  $\hat{S}$ ,  $\hat{W}$  and  $\hat{R}$  denoting the simultaneous wind and rain estimate, the wind-only estimate and the rain-only estimate respectively. The regime for each estimator as determined from the wind and rain model is shown in Fig. E.1. The results are quite intuitive and correspond well with the regimes defined using the Cramer-Rao lower bound in Chapter 6 as well as the regimes defined by the estimator performance priors in Chapters 6 and 7.

## E.5 Summary

In summary, the application of interference information to the multiple estimator problem clearly shows that there are times when a reduced-order model is close to the true model in addition to quantifying this difference using the interference information. Based on the interference information it is simple to divide a parameter space into regimes corresponding to the reduced-order approximate models and the true model. Additionally, based on the sample application, the interference information relates strongly to empirical performance of the estimators while only using information in the several models.